Università degli Studi di Modena e Reggio Emilia
Dipartimento di Ingegneria “Enzo Ferrari”

PhD Course in Industrial and Environment Engineering
Industrial PhD
Cycle XXXVI - PhD Program Coordinator: Prof. Alberto Muscio

DESIGN AND DEPOSITION OF COATINGS FOR THE SURFACE ENHANCEMENT OF ABUTMENTS IN DENTAL PROSTHESIS

Candidate:
Claudia Rubino

Tutor:
Prof. Luca Lusvarghi

Modena, 14th May 2025

Table of Contents

Acknowledgements i

Abstract ii

Sommario iii

Introduction 1

1. Chapter 1 – State of the Art 5

1.1. Abutment component 5

1.2. Surface Engineering 6

1.3. Bioceramics for Medical Application 9

1.3.1. Bioceramics: Types and Production 9

1.3.2. Zirconia 10

1.3.2.1. Toughening 11

1.3.2.2. Hydrothermal Instability 12

1.4. Yttria-Stabilized Zirconia Thin Films 15

1.4.1. Thin Films Deposition Technologies 15

1.4.2. Zirconia-based Ceramic Thin Film 16

1.5. Physical Vapour Deposition (PVD) 16

1.5.1. Reactive Sputtering 17

1.6. Hydrogels for TERM 21

1.7. Collagen-based Hydrogels 24

1.8. Collagen 26

1.8.1. Collagen Type 26

1.8.2. Collagen Fibrillogenesis 26

1.8.3. Functional and Structural Characteristics 28

1.8.3.1. Stability and Stiffness 28

1.8.3.2. D-banding 29

1.8.4. Key factors in the Production of Collagen-based Materials 32

1.8.4.1. pH 32

1.8.4.2. Ionic Strength 33

1.8.4.3. Acid Type for Collagen Dissolution 34

1.8.4.4. Collagen Concentration 35
1.8.4.5. Cross-linking 37
2. Chapter 2 - Materials and Method 42
2.1. Reactive Magnetron Sputtering Deposition 42
2.1.1. Substrates 42
2.1.2. Deposition Equipment 42
2.1.3. Target 44
2.1.4. Hysteresis cycle 45
2.1.5. Deposition cycle 48
2.2. Collagen-based hydrogel deposition 52
2.2.1. Substrates 52
2.2.2. Collagen solution 52
2.2.3. Deposition steps 53
2.2.3.1. Alkaline treatment 53
2.2.3.2. Biopolymeric solution preparation 53
2.2.3.3. Deposition of the biopolymeric solution 55
2.2.3.4. UV cross-linking 56
2.3. Characterization Methods 57
2.3.1. Optical microscopy 57
2.3.2. Electronic microscopy 57
2.3.3. Raman analysis 61
2.3.4. XRD analysis 62
2.3.5. Roughness measurements 63
2.3.6. Colorimetric analysis 64
2.3.7. Nano-hardness measurements 65
2.3.8. Scratch test 66
2.3.9. Wear test 68
2.3.10. Low temperature degradation testing 70
2.3.11. Rheometric test 70
2.3.12. DSC analysis 71

2.3.13. Contact angle measurement 72
3. Chapter 3 – Results 74
3.1. Yttria-Stabilized Zirconia coatings – screening phase 74
3.1.1. Macroscopic observations 74
3.1.2. Electron Microscopy observations 74
3.1.3. Roughness measurements 78
3.1.4. Nano-hardness measurements 79
3.1.5. Colorimetric analysis 79
3.1.6. Scratch test 80
3.1.7. Raman analysis 84
3.1.8. XRD analysis 86
3.1.9. Wear test 88
3.1.10. Conclusions 91
3.2. Yttria-Stabilized Zirconia coatings – optimization phase 94
3.2.1. Macroscopic observations 94
3.2.2. Electron Microscopy observations 95
3.2.3. Roughness measurements 99
3.2.4. Nano-hardness measurements 100
3.2.5. Colorimetric analysis 101
3.2.6. Scratch test 102
3.2.7. Raman analysis 105
3.2.8. XRD analysis 106
3.2.9. Low temperature degradation testing 108
3.2.10. Conclusions 109
3.3. Yttria-Stabilized Zirconia coatings – from plates to abutments 110
3.3.1. Macroscopic observations 110
3.3.2. Electron Microscopy observations 112
3.3.3. Raman analysis 118
3.3.4. Conclusions 119
3.4. Collagen-based hydrogel 119

3.4.1. SEM observations 119
3.4.2. Rheometric test 120
3.4.3. Contact angle measurements 124
3.4.4. Optical Microscopy observations 127
3.4.5. FEG-SEM observations 128
3.4.6. XRD analysis 131
3.4.7. DSC analysis 132
3.4.8. Conclusions 134
4. Conclusion and Future Prospective 136
References 138

Acknowledgements

I would like to express my heartfelt gratitude to UniMoRe for enabling this collaboration and for making the initiation of this project possible. In particular, I would like to thank Prof. Lusvarghi and Prof. Monaco, as well as Prof. Generali and Prof. Bolelli, for their constant support and guidance.
I am also deeply grateful to Prof. Andreola and PhD students Silvestri and Salvatori for their invaluable collaboration throughout this journey.

I sincerely thank Il Sentiero International Campus for facilitating this collaboration and supporting my research. I am deeply grateful to my entire team for their support throughout this journey. My sincere thanks go to my boss, Dott. Franci, as well as to my greatest supporters: Alessia, Elena, and Francesca.

Finally, I would like to extend my heartfelt thanks to my family and friends, my entire world, for being there for me throughout this challenging period of personal and professional growth. Without their constant support, I would not have reached this goal.

Abstract

Abutments play a crucial role in dental prostheses, acting as intermediaries between the crown and the implant screw while interfacing with the surrounding gingival tissue. Dental prostheses provide a long-term solution for tooth loss, offering comfort and restoring both function and aesthetics, thereby improving the quality of life. Typically made from titanium or zirconia, abutments made of titanium can pose challenges related to allergic reactions and aesthetic issues, despite being more cost-effective than zirconia. However, poor integration with soft tissues can lead to complications such as peri-implantitis, which can ultimately result in implant failure, a phenomenon that currently affects approximately 12% of implants.

The objectives of this thesis were to address the issues associated with titanium, minimizing aesthetic and allergic concerns, and to enhance early-stage soft tissue integration to prevent implant failure.

To achieve this, a bilayer coating was proposed, composed by zirconia and biopolymeric layers.

The zirconia coating was obtained employed reactive sputtering deposition adopting a PVD-PECVD system. Thus, yttria-stabilized zirconia (YSZ) coatings were deposited onto grade 5 titanium plates. A yellow-coloured coating was obtained to minimize gingival tissue discoloration. Morphological analyses (SEM, FEG-SEM, and FIB) confirmed the defect-free, well-adherent nature of the coating, with a thickness of a few hundred nanometres. X-ray diffraction (XRD) analysis revealed a stable cubic phase, even after low-temperature degradation testing simulating up to 75 years of in vivo exposure. Mechanical characterization, scratch and wear tests, demonstrated satisfactory performance, considering the maximum clinical force on an abutment is approximately 1N, when exposed to the oral cavity environment.

The biopolymeric layer was composed of type I collagen and Laponite RDS. Various formulations were developed and characterized with the focus of improve cell activity. Their processability and mechanical properties were evaluated through rheometric characterization, showing promising results in terms of mechanical properties. These formulations were homogeneously deposited onto alkaline-treated biomedical-grade zirconia, followed by in situ gelation at 37°C. The alkaline treatment was introduced to improve adhesion between the biopolymeric layer and the zirconia surface. SEM observations revealed a fibrillar structure and confirmed the presence of the D-pattern in the gelled layers. XRD analysis further confirmed the crystalline structure of collagen after processing, showing a pattern like its natural form. Differential Scanning Calorimetry (DSC) revealed an improvement in the thermal stability of the collagen-based layer when UV cross-linked and combined with Laponite RD

The results confirmed the successful deposition of a durable and resistant YSZ coating, which effectively addressed both aesthetic and allergic concerns associated with titanium abutments. Furthermore, the biopolymeric layers were thoroughly characterized, identifying the optimal formulation and deposition strategies to enhance cell adhesion and proliferation. Future studies will focus on in vitro and in vivo cytotoxicity and viability tests to validate the effectiveness of the developed materials in clinical applications.

Sommario

I monconi svolgono un ruolo cruciale nelle protesi dentali, fungendo da intermediari tra la corona e la vite dell'impianto e interfacciandosi con il tessuto gengivale circostante. Le protesi dentali rappresentano una soluzione a lungo termine per la perdita dei denti, offrendo comfort e ripristinando sia la funzionalità che l'estetica, migliorando così la qualità della vita. Generalmente realizzati in titanio o zirconia, i monconi in titanio possono presentare problemi legati a reazioni allergiche e ad estetica, sebbene siano più economici rispetto a quelli in zirconia. Tuttavia, una scarsa integrazione con i tessuti molli può portare a complicazioni come la perimplantite, che può causare il fallimento dell'impianto, un fenomeno che attualmente interessa circa il 12% degli impianti.

Gli obiettivi di questa tesi sono stati affrontare le problematiche associate al titanio, riducendo le preoccupazioni estetiche e allergiche, e promuovere l'immediata integrazione con i tessuti molli per prevenire il fallimento dell'impianto.

Per raggiungere questi obiettivi, è stato proposto un rivestimento bi-strato composto da uno strato di zirconia ed uno biopolimerico.

Il rivestimento in zirconia è stato ottenuto mediante deposizione per sputtering reattivo tramite un sistema PVD-PECVD. In particolare, sono stati depositati rivestimenti di zirconia stabilizzata con ittria (YSZ) su piastre in titanio di grado 5. È stato ottenuto un rivestimento di colore giallo per minimizzare la decolorazione del tessuto gengivale. Le analisi morfologiche (SEM, FEG-SEM e FIB) hanno confermato la natura priva di difetti ed una buona adesione del rivestimento, con uno spessore di poche centinaia di nanometri. L'analisi mediante diffrazione a raggi X (XRD) ha rivelato la presenza di una fase cubica stabile, anche dopo test di degradazione a bassa temperatura simulanti esposizione in vivo fino a 75 anni. La caratterizzazione meccanica ha previsto prove di resistenza ai graffi e di usura dimostrando prestazioni soddisfacenti, considerando che la forza clinica massima su un moncone è di circa 1N, quando esposto all'ambiente del cavo orale.

Lo strato biopolimerico era composto da collagene di tipo I e Laponite RDS. Sono state sviluppate e caratterizzate diverse formulazioni, con l'obiettivo di migliorare l'attività cellulare. La loro processabilità e proprietà meccaniche sono state valutate tramite caratterizzazione reometrica, mostrando risultati promettenti in termini di proprietà meccaniche. Queste formulazioni sono state depositate in modo omogeneo su zirconia biomedicale trattata con un processo alcalino, seguito da gelificazione a 37°C. Il trattamento alcalino è stato introdotto per migliorare l'adesione tra lo strato biopolimerico e la superficie della zirconia. Le osservazioni SEM hanno rivelato una struttura fibrillare e confermato la presenza del D-pattern nei rivestimenti post-gelificazione. L'analisi XRD ha inoltre confermato la struttura cristallina del collagene dopo il processo, mostrando un pattern simile alla sua forma naturale. La Calorimetria a Scansione Differenziale (DSC) ha evidenziato un miglioramento della stabilità termica dello strato a base di collagene quando reticolato con UV e combinato con Laponite RDS.

I risultati hanno confermato il successo della deposizione di un rivestimento YSZ resistente e durevole, in grado di affrontare efficacemente sia le problematiche estetiche che quelle allergiche associate ai monconi in titanio. Inoltre, gli strati biopolimerici sono stati caratterizzati in dettaglio, identificando la formulazione e le

strategie di deposizione ottimali per migliorare l'adesione e la proliferazione cellulare. Studi futuri si concentreranno su test di citotossicità e vitalità in vitro e in vivo, per validare l'efficacia dei materiali sviluppati nelle applicazioni cliniche.

Introduction

The objective of this thesis is to functionalize the surface of the abutment, a component of dental prostheses positioned between the crown and the implant screw. Dental prostheses replace missing teeth, providing a permanent solution that restores both masticatory function and aesthetic appearance leading to high patient satisfaction. When implanted, the abutment directly interfaces with the gingival tissue.

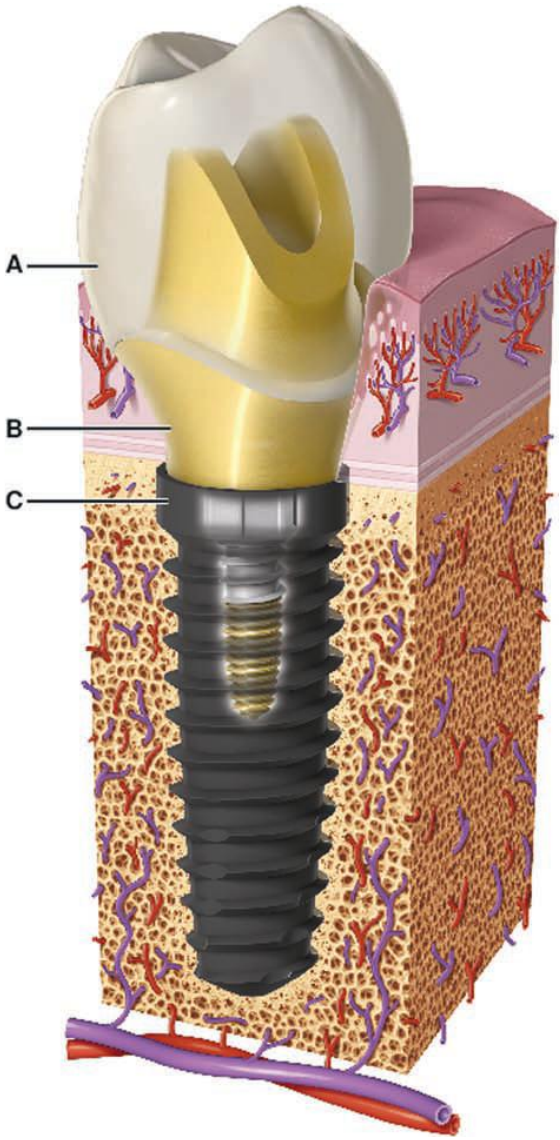

Figure 1.1-1 - Components of restored implant. A) Implant crown; B) Abutment and C) Implant screw [1].

Typically, abutments are made of grade 5 titanium or zirconia [2]. Both materials are biocompatible; however, titanium can induce allergic reactions in some patients and may also cause gingival discoloration, which affects the aesthetic outcome of the implant. Due to its higher cost, zirconia abutments are often less commonly used, despite offering better aesthetic and biocompatibility properties.

This research addresses two primary challenges:

- The aesthetic impact and potential allergic reactions caused by titanium.
- The integration of soft tissue post-implantation to prevent bacterial colonization and peri-implant complications.

The main issue related to the implantation of a dental prosthesis is the degradation of the soft tissue around the implant that becomes weak (Figure 1.1-2) leading to the formation of a micro-gaps between the abutment and the screw, as well as between the abutment and the gingiva [3]. This gap facilitates bacterial infiltration, increasing the risk of peri-implantitis and, ultimately, implant failure [4]–[8]. Data from systematic reviews and meta-analyses indicate that peri-implantitis accounts for approximately 20% of implant-related complications in patients with dental prostheses and around 12% of implants being rejected [9]–[12].

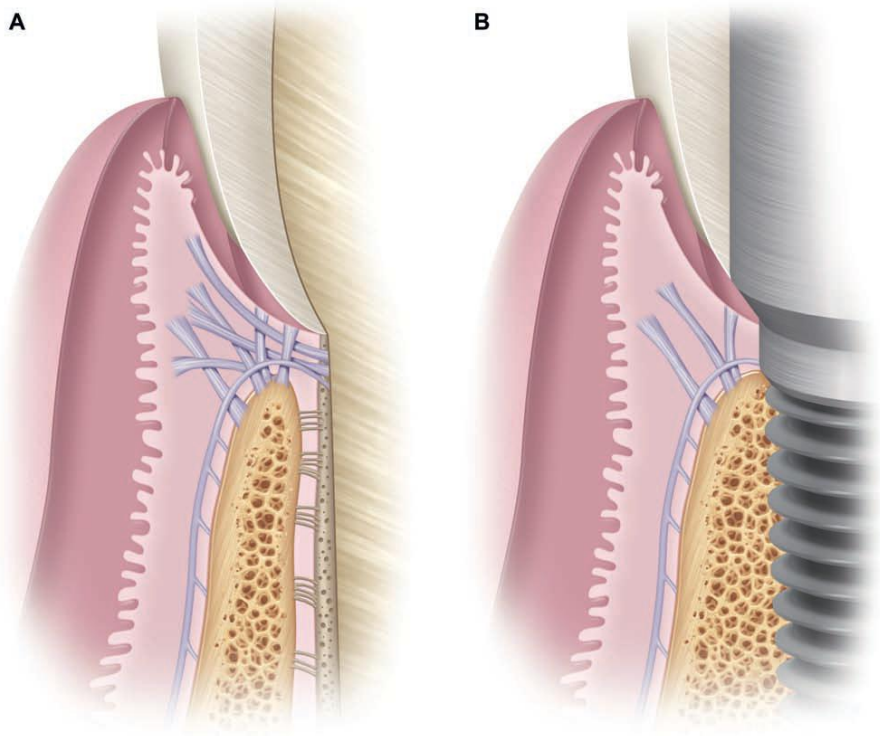

Figure 1.1-2 - Comparison of tissues around a healthy natural tooth (A) versus a healthy dental implant (B) [1].

Typically, coatings are applied to abutment surface to mitigate the bacterial adhesion occurring post-implantation. Several coating materials, such as diamond-like carbon (DLC), silver-doped DLC (Ag-DLC), nano-silver (nano-Ag), titanium nitride (TiN), zirconium nitride (ZrN), and nanostructured yttria-stabilized zirconia (Y-TZP), have been explored for their antimicrobial property. Among these, TiN, ZrN, and Y-TZP demonstrated the most promising results, whereas other coatings shown inconsistent performance [4]–[8], [13]–[17].

A key strategy to prevent implant rejection is to enhance early-stage soft tissue integration, which reduces bacterial adhesion and accelerates healing [18]–[21]. Recent studies have focused on developing coatings inspired by materials used in tissue engineering and regenerative medicine (TERM) to promote soft tissue regeneration by promoting adhesion and proliferation of fibroblasts. Particularly, fibroblasts are cells of the connective tissue and are fundamental in driving wound healing of soft tissue by producing and organizing the extracellular matrix (ECM) [22], [23]. These materials can be classified into synthetic and natural biomaterials.

Among synthetic options, polydopamine has been widely studied for its ability to enhance fibroblast adhesion and proliferation, thereby stimulating collagen secretion and tissue regeneration [21], [24].

However, natural biomaterials are preferred because they better mimic the extracellular matrix (ECM), providing an optimal biochemical and structural environment for cellular activation. Natural polymers such as collagen, hyaluronic acid, gelatine, and chitosan have been extensively investigated for their efficacy in improving soft tissue integration [25]–[28]. Collagen, in particular, is a fundamental structural protein found in various tissues, with type I collagen being the most abundant in the soft tissues of the human body. It is characterized by a porous and fibrillar structure that allows for cell adhesion and proliferation and, ultimately, promotes most effective gingival tissue regeneration [29].

This research proposes a synergistic approach by developing a bilayer coating on abutment surface. The bilayer consists of:

- A zirconia layer, which addresses aesthetic and allergic issues by minimizing gingival tissue discoloration allowing for a specific coating colour, such as pink or yellow hues [30]–[32]. Zirconia is also highly resistant, biocompatible and has non-allergenic properties.
- A biopolymeric layer, designed to promote immediate soft tissue integration upon implantation. The primary component of this layer is type I collagen, chosen for its ability to mimic the gingival ECM, promoting cell adhesion and the deposition of new ECM, leading to gingival tissue regeneration [29].

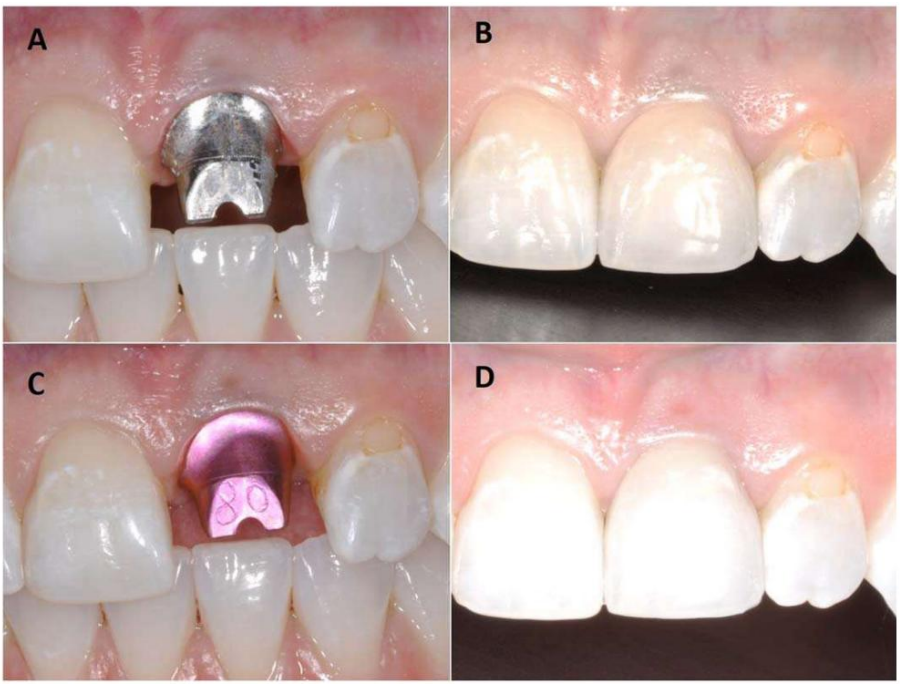

Figure 1.1-3 - gingival tissue appearance with (a) a titanium abutment and (b) an anodized pink abutment [32].

The zirconia layer is created through reactive sputtering deposition using a PVD-PECVD system with a Zirconium-Yttrium target containing 7 mol% Yttrium. This specific composition is chosen to achieve a stable

phase of zirconia [63]–[65]. This method allows for the production of precise and controlled coatings, free of pores and contamination, making them suitable for biomedical applications.

The biopolymeric layer is formulated with the addition of Laponite RDS for improving shear-thinning behaviour of the solution and, consequently, enhancing its processability, while not inducing cytotoxic effects [33], [34]. The biopolymeric solution is deposited by drop casting at 4°C to prevent premature gelation, allowing full gel formation at 37°C. Then, all the biopolymeric layers are gelled at 37°C and further UV cross-linking is conducted to improve stiffness, promoting cell signalling which ultimately can lead to improved cell diffusion [35]–[37].

To ensure the quality and performance of the zirconia coating, various characterization techniques were employed. Aesthetic consistency was evaluated through visual inspection and colorimetric tests, while structural and compositional analyses were conducted adopting Scanning Electron Microscopy (SEM), X-ray diffraction (XRD) and Raman spectroscopy. Mechanical properties were assessed through hardness measurements, scratch tests, and wear tests. Additionally, the stability and durability of the zirconia coating was evaluated using low-temperature degradation tests, in accordance with ISO 13356, typically conducted on Y-TZP-based ceramic implants used in surgical applications [38]–[40].

For the biopolymeric layer, optical observations and SEM analysis were conducted to verify the homogeneity of the deposition and to examine the morphological structure, respectively. The crystalline structure of the collagen was analysed using XRD to evaluate the presence and extent of fibrillogenesis, which indicates the formation of well-organized collagen fibrils. Finally, Differential Scanning Calorimetry (DSC) was performed to assess the thermal properties of the biopolymeric layer, specifically to evaluate the effects of the various post-deposition treatments and the addition of Laponite RDS.

By combining these two layers, this study aims to enhance both the aesthetic and biological performance of dental abutments, ultimately improving implant success rates and patient outcomes. Specifically, the research proposes applying both layers to titanium abutments, while limiting the biopolymeric coating to abutments with zirconia surface, as zirconia already meets aesthetic and hypoallergenic requirements. The zirconia layer is expected to reduce gingival tissue discoloration, minimize allergic reactions, and provide superior mechanical properties and biocompatibility, thereby enhancing the integration of the abutment with the surrounding gingival tissue. Meanwhile, the biopolymeric layer, primarily composed of type I collagen, is designed to promote rapid soft tissue integration, accelerating healing and preventing bacterial colonization. These advancements are anticipated to improve implant stability, reducing the incidence of peri-implantitis and, consequently, leading to better long-term outcomes enhancing overall patient satisfaction. Furthermore, this research may contribute to the development of biomaterial-based coatings for dental implants, with potential applications extending to other biomedical fields requiring soft tissue integration.

1. Chapter 1 – State of the Art

1.1.Abutment component

Dental prostheses provide a long-term solution for replacing missing teeth, playing a crucial role in maintaining both oral function and aesthetic appearance. As life expectancy increase, the demand for reliable and durable dental replacements is increasing, driving several investigation resulting in enhancements in materials and techniques to enhance their performance and lifetime [1], [41].

Global Market Insights (GMI) has published a forecast study using data collected up to 2023 and has projected an increase in demand for dental implants, reaching $9.6 billion by 2034, with an annual growth rate of 6.9%. According to GMI, this growth is driven by increased life expectancy as well as the rising prevalence of dental diseases worldwide [42].

Besides oral health, tooth loss can lead to other significant consequences such as nutritional deficiencies, digestive issues, and even speech difficulties. In addition, missing teeth can alter facial structure which, combined with psychological aspect of an altered appearance, can diminish self-confidence and overall quality of life. Consequently, the use of dental prostheses not only restores essential functions such as mastication and speech but also preserves facial aesthetics [1], [41].

Dental prostheses are composed by implant screw, abutment and crown. The abutment serves as an intermediary structure between the other two parts and is designed to create a natural emergence profile, facilitating good oral hygiene and ensuring a natural appearance of the dental prosthesis [1], [41].

Moreover, the abutment plays a fundamental role in evenly distributing mechanical loads, ensuring a stable and functional connection between the implant and the surrounding bone tissue. This is a crucial factor in the long-term success of dental prostheses, as highlighted by Per-Ingvar Brånemark, a Swedish physician and researcher, in 1957. Now recognized as the "father of modern dental implantology," he pioneered the concept of osseointegration, which remains a crucial point of implant success today [1], [41].

But the abutment is also crucial for another key aspect which is the support of soft tissue integration preventing complications such as peri-implantitis, which could ultimately lead to implant failure.

Peri-implantitis develops in two stages. The initial phase, peri-implant mucositis, resembles gingivitis and involves gum redness, swelling, and bleeding due to bacterial biofilm buildup, but without bone loss. If untreated, it progresses to peri-implantitis, leading to significant bone loss and implant instability, similar to periodontitis but progressing faster [43]–[45]. A thorough analysis of systematic reviews and meta-analyses reveals that approximately 20% of implant patients experience peri-implantitis, affecting about 10% of implants. Early diagnosis and intervention are crucial to prevent implant failure and ensure long-term success [9]–[12]. Given the projected increase in dental implant placements and the persistent incidence of failures caused by peri-implantitis diseases, addressing factors related to soft tissue integration is becoming increasingly crucial.

There are several types of abutments, each designed to address specific needs in dental prosthetics. Overall, abutments are classified into permanent and temporary types [46].

Permanent abutments can be fabricated, customized or customizable from pre-fabricated abutment.

- Stock abutments are fabricated component that offer a broad range of options and are distinguished basing on the height of the collar, the geometry that can be straight or angled and the material that typically is titanium or zirconia. They are the most adopted due to their ease of use, cost-effectiveness, and versatility.
- Customized abutments are tailored to meet the specific anatomical requirements of the patient, optimizing the fit and overall prosthetic outcome. Thus, it guarantees high patient satisfactory but consequently are more expensive.
- Customizable from pre-fabricated abutment, such as Variobase ® designed by Straumann. It is a pre-fabricated component that can be further customized after purchase through CAD/CAE software, allowing for personalized adjustments to meet the specific needs of the patient.

Temporary abutments can be categorized as healing and temporary.

- healing abutments which are installed immediately after the implant procedure to help shape and support the gingival tissue during the healing phase. They guide the growth of soft tissue around the implant, ensuring proper tissue contouring.
- temporary abutments are used to provide both functional and aesthetic support for a provisional prosthesis during the healing period or until a permanent solution is implemented.

The available materials for abutments include [2]:

- Titanium: A widely used material, ideal for posterior implants due to its strength and durability, though it may cause aesthetic concerns or allergic reactions. In particular, a titanium abutment leads to discoloration of gingival tissue around the grey implant leading to a no natural appearance of the tissue [30]–[32].
- Stainless Steel: Typically used for temporary abutments due to the potential immune response from nickel.
- Zirconia: Highly biocompatible, it is referred for aesthetic cases and patients with thin gingiva.
- PEEK: Mainly used for temporary restorations, offering a tissue response similar to that of titanium.

Considering the growing demand for lifetime, comfort, and aesthetics associated with dental prostheses, as well as the issues related to the abutment component, many research efforts are focused on developing new, more versatile abutment geometries, as well as advanced coatings and surface treatments. These innovations aim not only to enhance the aesthetic appearance of the abutment but also to improve its functionality by modifying the surface to promote immediate soft tissue integration, prevent bacterial adhesion, and ensure long-term durability.

1.2. Surface Engineering

Surface Engineering emerged in the 20th century and was further developed and solidified in the 1960s to respond at the requirements of the modern industrialization. This development required an improvement in

terms of functionality, efficiency, and lifetime of finite products to save energy and raw materials and to improve safety. This new branch has undergone significant development due two factors [47]:

- the development of novel coatings and treatment methods, enabling the achievement of properties that were previously unachievable.
- engineers and scientists recognize the critical impact of surfaces on performance, lifespan, and costs of components.

The term *"Surface Engineering"* was coined for the first time in England when the Surface Engineering Society was inaugurated [48].

There is no universally standardized definition for this new term. The most common are the following:

- "is a discipline of science, encompassing:
  - manufacturing processes of surface layers, thus, in accordance with the accepted terminology – superficial layers and coatings, produced for both technological and end use purposes;
  - connected phenomena;
  - performance effects obtained by them" [48];
- "is a treatment of the surface and near-surface regions of a material to allow the surface to perform functions that are distinct from those functions demanded from the bulk of the material" [49], [50];
- "is the design and modification of the surface and substrate of an engineering material together as system, to give cost effective performance of which neither is capable alone" [51];
- "is an informed selection of the appropriate coating or surface modification technology and its effective application to prevent or delay one or more forms of materials degradation thereby improving the performance of components and device" [52].

Surface Engineering focuses on modifying surface properties to optimize their behaviour and functionality during interaction with the environment. It involves the study and development of innovative solutions to enhance material characteristics, including physical, chemical, electrical, mechanical, and thermal properties, as well as improving wear and corrosion resistance, adhesion, and biocompatibility. Surface optimization is typically achieved through the application of a coating, which is selected to impart specific properties to a bulk material that, instead, provides toughness and strength. These coatings can be of various types, enabling the optimization of substrates through the application of metallic, ceramic, polymeric, or composite coatings, whether the substrates are similar or dissimilar.

However, Surface Engineering involves two fundamental aspects:

- **Coating technology**, which encompasses traditional methods such as galvanization, heat treatments, and electrochemical processes, as well as more recent techniques like chemical and physical vapor deposition and ion implantation.
- **Coating characterization**, which focuses on the evaluation of surface properties and interfaces.

Due to these characteristics, *Surface Engineering* is widely applied in the automotive, aerospace, defence, energy generation, electronics, biomedical, textile, petrochemical, chemical, steel, cement, machinery, and construction sectors.

Figure 1.2-1 illustrates the two main branches of *Surface Engineering*: *Surface Texturing* and *Surface Finishing*.

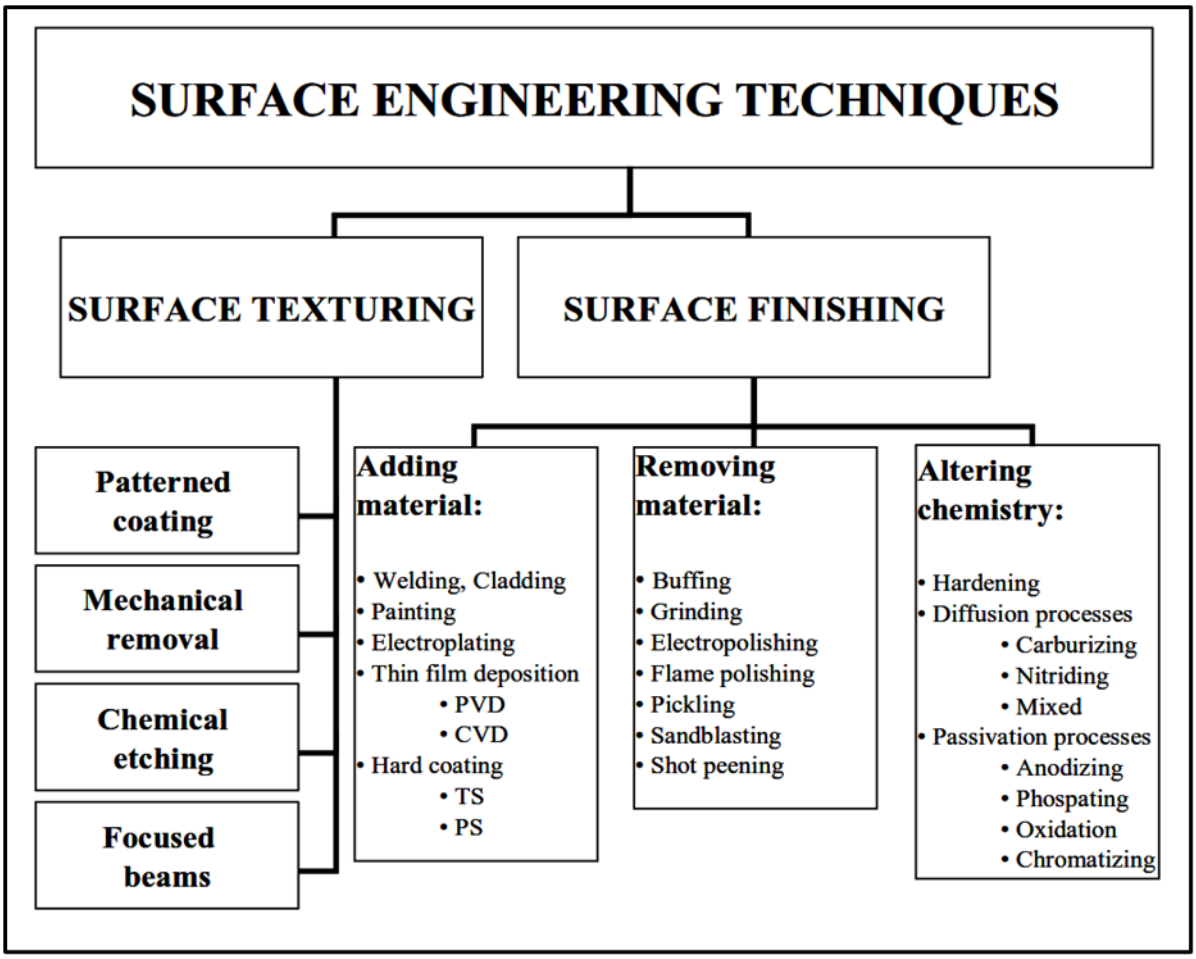

Figure 1.2-1 - Classification of Surface Engineering Techniques [53].

Surface Texturing refers to a set of technologies employed for the modification of surface topography aiming to the enhance of the performance in multiple aspects. Surface modifications are achieved by creating specific pattern defined by micro – relief features with regularly shaped asperities and depressions.

Surface Finishing involves all industrial processes aiming on the modify of a manufactured article, coating its surface and changing its chemical composition or varying its sub – surface microstructure. This modification is achievable altering the chemistry and removing or adding material. Among *Surface Finishing* techniques, coating deposition technologies are particularly noteworthy. This technology involves adding new material to an existing surface to create an interface that provides physical separation between the vulnerable substrate and external sources of damage. More specifically, thin film category includes many other processes besides PVD and CVD, as detailed in Figure 1.2-2. For instance, drop casting is a technique used to obtain a thin coating by depositing drops of a specific solution using a pipette, followed by post-treatment to evaporate the excess solvent [54].

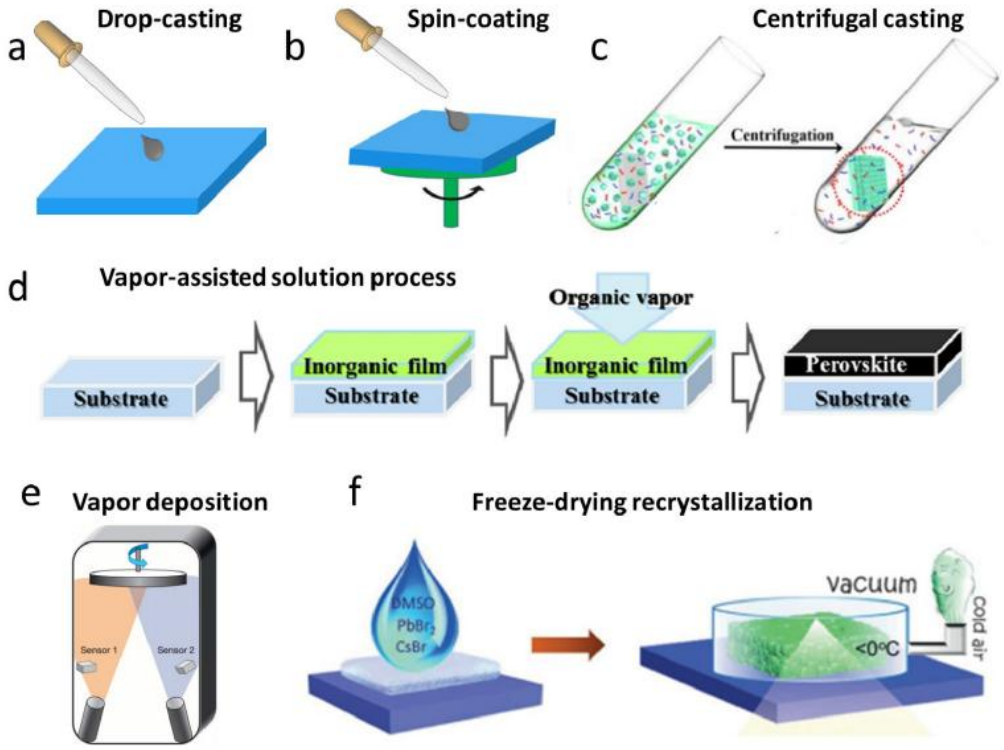

Figure 1.2-2 - Thin film processes [55].

1.3.Bioceramics for Medical Application

1.3.1. Bioceramics: Types and Production

The term "biomaterial" originates from the early symposia of Clemson University in the late 1960s and early 1970s. The scientific accomplishments of these symposia paved the way for the establishment of the Society for Biomaterials in 1975. Researchers and engineers developed materials tailored to meet specific requirements, while scientists investigated the nature of biocompatibility. This term "biomaterial" became the focal point of a distinct scientific field. The evolution of this discipline and the establishment of the Society for Biomaterials were closely linked [56].

“A biomaterial is a substance that has been engineered to take form, which, alone or as a part of a complex system, is used to direct, by control of interactions with components of living systems, the course of any therapeutic or diagnostic procedure, in human or veterinary medicine.’’ [57]. Biomaterials, whether in the form of implants (like dental implants and heart valves) or medical devices (such as artificial hearts and biosensors), aim to replace or enhance damaged tissues and organs, thereby enhancing the life quality of patients. In regenerative medicine, their properties are largely dictated by the materials used (polymers, ceramics, metals, carbon), their structure (solid or porous), and their physical and chemical attributes [58].

Particularly, bioceramics are materials characterized by high strength and stiffness, great hardness, insulating behaviour and resistance to high temperature, wear, and chemical degradation. The major disadvantages are the great fragility and the low toughness [59], [60]. Also, bioceramics can assume a structural function as joint or tissue replacement, can be used as coating to improve the biocompatibility of metal implants and can function as resorbable lattices providing a temporary structure that is dissolved and replaced as the body rebuild

tissue [60]. Thanks to these characteristics, bioceramics are available as microspheres, thin layers or coating on a metallic implant, porous network, composites with a polymer component and more [60].

A possible classification of bioceramic materials is about their response to the biological environment. In this way, it is possible to distinguish bioinert, bioactive and bioresorbable bioceramics. Typical bioinert ceramic materials, such as alumina (Al_2O_3) and zirconia (ZrO_2), are non-toxic and do not promote tissue integration. When implanted, they are encapsulated by fibrous connective tissue, and thanks to their excellent mechanical properties and biocompatibility, they are suitable for applications requiring high strength, such as permanent implants [59], [60].

Alumina (Al_2O_3) and zirconia (ZrO_2) are two of the most adopted bioinert ceramics for biomedical purposes thanks to their high biocompatibility and wear resistance. It is possible to coat a bioinert ceramic if the integration of the implants with the living tissue is required [59], [61].

1.3.2. Zirconia

During the 1990s a necessity to replace alumina as a ceramic material in the fabrication of certain prostheses due to its fragility emerged. Consequently, biomedical zirconia was introduced [62]. The use of zirconia has enabled the development of new implant designs, like 22 mm femoral heads, which were not feasible with alumina [62], [63].

3Y-TZP zirconia exhibits higher values of toughness, K_{IC}, and threshold, K_{I0}, than the alumina ones (Figure 1.3-1) leading to consequently higher variation of strength: higher values than 2 GPa and 800 MPa characterize respectively zirconia and alumina [63].

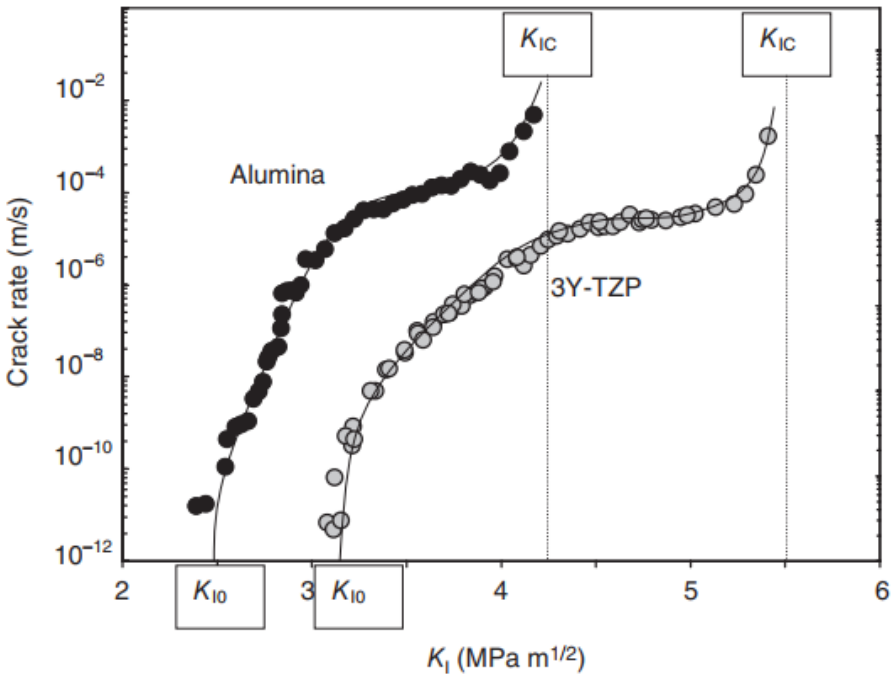

Figure 1.3-1 - Crack propagation behaviour of alumina and 3Y-TZP [63].

Zirconia-based ceramics are characterized by high strength, toughness and chemical resistance making them applicable in harsh environments under severe loading conditions [62]. Therefore, it's possible applied them

under critical chemical and mechanical stresses. An example is their suitability in the industrial field, such as the seals in slurry pump, and in the medical field, designing hip or knee to replace damaged joints [62].

Pure zirconia is a polymorphic ceramic exhibiting three crystal phases: monoclinic, tetragonal and cubic from low to high temperature [61]–[64]. The monoclinic phase is stable at temperature below 1170 °C, the tetragonal one exists in the range [1170÷2360] °C and the cubic phase is stable above 2360 and up to the melting point (2680°C) [63].

It's possible to stabilize the tetragonal and the cubic phases at room temperature adding oxides such as CaO, MgO, Y_2O_3 and CeO_2 [62]–[65]. For example, adding an amount of yttria (Y_2O_3) over 8 mol%, the cubic phase is stable at room temperature, which is called cubic-stabilized zirconia (CSZ). When yttria is 3 to 8 mol%, tetragonal and cubic phases are mixed at room temperature, and it is called partially stabilized zirconia (PSZ). When yttria is around 3 mol%, the tetragonal phase is close to 100% at room temperature, and it is called tetragonal zirconia polycrystal (TZP), also called toughened zirconia [64].

Zirconia is naturally found in nature as the free oxide baddeleyite, typically contaminated by hafnium oxide, or as zircon (ZrO_2-SiO_2) from which it was extracted for the first time by the Swedish chemist Jöns Jacob Berzelius in the year 1829 [65],[66].

1.3.2.1. Toughening

Zirconia is well-known for the concept of "transformation toughening". The toughening is given by the reversible transformation t → m (from the tetragonal to the monoclinic form) making zirconia a unique ceramic. When a crack propagates in a ceramic material, it can quickly lead to the fracture and the consequent failure of the piece. Instead, the presence of metastable tetragonal phase in the zirconia structure, can stop the propagation of the crack: the crack tip is characterized by high tensile stress that is used to transform the particles of the tetragonal phase in particles of monoclinic phase with consequent increment of the volume (3÷4 %) and shear stress leading to a compression stress field that stop the propagation (Figure 1.3-2). This phenomenon is also known as "microcracking" where the microcracks in the surrounding matrix are subcritical in term of the Griffith-Orowan fracture mechanics [61]–[63], [65].

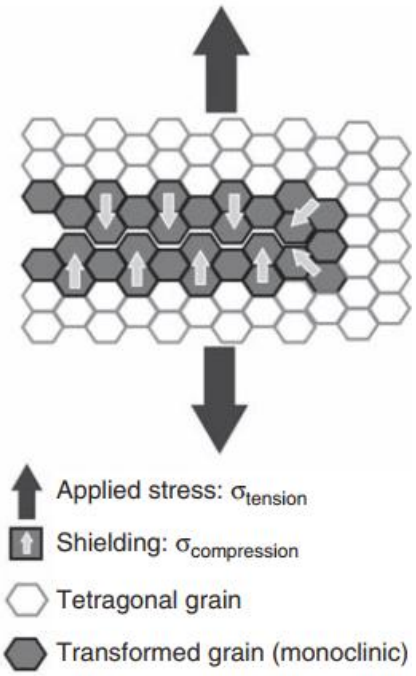

Figure 1.3-2 - Stress-induced tetragonal-monoclinic transformations at the crack tip in zirconia. leading to crack shielding [63].

The grain size strongly affects this phenomenon, in fact above a critical dimension the transformation is spontaneous and lead to an improvement of the toughness [62].

Another important benefit is the possibility to improve the toughness and to reduce the sensitivity to slow crack growth grinding the surface and creating a surface layer in a compressive state (Figure 1.3-3). It is not possible with other ceramic, such as alumina, that can fail during the machining process [63].

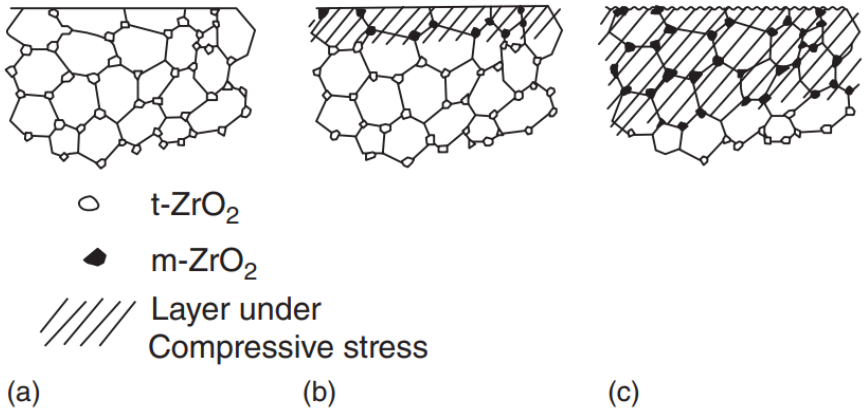

Figure 1.3-3 - Free surface of stabilised zirconia at sintering temperature (A). During cooling the t-ZrO2 particles near the surface transform to m-ZrO2 and thus induce a compressive stress in the matrix (B). The thickness of the compressive layer can be increased by abrading/polishing the surface (C) (D).

1.3.2.2. Hydrothermal Instability

Zirconia suffers the hydrothermal instability, a phenomenon also known as ageing of the metastable zirconia that affects especially the Y-TZP structure. It occurs in water presence and at room temperature, but it is accelerated at 250°C [60]–[63], [65]. The transformation t→m is a great advantage when it is localised around a propagating crack but if it occurs in correspondence of the surface, it can be a disastrous phenomenon [63].

This phenomenon is due by the presence of water radicals (es. body fluids) that, penetrating the lattice through the oxygen voids, causes its contraction generating a tensile field stress in the surface grains and leading to a stress corrosion-type mechanism [62], [63]. In the year 2001, around 400 implanted zirconia femoral heads failed within a very short period [61]–[63]. This is accentuated in Y-TZP because the water diffusion is facilitated by the presence of many vacancies due to the trivalent character of yttrium. After the nucleation phase, the phenomenon continues like a cascade of events, grain after grain, causing the volume increase of the lattice leading to microcracking and creating a pathway which helps further penetration of water. It is possible to observe also roughening if this phenomenon is associated with surface uplift (Figure 1.3-4).

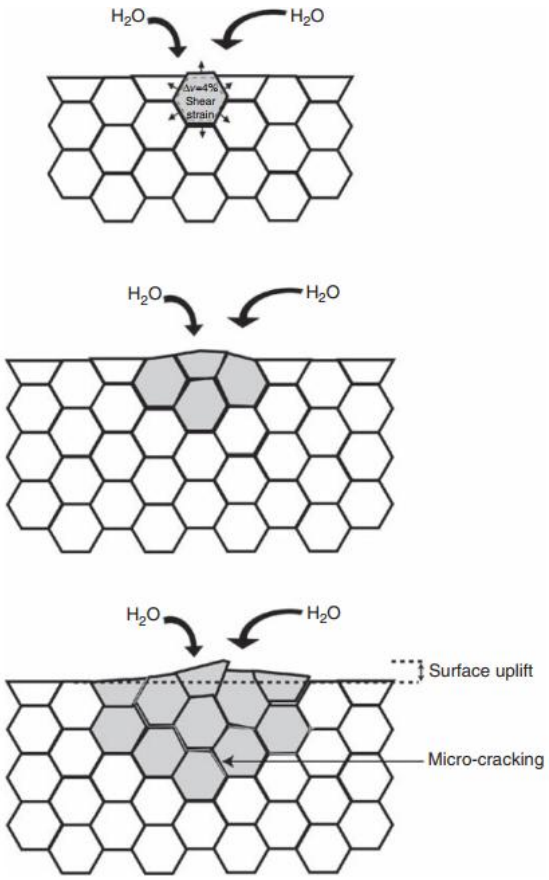

Figure 1.3-4 - Schematic representation of ageing at the surface of zirconia [63].

The roughening strongly impacts the application in medical field when wear resistance is required [63]. The ageing phenomenon is strongly influenced by the microstructure: grain size, homogeneity, surface state and, above all, density. High density results in less access to water in the structure strongly limiting the ageing effect of the zirconia. Also, the ageing is limited reducing grain size dimension; but consequently, the toughening effect is less effective, and giving a surface compressive stress field blocking the cascade reaction [63]. The chemical modification of the zirconia is another potential solution to limit the ageing phenomenon: addition of silica, adoption of yttria-coated rather than coprecipitated powders and the use of Ce-doped zirconia [62].

The aging phenomenon is not yet well known in the dental field but no issue has been reported for Y-TZP for dental application during the 20 years of research and optimization [62], [63].

Alumina-toughened zirconia (ATZ) and zirconia-toughened alumina (ZTA) are developed to overcome the hydrothermal instability of metastable zirconia. Mathys European Orthopaedics, Bettlach, Switzerland, developed Ceramys®, that is an alumina-toughened zirconia consisting of a nanocrystalline dispersion (average grain size 0.4 μm) of 80 mass% Y-TZP and 20 mass% alumina ensuring a biaxial flexural strength up to 1.2 GPa [65]. Also, zirconia-toughened alumina is first developed by Claussen, and it is composed by particles of tetragonal zirconia immersed in an alumina matrix [62]. The behaviour of ATZ, ZTA, 3Y-TZP, and 8Y-CSZ ceramics are evaluated in the as-is condition and after a Low Temperature aging or Degradation (LTD) in a solution of artificial saliva (Table 1-1). Cubic stabilized zirconia with 8 mol.% of Yttria (8Y-CSZ) seems to not be affected by the LTD in fact the mechanical properties did not change in as-is condition and after the treatment. The other samples suffered a change in the crystalline phases with a consequent decrease of the mechanical properties after the LTD.

Table 1-1 - Mechanical properties of the ceramics samples evaluated by nanoindentation [61].

Ceramics	Compositions	% Molar fraction (t→m)	Average Grain Size [nm]	Elastic modulus [GPa]	Nano-Hardness [GPa]	Stiffness [N/m]	K_{IC} MPa $\sqrt{m}$
ATZ ATZ With LTD	20 wt%Al_2O_3+ 80 wt%TZ-3Y	11	576 ± 165	335 ± 7 235 ± 11	21 ± 1.2 12 ± 1.5	157471 ± 12 91159 ± 34	4.2 ± 0.1 3.7 ± 0.2
ZTA ZTA with LTD	80 wt%Al_2O_3+20 wt%TZ-3Y	7	495 ± 285	360 ± 6 298 ± 10	35 ± 1 30.2 ± 2	161190 ± 12 151150 ± 14	3.50 ± 0.2 3.1 ± 0.4
3Y-TZP 3Y-TZP with LTD	97% mol ZrO_2 + 3% mol Y_2O_3	18	387 ± 95	354 ± 7 260 ± 7	25 ± 0.8 18 ± 1.5	83886 ± 9 76262 ± 11	5.1 ± 0.2 4.1 ± 0.3
8Y-CSZ 8Y-CSZ with LTD	92%mol ZrO_2 + 8% mol Y_2O_3	0	2303 ± 450	384 ± 2 383 ± 2	31.3 ± 0.2 31.2 ± 0.3	153423 ± 12 153414 ± 10	3.77 ± 0.02 3.78 ± 0.03

Around 20% of the prosthetic femoral heads produced globally are ceramic, and up until the year 2000, roughly 40% of these ceramic heads, were made of zirconia. Zirconia was recognized as the second generation of ceramic hip joint heads, offering both low wear rates and enhanced safety [63]. Thanks to the mechanical and aesthetic properties that characterize zirconia, this ceramic material is also widely used in the dental field for the fabrication of dental crowns and multiple-unit bridge frameworks [63].

In the past few decades, Zellwerk GmbH has introduced Sponceram®, a porous material primarily composed of zirconia and partially or completely stabilized with Ca, Mg, or Y (Figure 1.3-5). This material aims to promote tissue regeneration by enhancing cellular transport through it [65].

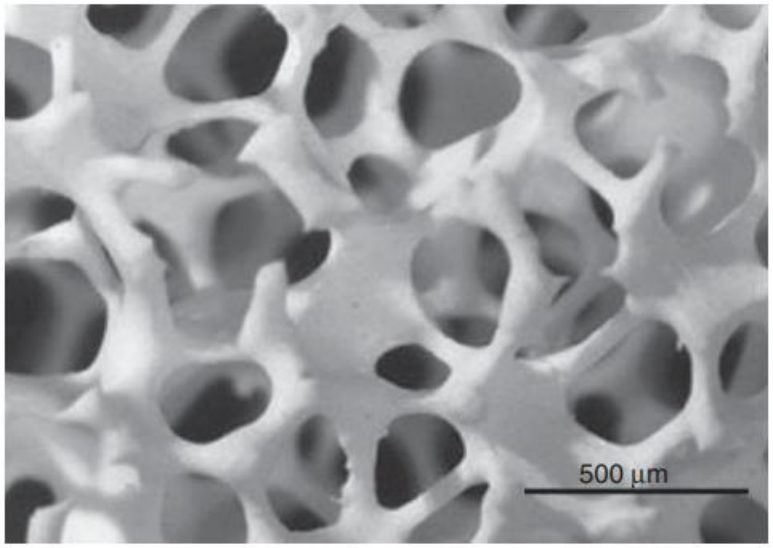

Figure 1.3-5 - Highly porous 3D-scaffold matrix of Sponceram®. (Image courtesy of Zellwer GmbH, Eichstädt, Germany) [65].

1.4. Yttria-Stabilized Zirconia Thin Films

1.4.1. Thin Films Deposition Technologies

Traditional coating techniques are being replaced by advanced methods designed for the production of thin films. These innovations leverage highly versatile and sophisticated vacuum – based technologies. Vacuum – based deposition processes can be distinguished in two main categories:

- *Chemical Vapour Deposition* (CVD), adopted to produce coatings by condensation of gaseous reactants, which are used as the source of coatings species.
- *Physical Vapour Deposition* (PVD), employed to deposit thin coatings by evaporating or atomizing at least one component from a solid target.

CVD and PVD techniques are in common the following steps:

1. synthesis or creation of the depositing species. The vapour phase can be achieved through methods such as evaporation, sputtering, laser ablation, etc.
2. transport from source to substrate. The species may undergo collisions between atoms and molecules or be ionized to create a plasma during the transport.
3. deposition on the substrate and consequent film growth. This step involves the condensation of the vaporized species on the substrate, followed by nucleation and growth of the film. These two phenomena can be significantly influenced by ionic bombardment leading to changes in microstructure, composition, residual stresses and properties [67], [68].

The degree of independent control of these three steps determines the flexibility and versatility of the deposition process.

Surface engineering focuses on modifying material surfaces by adding and removing material, as well as altering its chemistry, to enhance their properties. Coating process and surface modification are distinguishable. The substrate is covered with a layer of a different material in the first case, in contrast, the

second case involves altering the surface properties without adding material. It is possible to combine these two processes to achieve an optimal solution [69].

1.4.2. Zirconia-based Ceramic Thin Film

Typically, zirconia-based ceramic coatings are realized through *Chemical Vapour Deposition* or *Physical Vapour Deposition*, and, recently, many realizations through sol-gel adopting, for instance, spin coating, are founded in literature [70], [71]. Plasma spraying is a widely used technique for zirconia-based ceramics, but it is specifically employed for the deposition of thick coatings.

Chemical Vapour Deposition employs precursor of zirconium and reactive gases to react and forming a thin zirconia film on the surface of the substrate forming [72]–[74].

Physical Vapour Deposition realizes the coating through sputtering of the zirconium target and subsequent condensation of the vaporized material on the substrate [75]–[77]. Electron Beam Physical Vapor Deposition (EB-PVD) is a specific application widely adopted in this field for the deposition of thick films.

Sol-gel leads to the formation of a sol (zirconia colloidal suspension) that is converted into a gel through a gelation process, where the colloidal particles aggregate to form a three-dimensional network. The gel is subsequently dried and sintered to form a thin zirconia film [78], [79].

1.5. Physical Vapour Deposition (PVD)

Physical Vapour Deposition (PVD) is a technique adopted for thin films production of metallic, ceramic, polymeric and composite nature. The thin film thickness varies typically from few to thousands of nanometres. The film is obtained from the vaporization of liquid or solid source, therefore, atoms or molecules, in vapour form, are conducted in vacuum or low pressure to the substrate for the coating formation. Dimension and shape of the substrate vary in a wide range. The vaporization of the source material can occur through various methods, including thermal heating (vacuum evaporation), physical sputtering (sputter deposition), cathodic arc (Arc-PVD), laser ablation (PLD), and electron beam irradiation (EB-PVD), among others [51], [69].

Atoms and molecules are physically ejected from the target with a non-thermal vaporization process in the sputtering deposition. The ejection takes place from the momentum transfer of the energetic bombarding particles, typically plasma accelerated gas ions, of a solid source, target. The sputtering can take place in high vacuum (< 5 mTorr), where the sputtered particles suffer few or no gas phase collision in the space between the target and the substrate, or in low vacuum (5-30 mTorr), where, instead, the sputtered particles are thermolyzed by gas phase collision before reaching the substrate [69].

The plasma consists of electrons, ions and neutral species and it is the conductor of the particles in the deposition chamber. It is sustained in the space between the target (cathode) and the substrate (anode) and its properties vary near these two electrodes, where it is generated by the application of a voltage. [51].

The sputtering deposition is distinguishable as:

- DC diode sputtering where high negative DC voltage is applied to a conductive surface in a gas and positive ions are accelerated to the anode. The sputtering of the target causes the ejection of secondary electrons that, in equilibrium condition, lead to a constant discharge. However, this technique is largely

replaced by more modern sputtering methods, such as Radio Frequency (RF) and Mid Frequency (MF) sputtering, which are used to deposit materials also on non-conducting surfaces.

- Magnetron sputtering adopts a magnetic field (≈ 200 gauss) to force the plasma electrons close to the target surface with a spiral path around the magnetic field lines. This solution permits to sustain the DC gas discharge also at low pressures where collision and charge-exchange collision probabilities are low, leading to high sputtering yield and high sputtering rates. The drawback of magnetron sputtering is the unavailability of plasma for the activation of reactive gases. Possible solutions include applying a radio frequency (RF) potential to the sputtering target, establishing an auxiliary discharge near the substrate, or adopting an 'unbalanced' magnetron configuration. This configuration allows some ejected electrons to escape from the target surface due to a portion of the magnetic field being normal to the target surface [1].

1.5.1. Reactive Sputtering

Reactive sputtering is a Physical Vapor Deposition (PVD) technique used to produce oxide and nitride thin films. The coating results from the reaction between atoms sputtered from a metal target and reactive gas molecules injected into the deposition chamber. Common reactive gases, such as oxygen and nitrogen, are plasma-activated to enhance the chemical reactivity of the deposition process. Typically, reactive gases have a low atomic mass, so using an inert gas with a higher atomic mass aids the sputtering phase. Consequently, a mixture of reactive and inert gases is commonly used, with their ratio significantly affecting the film properties, ranging from almost metallic to semiconductor, insulator, or resistor. The pressure of the reactive gas during reactive sputtering deposition is crucial: excessive pressure leads to target poisoning and a consequent low deposition rate, while too low pressure results in inadequate reactions for coating formation, leading to improper chemical composition. DC magnetron sputtering is the typical equipment used to produce these coatings. This technique provides more control of the stoichiometry of the deposited coating by adjusting the gas flow [69], [80]–[82].

On the other hand, it is important to consider the hysteresis behaviour of the process [69], [80], [82]–[84]. An example of this behaviour is shown for the discharge voltage (Figure 1.5-2) and the deposition rate (Figure 1.5-3). Starting from point A (0 sccm of oxygen gas flow) and moving to point B, the discharge voltage and deposition rate are at their maximum because the metallic surfaces adsorb the oxygen present in the chamber, leading to oxygen-rich films. This is known as the metallic deposition mode. Further increasing the oxygen gas flow leads to a collapse in the deposition rate (from point B to point C) because the target is no longer purely metallic. Consequently, both the discharge voltage and deposition rate values decrease to that characteristic of the poisoning mode.

The decrease of the discharge voltage is explained by the following formula:

$$V_{\text{discharge}} = \frac{W_0}{\gamma_{\text{ISEE}} \varepsilon_e \varepsilon_i Em}$$

In a magnetron discharge, the effective ionisation energy (W_0) is approximately 30 eV for argon. The ion collection efficiency (ε_i) and the fraction of ions generated by electrons (ε_e) are values nearly unity due to the

trapping of the electrons near the target. The gas ionization probability (E) depends on gas pressure, while the multiplication factor (m) is influenced by the sheath thickness. The ion-induced electron emission coefficient (γ_{ISEE}) indicates the number of electrons emitted per ion impacting the target and varies with target conditions. Under experimental conditions, the magnetic field strength remains constant, thus not significantly affecting the sheath thickness. Consequently, the factors that significantly influence the discharge voltage are gas composition, gas pressure, and target condition [85].

The discharge voltage experiences a significant reduction during the formation of the oxide layer. This phenomenon occurs because the ion-induced electron emission coefficient (γ_{ISEE}) increases when the oxide layer forms [85]–[87].

This observation is applicable to many metals. Deviations from this behaviour can be noted when the number of secondary electrons emitted during oxide layer bombardment is relatively low. For instance, aluminium oxide (Al_2O_3) emitted significantly more secondary electrons during bombardment compared to titanium oxide. This difference accounts for the higher (γ_{ISEE}) of aluminium oxide relative to its metallic form, unlike the behaviour observed with titanium [87].

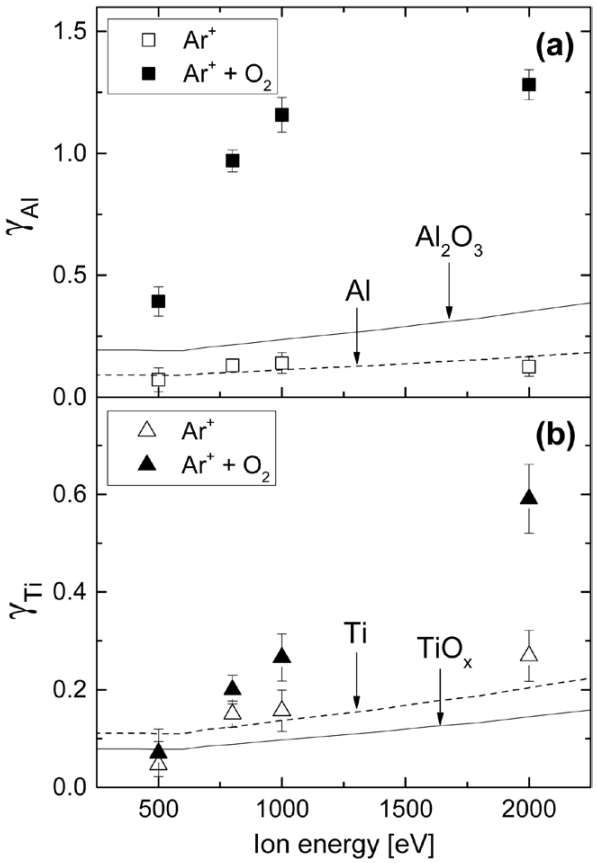

Figure 1.5-1 - Secondary electron yields of Al and Al_2O_3 (a); of Ti and TiO_x (b) as a function of the ion energy. Oxygen flow rate is 0.3 sccm ($j_{O2} = 2.85 \times 1016\ cm^{-2}\ s^{-1}$) [87].

The interaction between the adsorbent and the metal affects ion-induced secondary electron (SE) emission in several ways. In oxides, energy dissipation is more efficient, resulting in fewer but more energetic electrons. This leads to higher SE emission coefficients (SEEC) for oxidized surfaces compared to bare metals. Electron transport is also more efficient in oxides due to fewer electron-electron collisions, further increasing SEEC.

However, the escape probability of electrons is lower in oxides because the work function (Φ) increases with oxygen adsorption, reducing SEEC compared to metallic surfaces [86].

The oxide layer creates a dipole and an electric field, acting like an electron gun and enhancing electron emission. This field, combined with the effective ionization energy (W_0), reduces the energy needed to sustain the plasma, lowering the discharge voltage. Conversely, ion emission decreases because the metal is covered by the oxide layer, preventing deposition. This condition is known as poisoning, and upon reaching point C, additional oxygen gas does not cause a further decrease; instead, the system enters a plateau, indicating the poisoning mode. Moreover, the deposition rate and discharge voltage values do not immediately revert to the metallic behaviour if the oxygen gas flow is reduced (from point C to point D). Instead, the known hysteresis behaviour is observed. The return to the metallic mode is only observable when the target surface has been sputtered clean of the oxide film, causing the discharge voltage and deposition rate values to return to their initial levels almost instantly (from point D to point E).

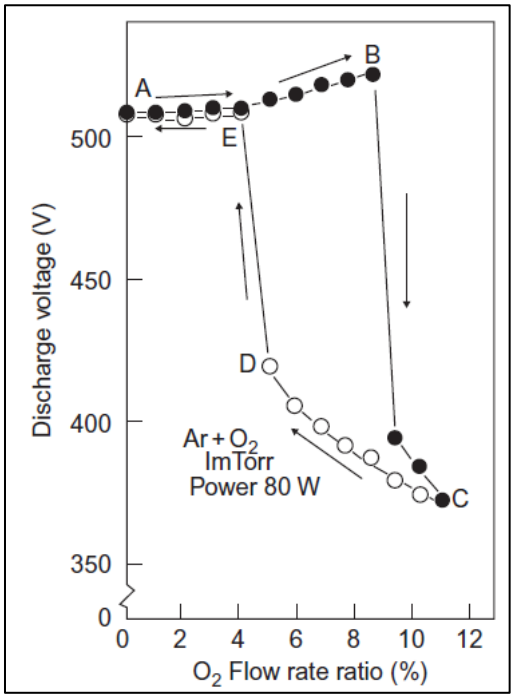

Figure 1.5-2 - Variations of the discharge voltage [82].

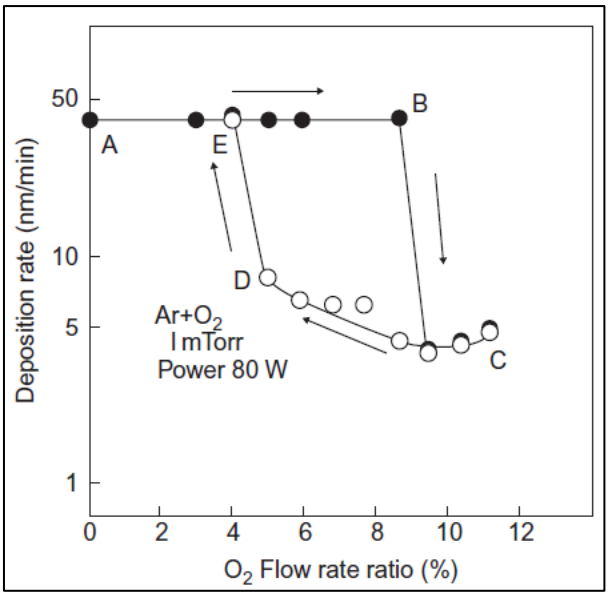

Figure 1.5-3 - Variations of the deposition rates with O2 flow rates [82].

Different solutions are implemented to reduce or eliminate the hysteresis effect. One possible solution is the injection of the inert gas and the reactive gas around the sputtering target and near the substrate surface, respectively, to avoid target poisoning [69].

The shape and dimensions of the substrate surface significantly impact the process outcome. Since the reaction involves the metallic film deposited on the substrate surface and the reactive gas flow near the substrate, changes in the shape and/or dimension of the surface directly affect the reaction of the metallic film and, consequently, the quality of the coating. Therefore, it is crucial to set the deposition parameters according to the final shape and dimension of the piece to ensure a reproducible reactive sputter deposition process. Evaluating the reaction rate is essential to ensure that the deposited metal film reacts immediately with reactive gases. Otherwise, part of the deposited metal film will remain buried by subsequent layers [69]. The reactivity of the process is influenced by multiple variables, including the likelihood of reaction between metallic and reactive gas species. The chemical reactivity of the process can be improved by concurrent bombardment of the depositing/reacting species by energetic ions accelerated from the plasma (bias sputtering) [69]. Effectively, several studies investigated the deposition of zirconia coatings by implementing reactive sputtering deposition. For example, cubic yttria-stabilized zirconia thin films were deposited via reactive magnetron sputtering on Si(100) substrates and (NiO-YSZ) fuel cell anodes. The target used was Zr-Y (82:18 wt%) with a purity of 99.9%, and the gases used were Ar (99.997%) at a partial pressure of 660 MPa as the sputtering gas, and O_2 (99.9995%) at a partial pressure of approximately 40 MPa as the reactive gas [88]. Additionally, cubic zirconia thin films were obtained through reactive sputtering using Argon and Krypton as sputtering gases, and O_2 as the reactive gas, on Si (001) substrates, employing a Zr-Y target (86:14 at%) with a purity of 99.5% [89].

Reactive sputtering was also employed to produce oxide zirconia coatings with varying percentages of oxide stabilizers. This study utilized a Zr-Y target (91:9 wt%) with a purity of 99.95% on Ti6Al4V substrates, using a mixture of Argon as the sputtering gas and O_2 as the reactive gas. Different coatings were achieved by

applying various voltage values, resulting in metallic coatings in metallic mode and oxide coatings characterized by different zirconia phases [90].

1.6.Hydrogels for TERM

Hydrogels are three-dimensional networks composed of polymer chains and water, with the water content ranging from 90% to 99%. The water molecules occupy the interstitial spaces between the polymer chains, rendering these structures highly hydrophilic. Additionally, biological components can be encapsulate in the hydrogel such as proteins and cells [91]–[94].

Hydrogels can be derived from both natural and synthetic materials. Natural hydrogels include substances like gelatine and collagen, while synthetic hydrogels can be made from polyethylene glycol (PEG) and polyacrylamide (PAA). In the context of tissue engineering and regenerative medicine (TERM), natural hydrogels are particularly valued due to their unique properties [92]:

- High biocompatibility: Natural hydrogels are generally well-tolerated by the body, minimizing adverse immune responses.
- Presence of cell-binding motifs: These motifs facilitate cell adhesion and diffusion, which are crucial for tissue regeneration.
- Fibrillar structure: The fibrillar architecture of natural hydrogels mimics the extracellular matrix (ECM), providing a supportive scaffold for cell growth.
- Metabolic recognition and processing: Natural hydrogels can be metabolically recognized and remodelled by the body, promoting cellular reorganization and the deposition of newly synthesized ECM.

Due to these advantageous properties, hydrogels are extensively utilized in TERM. Tissue engineering aims to replace damaged tissues and organs by using hydrogels or scaffolds that can support cell growth and tissue formation. These hydrogels can also be seeded with cells that are cultured specifically for integration into the host tissue. Regenerative medicine leverages the principles of tissue engineering to restore function to damaged areas of the body by promoting the regeneration of tissues and organs [94].

Hydrogels can be classified as ECM-like hydrogels, which mimic the extracellular matrix (ECM). The ECM serves as a physical support to maintain tissue integrity, an adhesive substrate for cell adhesion and reorganization, and a reservoir of biochemical signals that support cell survival and differentiation. The ECM's properties vary depending on the tissue or organ type; for example, it can be more rigid and mineralized in bone tissue or rich in elastic fibres in tendons. ECM-like hydrogels are categorized as follows [92]:

- Protein-based hydrogels: These are derived from purified ECM components and can include:
    - Collagen: The most abundant protein in the ECM, collagen is highly available in nature, biocompatible, biodegradable, and recognizable by cells.
    - Gelatine: A partially hydrolysed form of collagen, gelatine is easy to work with and modify.
    - Elastin: Known for its high elasticity, elastin allows tissues to stretch and contract repeatedly.

- Polysaccharide-based hydrogels: These typically consist of glycosaminoglycans (GAGs), which are the most common polysaccharides in the ECM. GAGs are negatively charged and play a crucial role in cellular signalling, impacting tissue growth and development. Common GAGs include chondroitin sulphate and hyaluronic acid.
- Decellularized tissues and organs: These allow to produce 3D hydrogels with a native organic structure. Cells specifically cultured for integration can repopulate structure. The most common decellularized tissue in the decellularized ECM (dECM).

In addition to ECM-inspired hydrogels, other types include:

- Nucleic acid-based hydrogels: Composed of nucleic acids such as DNA, these hydrogels can encapsulate cells and biomolecules. They exhibit self-healing properties and respond to various stimuli, including temperature, pH, and light.
- Blood-derived hydrogels: Designed to regenerate damaged tissues, these hydrogels utilize components derived from blood [92].

Hydrogels can also be classified based on their applications [92], [93], [95]:

- Dynamic hydrogels: These are designed for self-healing purposes due to their reversible cross-linking capabilities, which can involve covalent dynamic and hydrogen bonds. This allows the hydrogels to break down and rebuild reversibly in a physiological environment. They are particularly useful when maintaining structural integrity under mechanical stress is crucial, such as in the self-healing of cartilage tissue.
- Reinforced hydrogels: These hydrogels are engineered to enhance or introduce specific properties. Typically, mechanical properties are improved using two main approaches. The first approach involves the creation of double-network (DN) hydrogels, which consist of a rigid network that provides mechanical strength and a flexible network that offers toughness and prevents rupture. The second approach involves the incorporation of nanoparticles, often inorganic, which significantly enhance mechanical properties. Additionally, nanoparticles can be used to alter cellular processes. For example, magnetic or electroconductive nanoparticles can be incorporated to create reactive hydrogels that respond to magnetic or electrical fields.
- Smart hydrogels: These hydrogels are designed to respond to specific stimuli such as pH changes, temperature variations, or light exposure. They are often used in drug delivery systems, where they can swell or shrink in response to a stimulus, thereby controlling the release of the drug.
- Hybrid hydrogels: These combine the biocompatibility and bioactivity of natural polymers with the mechanical properties of synthetic ones. This approach allows for the creation of hydrogels with a diverse range of chemical, mechanical, and biological properties, making them suitable for various biomedical applications.

Various properties characterize hydrogels, including [94], [95]:

- Degradation: This property is influenced by the formulation of the hydrogel, cross-linking rate, and environmental factors. In TERM, degradation is typically desired because the hydrogel needs to be

replaced by regenerated tissue. Degradation can occur through hydrolytic processes, where water molecules interact with polymer chains, or through enzymatic processes, involving enzymes such as collagenase.

- Wettability: This surface property is affected by the chemical composition of the hydrogel, surface roughness, and functional groups. Hydrophilic hydrogels, which have high wettability, are particularly suitable for applications such as wound dressings and drug delivery.
- Swelling: The swelling behaviour of hydrogels is influenced by their chemical composition, cross-linking rate, and environmental factors. This property is highly exploited in drug delivery systems. The swelling ratio is defined as:

$$SW = \frac{M\ water}{M\ dried} = \frac{M\ swallen - M\ dried}{M\ dried}$$

  Where M water is the mass of absorbed water by the gel, M dried is the mass of the polymeric matrix, before the swelling, and M swollen is the mass of the polymeric gel in equilibrium after the swelling. The swelling process is highly exploited for drug delivery.
- Mechanical properties: These are influenced by the cross-linking rate, the length of the polymeric chains, and chemical reinforcement. Enhancing mechanical properties is crucial for applications that require structural integrity under stress.
- Rheology: This property helps understand the flow behaviour of the hydrogel solution. Rheology is fundamental in the design phase, particularly for the injection of the hydrogel solution, ensuring it responds correctly to stress during application.
- Porosity: Porosity is the ratio between the volume of voids and the total volume. Pores can be open or closed to the environment, and their size is critical for the access of biological fluids essential for cell activities. Porous structures can be achieved through templating with porogens, lyophilization, electrospinning, 3D bioprinting, etc.
- Cell activities: These include adhesion, migration, proliferation, differentiation, and cell viability. Ensuring cell adhesion is the first crucial step, influenced by surface topography and the number of active adhesion sites. Cell viability depends on pore size, structure type, and the presence of oxygen and nutrients. Subsequent proliferation and migration are influenced by adhesion and viability, which can be enhanced by growth factors in the hydrogel.
- Angiogenesis and vascularization: These processes are influenced by the porosity of the hydrogels, affecting the exchange of waste products and the supply of oxygen and nutrients.
- Antibacterial and antiviral activities: These properties can be enhanced by functionalizing hydrogels with antibacterial elements such as antimicrobial peptides or silver nanoparticles.

Hydrogels can be crosslinked either physically or chemically [92].

- Physical crosslinking involves ionic bonds, which provide greater biocompatibility but result in lower mechanical properties and more significant stress relaxation. Physical crosslinking can be further categorized into:

- Thermal condensation: This occurs due to the physical entanglement of polymer chains caused by thermal changes during the gelation process.
- Self-assembly: This relies on the formation of weak non-covalent bonds between polymer chains, such as hydrogen bonds and van der Waals forces. For example, in collagen, self-assembly is driven by the formation of a triple helix by amino acids, which organize themselves into a well-defined structure.

- Chemical crosslinking involves covalent bonds, which offer better mechanical properties and less stress relaxation but often compromise biocompatibility.

A rigid hydrogel provides good cellular signalling, while a hydrogel with greater stress relaxation allows for better cell diffusion [91]. Therefore, it is important to clearly define the objective, specifically the type of tissue to be integrated, and determine whether a more rigid or less rigid hydrogel is preferable.

1.7.Collagen-based Hydrogels

Collagen is a widely used protein for creating hydrogels across various fields. For example, in bone tissue regeneration, collagen must be combined with hydroxyapatite (HA) as they are both principal components of bone tissue [96], [97]. Often, additional elements are incorporated to induce osteoinduction, which would otherwise not be favoured. Another significant application of collagen hydrogels is in the cornea [98], [99]. In this case, collagen hydrogels ensure the maintenance of water content and transparency, preventing gelation or aligning fibres in a single direction. Furthermore, collagen-based biomaterials have been developed for cardiac and neural applications by incorporating nanoparticles to closely mimic the natural specific tissue [100]–[102].

Another promising application of collagen biomaterials is in the field of dentistry, particularly in addressing peri-implantitis, a common post-operative complication. Peri-implantitis progresses through two distinct phases. The initial phase, known as peri-implant mucositis, is akin to gingivitis in natural teeth and is characterized by redness, swelling, and bleeding of the gums surrounding the dental implant. This inflammatory response is primarily caused by the accumulation and maturation of bacterial biofilm around the dental implant. Importantly, no bone loss occurs during this phase. If peri-implant mucositis is not effectively managed, it can progress to the more severe phase known as peri-implantitis. This phase is marked by the loss of supporting bone, which can be several millimetres in extent. The bone loss associated with peri-implantitis can compromise the stability of the implant and may ultimately lead to implant failure. This condition is analogous to periodontitis in natural teeth but tends to occur more rapidly around implants. Epidemiological studies have shown that peri-implantitis is a prevalent issue, affecting approximately 20% of patients who receive dental implants. This corresponds to about 10% of the implants themselves being affected by this condition. These statistics underscore the importance of early detection and intervention to prevent the progression from peri-implant mucositis to peri-implantitis and to ensure the long-term success of dental [43]–[45].

Studies have demonstrated that maintaining healthy soft tissue is essential for preventing implant rejection and ensuring the long-term success of surgical procedures [23], [103]. There are two primary approaches to achieving this: surgical techniques and the administration of cells and/or scaffolds through a tissue engineering approach.

The wound healing process, which is critical after surgical procedures such as dental implant installation, involves several distinct phases [22], [23]:

1. Hemostasis: This initial phase occurs immediately after injury, where the body works to stop bleeding through the process of coagulation.
2. Inflammation: During this phase, the immune system responds by sending white blood cells (leukocytes) to the wound site. These cells help to clean the wound by removing debris and pathogens, thereby preventing infection. This phase is characterized by redness, heat, swelling, and pain as the body works to protect and repair the damaged tissue.
3. Proliferation: In this phase, new tissue begins to form. Angiogenesis, the formation of new blood vessels, occurs to supply the wound with necessary nutrients and oxygen. Granulation tissue, rich in type III collagen, forms to provide a temporary matrix that supports cell migration and tissue repair. This granulation tissue is essential for rapid repair and protection of the damaged area.
4. Remodelling: The final phase involves the maturation and reorganization of the granulation tissue into a more resilient and structured tissue composed primarily of type I collagen. This phase can last for several months to years, during which the newly formed tissue gains strength and functionality.

Fibroblasts play a crucial role throughout the wound healing process. These essential connective tissue cells are involved from the inflammation phase, where they migrate to the wound site, through to the proliferation and remodelling phases. Fibroblasts produce and organize the extracellular matrix (ECM), which is vital for the formation of new tissues and the regeneration of damaged tissue. They are responsible for producing collagen, a key component of the ECM, which is necessary for the development of new tissue and the regeneration of specific tissues [22], [23].

Research has shown that the use of collagen biomaterials can significantly enhance the regeneration of soft tissues [104], [105]. For instance, type I collagen membranes inserted into the mandibular area of pigs have demonstrated effective soft tissue regeneration without causing inflammatory reactions, indicating optimal integration of the device [105].

Other studies have focused on the direct role of collagen on fibroblasts. Indeed, the creation of collagen-based scaffolds has consistently shown rapid fibroblast adhesion and subsequent proliferation over time [25], [26], [28], [106].

Therefore, collagen-based biomaterials provide a structure that mimics the extracellular matrix, influencing cellular activity. Specifically, in tissue regeneration and regenerative medicine, collagen offers an optimal environment for fibroblast adhesion, promoting their subsequent migration and proliferation. This is crucial for fibroblasts to play their role in the wound healing phases, which is essential for the formation of new tissue

around the wound. Thus, the use of collagen-based biomaterials can be a key strategy in the field of TERM, providing physical support and actively participating in the healing process [107].

1.8.Collagen

Collagen comes from the Greek word (kólla), which translates to 'glue', and the suffix -, -gen, which means 'producing'. Collagen is the most abundant protein in mammalian organisms. It is the main component of skin, bone, tendon, ligament, cartilage, and other specific tissues, providing strength and durability, along with flexibility, and a broad range of specific biological interactions. Collagen is a protein family that is crucial in the structure of the extracellular matrix. 28 collagen types are known which are encoded by over 40 different genes and they are linked through a common structural element, the triple-helix, as well as several shared biochemical themes. [29], [108]–[110]

The collagen monomer consists of three polypeptide chains also called α chains. The polypeptide is an amino acids sequence, typically glycine and proline: glycine is the smaller amino acid and creates spaces between the polypeptide chains promoting the interaction and the formation of a compact helix, instead, the proline defines the bulky structure thanks to the kinks formation leading to the helix formation. Therefore, the three polypeptides interact and link with each other through hydrogen bonds. Some exposed residues of each polypeptide remain, and they are exploited from the collagen monomer during the cross-linking phase [29].

1.8.1. Collagen Type

Since many types of amino acid sequences are possible, there are over twenty types of collagen, each of which performs specific functions that characterize particular mammalian tissue. The most known types are:

- Type I, that is the most abundant type (90% of the existing collagen), and it is present in bone, skin, tendon and cornea tissues;
- Type II exists in cartilage and vertebrae tissues;
- Type III is in blood vessels and granular tissue and
- Type VI characterized the basement membrane.

The type I, II and III are in the fibrillar form providing specific tensile or shear strengths at the specific tissue. The type IV, instead, is constituted by a sheet structure giving support function of the tissue [29].

1.8.2. Collagen Fibrillogenesis

Fibrillogenesis is the process by which collagen molecules self-assemble into fibrils, the fundamental structural units of collagen fibres. This process involves the precise alignment and subsequent cross-linking of collagen molecules, resulting in the formation of long, thin fibrils. These fibrils provide essential mechanical strength and structural support to various tissues, such as skin, tendons, and bones.

In vivo fibrillogenesis of the collagen begins in the fibroblast and concludes with its secretion into the extracellular matrix. The synthesis process initiates when mRNA encounters ribosomes, leading to the formation of polypeptide chains. The first molecule produced is the pre-pro-peptide, characterized by an N-terminal signal sequence. This terminal directs the molecule to the rough endoplasmic reticulum (ER), where

it is cleaved by specific enzymes to form the pro-peptide. Multiple pre-pro-peptides are synthesized simultaneously, resulting in the creation of numerous pro-peptides within the fibroblast cell.

Hydroxylation reactions, catalysed by hydroxylase enzymes, convert amino acids into hydroxylated forms; for example, proline is converted into hydroxyproline. These hydroxyl groups significantly influence the properties of the collagen monomer. Co-factors such as vitamin C and oxygen are essential for effective hydroxylation. A deficiency in either co-factor results in suboptimal collagen chain formation.

Subsequently, three of these peptides assemble into the collagen triple helix. The pro-peptide, containing N-terminal and C-terminal sequences, maintains molecular integrity during this process. The pro-peptide is then secreted from the cell via exocytosis. Specific enzymes, known as peptidases, cleave the terminal sequences, activating the molecule and forming the collagen monomer, also known as a fibril.

Multiple fibrils overlap and, through the action of lysyl oxidase enzymes, undergo oxidation reactions that establish covalent bonds between fibrils, resulting in cross-linking. This cross-linking process requires the co-factor Cu2+. In the absence of adequate Cu2+, cross-linking is insufficient, leading to poorly structured collagen tissue [29], [111], [112].

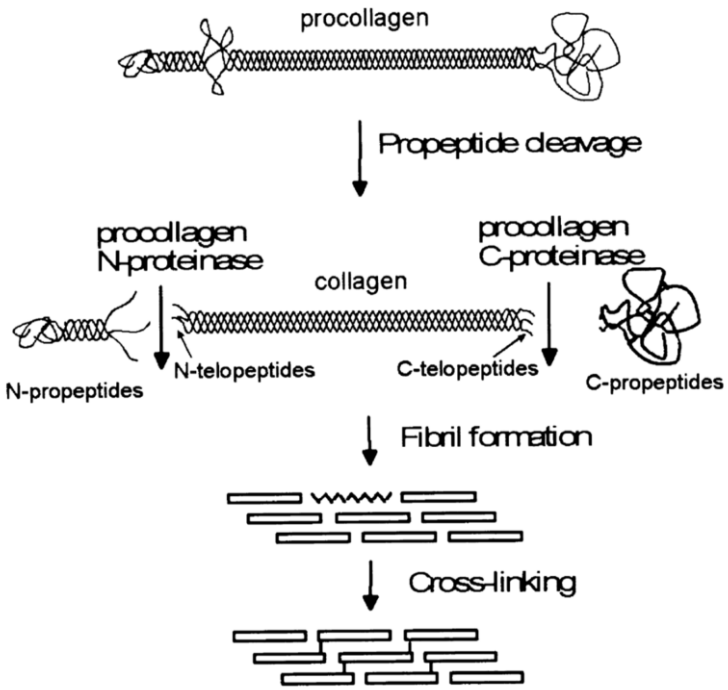

Figure 1.8-1 - A schematic of the processing stages by which collagen fibres are formed in vivo, emphasizing the modifications which occur before fibrils form [111].

In vitro fibrillogenesis involves studying the formation of collagen fibrils outside a living organism, typically in a laboratory setting. Researchers use controlled conditions, like specific pH and temperature, to observe how collagen molecules assemble into fibrils. This helps understand the mechanisms of fibril formation and aids in applications like tissue engineering. The initial step in this process involves obtaining the raw material,

which requires the dissolution of collagen tissue. This procedure results in the extraction of collagen, which can then be processed into either a liquid or powder form. In the case of powder, it can be dissolved as needed to achieve the final formulation. In the case of liquid, the dissolving acid is already included in the formulation and cannot be changed, but the solution can be adjusted to obtain the desired properties.

This phase is crucial as it provides the necessary collagen substrate for subsequent in vitro fibrillogenesis experiments, ensuring that the collagen is in a suitable state for controlled study and manipulation in the laboratory setting. It is fundamental to preserve the natural characteristics of collagen fibrils, such as the triple-helix and the telomere regions, during dissolution to maintain its properties. Since the triple-helix is significantly influenced by electrostatic interactions along the fibril chains, the pH and ionic strength of the buffer solution are fundamental environmental factors that affect it. Additionally, the dissolution process affects the formation of the D-banding, resulting in various solutions, including gelatine, which contains short segments of the triple-helix, and collagen, which retains its fundamental properties.

In vitro fibrillogenesis occurs in two stages: nucleation of the triple-helix, leading to the aggregation of collagen molecules, and, upon reaching a high concentration, lateral growth of the fibrils [112]. Figure 1.8-2 shows images of collagen fibril formation from 0 seconds (A) to 200 seconds (I), highlighting the evidence of lateral growth [113].

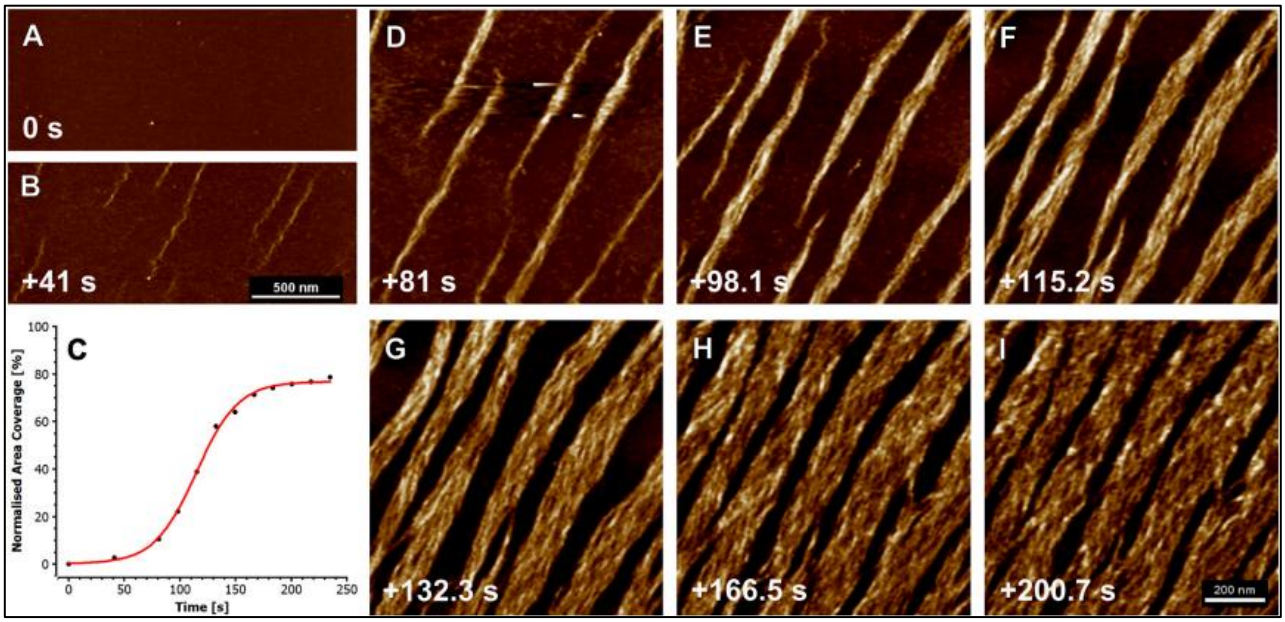

Figure 1.8-2 - Collagen kinetics observed at physiological pH. Collagen type I fibrillogenesis in PBS buffer (standard) with pH 7.4 and monomer concentration of 30 mg/ml [113].

1.8.3. Functional and Structural Characteristics

1.8.3.1. Stability and Stiffness

The stability and stiffness of collagen are fundamental properties that play a crucial role in maintaining the structural integrity and functionality of various tissues in the body. Collagen, being the primary structural protein in the extracellular matrix (ECM), provides essential support and strength to tissues such as skin, tendons, and bones.

Stability of collagen refers to its ability to maintain its structural integrity under various environmental conditions, including changes in temperature, pH, and chemical exposure. This stability is largely influenced by factors such as the content of hydroxyproline (Hyp), cross-linking processes, and the presence of specific environmental conditions.

Stiffness, on the other hand, refers to the mechanical resistance of collagen to deformation under applied forces. It is a critical factor that determines the mechanical properties of tissues, influencing their ability to withstand mechanical stress and maintain their shape and function. Stiffness is strictly influenced by integrins. Integrins are proteins that mediate adhesion between cells and the extracellular matrix (ECM) through focal adhesion points (FAs). A rigid ECM substrate supports higher traction forces, aiding the stabilization of these cell-ECM adhesions. Focal adhesion points are sensitive to the mechanical properties of the ECM substrate and remodel the actin cytoskeleton, generating forces within it. The rigidity of the substrate regulates the magnitude of these forces. Consequently, the actin cytoskeleton produces stress fibres that activate multiple biomechanical signalling pathways. Among these biomechanical signals, intracellular signals that propagate through cell-cell junctions are fundamental, influencing the cellular response [114]–[116].

The melting temperature (Tm) of collagen is a critical characteristic that significantly influences its stability and stiffness. By modifying the Tm through factors such as hydroxyproline content, cross-linking processes, and environmental conditions, it is possible to enhance both the stability and stiffness of collagen. This is essential for developing collagen-based materials capable of withstanding various physiological conditions and mechanical stresses, thereby making them more suitable for biomedical applications.

Typically, collagen I, II and III have a single Tm value of approximately 41°C [117].

Collagen tissue with a higher content of hydroxyproline (Hyp) is more stable, as Hyp enhances the stability of the triple helix. The quantity of Hyp can increase if the tissue is subjected to temperature variations, such as transitioning from cold to hot temperatures [118].

Acid pH, various salts, and numerous chemical modifications can significantly compromise the stability of the collagen tissues, reducing the melting temperature by several degrees Celsius [29], [119], [120].

Additionally, cross-linking increases the melting temperature value by tens of degrees Celsius, thereby leading to more stable tissue. Cross-linking introduces additional covalent bonds between collagen molecules, which enhances the thermal stability and mechanical strength of the tissue. This process is essential for applications where collagen needs to withstand higher temperatures and maintain its functional properties [29].

1.8.3.2. D-banding

The collagen chain is characterized by a distinctive D-pattern, which exhibits a periodicity ranging from 600 Å to 700 Å, commonly referred to as the D-period. This periodicity is a fundamental structural feature of collagen fibrils and is crucial for their mechanical properties and biological functions.

The D-period is not uniform across all tissue types; rather, it varies depending on the specific type of tissue. For instance, a D-period of approximately 670 Å is typically observed in native wet tendon collagen and in reconstituted fibrils of collagen types I and III. It indicates highly organized and tightly packed structure of collagen in tendons, which is essential for their ability to withstand high tensile forces.

In contrast, shorter D-period values, ranging from 652 Å to 655 Å, are observed in the skin and other extensible tissues that contain both type I and type III collagen. These tissues require a certain degree of flexibility and extensibility, which is reflected in the slightly shorter D-period [29], [121].

The variation in the D-period among different tissues highlights the adaptability of collagen fibrils to meet the mechanical and functional demands of various biological environments.

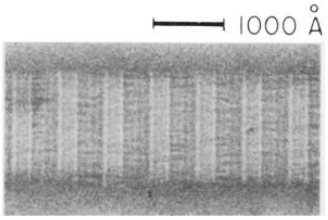

Figure 1.8-3 – Electron micrograph of rat tail collagen fibril [121].

The aggregates in the initial nucleation phase had a length exceeding 1500 nm and a diameter up to 8 nm, as evidenced by light scattering data. Subsequent growth led to a critical length, resulting in mature fibrils [122]. Since the implantation of a host material induces a wound, it triggers a series of biological responses. During the assessment of tissue growth using transmission electron microscopy (TEM), collagen secretion was observed after 14 days. At this point, the fibrils were characterized by lengths of 9.2 µm and diameters of 48 nm. As the healing process continued, these fibrils increased in length to 28.1 µm while maintaining the same diameter of 48 nm after 28 days [123].

The D-pattern of collagen fibrils is synergistically influenced by pH, ionic strength, and the type of acid solution used during in vitro fibrillogenesis. These factors collectively determine the structural integrity and organization of the collagen fibrils. Figure 1.8-4 illustrates the mature D-banding pattern of acetic acid-soluble collagen type I when mixed with phosphate and Tris-HCl buffers, achieving pH levels of 7.0 and 9.0, respectively.

The presence of NaCl was crucial for obtaining a well-defined D-banding pattern. In the absence of NaCl, even when Tris-HCl was added to the collagen solution, the fibrils exhibited a helical pattern that was angled at 45° with respect to the fibril axis. This indicated that NaCl played a vital role in stabilizing the D-banding pattern and ensuring the proper alignment of collagen molecules. Furthermore, as the pH increased, the degree of disorder within the fibrils also increased, suggesting that higher pH levels could disrupt the regular D-banding pattern and led to less organized fibril structures [124].

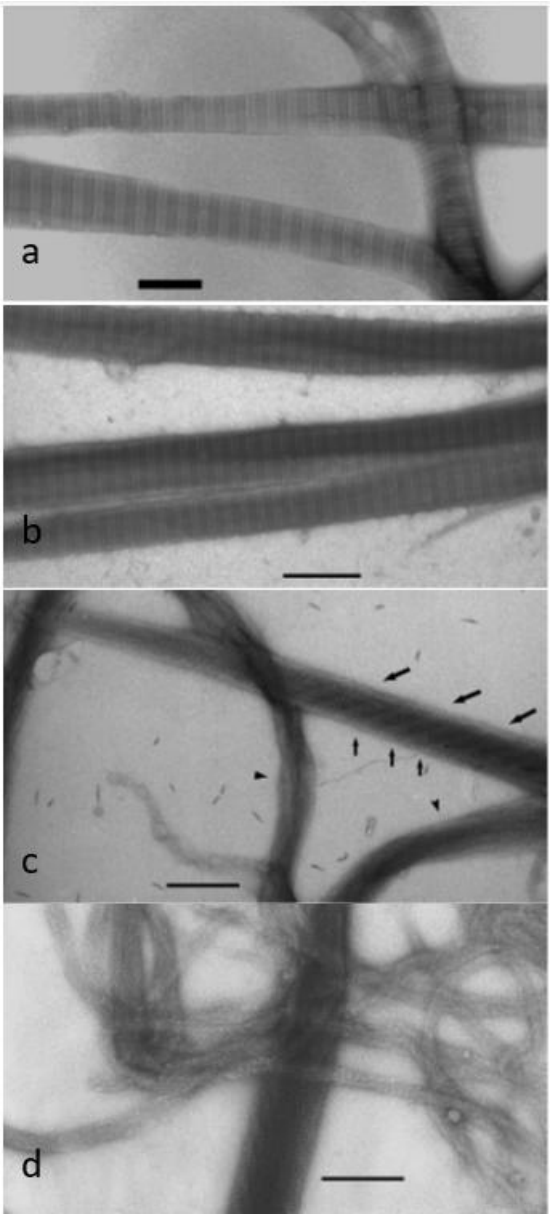

Figure 1.8-4 - Acetic acid-soluble collagen type I following pH adjustment to (a) 7.0 with phosphate-buffered 150 mM NaCl, (b) 9.0 with Tris-buffered 150 mM NaCl, (c) 7.0 with addition of 50 mM Tris–HCl buffer and (d) 8.0 with addition of 50 mM Tris-HCl buffer. The scale bar indicates 200 nm [124].

D-banding pattern in collagen fibres immersed in different solutions was investigated [125]. The highest production of long and compact D-banded collagen fibres occurred in NaCl concentrations ranging from 200 to 500 mM, buffered in 10 mM phosphate at pH 7.0.

Figure 1.8-5 illustrates the formation of pre-fibrils at low NaCl concentrations up to 50 mM. At this concentration, the collagen fibres were not well-defined, indicating that the D-banding pattern was weak or absent. As the NaCl concentration increased to 75 mM, weak D-bands began to appear. These bands became more pronounced and well-defined at concentrations of 100 mM and above, with a D-periodicity of 67 nm. The most pronounced D-banding was observed at a concentration of 500 mM, where the collagen fibres exhibited a clear and compact D-banding pattern.

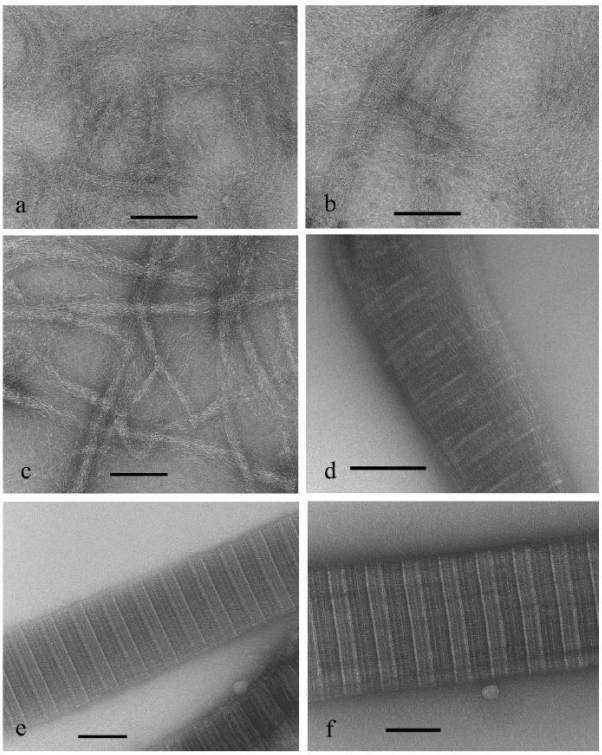

Figure 1.8-5 - Collagen type I fibrillogenesis in the presence of increasing concentration of NaCl in 10 mM phosphate buffer, pH 7.0 at different NaCl concentration: 10mM (a), 20 mM (b), 50 mM (c), 75 mM (d), 100 mM (e) and 500 mM (f). The scale bar indicates 100 nm [125].

1.8.4. Key factors in the Production of Collagen-based Materials

1.8.4.1. pH

The formation of collagen fibrils, and consequently the final structure of collagen, is highly influenced by the pH of the solution in which the synthesis occurs. Maintaining an appropriate pH is crucial for ensuring the proper assembly and stability of collagen fibrils.

Maintaining a pH close to the isoelectric point is crucial for the correct formation of the D-banding in collagen fibrils. Deviations from this pH result in the loss of D-banding. Turbidity measurements indicate that fibril formation increases with rising pH (Figure 1.8-6). The morphology and D-period of the fibrils were analysed using TEM and SEM microscopy [126]. Figure 1.8-7 highlights the size inhomogeneity of fibrils up to pH 6.9, with smaller fibrils lacking D-banding. As the pH increases, a homogeneous fibril network characterized by D-banding becomes evident, as observed through SEM analysis. The D-periodicity values are approximately 62 nm after three days of fibrillogenesis across all pH conditions (Table 1-2), which aligns well with the native D-period value observed during in vivo fibrillogenesis.

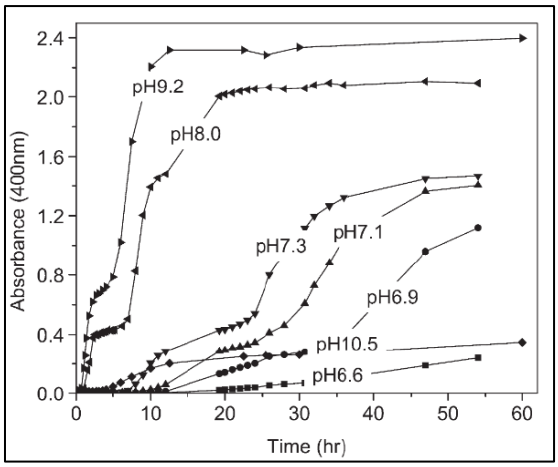

Figure 1.8-6 – Turbidity measurement of collagen fibrillogenesis at 30°C under the effect of pH [126].

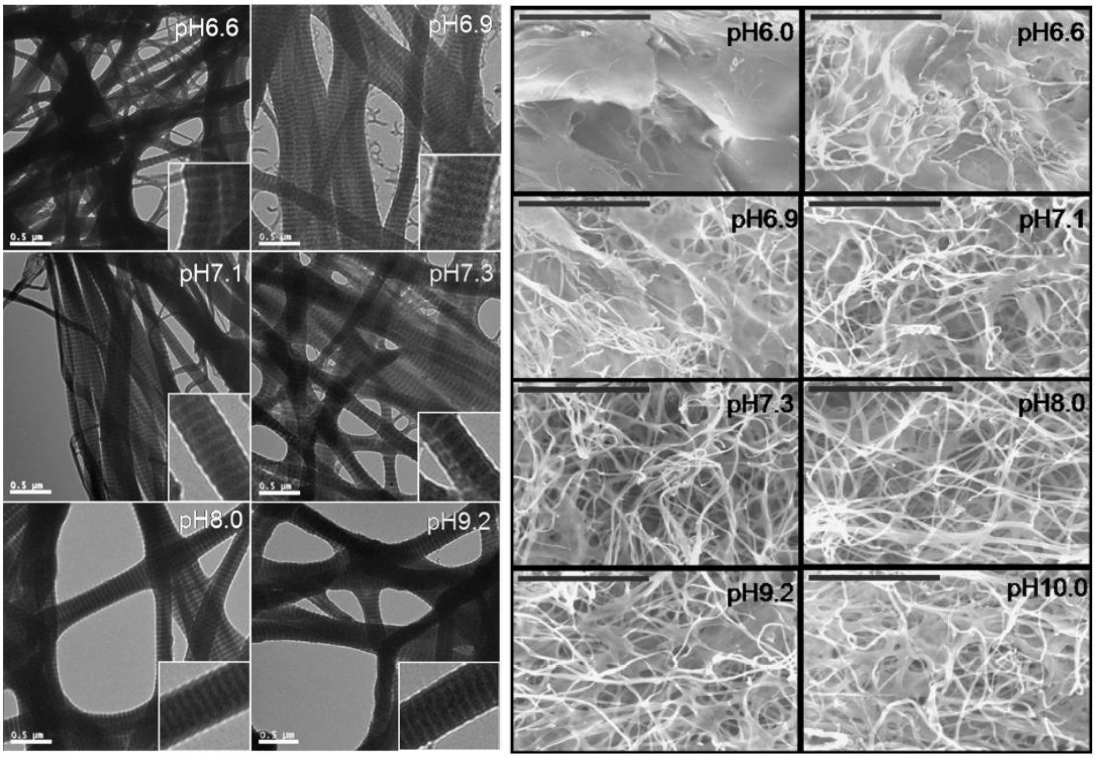

Figure 1.8-7 – TEM images of self-assembled collagen fibrils after three days of fibrillogenesis (sx) and SEM images of collagen fibrils obtained in different pH conditions (dx) [126].

Table 1-2 - D-periodicity of collagen fibrils at various pHs and fibrillogenesis times [126].

pH	D-periodicity (nm)		
	One day	Two days	Three days
6.9	60.4 ± 7.8	64.9 ± 3.8	62.1 ± 5.7
7.1	50.5 ± 4.5	54.3 ± 9.1	62.3 ± 6.0
7.3	65.8 ± 7.6	64.0 ± 6.7	62.2 ± 3.6
8.0	62.4 ± 5.3	62.5 ± 5.1	61.6 ± 4.4

1.8.4.2. Ionic Strength

Ions present in the buffer solution can interact with the charges of the amino acid chains of collagen. These interactions can prevent the amino acids from participating in reactions that are crucial for collagen stability

and fibril formation stabilizing the collagen triple helices, and, consequently, making the structure more robust. Specifically, optimal concentrations of salts help to screen the electrostatic repulsions between collagen molecules, facilitating their closer packing and alignment into well-defined fibrils. This leads to the formation of a more organized and stable fibrillar network.

Different types of salts can influence this equilibrium in various ways because each salt can cause a shift in the pH value of the solution [112]. This shift in pH can further affect the stability and formation of collagen fibrils. For instance, the addition of 0.5 wt.% NaCl (sodium chloride) to the solution has been shown to promote the formation of more fibrillar tissue. This results in a final tissue with a more fibre-like surface, as observed in Figure 1.8-8.

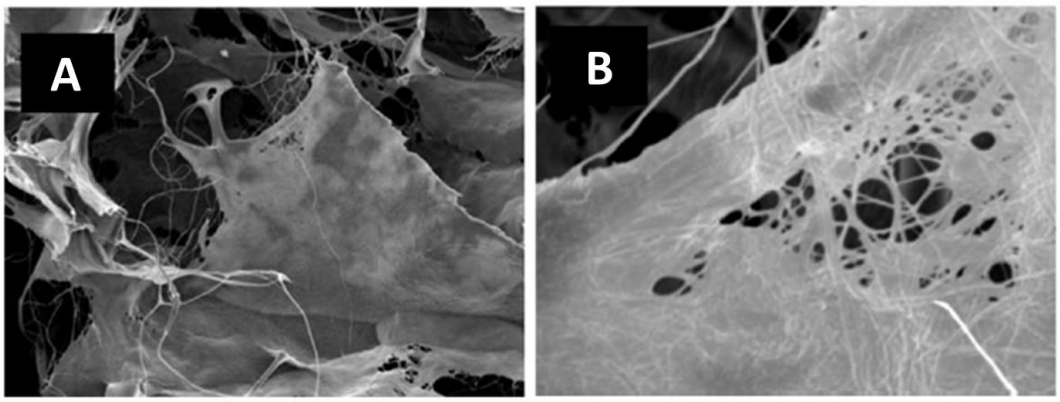

Figure 1.8-8 - Highly fibrillar structure with 0,5 %wt NaCl addition at high magnification(A) X400 and (B) X 3300 [112].

1.8.4.3. Acid Type for Collagen Dissolution

A specific acid is required to dissolve the collagen tissue. Acids are used to break down collagen into a soluble form, which is necessary for various biomedical applications. The choice of the acid type is crucial for ensuring efficient dissolution and optimal tissue formation influencing structural and functional properties of the resulting collagen solution and the final tissue.

Typically, hydrochloric acid (HCl) or acetic acid is used. However, hydrochloric acid led to improved characteristics, particularly in terms of the pore size of the final tissue (Figure 1.8-9) and the proliferation of fibroblast cells [127]. At neutral pH the collagen solution gelled when warmed to 37°C within the first hour. Conversely, at acidic pH, the same solution became almost completely insoluble after two weeks [128].

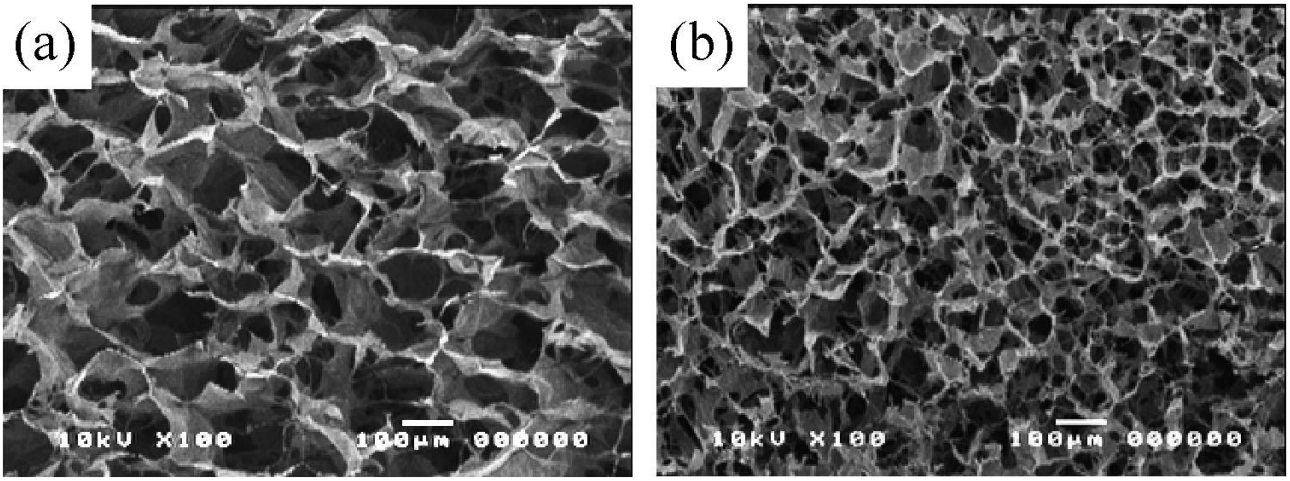

Figure 1.8-9 - SEM photographs of collagen scaffolds freeze-dried from (a) hydrochloric solution (C–HCl) and (b) acetic solution (C-Acetic) [127].

1.8.4.4. Collagen Concentration

The collagen concentration of the solution impact considerably several characteristics of the final product, above all in terms of morphology and mechanical behaviour. Collagen concentrations commonly used for hydrogel formation typically range from 0.2% w/v to 1% w/v [129]–[132]. The standard concentration adopted for tissue regeneration is 0.5% w/v [133], [134].

Collagen concentration directly affects cell proliferation [130]–[132]. This is because cell attachment is inversely related to pore size: smaller pore sizes result in a higher exposed surface area, thereby increasing the number of ligands. Since pore size is inversely related to collagen concentration, cell attachment improves as collagen concentration increases as shown in various experiments and whose results are displayed in Figure 1.8-10 and Figure 1.8-11 [129], [130].

The attachment of MC3T3-E1 cells was evaluated on collagen scaffolds with different collagen concentrations [130]. Low collagen concentrations, ranging from 0.25% w/v to 0.38% w/v, caused structural collapse, leading to reduced cell adhesion. At 0.5% w/v, a uniform pore structure supported good cell adhesion. The optimal cellular response was seen at 1% w/v, which greatly enhanced adhesion by forming an elongated plates of collagen structure (Figure 1.8-11).

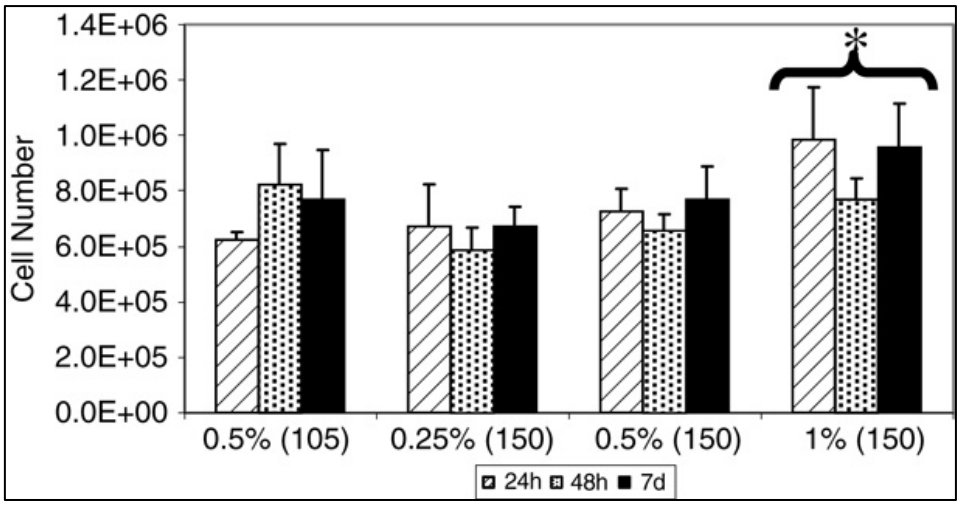

Figure 1.8-10 - Cell number on the collagen-GAG scaffolds [129].

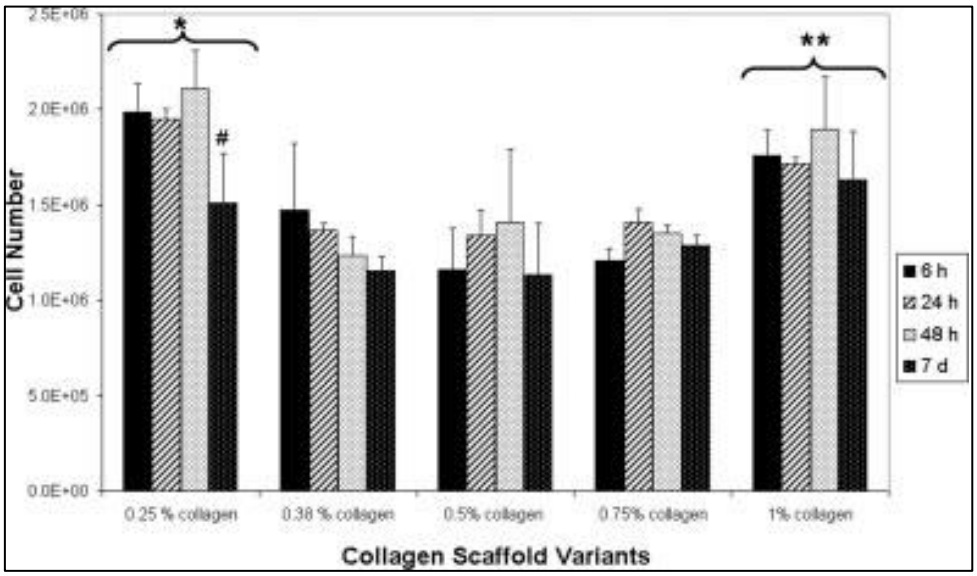

Figure 1.8-11 - Cell number on collagen scaffold variants [130].

Additionally, higher collagen concentrations improve mechanical properties. For instance, the compressive modulus of dehydrothermal cross-linked collagen scaffolds increased with higher collagen concentrations (Figure 1.8-12).

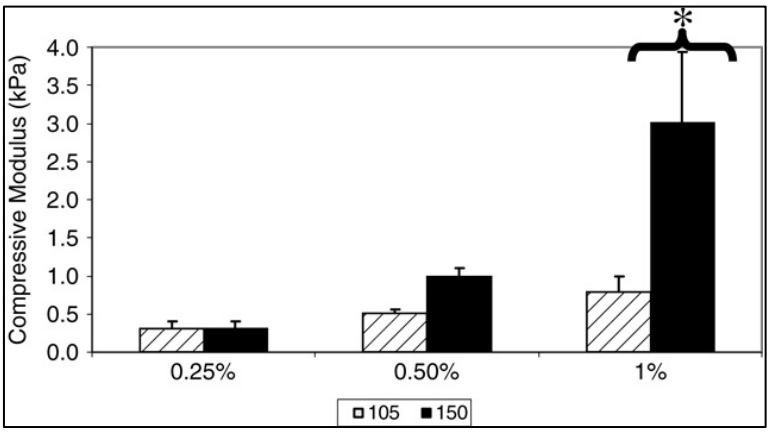

Figure 1.8-12 - Compressive moduli of the collagen-GAG scaffolds crosslinked at 105°C and 150°C DHT [129].

1.8.4.5. Cross-linking

Cross-linking enhances the mechanical stability and rigidity of the ECM, supporting higher traction forces at focal adhesion points and reinforcing cell-ECM adhesions. It also influences the actin cytoskeleton, modulating biomechanical signalling pathways activated by stress fibres. Moreover, cross-linking is essential when durability and resistance are required for the final tissue. It ensures that the ECM can maintain its structural integrity and functionality over time, even under continuous or heavy use, providing the necessary strength and resilience for long-term durability and performance.

Cross-linking can be achieved through chemical or physical methods. Chemical cross-linking involves using specific reagents that create covalent bonds between polymer chains in the extracellular matrix (ECM). These reagents, such as glutaraldehyde (GA) or genipin, react with functional groups on the polymers, forming stable, interconnected networks. Physical cross-linking, on the other hand, can be achieved through methods such as applying heat or radiation. These physical processes induce the formation of bonds between polymer chains without the need for chemical reagents, which can potentially degrade the material. Both chemical and physical cross-linking methods enhance the mechanical properties of the material, making it more durable and resistant to mechanical stress, thereby ensuring the long-term functionality and stability of the tissue.

GA has been a widely used chemical cross-linker for over 50 years, but it has significant drawbacks, such as cytotoxicity due to its bonding with the ε-amino groups of the collagen monomer. This bonding renders these groups unavailable, causing the monomer to lose its characteristics. Consequently, research is focused on more biocompatible chemical cross-linkers. Carbodiimides, which react with amino acids through peptide bonds, do not have cytotoxicity issues. The most commonly used carbodiimide reagent is EDC (1-Ethyl-3-(3-dimethylaminopropyl)carbodiimide), which increases tissue stability up to approximately 70°C, especially when combined with NHS (N-Hydroxysuccinimide) [29].

A collagen solution is cross-linked using EDC-NHS, genipin, and TG2 to compare the mechanical properties [135]. The tensile modulus and tensile failure strength reached the highest values with EDC-NHS, increasing with the degree of cross-linking: approximately 300 MPa for EDC-NHS, 50 MPa for genipin, and a few MPa for TG2 at 50% cross-linking. The strain at failure was higher for TG2, whereas it approached 0% when EDC-NHS and genipin were used (Figure 1.8-13). Additionally, cell number evaluation (Figure 1.8-14) and fluorescence microscopy (Figure 1.8-15) shown good proliferation of human dermal fibroblasts with 10% EDC-NHS, reaching values comparable to genipin and TG2 cross-linkers. These results confirmed that none of the three cross-linkers are cytotoxic.

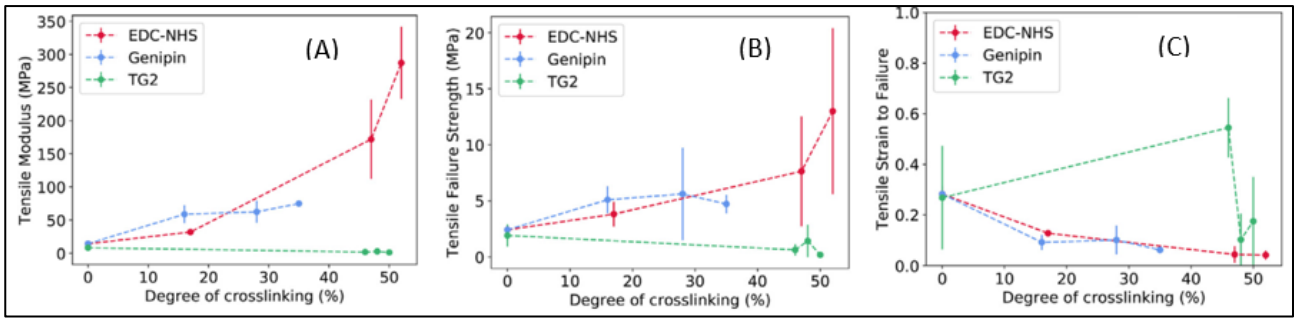

Figure 1.8-13 - Mechanical characterisation of collagen crosslinked with EDC-NHS, genipin and TG2: a) Tensile modulus b) Tensile failure strength and c) Strain at failure mode [135].

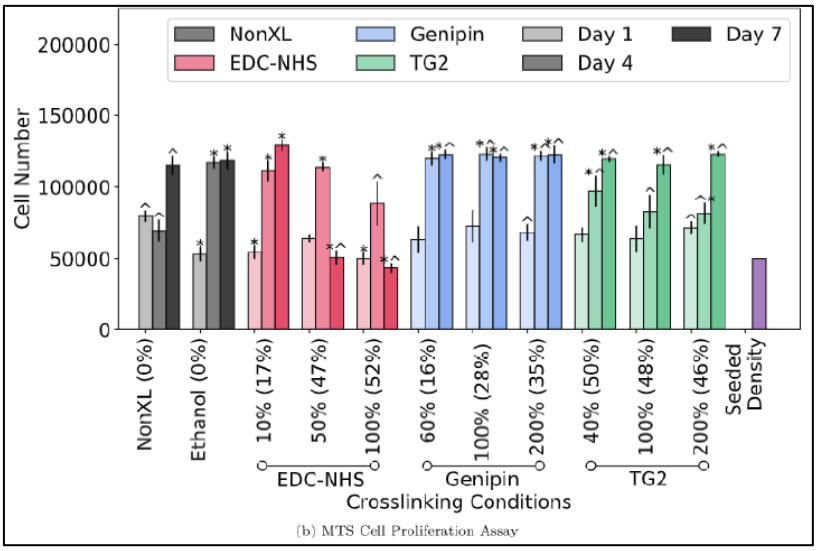

Figure 1.8-14 - Cell number evaluation with different cross-linkers [135].

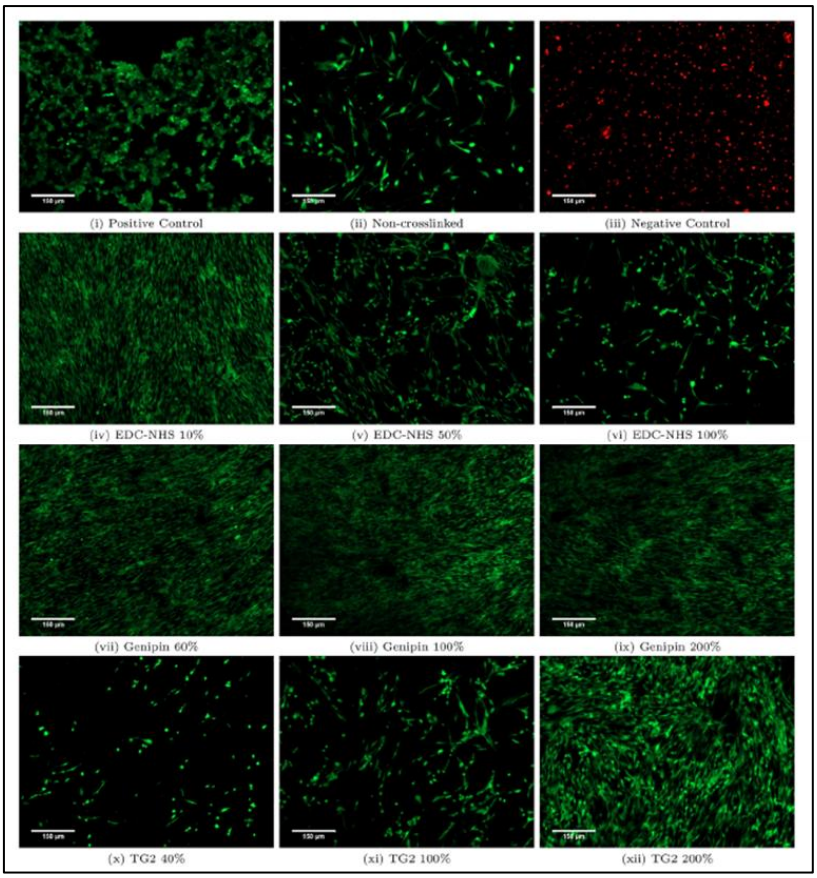

Figure 1.8-15 - Fluorescence microscopy for the evaluation of the cell behaviour at different cross-linkers [135].

Another approach involves using physical methods like UV radiation to generate free radicals within the collagen. These free radicals then react to form cross-links, creating a network of bonded collagen fibres. Collagen, collagen-gel, and gel solutions were cross-linked using EDC-NHS [136] and UV treatment [137], resulting in a collapse of the Young's Modulus in the presence of the gel (Figure 1.8-16 and Figure 1.8-17). Additionally, the Young's Modulus of EDC-NHS cross-linked collagen scaffolds was at least twice as high as that of UV cross-linked collagen scaffolds. Conversely, the content of free amino groups remained almost intact with UV treatment compared to EDC-NHS use (Figure 1.8-18).

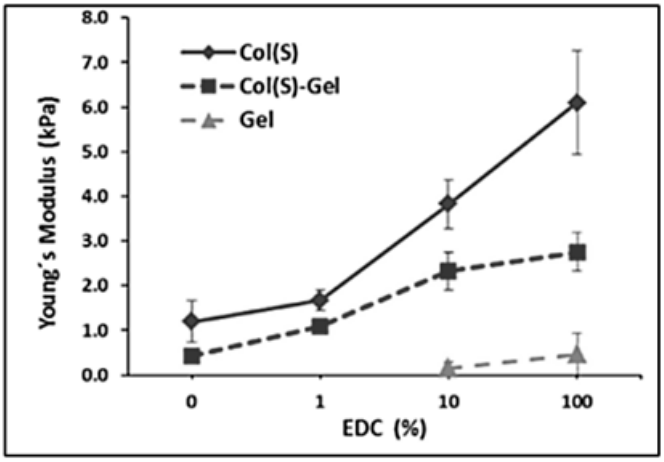

Figure 1.8-16 - Influence of EDC concentration on the compressive modulus (E) of the scaffolds of different compositions [136].*

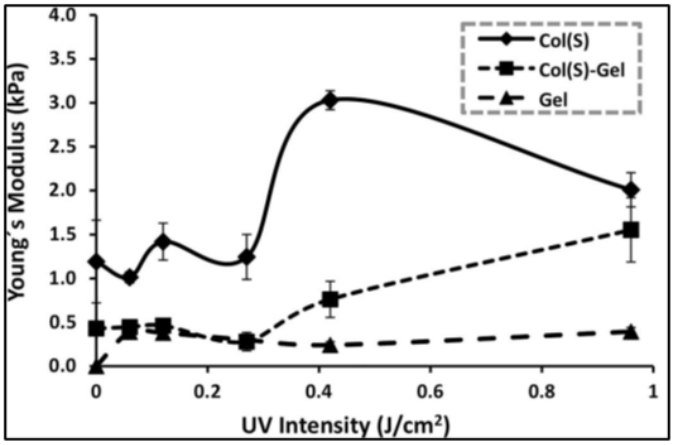

Figure 1.8-17 - Influence of UV intensity on the compressive modulus (E) of scaffolds composed of Col(S) (diamond), Col(S)–Gel (square) and Gel (triangle) [137].*

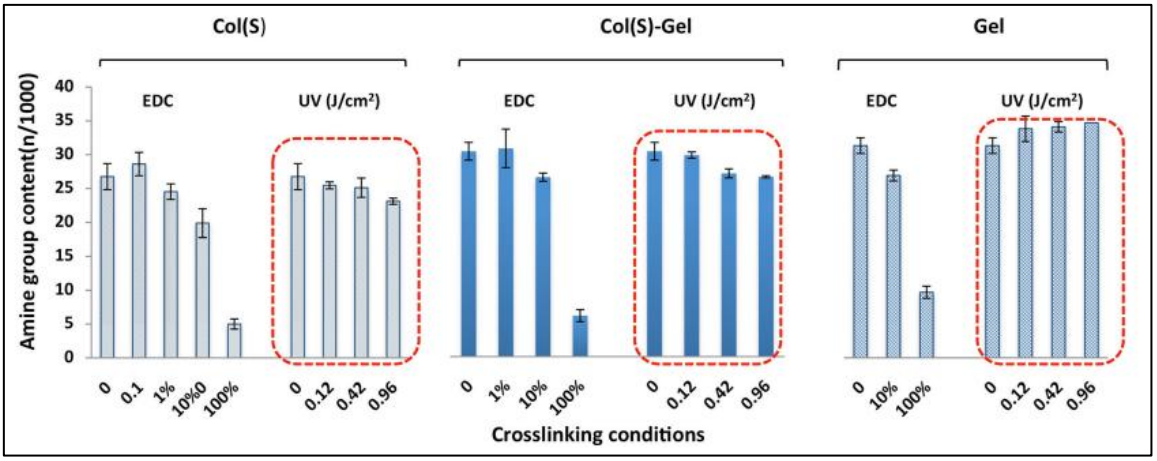

Figure 1.8-18 - Comparison of the influence of EDC treatment with different concentrations and UV irradiation at different intensities (J/cm2) on the free amine group content of Col(S), Col(S)–Gel and Gel scaffolds [137].

Using UV cross-linking at 254 nm required only 30 minutes to achieve optimal stiffness and ultimate tensile strength (UTS). This rapid process is due to the formation of free radicals on aromatic amino acids, which quickly form covalent bonds. In contrast, dehydrothermal (DHT) cross-linking, needed several days, up to 5, to achieve similar mechanical properties. This longer duration is because DHT relies on the slow removal of bound water and subsequent condensation reactions between amino acid side chains [138].

EDC appears to be a suitable option for achieving both good mechanical properties and a high number of amino groups. Another potential benefit of using EDC-NHS is demonstrated by AFM images, which shown the natural D-pattern with D-banding of 66.1 ± 1.29 nm in collagen cross-linked with EDC-NHS (Figure 1.8-19).

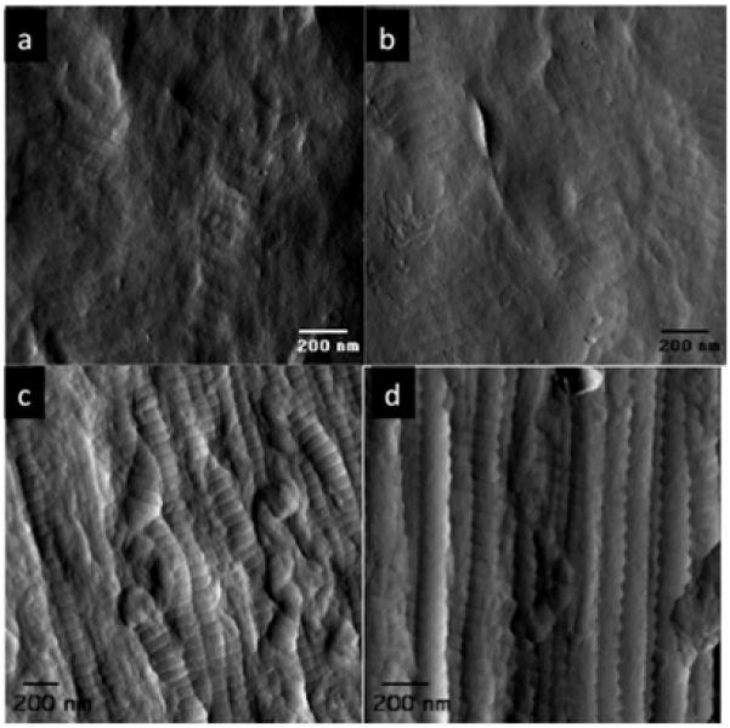

Figure 1.8-19 - AFM image of: (a, b) fibres without cross-linking, (c, d) with the EDC-NHS treatment [139].

2. Chapter 2 - Materials and Method

2.1.Reactive Magnetron Sputtering Deposition

2.1.1. Substrates

The deposition phase was split in three phases. The first one is the *screening* one where the process was optimised and the deposition parameters set. The second phase is the *optimization* phase where the parameter giving the better results are reapplied. The last phase regarded the *deposition on cylindric geometry and finally on the abutment* adopting the optimal set of parameters.

First and second phase: coatings were deposited onto 1.8 mm-thick plates of 25 mm x 60 mm surface. The plates were polished to achieve a surface roughness of Ra = 0.03 µm.

The substrate needs to mimic the metallic abutment for coating purpose, therefore, the chosen material for the substrate is Ti6Al4V.

The polishing needs to achieve a low roughness to obtain a coating finishing suitable for antibacterial purposes. This is particularly important because it is well-documented that bacterial activity tends to increase with higher surface roughness [140], [141]. Therefore, maintaining a smooth surface is essential to minimize bacterial colonization and enhance the antibacterial efficacy of the coating.

Third phase: coatings were deposited onto a 1 mm-thick cylinder with a diameter of 8 mm. The surface roughness of the cylinder, with an Ra value of 0.1 µm, is higher than that of the plates. AISI 316 stainless steel was chosen due to its availability and budget constraints, as the focus was on assessing deposition uniformity. The cylinder was used to verify the homogeneity and feasibility of deposition on a cylindrical geometry, which mimics the abutment. This pre-step is crucial before proceeding with the deposition on the abutment. Two different types of abutments were selected for this study: a healing abutment and a Variobase® abutment. The abutments were deposited in the as-received condition.

2.1.2. Deposition Equipment

All coatings were deposited using the PVD-PECVD CENTURION coating equipment of Il Sentiero International Campus which exploits a hybrid Physical Vapor Deposition (PVD) and Plasma-Enhanced Chemical Vapor Deposition (PECVD) techniques.

Figure 2.1-1 - PVD-PECV CENTURION coating system (Duralar Italia s.r.l.)

The system allows choosing among three different deposition methods, which can be employed sequentially or simultaneously. It also provides various options for surface pre-treatment and conditioning prior to the deposition process.

The system features a cathodic arc evaporation (CAE) PVD system, an unbalanced magnetron sputtering (MS) PVD system and RF-PECVD source. All these systems are water-cooled. Each system is located along the chamber walls and can be isolated from the chamber with a shutter when not in operation, to prevent contamination from other sources.

The system can be heated up to 400 °C by electrical resistances located on the chamber walls.

The vacuum system consists of three turbo-molecular pumps for high vacuum and of a mechanical dry pump, connected in series, which provide pre-vacuum conditions for the turbo-molecular pumps. Each turbo-molecular pump is controlled by a throttle valve, which can be closed to isolate the pump from the chamber.

The chamber pressure is monitored through two vacuum gauge:

Full Range vacuum gauge (FRG1) for medium and high vacuum conditions to measure the vacuum condition when the flow meters are not in use.

Capacitive vacuum gauge (CMG1) in the [0.01 ÷ 2.8] Pa to measure the vacuum condition when the flow meters are in use.

The chamber is vented going to atmospheric pressure.

It has an octahedral geometry, allowing for six possible positions for different sources. The frames are connected to a motor system that provides three types of rotation: a primary rotation of the entire frame assembly around the central axis of the chamber, a secondary rotation of each frame around its own axis, and a third rotation facilitated by additional movable sample holders that can be attached at the positions of the secondary rotation. For the third phase, the system was upgraded with a new frame to enable an additional rotation. This enhancement allowed the cylindrical samples and the abutment to rotate, ensuring a homogeneous coating deposition on their surfaces.

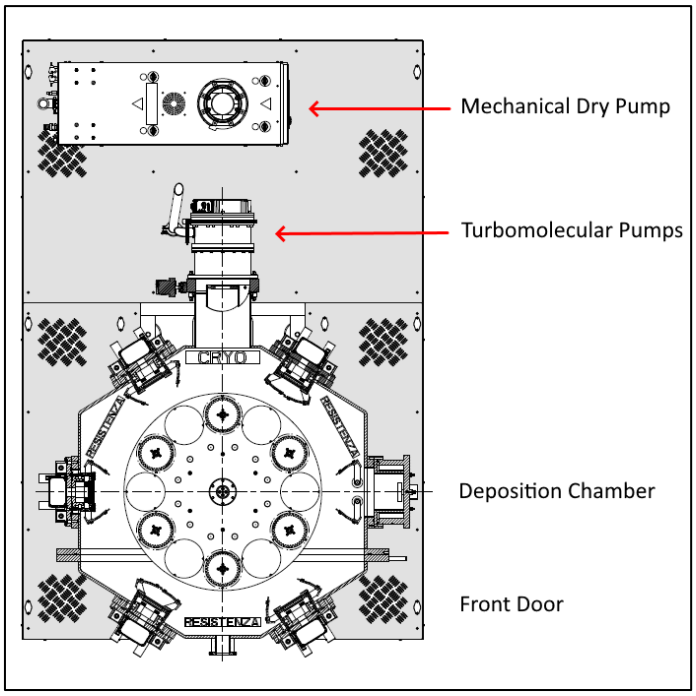

Figure 2.1-2 - top view of macro-block with indication of the main components.

The PECVD source is capable of dissociating both gaseous and liquid precursors by generating plasma within the chamber and the source itself. The gas system comprises seven gas lines, each equipped with a *gas mass flow controller* (GMF) and pneumatic valves for injection into the chamber. A *mix box* is used for mixing gases before they enter the chamber. The system can handle up to seven gases simultaneously (Ar, N_2, O_2, C_2H_2, H_2/CH_4, He, and one reserved line) and includes an additional liquid delivery system that can feed a nebulized flow of liquid precursors mixed with an atomizing gas.

The entire system is managed by a *Programmable Logic Controller* (PLC), which communicates with all components and sensors to regulate its operation.

2.1.3. Target

Since the desired coating must mimic the properties of natural teeth, zirconia was selected as the coating material. To achieve this, a metallic target is necessary for evaporating the required elements using magnetron sputtering deposition, thus a zirconium target is needed.

The objective of this study is to achieve stabilized zirconia while preventing the brittle transformation to the monoclinic phase. Therefore, a stabilizer is required in the target composition. Common stabilizers are CaO, MgO, and CeO_2, oxides used for stabilizing the tetragonal and cubic phases of zirconia. However, Y_2O_3 is preferred because exhibits superior properties and provides more effective stabilization. Consequently, yttrium was selected as the stabilizer in the target composition [59], [62], [63], [65]. The stabilized phase of zirconia is highly dependent on the yttria content. When the yttria content is up to 3 mol%, zirconia remains in the monoclinic phase, which is characterized by its brittleness and lower stability. As the yttria content increases ranging from 4 mol% to 5 mol%, a transition region is observed where both monoclinic and tetragonal phases coexist. This transition is crucial as it marks the beginning of the stabilization process. When the yttria content reaches 5 mol%, zirconia transitions fully to the tetragonal phase, while in the 5–8 mol% range, it exhibits a

mixture of tetragonal and cubic phases. Finally, when the yttria content exceeds 8 mol%, zirconia transitions entirely to the cubic phase [143].

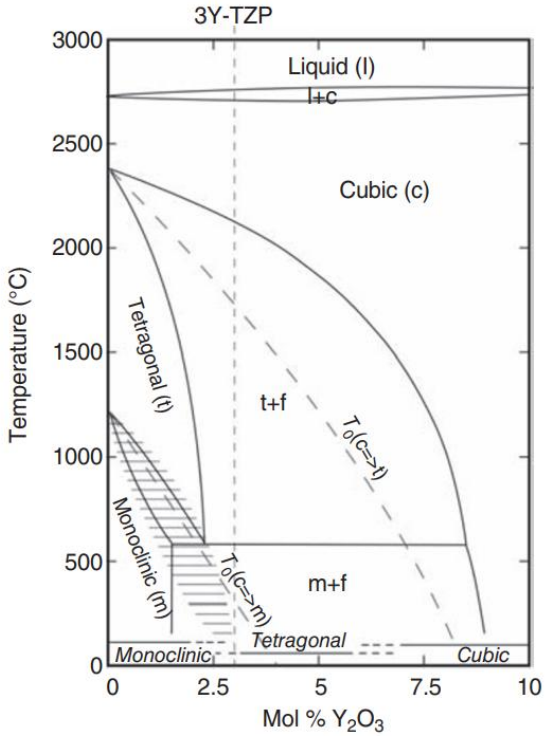

Figure 2.1-3 - Phase diagram for the zirconia rich portion of the zirconia-yttria system. Hatched region indicates non-equilibrium monoclinic-tetragonal transition [143].

Experimental results have demonstrated that the concentration of yttria in the coating can be equal to or exceed that of yttrium in the target [88]–[90].

The selection of yttrium concentration in the target for research purposes is influenced by two key factors: the desired final phase of the zirconia and the brittleness of the target. The desired phase is the tetragonal to guarantee the best mechanical properties which closely mimic those of natural teeth. The tetragonal phase of zirconia is renowned for its exceptional hardness and fracture toughness, which are critical for dental applications. Additionally, to preserve the integrity of the target, which becomes fragile when the yttrium content is high, it is crucial to carefully control the yttrium concentration. Consequently, a concentration of 7 mol% yttrium in the target has been selected. This specific concentration is not only optimal for maintaining the structural integrity of the target but also essential for achieving the desired tetragonal phase in the coating. However, it is crucial to consider the hydrothermal instability that poses a significant challenge for tetragonal zirconia, particularly during the sterilization process of the abutment, which involves exposure to water vapor at 134°C. Low Temperature Degradation (LTD) tests are essential to assess this aspect [39], [40], [61], [144], [145].

2.1.4. Hysteresis cycle

The hysteresis cycle delineates the operational range in terms of potential, making it the initial and crucial step for the deposition process. Understanding this cycle is essential as it determines the appropriate conditions under which the deposition can occur effectively.

The specific steps involved in this process are detailed in Table 2-1.

1. *Vacuum and heating* to reach the needed pressure and temperature in the chamber.
2. *Glowing* to clean the chamber from any contaminations introducing argon gas.
3. *Target cleaning* to clean the target using argon gas to ensure it is in a metallic state, free from any impurities.
4. *Magnetron Sputtering (MS) Deposition* to simulate the magnetron reactive sputtering condition. During this step, the hysteresis cycle is performed to define the operational range in terms of potential.

Table 2-1 - steps of the hysteresis cycle with the detail of the adopted parameters

STEP	**Time**	**Temperature**	**O2 flow**	**Ar flow**	**Magnetron Sputtering (MS)**				
					Current	Potential	Tension	Frequency	duty cycle
	[s]	[°C]	[sccm]	[sccm]	[A]	[kW]	[V]	[kHz]	[%]
Vacuum And Heating	240	150							
Glowing	420	150		1000÷1500					
Target cleaning	300	150		800	24 (monopulsed)	2÷6	1000	80	80
MS deposition - ZrO	7200	150	managed by speedflow	500	24 (monopulsed)	6	1000	80	80

Graph plotting the magnetron tension (V) in function of the gas flow (sccm) is a representation of the output of the hysteresis cycle. The graphs collected during this study are in accordance with literature [82]. Initially, the target was in a metallic condition, and at the start of the cycle, the recorded potential reflects this state, resulting in the highest deposition rate. As oxygen was introduced into the chamber, the potential decreased with increasing oxygen flow until the poisoning condition was reached. This occurs because the exposed surface of the target oxidized, making it impossible to deposit the coating, and the deposition rate reached its lowest value. As the oxygen flow decreased, the potential returns to higher values, indicating a reversion to the metallic state. This continues until the oxygen flow reached zero, at which point the highest potential value of the return curve of the cycle was recorded. This point marked the new metallic condition, free from surface oxidation.

The deposition potential values derived from the hysteresis cycle, typically selected from a well-defined range between the metallic and poisoning working points. Minimum (poisoning point) and maximum (metallic point) tension values were recorded for each cycle (Table 2-2), and the operational midpoint was determined. This point corresponds to 50% of the oxygen flow. Based on this data, the parameters of the deposition cycles for reactive sputtering were established.

Since the oxidation of the metallic target during multiple operation affects its state altering its behaviour, it is essential to verify the hysteresis cycle multiple times during use and redefine a new operational midpoint each time.

Initially, the hysteresis cycles were collected for defining the middle point of the cycle depositions related to the plane geometry. The last hysteresis cycle is conducted to check the parameter of the last deposition phase related to the YSZ deposition on the cylinder sample and abutment.

All the graphs are presented in Figure 2.1-4. The curves are collected during this study and exhibited a similar trend. The starting and ending points changed with each deposition cycle and it is possible due to an irrecoverable level of oxidation of the target, leaving it slightly dirtier than the initial condition.

Table 2-2 - middle point of the working range.

Hysteresis cycle code	**Sample geometry**	**Magnetron tension [V]**		
		Min	Max	Middle point
Deposition cycles 1-9	plane	340	470	405
Deposition cycle 10	plane	360	390	375
Deposition cycles 11-13	plane	370	400	385
Deposition cycles 14-16	plane	350	390	370
Deposition cycles 1-4	cylinder/abutment	340	450	395

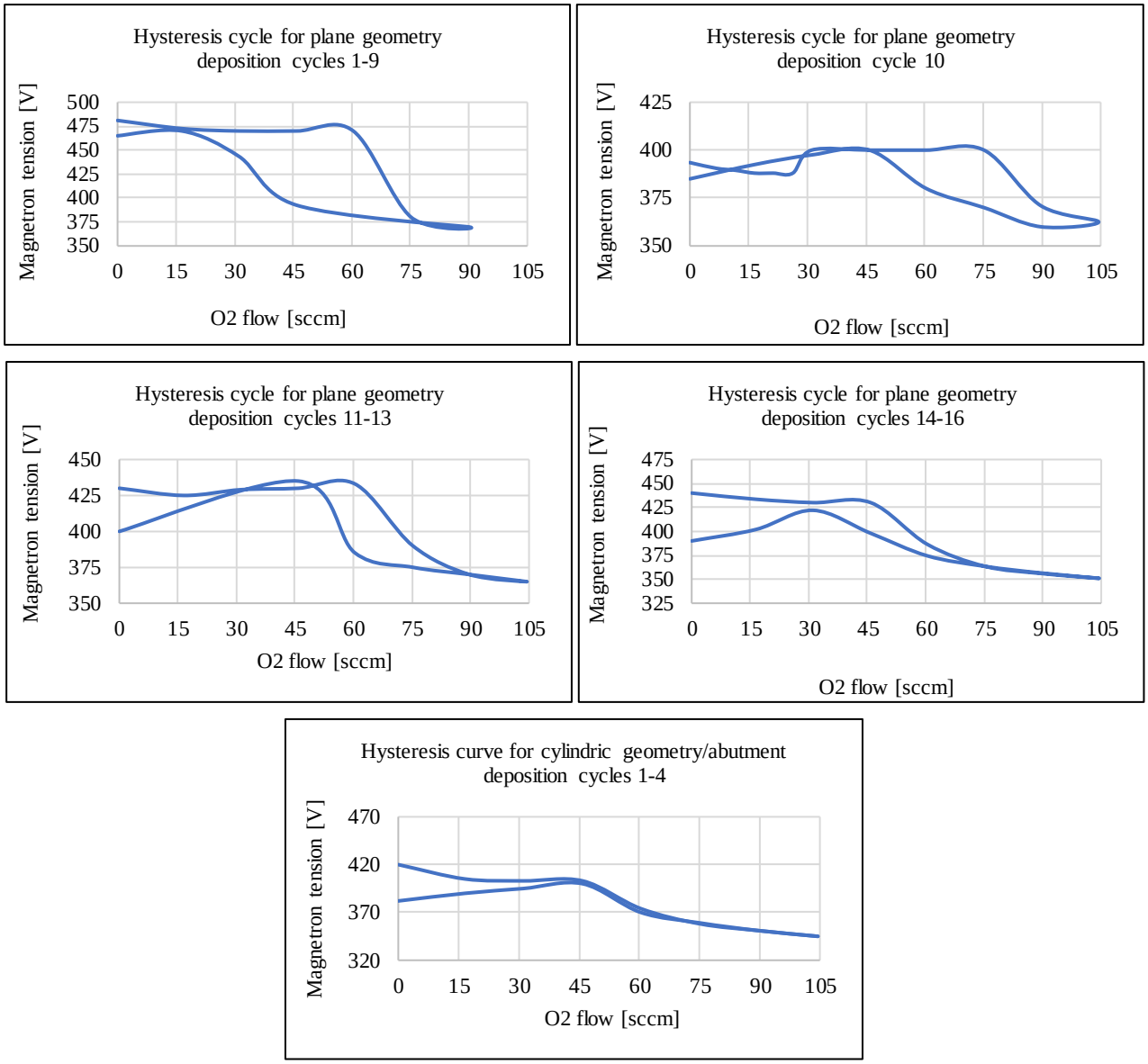

Figure 2.1-4 - Hysteresis cycle for deposition potential calculation.

2.1.5. Deposition cycle

Reactive magnetron sputtering is employed for the implementation of the deposition cycle.

The steps are listed in Table 2-3.

- *Vacuum and heating* to establish the necessary vacuum and temperature conditions within the chamber to create an ideal environment for deposition.
- *Glowing* to clean the chamber using argon gas to remove any contaminants that could affect the quality of the coating.
- *Target cleaning* to clean the target adopting argon gas and ensuring its metallic condition free from impurities.
- *Magnetron Sputtering (MS) Deposition – Zr* to deposit an interlayer of zirconium on the substrate to enhance the adhesion between the titanium and the zirconia. This step is conducted employing the magnetron sputtering source, which evaporates the zirconium target in the presence of argon gas.

- *Magnetron Sputtering (MS) Deposition – Zr-O* to deposit the zirconia coating. Like the previous step, the magnetron sputtering source is activated to evaporate the zirconium target using argon gas. Simultaneously, oxygen is injected into the chamber, allowing the formation of the ceramic zirconia coating on the previously deposited zirconium layer. Additionally, in a few selected cases, the *Reactive Magnetron Sputtering* process was coupled with *Radio Frequency-Plasma Enhanced Chemical Vapour Deposition* (RF-PECVD) by employing the *Plasma Beam Source*. The plasma beam source, activated by helium gas, dissociates oxygen molecules, thereby increasing the reaction rate and, consequently, the deposition rate. This configuration was tested to evaluate its possible impact on the process.

The MS deposition process involves varying parameters for each cycle, which were defined for each step. These parameters included the duration of the deposition, the flow rates of oxygen and helium gases, the magnetron tension, and the RF potential. Specifically, the magnetron tension was set based on hysteresis cycles, using midpoint values and nearby values to evaluate results around the midpoint.

The detailed steps of this process are outlined in Table 2-3 and Table 2-4, corresponding to the screening phase and the optimization phase of the plane geometry, respectively. Table 2-4 collects the parameters for the optimised cycle of the cylindrical geometry and abutments. Specifically, deposition cycles 1 and 2 were conducted exclusively on the cylindrical geometry, while the third and fourth cycles also included the abutments.

Table 2-3 – steps of the deposition cycle with the detail of the adopted parameters for the screening cycles set

STEP	Time	Temp.	O2 flow	Ar flow	He flow	Magnetron Sputtering (MS)					RF potential
						Current	Potential	Tension	Frequence	duty cycle	
	[s]	[°C]	[sccm]	[sccm]	[sccm]	[A]	[kW]	[V]	[kHz]	[%]	[W]
Vacuum and Heating	900	220	0	0	0	0	0	0	0	0	0
Glowing	600	180	0	1000÷1500	0	0	0	0	0	0	0
Target cleaning	900	180	0	800	0	24	2÷6	1000	80	80	0
MS dep. Zr	300	180	0	500	0	24	6	1000	80	80	0
MS dep. ZrO											
YSZ 1 plate	**7200**	180	**50÷60**	500	**0**	24 (monop.)	6	**400**	80	80	**0**
YSZ 2 plate	**7200**	180	**60**	500	**0**	24 (monop.)	6	**400**	80	80	**0**
YSZ 3 plate	**14400**	180	**55÷60**	500	**0**	24 (monop.)	6	**400**	80	80	**0**
YSZ 4 plate	**14400**	180	**70÷85**	500	**0**	24 (monop.)	6	**390**	80	80	**0**
YSZ 5 plate	**14400**	180	**55**	500	**0**	24 (monop.)	6	**420**	80	80	**0**
YSZ 6 plate	**14400**	180	**55**	500	**200**	24 (monop.)	6	**420**	80	80	**1500÷2000**
YSZ 7 plate	**14400**	180	**60**	500	**200**	24 (monop.)	6	**400**	80	80	**1500÷2000**
YSZ 8 plate	**14400**	180	**65÷70**	500	**200**	24 (monop.)	6	**390**	80	80	**1500÷2000**

Table 2-4 - steps of the deposition cycle with the detail of the adopted parameters for the optimized cycles set

STEP	Time	Temp.	O2 flow	Ar flow	He flow	Magnetron Sputtering (MS)					RF potential
						Current	Potential	Tension	Frequence	duty cycle	
	[s]	[°C]	[sccm]	[sccm]	[sccm]	[A]	[kW]	[V]	[kHz]	[%]	[W]
Vacuum and Heating	900	220	0	0	0	0	0	0	0	0	0
Glowing	600	180	0	1000÷1500	0	0	0	0	0	0	0
Target cleaning	900	180	0	800	0	24	2÷6	1000	80	80	0
MS dep. Zr	300	180	0	500	0	24	6	1000	80	80	0
MS dep. ZrO											
YSZ 9 plate	**25200**	180	**55**	500	**0**	24 (monop.)	6	**400**	80	80	**0**
YSZ 10 plate	**25200**	180	**50÷55**	500	**0**	24 (monop.)	6	**420**	80	80	**0**
YSZ 11 plate	**7200**	180	**50÷55**	500	**0**	24 (monop.)	6	**400**	80	80	**0**
YSZ 12 plate	**8700**	180	**60÷75**	500	**0**	24 (monop.)	6	**390**	80	80	**0**
YSZ 13 plate	**8700**	180	**55÷75**	500	**0**	24 (monop.)	6	**390**	80	80	**0**
YSZ 14 plate	**7200**	180	**60**	500	**0**	24 (monop.)	6	**385**	80	80	**0**
YSZ 15 plate	**5100**	180	**55**	500	**0**	24 (monop.)	6	**385**	80	80	**0**
YSZ 16 plate	**4800**	180	**55**	500	**0**	24 (monop.)	6	**380**	80	80	**0**

Table 2-5 - steps of the deposition cycle with the detail of the adopted parameters for the optimized cycles set

STEP	Time	Temp.	O2 flow	Ar flow	He flow	Magnetron Sputtering (MS)					RF potential
						Current	Potential	Tension	Frequence	duty cycle	
	[s]	[°C]	[sccm]	[sccm]	[sccm]	[A]	[kW]	[V]	[kHz]	[%]	[W]
Vacuum and Heating	900	220	0	0	0	0	0	0	0	0	0
Glowing	600	180	0	1000÷1500	0	0	0	0	0	0	0
Target cleaning	900	180	0	800	0	24	2÷6	1000	80	80	0
MS dep. Zr	300	180	0	500	0	24	6	1000	80	80	0
MS dep. ZrO											
YSZ 1 cyl	**10800**	180	**60÷65**	500	**0**	24 (monop.)	6	**370**	80	80	**0**
YSZ 2 cyl	**12000**	180	**60÷65**	500	**0**	24 (monop.)	6	**370**	80	80	**0**
YSZ 3 cyl./abut.	**12000**	180	**60÷65**	500	**0**	24 (monop.)	6	**370**	80	80	**0**
YSZ 4 cyl./abut.	**12000**	180	**60÷65**	500	**0**	24 (monop.)	6	**370**	80	80	**0**

2.2.Collagen-based hydrogel deposition

2.2.1. Substrates

In this study, hydrogels were deposited onto 3 mm-thick plates, each with a surface area of 20 mm x 20 mm, made from biomedical-grade zirconia. These substrates, supplied by the Dental Department, UniMoRe, exhibited two distinct surface roughness values: Ra = 0.05 µm, achieved through a tooth-like finishing process, and Ra = 0.4 µm, produced using Computer Numerical Control (CNC) machining techniques. The variation in surface roughness was strategically chosen to examine its effect on the adhesion of the coatings, aiming to optimize the proposed multilayer.

2.2.2. Collagen solution

A bovine corium telocollagen, type I, with a concentration of 6 mg/mL was selected. Type I collagen was chosen to promote the regeneration of connective tissues, such as gingival tissue [29]. Telocollagen was selected for its intact telopeptide terminals, which ensure high mechanical properties essential for effective cell signalling and subsequent proliferation.

Hydrochloric acid was chosen as the solvent for the collagen because it improves the structure of the collagen hydrogel and promotes cell proliferation [127]. The selected collagen was dissolved in 0.01 N HCl and maintained at pH 2.

The concentration of the collagen solution was carefully selected to be 6 mg/mL, which is close to the standard concentration of 5 mg/mL typically used in tissue engineering [133], [134]. This ensures that the formulation remains within the optimal range for promoting cell activity.

2.2.3. Deposition steps

The following steps are crucial for the deposition of the biopolymeric layer on the biomedical-grade zirconia plates:

2.2.3.1. Alkaline treatment

The surface treatment process involves immersing the zirconia plates in a 5 M NaOH solution for 24 hours in an oven maintained at 60°C. This immersion process is designed to generate hydroxyl groups on the surface of the zirconia, which facilitate better bonding with the biopolymeric layer compared to the untreated ceramic surface acting as immobilization treatment.

To prepare the alkaline solution, NaOH pellets, purchased from PanReac, were dissolved in demineralized water. The zirconia plates were then immersed in a flask containing the prepared NaOH solution, ensuring that the side with the tooth-like finish was fully exposed. This careful positioning maximizes the interaction between the NaOH solution and the surface of interest, enhancing the formation of hydroxyl groups on the side of interest intended for the deposition process.

After the 24-hour treatment period, the plates were removed from the solution and dried using compressed air removing any residual solution and preparing the plates for subsequent steps. The treated plates, featuring hydroxyl groups on their surfaces, are ready for the next stages of the coating process.

2.2.3.2. Biopolymeric solution preparation

The preparation of a 3D collagen layer was conducted in accordance with the product information provided by the collagen supplier, Sigma-Aldrich. The detailed preparation steps are as follows [146]:

1. Storing of the collagen solution: The collagen solution, with a pH of 2.1 and dissolved in hydrochloric acid, was stored at a temperature range of 2 to 8 °C. This storage condition was crucial for maintaining the stability and integrity of the collagen solution.
2. Preparation of the neutralization buffer: A neutralization buffer with a concentration of 0.2 M sodium phosphate and a pH of 11 was prepared. This buffer is essential for adjusting the pH of the collagen solution to a neutral range, facilitating the formation of a stable 3D collagen network [146]–[148].
3. Mixing of buffer and collagen solution: The neutralization process involved mixing one part of the prepared buffer with nine parts of the collagen solution. This mixing was performed at a temperature range of 2 to 8 °C to ensure uniformity and prevent premature gelation. Specifically, 1 ml of the neutralization buffer was added to 9 ml of the collagen solution, and the mixture was thoroughly mixed under the specified temperature conditions.
4. Deposition and incubation: The cold mixture of neutralized collagen was then deposited onto the zirconia substrates. Following deposition, the plates were incubated at 37 °C for a minimum of 45 minutes allowing the collagen to form a stable and homogeneous 3D network.

The neutralizing sodium phosphate buffer was prepared using sodium phosphate dibasic dihydrate ($Na_2HPO_4 \cdot 2H_2O$), sourced from Carlo Erba, and sodium phosphate monobasic (NaH_2PO_4), from Sigma-Aldrich. The values of the required volume of the acidic NaH_2PO_4 and the conjugate base Na_2HPO_4 required for the buffer were calculated exploiting the Henderson-Hasselbalch equation [149]:

$$pH = pKa + \log\left(\frac{[base]}{[acid]}\right)$$

Where *pKa* is the negative logarithm of the acid dissociation constant (Ka) of an acid, indicating the strength of an acid in solution.

The buffer system involves the equilibrium between NaH_2PO_4 and Na_2HPO_4:

$$NaH2PO4 \leftrightarrow H^+ + Na2HPO4$$

The equilibrium of the system is:

$$H2PO4^- \leftrightarrow H^+ + HPO4^{2-}$$

with $pKa_2 \approx 7.20$, typically adopted at moderate pH (6÷8).

It is possible to rewrite the Henderson–Hasselbalch equation as:

$$pH = pKa + \log\left(\frac{[HPO4^{2-}]}{[H2PO4^-]}\right)$$

By imposing a pH of 8 and considering a value of total concentration equal to 0.2M, the concentrations can be calculated as follows:

- $[HPO4^{2-}] = 0.1726$ M
- $[H_2PO^{4-}] = 0.0274$ M

To prepare 1L of solution (1 M) for each component, the required volumes are:

- Na_2HPO_4: 0.1726M*1L=0.1726 mol → Volume (Na2HPO4) = $\frac{0.1726\ moles}{1M}$ = 172.6 mL
- NaH_2PO_4: 0.0274M*1L= 0.0274 mol → Volume (NaH2PO4) = $\frac{0.0274\ moles}{1M}$ = 27.4 mL

Additionally, the mass of each substance can be calculated as the product of molarity, volume and molar mass:

- Na_2HPO_4 = 177.99 g
- NaH_2PO_4 = 120.98 g

To produce the 0.2 M buffer solution at pH 8, it is sufficient to mix the two prepared solutions (172.6 mL of Na_2HPO_4 and 27.4 mL of NaH_2PO_4) and make up the mixed solution with distilled water up to 1L.

To adjust the pH of a 1 L sodium phosphate buffer solution from 8 to 11, the addiction of a strong base, typically sodium hydroxide (NaOH), is required.

The equilibrium of the system at pH 11 is:

$$HPO4^{2-} \leftrightarrow H^+ + PO4^{3-}$$

with $pKa_3 \approx 12.35$. The relevant species change and NaOH help to deprotonate H_2PO^{4-} to $HPO4^{2-}$ and $HPO4^{2-}$ to $PO4^{3-}$.

It is possible rewrite the Henderson–Hasselbalch equation for this case as:

$$pH = pKa + \log\left(\frac{[PO4^{3-}]}{[HPO4^{2-}]}\right)$$

By imposing a pH of 11 and considering a total concentration of 0.2 M, the concentrations are:

- $[PO4^{3-}] = 0.00856$ M
- $[HPO4^{2-}] = 0.1914$ M

Considering 1 L of solution, it is possible to obtain 0.00856 moli of $PO4^{3-}$ and 0.1914 moli of $HPO4^{2-}$.
Specifically, NaOH 1M solution is required to neutralize 0.0274 moles of $H_2PO_4^-$ (at pH 8) and an additional 0.019 moles to convert the HPO_4^{2-} concentration from 0.1726 moles (at pH 8) to 0.1914 moles (at pH 11). This results in a total requirement of 0.0464 moles of NaOH (0.0274 moles for $H_2PO_4^-$ + 0.019 moles for HPO_4^{2-}). Therefore, 46.4 mL of the 1 M NaOH solution should be added to the 1 L buffer solution.
It is essential to monitor the pH both before and after the addition of NaOH to accurately track the pH changes ensuring the desired pH is achieved.
The buffer solution is ready for the subsequent step of mixing with collagen.
To determine the appropriate volume of deposition solution for the plate, relevant literature was consulted to guarantee accurate and reliable calculations based on established protocols and guidelines. According to the literature:

- the surface density of the collagen solution varies from 5 μg/cm^2 to 10 μg/cm^2 [150]. Particularly, the calculation of this activity is in accordance with the 100% of the surface density for the Tennessee University, that is 7 μg/cm^2.
- the standard concentration of the collagen solution for tissue regeneration is 5 mg/ml [133], [134].

Therefore, in the first instance, considering a buffer-collagen ratio of 9:1 and a biomedical-grade zirconia plate surface area of 4 cm², the required volume of the deposition solution is calculated to be 0.047 mL. This includes 0.0426 mL of collagen at a concentration of 6.5 mg/mL and 0.0047 mL of buffer solution. The buffer solution is specifically formulated to define three different formulations: pure buffer solution, buffer solution with 0.1% w/v and buffer solution with 0.3% w/v of Laponite RDS. The addition of Laponite leads to an enhanced shear thinning behaviour of the solutions. Experimental studies indicate that adding Laponite to collagen solutions enhances shear thinning behaviour without compromising biocompatibility [33], [34]. Laponite RDS furnished by BYK was adopted.

2.2.3.3. Deposition of the biopolymeric solution

The deposition phase must be conducted at temperature close to 4°C preventing premature gelation of the collagen. Given that the deposition phase follows an iterative process, it is not feasible to establish a single, standardized method for each trial. Instead, the method is continuously adjusted and refined based on real-time observations and results. This adaptive approach allows for the optimization of the deposition technique leading to the development of an optimal deposition protocol.
According to the technical specifications for the collagen-to-buffer ratio, a biopolymeric solution was prepared with a total volume of 1 mL. Specifically, 0.91 mL of collagen (at 6 mg/mL) was mixed with 0.09 mL of buffer, yielding a final collagen concentration of 5.8 mg/mL. To evaluate the impact of collagen concentration on the hydrogel's properties, a more diluted solution was also prepared at 4.2 mg/mL. After determining the optimal concentration, the selected formulation was deposited while considering the following variables:

- three types of formulations: pure collagen, collagen solution with 0.1% w/v of Laponite, and collagen solution with 0.3% w/v of Laponite.
- three types of cross-linking: gelation, UV cross-linking for 30 minutes and UV cross-linking for 60 minutes.

To prepare the biopolymeric solution, a beaker filled with crushed ice was used to hold a smaller beaker used for the mixing phase, ensuring the mixture remained at a low temperature and preventing premature gelation. Both collagen and buffer solutions were dispensed using a Gilson pipette, allowing for precise measurement and addition.

The mixture is stirred using a magnetic stirrer at low speed to avoid bubble formation while ensuring optimal mixing.

Once the biopolymeric solution was ready, it was deposited onto the plates placed in silicon moulds using the Gilson pipette according to the optimal amounts determined in the feasibility phase.

The gelation of the biopolymeric layer was conducted in an oven set at 37°C for a time determined by specifically conducted rheometric tests. This controlled heating process facilitated the formation of a stable gel network with a specific stiffness (G').

After the gelation process, the layer that required UV cross-linking were subjected to a further step adopting an UV-C lamp with a wavelength of 254 nm.

Finally, all the samples were stored in a refrigerator. This storage condition was necessary to maintain the moisture level of the biopolymeric layer, preserving its properties until further characterization could be performed. Particularly, most of the characterization methods required an additional drying step to prevent damage to the instrumentation caused by the water content of the biopolymeric layer.

Samples were labelled as:

- PG: pure collagen, only gelled
- PR1: pure collagen, gelled and UV cross-linking for 30 minutes
- PR2: pure collagen, gelled and UV cross-linking for 60 minutes
- LG: collagen with 0.3 w/v% Laponite, only gelled
- LR1: collagen with 0.3 w/v% Laponite, gelled and UV cross-linking for 30 minutes
- LR2: collagen with 0.3 w/v% Laponite, gelled and UV cross-linking for 60 minutes

The collagen concentration was 5.8 mg/mL in all cases.

2.2.3.4. UV cross-linking

A physical cross-linking treatment was performed on the biopolymeric hydrogel to enhance the mechanical properties of the coating without compromising its biocompatibility. This procedure was carried out at the BIOMAT Laboratory of UniMoRe. A UV-C lamp operating at 254 nm with a power of 40 W was selected for this purpose. After being carefully deposited and allowed to gel, the hydrogel was positioned 20 cm from the UV-C source to ensure uniform exposure. To evaluate the effect of UV treatment duration, two exposure times were tested: 30 minutes and 60 minutes. Previous studies have demonstrated that even a 30-minute UV-C

treatment can significantly improve the mechanical strength of hydrogels [137], [138], [151], which guided the selection of these durations.

2.3.Characterization Methods

2.3.1. Optical microscopy

Optical microscopy is a tool for imaging at low to medium magnifications. It is commonly employed for the analysis of material surfaces, whether they are in their as-received state or have been prepared through processes such as lapping or chemical etching. Proper preparation of the sample is essential to ensure accurate and reliable observations. The key factors in optical microscopy are resolution and contrast, which are crucial for discerning microstructural details. The ability to resolve two points separated by a distance (d) is governed by the equation = $d = \frac{k\lambda}{NA}$, where λ is the wavelength of light, K is a constant, and NA is the numerical aperture of the objective lens.

The bright field method is the most widely used technique in optical microscopy. In this method, light passes through the objective lens and strikes the sample surface perpendicularly. The surface features reflect the light beam back towards the eyepiece. Features that are perpendicular to the light appear bright, while those at an angle reflect less light and appear progressively darker as the angle of reflection decreases to 0°. This method is particularly effective for observing the topography and texture of the sample surface.

The Axio Zoom V16 (ZEISS) microscope was adopted for this study. It is a stereomicroscope designed for 3D visualization of surfaces offering a range of magnifications from 7x to 112x.

The observations were conducted on the biopolymeric hydrogels subjected to different treatments:

- after gelation biopolymeric hydrogel
- after gelation + UV cross-linking at time 1
- after gelation + UV cross-linking at time 2

2.3.2. Electronic microscopy

Scanning electron microscopy (SEM) enables high-resolution imaging by scanning a small portion of the sample with an electron beam. Electrons are emitted from various sources, such as tungsten (W) filaments or lanthanum hexaboride (LaB6) single crystals, through thermionic emission, or from field emission sources. These electrons are accelerated by an annular anode and focused into a small-diameter beam (approximately 10 Å) using suitable electromagnetic lenses. The beam is scanned in a raster pattern over the substrate via a pair of coils located near the objective lens. Beam energies typically range from 1 keV to 30 keV [152].

In a standard SEM instrument, three types of interactions are typically utilized, each capturing specific phenomena between the electron beam and the sample, which can be exploited for image generation through appropriate detectors [152]:

- Secondary Electrons (SE): Emitted from the topmost layers of the sample due to inelastic collisions of the primary beam with electrons in the outer shells of the sample atoms. Due to their low energy, only SEs produced within a few nanometres of the sample surface can escape, providing topographical information.

Peaks and edges appear brighter than pits and valleys because SEs from the latter regions are more likely to be absorbed by surrounding material and not reach the detector.

- Back Scattered Electrons (BSE): Primary beam electrons that undergo elastic scattering by the sample atoms. BSEs are more energetic and can provide information from deeper within the sample, up to a few micrometres. The intensity of backscattering depends on the average atomic weight of the area hit by the electron beam, thus conveying compositional information: brighter areas in BSE images correspond to regions with higher average atomic weight.
- X-rays and Auger Electrons: Inelastic interactions between the primary electron beam and sample atoms can result in the ejection of electrons from deeper shells, leaving the atom in a high-energy state. Relaxation occurs almost instantly as an electron from an outer shell moves to fill the vacancy, releasing excess energy as a photon (X-ray) or transferring it to another electron (Auger electron). While Auger electron emission is typically analysed with specialized instruments due to the sensitivity required, X-rays can be detected using energy-dispersive spectroscopy (EDS). The energy of the emitted X-ray photon is characteristic of the emitting atom, allowing for spatially resolved qualitative and semi-quantitative chemical analysis of the sample.

In this study, three different models of Scanning Electron Microscopes (SEMs) were employed to analyse the coatings, each offering unique capabilities and features suited for various aspects of the investigation.

***EVO MA10* (ZEISS)** is equipped with a tungsten (W) filament source, which is a common choice for general-purpose imaging due to its robustness and ease of use. The instrument includes an Energy-Dispersive X-ray Spectroscopy (EDS) system (XFlash® 6, BRUKER) for elemental analysis (Figure 2.3-1).

Observation Details:

YSZ layers

Different sample types were analysed to assess their surface quality and chemical composition during the optimization process of reactive sputtering deposition:

- as-deposited YSZ coatings on plane geometry
- as-deposited YSZ coatings on cylindric geometry
- as-deposited YSZ coatings on abutment

The samples were not gold-coated, and the electron beam energy was set to 20 keV. For each sample, one representative position was analysed. However, for the cylindrical case, two different sides were examined to assess the homogeneity of the deposited coating.

Biopolymeric layers

Layers with two different concentrations of collagen:

- 4.2 mg/mL
- 5.8 mg/mL

Biopolymeric layers were previously dehydrated, to avoid any contamination in the vacuum chamber, and gold-plated.

The samples were gold-coated, and the electron beam energy was set to 20 keV. Representative images were collected for each case.

Both layer types were mounted on aluminium (Al) sample holders (stubs) using adhesive carbon tapes. This setup ensures that the entire assembly is electrically conductive, preventing the accumulation of static electric charges on the sample during electron beam exposure, which could otherwise interfere with the imaging process.

Figure 2.3-1 - ZEISS EVO MA 10

Nova NanoSEM 450 FEG-SEM **(FEI)** features a Schottky Field Emission Gun (SFEG) source, which is particularly suitable for high-resolution and low-voltage imaging, providing superior image quality and detail. *Observation Details:* The observations were conducted on the as-deposited YSZ coatings in cross-section to assess the internal structure and quality of the coatings.

Observation Details:

YSZ layers – Cross-section images of YSZ layers were captured at a magnification of 100000x, and three positions were analysed for each selected coating to provide a comprehensive understanding of the coating characteristics. The samples were gold-plated and seven specific coatings (YSZ-2, YSZ-3, YSZ-5, YSZ-9, YSZ-12, YSZ-14, and YSZ-16) were selected for this analysis. The electron beam energy was set at 15 keV, and the Concentric Back Scattered (CBS) detector was employed. This detector configuration ensures well-defined detection geometry without distortions caused by the optical system of the SEM column [152].

Biopolymeric layers – surface observations of layers with 5.8 mg/mL collagen concentration subjected to different treatments:

- gelation
- gelation with 30 minutes of UV cross-linking
- gelation with 60 minutes of UV cross-linking

Biopolymeric layers were previously dehydrated, to avoid any contamination in the vacuum chamber, and gold-plated. The Through Lens Detector - Secondary Electrons (TLD-SE) was selected, capturing

images at different magnifications to highlight the morphology. The electron beam energy was set to 8 keV. Representative images were collected.

Both layer types were mounted on aluminium (Al) sample holders (stubs) using adhesive carbon tapes. This setup ensures that the entire assembly is electrically conductive, preventing the accumulation of static electric charges on the sample during electron beam exposure, which could otherwise interfere with the imaging process.

Helios NanoLab 600i DualBeam SEM/FIB **(FEI)** is an advanced instrument combines a Ga+ ion beam ("Tomahawk") with a Gas Injection System (GIS) and a high-resolution field emission scanning electron ("Elstar") column. The FIB column uses a Ga+ Liquid Metal Ion Source (LMIS), which acts as a point source of ions (Figure 2.3-2). The ion beam is accelerated and focused by a series of electromagnetic lenses towards the sample. During ion-sample interactions, various phenomena can occur, including the displacement of atoms from the sample. While the electron beam produces non-destructive images, the ion beam modifies the sample surface and can be used for micromachining, such as creating in-situ cross-sections. To prevent artifacts from atom re-deposition during cross-sectioning, the sample surface can be coated with a thin platinum (Pt) layer via ion beam-assisted deposition (IBID) using organometallic precursors delivered through the GIS. When the ion beam is used for imaging, the interaction with atomic planes of polycrystalline materials can cause a channelling effect. This effect depends on the specific orientation of each crystal in the sample, allowing ions to penetrate to different depths and producing varying contrast levels based on crystal orientation. This provides detailed information on the size and shape of crystalline domains [153].

Observation Details: The observations were conducted on the as-deposited YSZ coatings in cross-section to have a better resolution of the internal structure and quality of the coatings. Three specific coatings (YSZ-12, YSZ-14 and YSZ-16) were selected for this analysis. Three detectors were employed:

- **ETD (Everhart-Thornley Detector):** A standard detector for SEM observations, utilizing a highly polarizing grid to detect electrons after their interaction with the material.
- **TLD (Through-Lens Detector):** Located in the electron column, this detector collects electrons moving in the same direction as the electron beam, enhancing image resolution and reducing noise. In "Immersion" mode, a magnetic field can be applied to increase the number of collected electrons.
- **CDEM (Channel Electron Multiplier):** This detector offers higher contrast than the ETD and, in combination with channelling effects, highlights the crystallographic characteristics of the material.

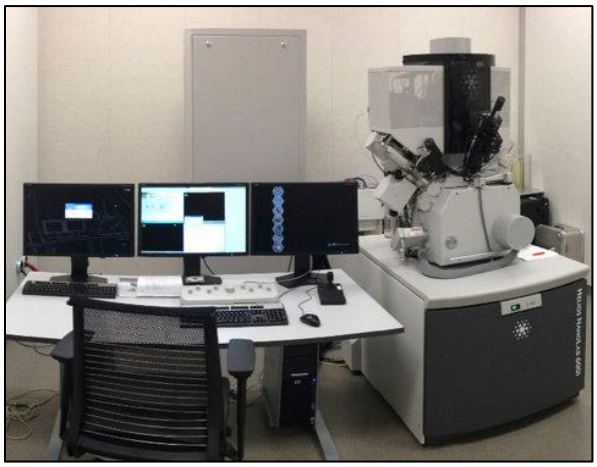

Figure 2.3-2 - FEI Helios NanoLab 600i DualBeam SEM/FIB.

Sample Preparation is conducted to ensure accurate and reliable SEM analysis. Initially, the samples were cleaned in an ultrasonic bath using acetone for a total duration of 10 minutes to remove any surface contaminants.

Cross-section images of YSZ coatings were captured during the optimization phase to observe at higher magnification the formed structure. The images were captured at 100000x and 200000x.

2.3.3. Raman analysis

Raman Spectroscopy (RS) operates basing on the Raman effect, which is a form of inelastic scattering of monochromatic light within the visible, infrared (IR), or ultraviolet (UV) spectrum. During the interaction of light with the sample, a smaller fraction of the light undergoes inelastic scattering, known as the Raman effect, while most of the light scatters without changing its wavelength, a phenomenon known as the Rayleigh effect. Incident photons interact with the sample during the Raman effect, causing the vibration modes of the sample to be temporarily elevated to a "virtual" state. The energy, and thus the wavelength, of the scattered photon differs from that of the incident photon by an amount equivalent to the difference between two permissible vibrational states of the sample if the relaxation transitions to another permissible energy state before returning to the original state. This wavelength shift is characteristic of the vibrational modes of the sample and is influenced by interatomic forces, atomic mass, bonding distances, and angles. Alternatively, the relaxation can return directly to the original state [154].

The resulting Raman spectrum is typically plotted in terms of wavenumber shift, which is the difference between the incident and scattered wavenumbers, where the wavenumber is the inverse of wavelength and is usually measured in cm^{-1}. The spectrum reveals important details about the composition and structure of the sample making Raman spectroscopy a versatile tool for analysing both inorganic and organic materials, including minerals, powders, ceramics, and organic coatings.

LabRAM Evolution (Horiba) Raman spectrometer was employed during this study for assess all the YSZ coatings (Figure 2.3-3).

This analysis was conducted on the YSZ coatings adopting test parameters as follows:

- Laser Source: A Helium-Neon (He–Ne) laser with a wavelength of 532 nm was used as the excitation source;

- Objective lens: A 100x objective was utilized to focus the laser beam onto the sample and to collect the scattered light;
- Slit width range: The slit width was adjusted to cover a range from 100 cm^{-1} to 1750 cm^{-1}, with the centre at 989.56 cm^{-1};
- Confocal hole: A confocal hole size of 200 µm was used;
- Acquisition time: 10 seconds;
- Measurement repetition: each measurement was repeated 10 times for improving statistical reliability and reducing the noise signal.

Figure 2.3-3 - LabRAM HR Evolution.

2.3.4. XRD analysis

X-ray Diffraction (XRD) analysis is a technique used to determine the crystallographic structure of a material by employing an X-ray beam. In this process, an X-ray beam is directed at the material sample at a specific angle, denoted as ω (omega). This angle is crucial as it determines how the X-rays interact with the atoms in the crystal lattice. The X-rays hit the material interacting with the atoms in the crystal, causing the diffraction of the X-rays. The diffracted X-rays are captured by a detector as it scans over a defined range of angles, typically denoted as 2θ (2\theta). During the scanning process, the detector measures the intensity of the diffracted rays at various angles. This measurement exploits the diffraction pattern produced by the interaction of X-rays with the crystal lattice. The resulting data is plotted as peaks in the spectrum, with each peak corresponding to specific planes of atoms within the crystal. The position and intensity of these peaks are critical for understanding the crystallographic structure of the material. The analysis of these peaks involves determining their intensity and position, which provides insights into the atomic arrangement within the crystal. This analysis is guided by Bragg's Law, expressed as:

$$n\lambda=2d\text{sen}(\theta)$$

where λ is the wavelength of the incident X-ray radiation, d is the distance between adjacent planes in the crystal lattice, and θ is the angle that the outgoing ray forms with the crystal plane.

By applying Bragg's Law, the crystal structure is known, including the lattice parameters and potential defects within the material.

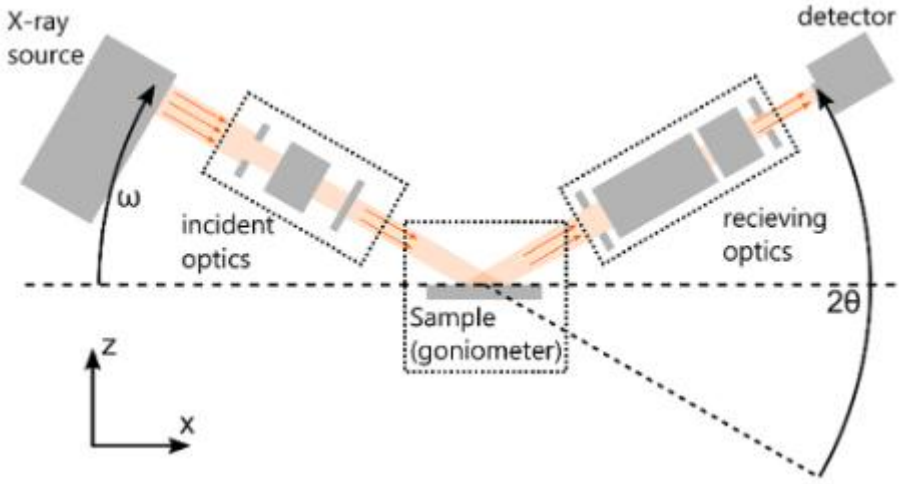

Figure 2.3-4 - scheme of the diffractomer [155].

For this investigation, the Empyrean diffractometer (Malvern-Panalytical) was utilized to analyse the crystal structure of both Yttria-Stabilized Zirconia (YSZ) and collagen-based layers. Given the thin nature of both layers, the ω value was set at 1° to achieve a grazing incidence. This setting was crucial to maximize the signal obtained from the layers while effectively eliminating noise from the substrate. Furthermore, a parallel plate collimator was employed for both types of layers to eliminate divergent reflections and ensure the detection of only parallel reflections. Although this approach results in the loss of some signal, it significantly enhances the resolution of the resulting spectrum.

The 2θ range was selected for each type of layer to optimize spectrum collection:

- For the YSZ layer, the 2θ range was set between 25° and 80°.
- For the biopolymeric layer, the 2θ range was set between 4° and 28°.

2.3.5. Roughness measurements

The surface roughness of the coatings is determined through the SURFTEST SJ-410 roughness meter in accordance with ISO 4287 [156]. It consists of a stand to support the sample and a stylus in contact with the surface. The stylus scans the surface of the sample and collect height variation data on the roughness profile displaying the collected data in real-time on a digital screen or stored for later analysis.

This detector can scan length of 50 mm and scan speeds can vary in the 0.05 ÷ 1 mm/s range.

The non-skid detector detects primary profile (P), roughness profile (R), waviness (W), and other parameters [157]. From the roughness profile it is possible to obtain Ra (arithmetic average of the distance between the profile and the mean line), Rq (average mean square value of the distances between the profile and the mean line), Rsk (skewness or asymmetry index) and Rku (kurtosis which is a parameter related to the amplitude of the height values distribution). The skewness measures the asymmetry of the distribution of profile height values: it is positive for a distribution with asymmetric tails above the mean and negative for distributions with asymmetric tails below the mean. In practice, it means a surface with positive skewness has some marked peaks, whilst a surface with negative skewness has some deep valleys. The kurtosis is equal to 3 for a Gaussian

distribution; Rku > 3 indicates a sharper distribution with longer tails instead Rku < 3 indicates a broader distribution with less marked tails.

Another important parameter is the cut-off wavelength, which filters out longer wavelength components (waviness) to focus on shorter ones (roughness) for the extrapolation of a roughness profile, ensuring accurate surface quality analysis.

The roughness measurements were collected for the plates coated with the produced Yttria-Stabilized Zirconia. The parameters employed in the present study include:

- scan speed: 0.5 mm/s
- scanned length: 1.75 mm
- cut-off wavelength (λ_C): 0.25 mm

Figure 2.3-5 – Surftest SJ-410 (Mitutoyo)

2.3.6. Colorimetric analysis

The CIE 1976 $L^*a^*b^*$ colour space is a widely adopted system for measuring and organizing object colours in accordance with ISO 11664-4. This colour space encodes colours into three distinct signals: light-dark (L^*), red-green (a^*), and yellow-blue (b^*). Essentially, any given colour can be described as a combination of these signals, such as red and yellow, red and blue, green and yellow, or green and blue [158].

The coordinates of this space are defined as follows:

- L^*: This coordinate represents the lightness of the colour, ranging from 0 (black) to 100 (white).
- a^*: This coordinate indicates the position between red and green. Positive values of a^* ($+a^*$) denote red, while negative values ($-a^*$) denote green.
- b^*: This coordinate indicates the position between yellow and blue. Positive values of b^* ($+b^*$) indicate yellow, whereas negative values ($-b^*$) indicate blue.

Each colour is uniquely identified by its L^*, a^*, and b^* coordinates.

A spectrometer is employed to measure these coordinates. A light source is adopted to illuminate the object, and the reflected light is analysed to determine the tristimulus values (X, Y, Z). These values are derived from the interaction between the light, the object, and the observer. The tristimulus values are then converted into the L^*, a^*, and b^* coordinates using the CIE 1976 equations as follows [159]:

- $L^*=116f(Y/Yn)-16$

- $a^*=500[f(X/Xn)-f(Y/Yn)]$
- $b^*=200[f(Y/Yn)-f(Z/Zn)]$

where:

$f(X/Xn) = (X/Xn)^{1/3}$ if $(X/Xn) > (6/29)^3$

$f(X/Xn) = (841/108)\ (X/Xn) + 4/29$ if $(X/Xn) \leq (6/29)^3$

and

$f(Y/Yn) = (Y/Yn)^{1/3}$ if $(Y/Yn) > (6/29)^3$

$f(Y/Yn) = (841/108)\ (Y/Yn) + 4/29$ if $(Y/Yn) \leq (6/29)^3$

and

$f(Z/Zn) = (Z/Zn)^{1/3}$ if $(Z/Zn) > (6/29)^3$

$f(Z/Zn) = (841/108)\ (Z/Zn) + 4/29$ if $(Z/Zn) \leq (6/29)^3$

This conversion allows for a precise and standardized representation of colours. Typically, these coordinates are plotted on a graph to visualize the location of colours within the CIELAB colour space.

To quantify the difference between two colours in this space, the colour distance (ΔE^*) is calculated using the following formula [158], [159]:

$\Delta E^*=(\Delta L^*)^2+(\Delta a^*)^2+(\Delta b^*)^2$

where:

- ΔL^* represents the difference in lightness between the two colours.
- Δa^* represents the difference in the red/green coordinate.
- Δb^* represents the difference in the yellow/blue coordinate.

The ΔE^* provides a numerical value that indicates how perceptually different two colours are from each other. A smaller value signifies that the colours are very similar, while a larger value indicates a more noticeable difference.

In this work the Easycolor (SmartVision) was employed for the YSZ coating colour evaluation with the following parameters:

- Illuminant type: D50, where D = Daylight and 50 is the temperature of the colour in kelvin)
- Delta E type: CIE CMC
- Observer degree: 2, for laboratory measuring
- Analysed area: 1,51x0,76 mm
- Measurement repetition: 1

2.3.7. Nano-hardness measurements

Nano-hardness tests were conducted using the STeP 4 Open Platform device (Anton Paar). The instrument continuously records both the load applied to the indenter and the penetration depth into the sample during the indentation test. This process generates a complete loading and unloading curve, where the force is plotted as a function of the indenter penetration depth.

The instrumented hardness (HIT) is calculated by analysing the loading-unloading curves and considering the precise geometry of the indenter. This calculation follows the method specified in the ISO 14577 standard [160].

A Berkovich tip was employed for these tests which is a three-sided pyramidal diamond tip with a specific geometry designed to produce an indentation area equivalent to that of a Vickers indenter at the same penetration depths.

Indentation hardness HIT is defined as the ratio between the maximum applied load (Fmax) and the projected contact area (Ap):

$$H_{IT} = \frac{F_{max}}{A_p}$$

In the present study, nano-hardness tests were conducted to evaluate the mechanical properties of YSZ coatings deposited on Ti6Al4V substrates. A total of 90 indentations were performed on each coating to ensure statistical reliability and accuracy of the results. The indentations were carried out at three different penetration depths, with 30 indentations performed for each depth value. This approach allows for a rigorous analysis of the behaviour of the coating under varying conditions.

The specific test conditions were as follows:

- Indenter approach speed: The speed at which the indenter approaches the sample was set to 3000 nm/min.
- Acquisition frequency: Data acquisition was performed at a frequency of 10 Hz.
- Penetration depth and loading/unloading rates: Three different penetration depths were selected to investigate the properties of the coating at various levels of indentation:
    - for a penetration depth of 100 nm, the loading and unloading rate was set to 4 mN/min.
    - for a penetration depth of 200 nm, the loading and unloading rate was increased to 18 mN/min.
    - for a penetration depth of 300 nm, the loading and unloading rate was further increased to 36 mN/min.

  These varying rates ensure that the response of the material is thoroughly examined under different loading conditions.
- Holding time at maximum load: The indenter was held in position for 15 seconds, after reaching the maximum load, ensuring that the measurements reflect the true hardness of the material.

2.3.8. Scratch test

The scratch test, conducted in accordance with the ISO 20502 standard, provides an assessment of the adhesion of hard, ceramic thin films on both hard and soft substrates. This method involves moving a tip with a specified geometry across the sample surface under either a constant or varying normal load. The test is designed to evaluate the mechanical integrity and adhesion properties of the YSZ coating by observing the response of the material to the applied stress.

There are three distinct modes of scratch testing:

- **Progressive Force Scratch Test (PFST)**: the normal load applied to the tip increases steadily as it moves across the sample surface. This gradual increase in load leads to potential failures highlighting the adhesion properties of the coating.
- **Constant Force Scratch Test (CFST)**: multiple scratch tests are conducted, each at a predetermined, fixed load. By maintaining a constant load, this test mode assesses the behaviour of the coating under specific stress conditions, providing information about its durability and resistance to wear.
- **Multi-Pass Scratch Test (MPST)**: the scratch test is repeated multiple times on the same spot of the sample surface. This mode provides more insights on wear mechanisms, the interactions of scratches and the effects of work hardening.

In the PFST mode, the load is usually increased until there is adhesive and/or cohesive failure within the coating/substrate system. Detection of this failure is achieved through direct visual inspection of the scratch track, which is often supplemented by additional instrument outputs such as acoustic emission, penetration depth, and friction coefficient recordings during the test. The load value(s) at which a specific failure mode initiates is termed the critical normal force or critical load (Lc). Critical loads are typically categorized as follows (Figure 2.3-6):

- L_{C1}: Marks the initiation of cracking within the coating.
- L_{C2}: Indicates the start of partial delamination, usually observed around the edges of the scratch track.
- L_{C3}: Represents complete delamination extending across the entire scratch track.

The delamination load refers to the instant when the coating becomes completely detached from the substrate, signifying a total failure of adhesion.

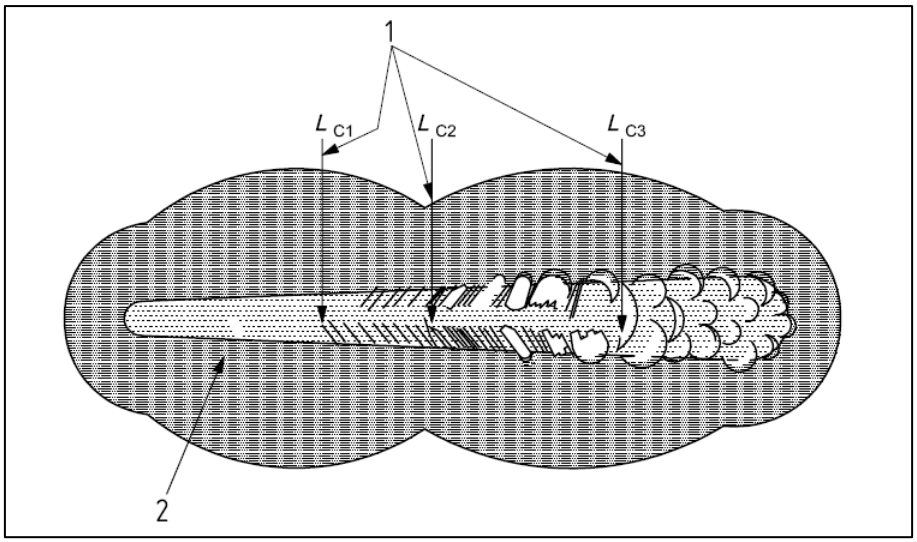

Figure 2.3-6 - critical loads definition according to ISO 20502 [161].

The current testing comprised two main phases:

1. **Initial Setup of the Scratch Test** for determining the optimal testing method. The setup phase followed these specific conditions:
   - **Scratch mode**: PFST
   - **Begin load**: 20 mN

- **Final load**: Variable in the range [1000÷30000] mN
- **Loading rate**: Variable in the range [163.33÷4996.67] mN/min
- **Pre-scan and post-scan load**: 20 mN
- **Scratch speed**: 1 mm/min
- **Scratch length**: 6 mm
- **Data acquisition frequency**: 30 Hz

Set-up tests were performed using two conical diamond indenters with a cone angle of 120° and tip radii of 200 µm and 800 µm.

2. **Execution of the Test Campaign** based on the methodology determined in the first phase, the test campaign was carried out under the following conditions:
   - **Scratch mode**: PFST
   - **Begin load**: 20 mN
   - **Final load**: 20000 mN
   - **Loading rate**: 3330 mN/min
   - **Pre-scan and post-scan load**: 20 mN
   - **Scratch speed**: 1 mm/min
   - **Scratch length**: 6 mm
   - **Data acquisition frequency**: 30 Hz

Tests were performed using a conical diamond indenter with a cone angle of 120° and a tip radius of 200 µm.

2.3.9. Wear test

The pin-on-disk test is a widely used experimental technique for evaluating the tribological properties of materials, specifically focusing on their wear and friction behaviour during sliding. This method is conducted in accordance with ASTM G99-23 standard [161].

In the "*pin–on–disk*" tribometer (Figure 2.3-7), a stationary pin, which has a cylindrical or spherical geometry, is pressed by a known normal load against the surface of a flat sample, fixed onto a rotating disk with a controlled speed for a fixed duration. The test can be conducted at different temperatures to understand the thermal effects on wear and friction.

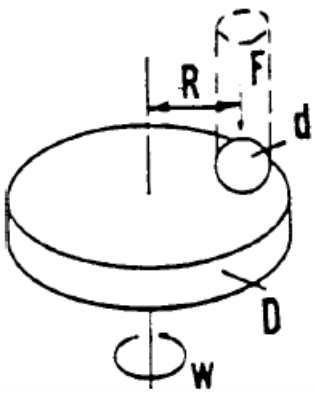

Figure 2.3-7 - Schematic of pin-on-disk wear test system [161].

During the test, frictional forces and wear are continuously monitored and data of the coefficient of friction (COF), wear depth, and wear volume are recorded. After the test, the wear loss on both the pin and the disk are analysed using various techniques such as optical microscopy, profilometry and SEM.

T50 Tribometer (Nanovea) was employed for this investigation adopting a customized counterpart for the evaluation of the wear behaviour of the deposited YSZ coating. Specifically, bristles from a medium-abrasion toothbrush were cut, collected, and fixed together to create a customized pin. This setup was designed to simulate, with high reliability, the conditions that might occur during tooth brushing. It is important to emphasize that this simulation represents an extreme scenario where the abutment is exposed relative to the gum line, such as in cases of periodontal disease. During this study, we specifically chose to investigate this scenario to gain deeper insights into the wear behaviour of the deposited coating under such conditions. This approach allowed us to not only assess the durability and performance of the coating but also to explore its protective capabilities in a highly challenging environment.

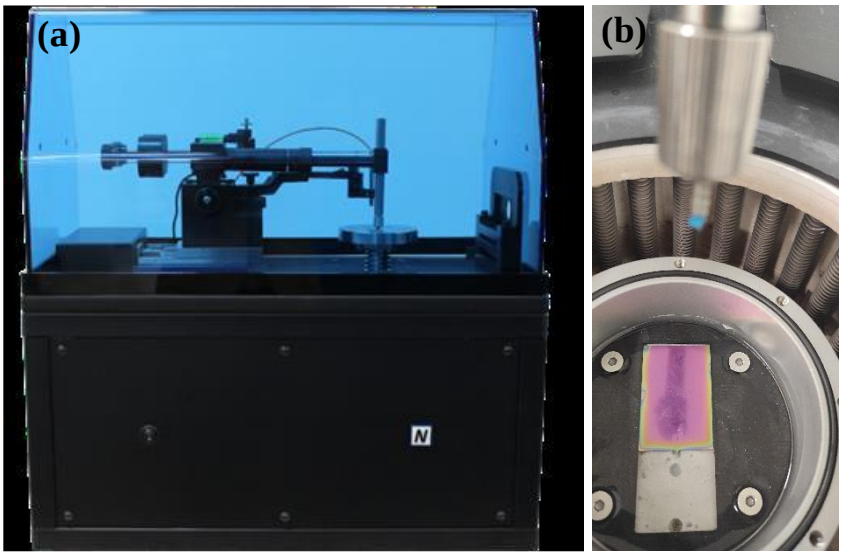

Figure 2.3-8 – (a) T50 tribometer (Nanovea); (b) customized set-up for the tribological test on YSZ coatings.

The following test conditions were adopted:

- Configuration: pin-on-disk
- Movement: alternative
- Normal load: variable in the range [0.25÷1] N;
- Track radius: 30 mm
- Sample speed: 2500 mm/min;
- Arc length: 5000 µm
- Counterbody: Nylon toothbrush bristles, 2 mm diameter;
- Temperature: 37°C;

- Time: 6 hours, to simulate 3 months of brushing.
- Solution: Hank's Balanced Salt Solution (Sigma-Aldrich) with variable concentrations of toothpaste containing silica particles.

The results were analysed using optical microscopy and scanning electron microscopy. Optical images of the traces were acquired at a magnification of 2,5x. SEM analysis in backscattered electron (BSE) mode was performed at an accelerating voltage of 10 kV to examine the trace areas, with BSE images captured at magnifications of 300x and 1000x. Additionally, energy-dispersive X-ray spectroscopy (EDS) was carried out on selected areas of interest to gain a deeper understanding of the trace characteristics.

2.3.10. Low temperature degradation testing

Zirconia coating is prone to low temperature degradation under moist environments at human body temperature. This phenomenon poses a significant risk to the structural integrity of the YSZ coating and long-term performance. Therefore, it is crucial to thoroughly evaluate the hydrothermal stability of these coatings to ensure their reliability in biomedical conditions. To replicate and accelerate the effects of such degradation, standardized aging tests are commonly performed under controlled conditions. These tests are typically conducted in an autoclave at a temperature of 134°C and a pressure of 2 bar, simulating an aggressive environment that allows for a more rapid assessment of the durability of the coating and performance over time.

During this investigation, low temperature degradation testing was conducted in accordance with ISO 13356, which outlines the requirements for implants made of Y-TZP-based ceramics used in surgical applications which are typically more susceptible to this phenomenon. The aging process involves placing the samples in an autoclave at the same temperature and pressure conditions (134°C and 2 bar) to simulate the sterilization environment [38]–[40].

To evaluate the extent of hydrothermal degradation, the amount of monoclinic phase present in the zirconia coating is quantified both before and after the aging process. This is achieved using techniques such as X-ray diffraction (XRD) or Raman spectroscopy, which are capable of distinguishing between the different crystallographic phases of zirconia. By comparing the results obtained before and after aging, it is possible to assess the degree of degradation that has occurred.

In this study, we utilized an autoclave model W&H Lara 22, provided by Modena Polyclinic, to investigate the hydrothermal degradation of the YSZ-14 coating, which was selected as the reference coating. The plate was subjected to testing at a temperature of 134°C and a pressure of 2 bar. To thoroughly investigate the effects of these conditions, the plate was divided and tested over two different durations: 1 hour and 5 hours which represent a minimum of 15 years and 75 years of exposure to the oral environment, respectively. This division allowed for a comprehensive analysis of the behaviour material under varying exposure times.

2.3.11. Rheometric test

Rheology is the science that studies the flow and deformation of materials. In this study, the measures were conducted in shear flow (under shear stress) and oscillatory mode to investigate the viscoelastic properties of

the collagen-based solution. The study analysed the properties of the solution during deposition and gelation. These materials are non-Newtonian fluids, so the viscosity varies with applied force or flow rate.

Rheometer MCR 102e (Anton Paar) was adopted to perform flow curves, evaluating the viscosity of the fluid at different shear rates [162], [163]. At shear rate equal to zero, the viscosity represents the static state of the fluid, while at the highest shear rate, it reflects the state during injection, such as from a syringe. This test helps to optimize deposition by achieving shear thinning behaviour, where the fluid has low viscosity under a high shear rate (during injection) and high viscosity when at rest (after deposition). We subjected the collagen-based solution to a shear rate range of $0.01 \div 100\ s^{-1}$. Tests were conducted at 4°C to simulate deposition conditions, and at 25°C to understand the behaviour changes when collagen gelation begins. A cone-and-plate sensor with a diameter of 25 mm and an angle of 1° was used.

The second series of tests aim to understand the behaviour of the fluid during gelation. A time sweep test was conducted to evaluate the gel time of the collagen solution [163]. This test provides a graph where the G'/G" modulus is plotted as a function of time, using the Rheometer MCR 102e (Anton Paar). The test was performed at 1 Hz at a low strain value (γ=0.5%) to ensure it remained within the linear viscoelastic region (LVR) adopting the same cone-and-plate sensor used to obtain the frequency flow curves. The test was carried out at a temperature of 37°C, which is the standard temperature for collagen gelation.

Both the investigations were conducted on three collagen-based solutions: collagen, collagen with 0.1% w/v of Laponite, and collagen with 0.3% w/v of Laponite.

2.3.12. DSC analysis

Differential Scanning Calorimetry (DSC) analysis was performed to assess the thermal stability of materials by evaluating the heat flow exchange, comparing the samples to a reference. The analysis produced a graph showing heat flow as a function of temperature.

In this study, collagen-based layers were analysed to evaluate the impact of Laponite addition and UV cross-linking. Specifically, four formulations were investigated: pure collagen subjected to gelation (PG), gelation followed by UV cross-linking for 30 minutes (PR1), and gelation followed by UV cross-linking for 60 minutes (PG2) to assess the effects of these treatments. Additionally, pure collagen with 0.3 w/v% Laponite, subjected to gelation and UV cross-linking for 60 minutes (LG2), was analysed to compare its results with PR2 and evaluate the effect of Laponite addition.

A preliminary setup was conducted on gelled pure collagen from 30°C to 300°C to evaluate its overall behaviour and to define the thermal ramps for the subsequent tests. Based on this initial setup, the following thermal ramps were established for the DSC analysis:

- First heating ramp from 30°C to 240°C at a rate of 5°C/min.
- First cooling ramp from 240°C to 30°C at a rate of 10°C/min.
- Second heating ramp from 30°C to 240°C at a rate of 5°C/min.

Pierced aluminium pans were used to contain the samples, and all ramps were conducted in a nitrogen-controlled atmosphere. The instrument used for these analyses was the DSC 214 Polyma (Netzsch).

The first heating ramp is used to detect the denaturation temperature, which corresponds to the temperature at which the triple helix of collagen ruptures. The second heating ramp is performed to evaluate the glass transition of the polypeptides, which are now free to move [164], [165].

2.3.13. Contact angle measurement

Wettability is a property influenced by various factors, including pH, temperature, charge density, and surface energy. It can be quantitatively assessed by measuring the contact angle of a pure water droplet on a given surface. The chemical composition and surface chemistry significantly affect the interaction with water molecules, thereby influencing wettability. Two distinct scenarios can be observed based on the contact angle measurements:

- High contact angles indicate that the material is hydrophobic, meaning it does not interact favourably with water.
- Low contact angles suggest that the material is hydrophilic, demonstrating an affinity for water. In this case, water droplets are adsorbed onto the surface due to the presence of functional groups.

The measurement of the contact angle involves placing a water droplet on a flat surface and evaluating the angle formed at the intersection of the liquid/vapor and liquid/solid interfaces. This angle is tangent to the equilibrium point where the phases meet [166], [167].

Evaluating collagen adhesion is challenging because water and collagen molecules behave differently. Nonetheless, an increase in surface hydrophilicity suggests that the surface becomes more conducive to collagen adhesion, as the OH^- groups can more readily interact with the polar groups of the collagen molecule.

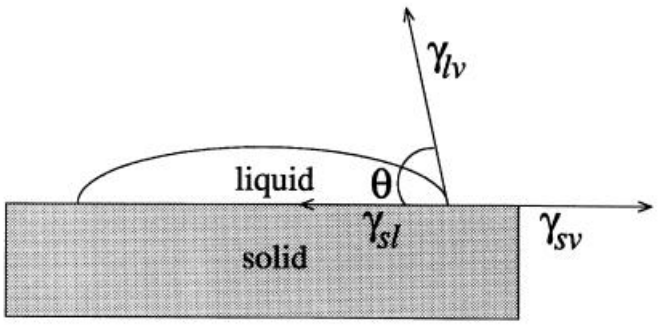

Figure 2.3-9 - Schematic of a sessile-drop contact angle system [166].

For this investigation, the measurement of contact angles was conducted using an optical microscope equipped with backlighting. The video footage captured by the microscope was transmitted to a computer and analysed using the SCAN software package (Figure 2.3-10 (a)). Water droplets of 2µl were injected through a syringe needle onto both biomedical zirconia surfaces (polished and CNC-finished) and YSZ-deposited plates. The instrument utilized for this analysis was the "Contact Angle System-OCA" (Dataphysics).

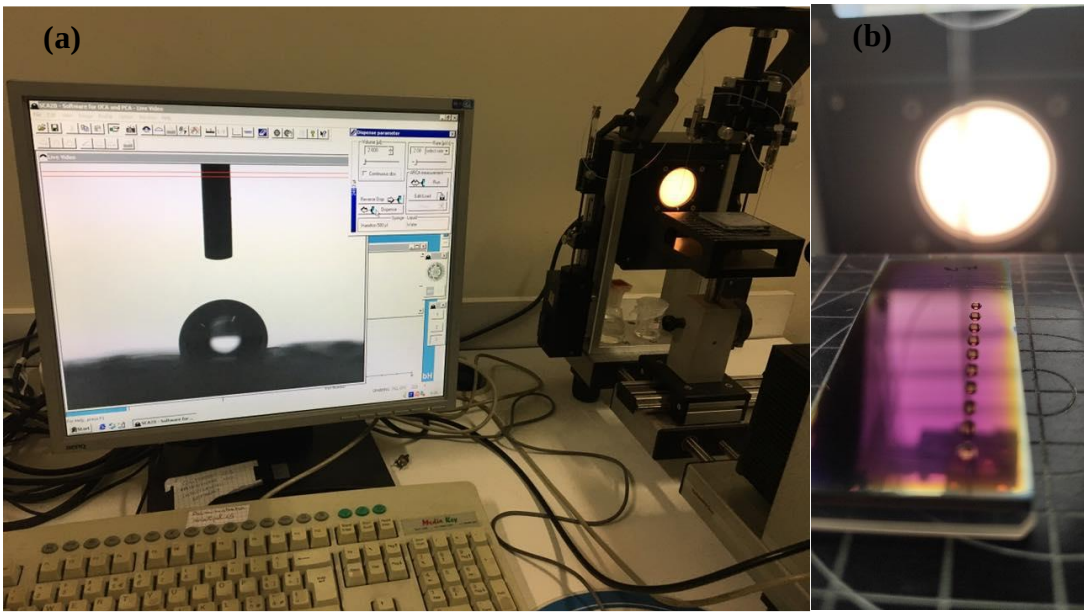

Figure 2.3-10 – (a) software package (SCAN); (b) example of droplet deposition.

3. Chapter 3 – Results

3.1. Yttria-Stabilized Zirconia coatings – screening phase

3.1.1. Macroscopic observations

The YSZ coatings deposited during the screening phase exhibited a range of colour variations, as shown in Figure 3.1-1. Typically, pink, green, and blue hues were observed with varying opacity levels, arising from interference effects inherent to zirconia, which remains transparent at the achieved thicknesses. Notably, all coatings deposited using the RF-PECVD method (YSZ-6, YSZ-7, and YSZ-8) displayed inconsistencies in surface appearance with colour variations.

The goal of this research was to achieve pink or yellow coatings, as these colours have been reported in the literature to minimize peri-implant discoloration [30]–[32]. Their potential lies in providing a more natural appearance to the gingival tissue interfacing with the abutment, thereby enhancing aesthetic outcomes.

During this initial phase, the YSZ-2 and YSZ-4 coatings emerged as the most promising candidates for further investigation due to their distinct pink coloration, which suggests a potential aesthetic advantage. Among these, the YSZ-2 coating was particularly favoured due to the aesthetic and technical requirements of clinical dental implantology.

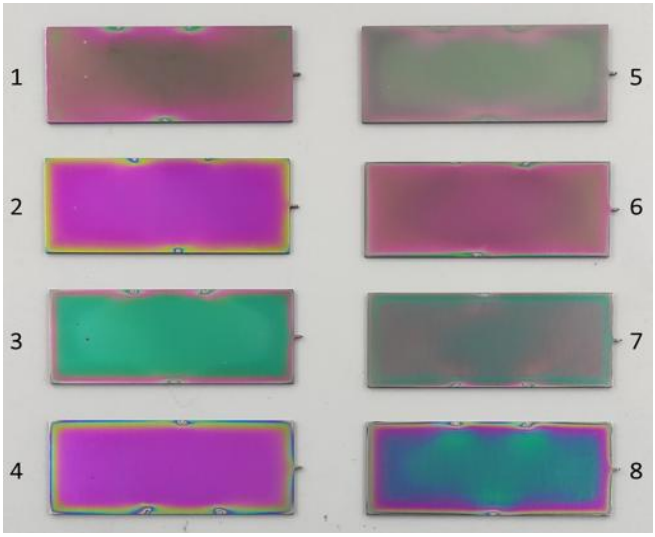

Figure 3.1-1 - appearance of YSZ plates of the screening phase.

3.1.2. Electron Microscopy observations

Scanning electron microscopy (SEM) conducted on the coating surface reveals a homogeneous and defect-free surface in all coatings deposited during the initial screening phase. Figure 3.1-2 shows one image captured using the SE detector showcasing the surface morphology of the YSZ-1 coating, which is representative of the overall quality observed across all eight coatings deposited. Given the thin nature of these coatings, it is particularly noteworthy how the surface morphology of the coatings closely mirrors that of the underlying substrate.

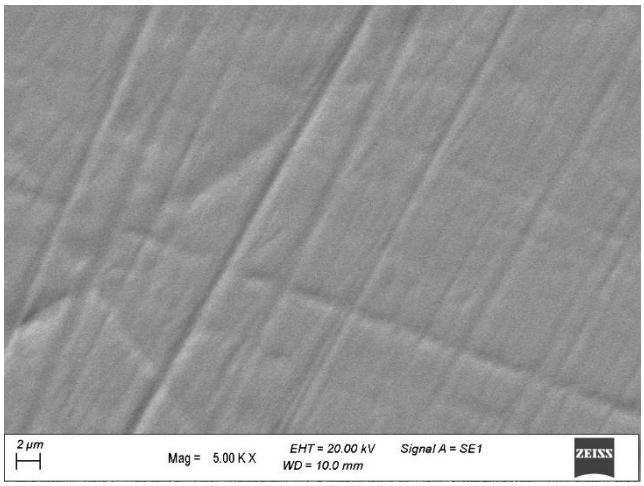

Figure 3.1-2 - SEM image through SE detector of YSZ-1

EDS spectra were collected from each coating surface to obtain a semi-quantitative analysis, one example is shown in Figure 3.1-3. In all cases, zirconium, oxygen, yttrium, argon, and hafnium were detected, with their respective amounts specified in the graphs shown in Figure 3.1-4. Titanium, aluminium and vanadium are elements of the substrate, which is reached by electron beam below the thin film.

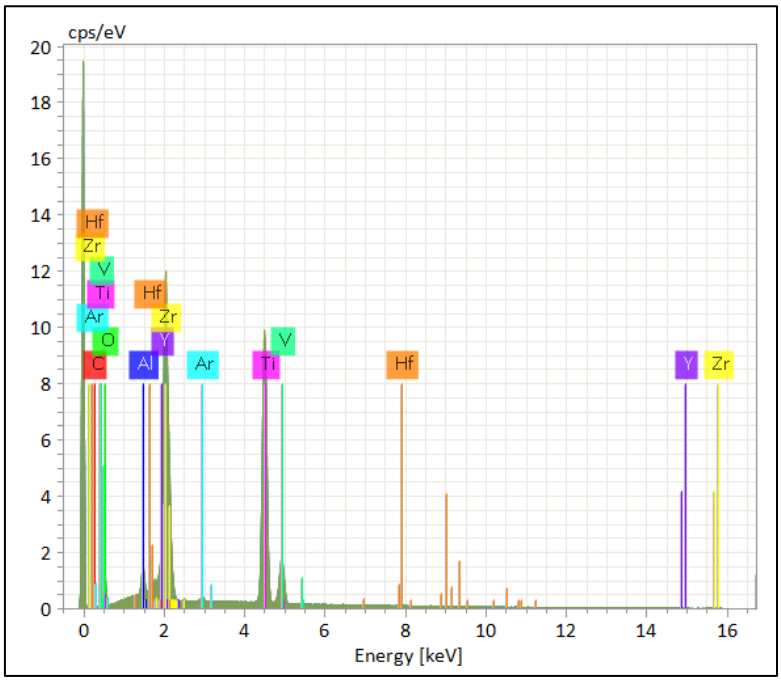

Figure 3.1-3 - EDS spectrum of YSZ-1

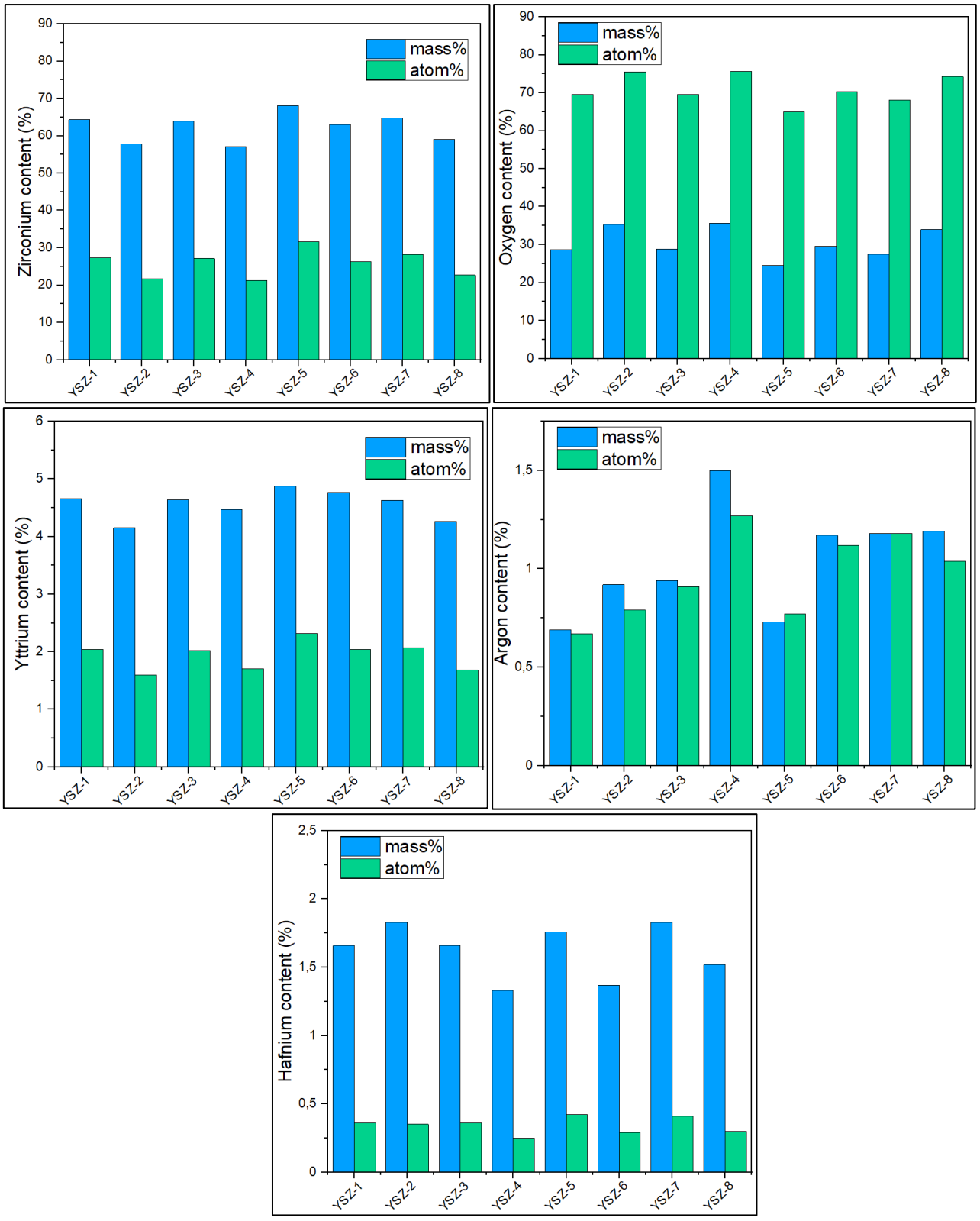

Figure 3.1-4 - Element contents of the YSZ coatings deposited in the screening phase through EDS analysis.

The average percentages, in terms of weight, of zirconium (Zr), yttrium (Y), and oxygen (O) in the sample are 62.3 wt. %, 4.6 wt. %, and 30.5 wt. %, respectively. In contrast, hafnium (Hf) and argon (Ar) are contaminants found in average percentages of 1.5 wt. % and 1 wt. %, respectively. Hafnium is naturally associated with zirconium, while argon is introduced during the deposition process. The measured values of zirconium, oxygen, and yttrium align with expectations and are confirmed by the following calculations.

First, the molar masses of zirconium, yttrium, and oxygen, which are 91.22 g/mol, 88.91 g/mol, and 16.00 g/mol, respectively. Starting with a target composition of 93 wt.% Zr and 7 wt.% Y, the moles of each element in the target are calculated. This results in 1.019 moles of zirconium and 0.079 moles of yttrium.

To determine the moles of oxygen, we need to account for its presence in the ZrO_2 and Y_2O_3 phases. For ZrO_2, each mole of zirconium corresponds to 2 moles of oxygen. For Y_2O_3, each mole of yttrium corresponds to 1.5 moles of oxygen. Therefore, the total moles of oxygen are calculated as follows:

- From ZrO_2: (2 \times 1.019 = 2.038) moles of oxygen
- From Y_2O_3: (1.5 \times 0.079 = 0.119) moles of oxygen

Adding these contributions, the total moles of oxygen amount to 2.157. Given the molar mass of oxygen (16 g/mol), the mass of oxygen is 34.5 grams.

The total mass was calculated and includes 93 grams of zirconium, 7 grams of yttrium, and 34.5 grams of oxygen, summing to approximately 134.5 grams. Additionally, we must include the mass of the contaminants: 1.5 grams of hafnium and 1 gram of argon. Therefore, the total mass is approximately 137 grams.

Consequently, the expected weight percentages of zirconium, yttrium, and oxygen in the coating are:

- Zirconium: 68 wt.% (93 g / 137 g)
- Yttrium: 5wt.% (7 g / 137 g)
- Oxygen: 25 wt.% (34.5 g / 137 g)

The results are generally consistent with the experimental expectations, although it appears there is a higher amount of oxygen than anticipated. On the other hand, EDS is an analytical technique which is not reliable to quantify the amount of light elements, oxygen included.

Moreover, it is possible to evaluate the stoichiometry of the formed phases by considering the total mass of the coatings, excluding the amounts of contaminants. The average weight concentrations of zirconium, yttrium, and oxygen in the coatings are 63.9 wt.%, 4.7 wt.%, and 31.3 wt.%, respectively. To determine the mole amounts, the normalized weight values are multiplied by the respective molar masses of the elements. This calculation yields mole values of 0.7 for zirconium, 0.053 for yttrium, and 1.96 for oxygen. For the formation of zirconium dioxide (ZrO_2), two moles of oxygen are required for each mole of zirconium. The current ratio of oxygen to zirconium is 2.8, which is slightly higher than the stoichiometric requirement. In contrast, for the formation of yttrium oxide (Y_2O_3), 1.5 moles of oxygen are needed for each mole of yttrium. The current ratio of oxygen to yttrium is 37, which is significantly higher than the stoichiometric requirement. In general, this excess of oxygen, particularly relative to Y_2O_3 but also to ZrO_2, could influence the phase composition and properties of the coating.

Some of these coatings were selected for FEG-SEM analysis to observe the cross-section of these thin films with higher resolution compared to standard SEM. Three coatings are arbitrarily chosen for this analysis: YSZ-2, YSZ-3, and YSZ-5 (Figure 3.1-5). The FEG-SEM observations revealed that the thickness of these coatings varies significantly, ranging from 150 nm to 600 nm. Moreover, the coatings appeared to be homogeneously deposited, with no visible defects such as cracks, voids, or delaminations along the entire observed cross-section.

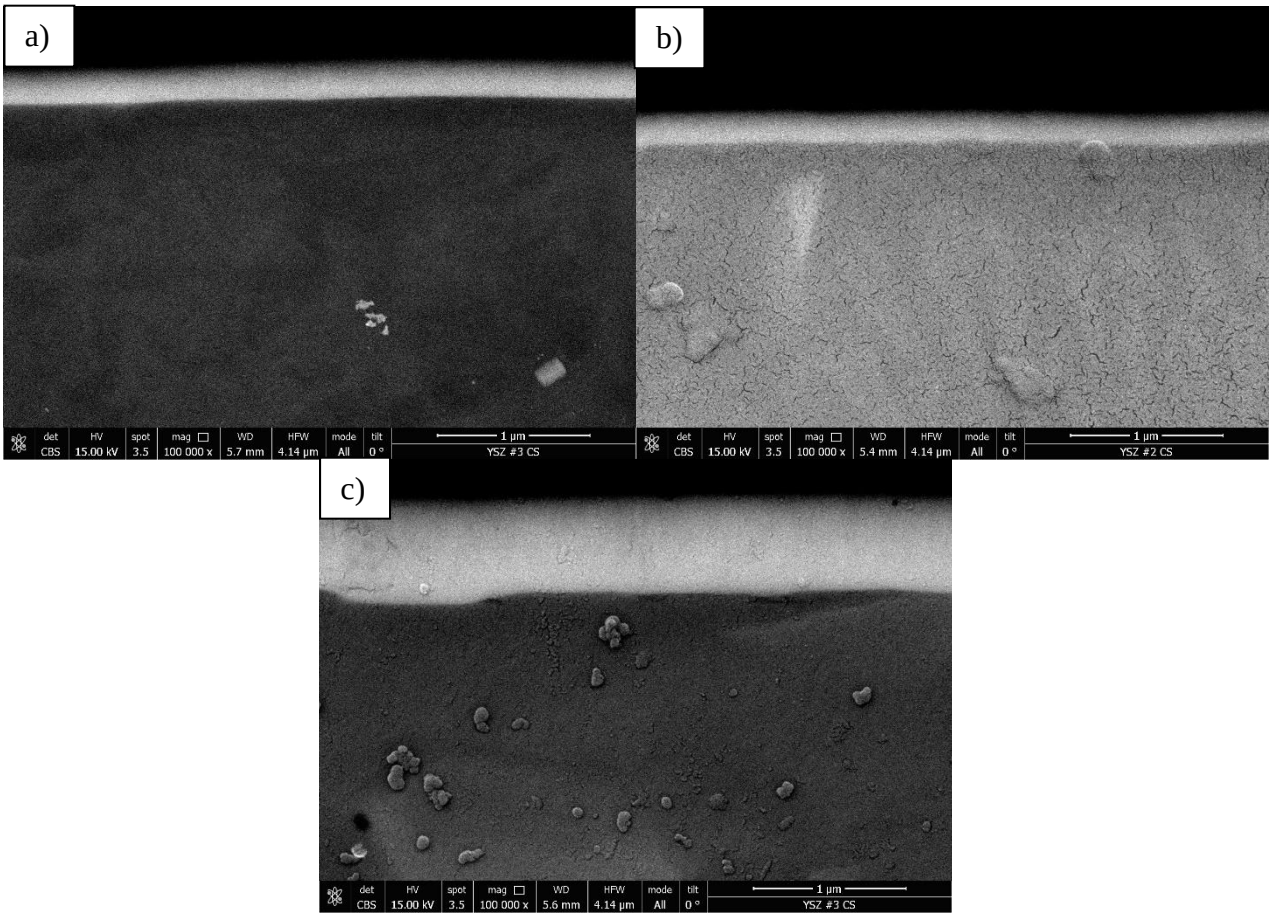

Figure 3.1-5 - FEG-SEM observation of cross-sectioned YSZ samples: a) YSZ-2; b) YSZ-3 and c) YSZ-5.

3.1.3. Roughness measurements

The results of the roughness measurements of the YSZ coating, deposited during the screening phase, indicate no significant variation compared to the values recorded on the bare titanium substrate. This outcome was anticipated, given the thin nature of the coatings applied. The recorded roughness values averaged around 0.030 µm. This consistency in roughness is crucial as it meets the requirement for having a surface with low roughness when exposed to the oral environment preventing bacterial colonization and subsequent infection. All the roughness values are collected in Table 3-1.

Table 3-1 - Roughness measurements on YSZ coatings during screening phase

	naked Ti plate		**YSZ-coated Ti plate**	
YSZ	**Average [um]**	**Std Dev [um]**	**Average [um]**	**Std Dev [um]**
1	0,029	0,002	0,027	0,003
2	0,027	0,003	0,025	0,004
3	0,032	0,005	0,034	0,009
4	0,039	0,002	0,040	0,002
5	0,041	0,002	0,043	0,003
6	0,039	0,001	0,042	0,001
7	0,047	0,003	0,046	0,003
8	0,040	0,001	0,041	0,001

3.1.4. Nano-hardness measurements

The nano-hardness values were extracted from all the Yttria-Stabilized Zirconia (YSZ) coatings deposited during the screening phase at varying depths, extending up to 300 nm. To assess the influence of the substrate, identical measurements were performed on the Ti6Al4V alloy plate. Additionally, these measurements were conducted on a biomedical-grade zirconia plate, serving as a reference standard.

The nano-hardness values exhibited a range from 11 GPa at a depth of 100 nm to 8 GPa at a depth of 300 nm. It is evident that the values at greater depths are significantly influenced by the underlying titanium substrate. The thickness of the coatings varied between 150 nm and 600 nm. According to ISO 14577 standards, to minimize substrate effects, the coating thickness should be at least ten times the depth of the indentation. Consequently, while the measurements at 100 nm provide a closer approximation of the true nano-hardness, they are still subject to some degree of substrate influence.

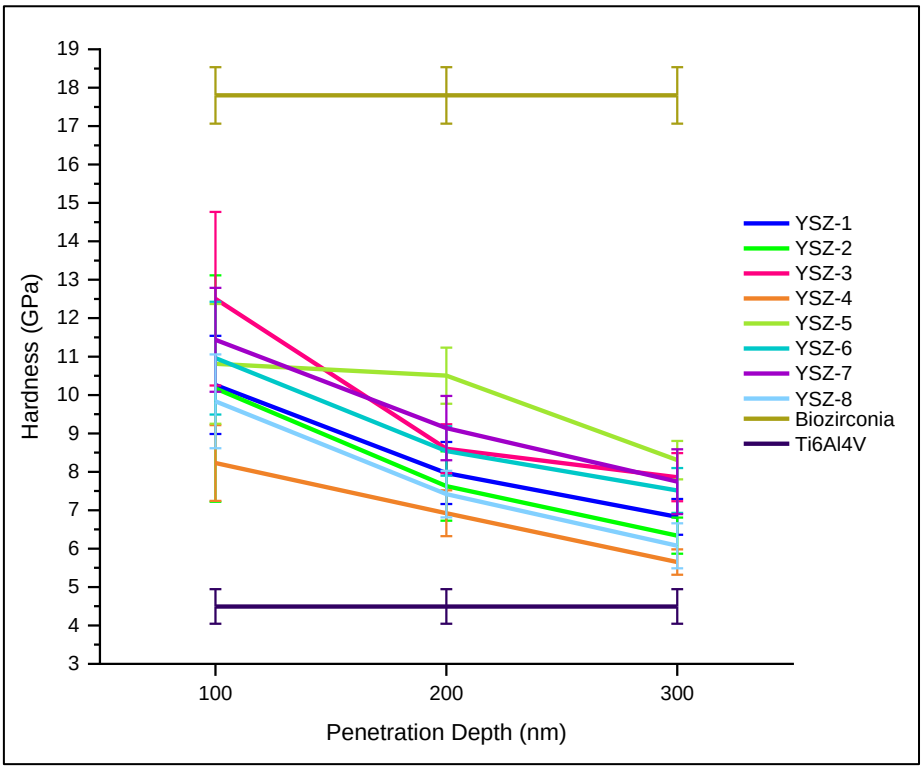

Figure 3.1-6 - Nano-hardness values of the YSZ coating deposited during the screening phase.

3.1.5. Colorimetric analysis

Colorimetric analysis was conducted on the eight YSZ plates deposited during the screening phase (Figure 3.1-1). The CIELAB coordinates (L*, a*, and b*) are collected in Table 3-2, and the ΔE* value was calculated for each plate using the gingival values as reference [30].

The evaluation of these results was based on existing literature data. Implantation of colour strips at the interface between the abutment site and gingival tissue has a beneficial effect when light pink, pink, light orange, and orange colour strips were selected. These specific colour strips yielded a ΔE* value close to the perceptibility threshold [31]. Additionally, another study [30] examined the impact of gold-anodized, pink-anodized, unanodized titanium abutments, and zirconia abutments on the coloration of peri-implant soft tissue.

The findings indicated that gold-anodized and pink-anodized titanium abutments resulted in minimal discoloration of the peri-implant soft tissue, whereas zirconia was identified as the optimal abutment material for aesthetic regions. This is supported by the colour distance values reported in the literature, where a ΔE* value of 8.74 is recognized as the threshold for distinguishing mucosal colour differences between an optimal match and those perceptible to the human eye.

According to these findings, pink and yellow colours appear to induce the least peri-implant discoloration. Therefore, the YSZ-2 and YSZ-4 plates, which exhibited a pink colour, were expected to yield favourable results. However, the data presented in Table 3-2 indicate that their ΔE* values were around 68, which was significantly higher than anticipated.

This discrepancy might have stemmed from limitations in the colorimetric analysis method employed. Specifically, the presence of a titanium substrate and the nanometric, translucent coating could have influenced the measurements. Given the nature of these coatings, a more specialized analytical approach would have been required to obtain more accurate colorimetric data.

Nevertheless, the visual assessment aligned well with both the aesthetic and technical requirements of clinical dental implantology, fully supporting the outcome. As a result, despite the discrepancies observed in the instrumental analysis, YSZ-2 and YSZ-4 coatings remained the reference samples for the optimization phase of deposition.

Table 3-2 - CIELAB coordinates of the eight plates of the screening phase.

YSZ plate	L*	a*	b*	ΔE
YSZ-1	46.1	17.8	-4.2	22.0
YSZ-2	45.5	54.8	-41.3	67.3
YSZ-3	59.3	-41.8	16.9	63.6
YSZ-4	48.8	52.1	-44.0	68.2
YSZ-5	57.3	2.0	3.3	24.3
YSZ-6	41.1	31.2	-10.8	31.1
YSZ-7	44.8	-14.7	12.0	37.0
YSZ-8	49.7	-31.5	-2.8	56.4

3.1.6. Scratch test

An initial setup of the test methodology was conducted on the YSZ-2 coating to establish the optimal procedure for application across all coatings. This preliminary phase involved creating one scratch per type, as documented in Table 3-3. At a consistent end load of 30 N, two different tips with radii of 200 µm and 800 µm were utilized, resulting in distinct outcomes. The scratch track produced with the 800 µm tip was barely visible, whereas the track created with the 200 µm tip showed almost complete delamination at lower loads. Consequently, the setup with the 200 µm tip was optimized by reducing the end load and evaluating the tracks at 5 N, 15 N, and 20 N. The selected methodology involved using the tip with a radius of 200 µm and an end load of 20 N. This combination provided a clear and reliable track, facilitating the detection of various critical loads and ensuring the accuracy and reproducibility of the results across all samples.

Table 3-3 - panorama view of the scratch tracks – set-up

YSZ-2 Tip: 800µm End load: 30N	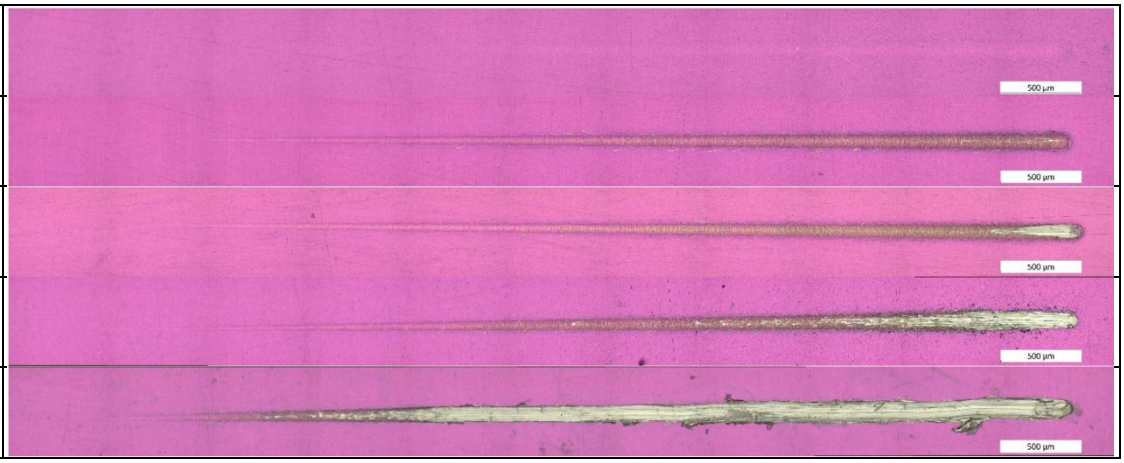
YSZ-2 Tip: 200µm End load: 5N	
YSZ-2 Tip: 200µm End load: 15N	
YSZ-2 Tip: 200µm End load: 20 N	
YSZ-2 Tip: 200µm End load: 30 N	

For the test campaign, at least two scratch tests for coating were conducted to understand the adhesion quality of the YSZ coatings deposited during the screening phase on the Ti6Al4V bulk.

In Table 3-4, one scratch track for each coating was collected.

The initial type of damage identified was the formation of semicircular microcracks along the transversal section of the track, which was labelled as Lc1. The values for Lc1 ranged between 3 N and 9 N. Notably, the coatings YSZ-2 and YSZ-8 exhibit the lowest Lc1 values, while YSZ-5 shows the highest (Figure 3.1-8 (a)). As the applied load increased, these microcracks began to extend towards the edge of the track starting at loads ranging from 4 N to 10 N, which was denoted as Lc2. Among the coatings, YSZ-8 exhibited the minimum Lc2 value, whereas YSZ-5 had the maximum (Figure 3.1-8 (b)). Partial delamination, referred to as Lc3, became observable at load values starting from approximately 10 N for the YSZ-8 coating (Figure 3.1-8 (c)), and extended up to 18 N for the YSZ-3 and YSZ-7 coatings. Finally, total delamination was detectable in YSZ-2 and YSZ-8 (Figure 3.1-8 (d)) at around 18 N, and in YSZ-6 and YSZ-7 in one of the two repetitions, reaching approximately 19 N.

Table 3-4 - panorama view of the scratch tracks – campaign (screening phase)

YSZ-1 V=400V, t=2h, RF off	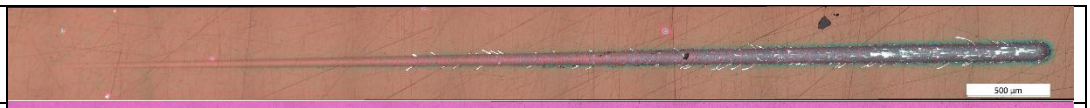
YSZ-2 V=400V, t=2h, RF off	
YSZ-3 V=400V, t=4h, RF off	
YSZ-4 V=390V t=4h, RF off	
YSZ-5 V=420V t=4h, RF off	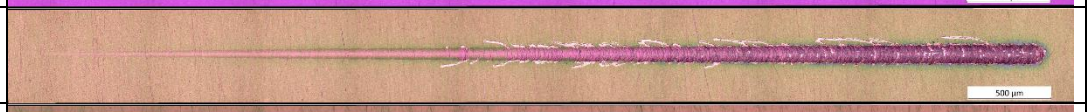
YSZ-6 V=420V t=3.5h, RF on	
YSZ-7 V=390V t=4h, RF on	
YSZ-8 V=400V t=4h, RF on	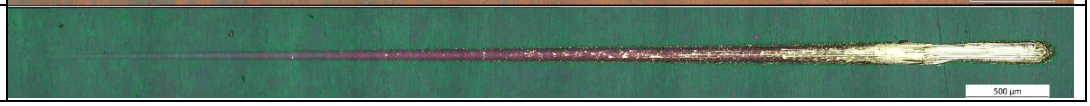

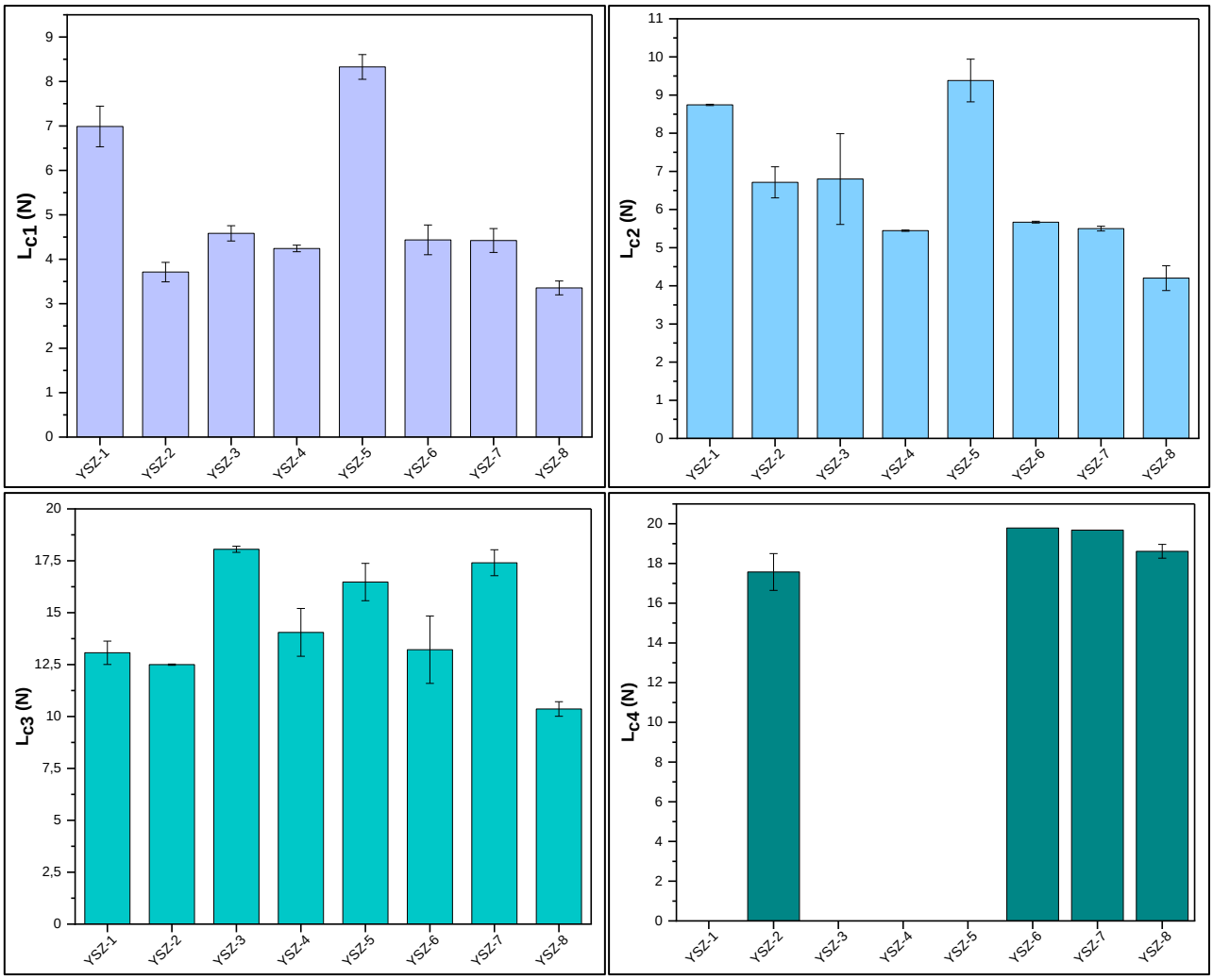

Figure 3.1-7 - Critical load values (screening phase)

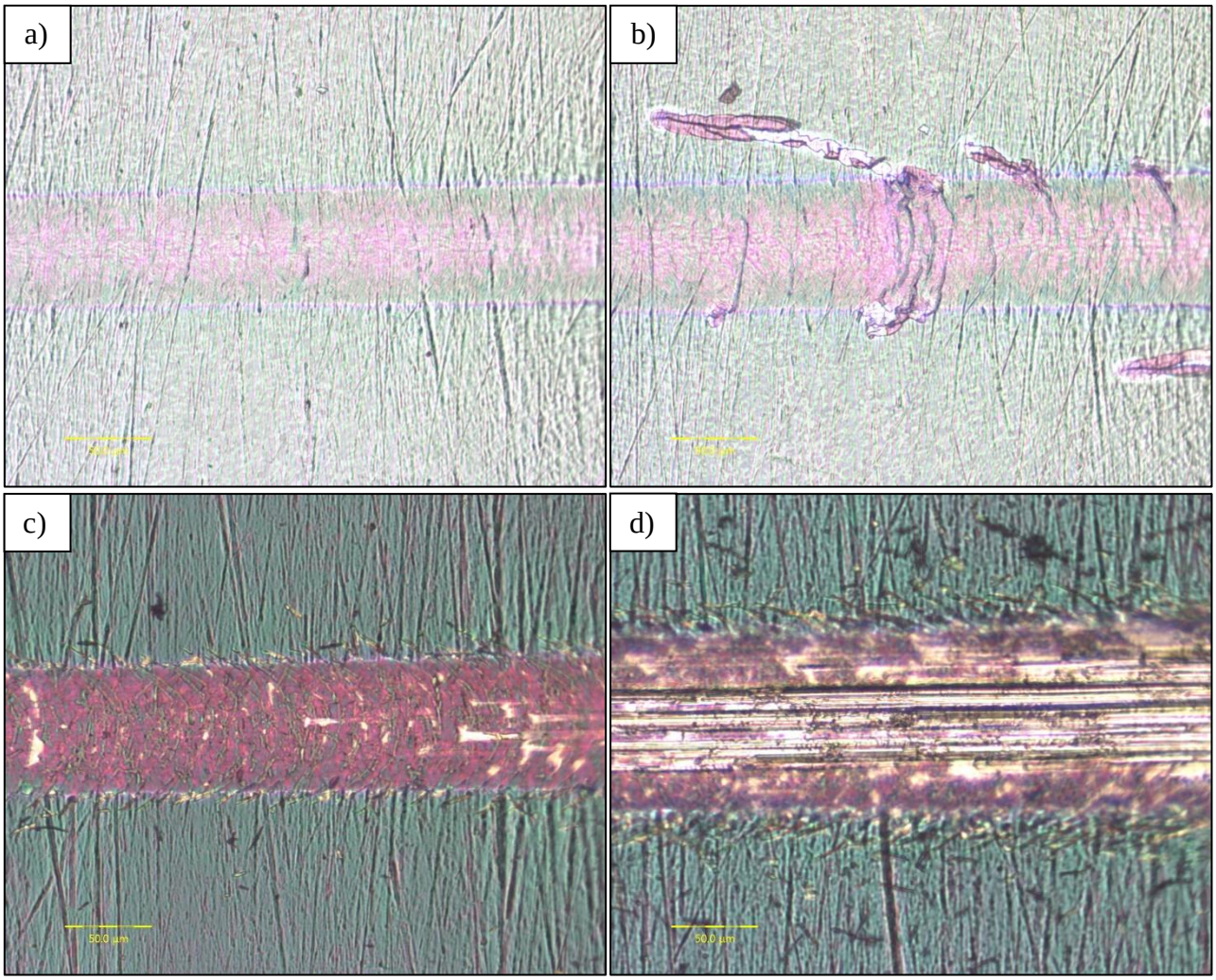

Figure 3.1-8 - critical load image examples. a) Lc1 (YSZ-5), b) Lc2 (YSZ-5), c) Lc3 (YSZ-8), d) and Lc4 (YSZ-8).

3.1.7. Raman analysis

Raman spectroscopy was conducted for evaluating the phases obtained during the reactive sputtering deposition of the screening phase. Figure 3.1-9 illustrates the interrelation between the cubic F2g mode and the tetragonal A1g and Eg modes of vibration, highlighting their association with the stretching of Zr-O_1 bonds, where O_1 denotes the oxygen atom in the first coordination shell of zirconium within the ZrO_2 lattice.

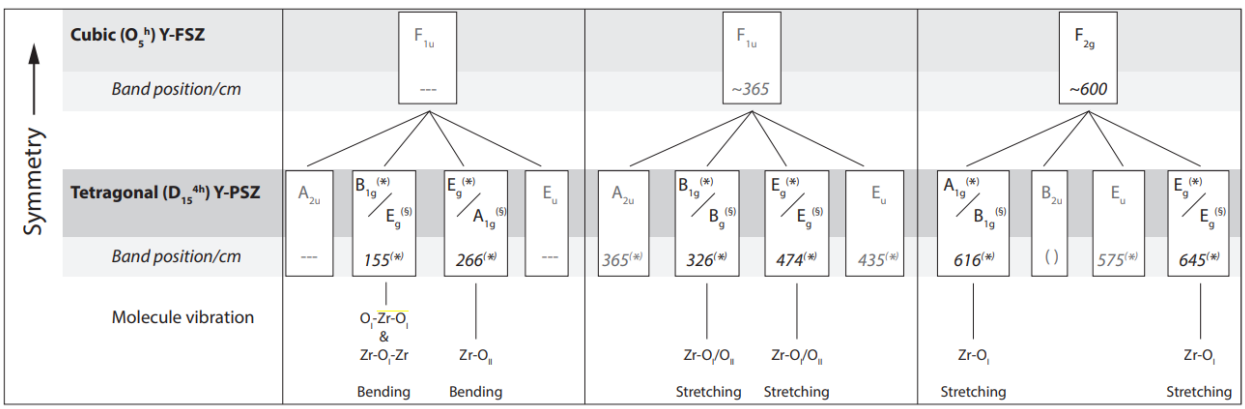

Figure 3.1-9 - Vibration mode of the tetragonal and the cubic Y-ZrO_2 phase [168].

Each phase of zirconia exhibits a specific Raman spectrum characterized by distinct peaks. Figure 3.1-10 (b) highlights the Raman spectrum for each phase [169]. The peak at 150/cm is common to both the tetragonal and cubic phases. In contrast, the peaks at ~245/cm and ~460/cm are representative of the cubic and tetragonal phases, respectively. Finally, the peak at ~645/cm, characteristic of the tetragonal phase, shifts to ~600/cm in the cubic phase [170].

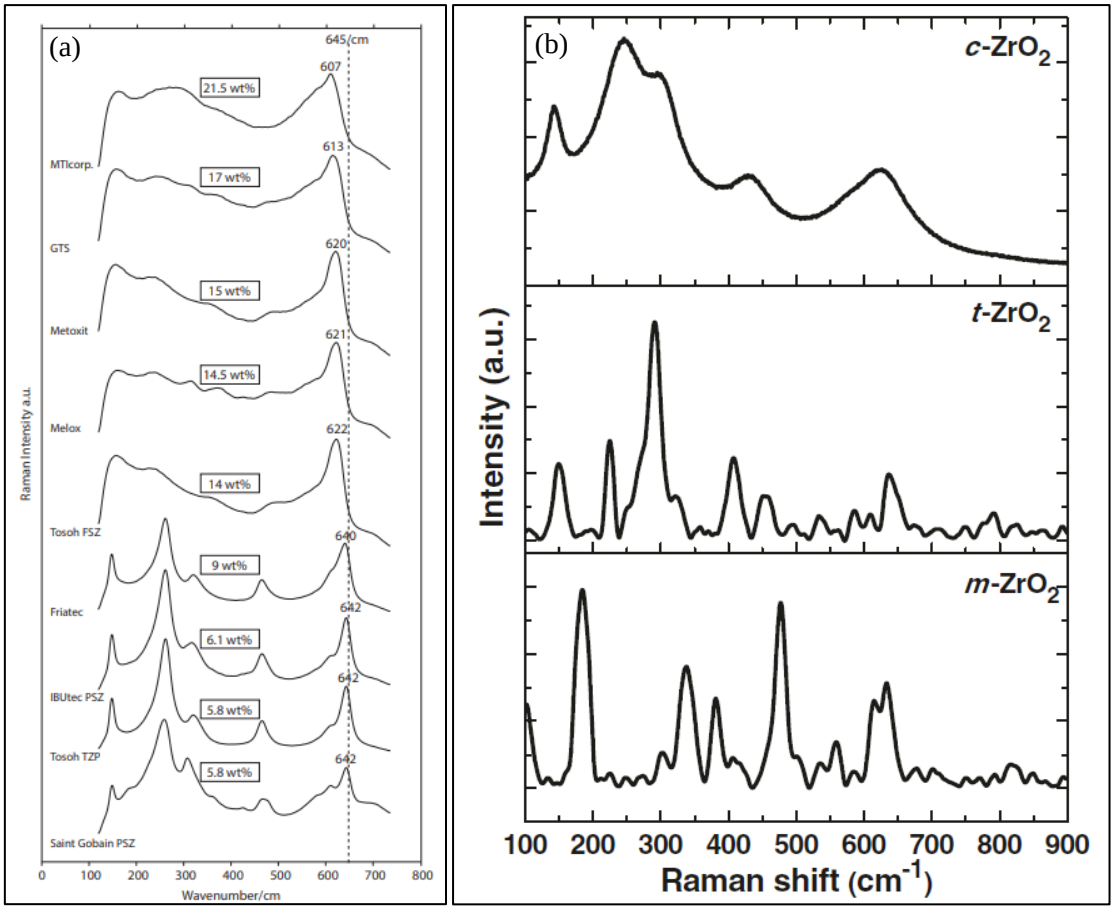

Figure 3.1-10 – a) Raman spectra of the analysed sintered Y2O3-stabilized ZrO2 samples. The dotted line marks the 645/cm band position [170] *and b) Raman spectra of different zirconia samples* [169].

Spectra for all the YSZ coatings of the screening phase are collected in Figure 3.1-11. All the spectra exhibited a peak around 150/cm. The spectra of the YSZ-1 and YSZ-2 coatings showed peaks characteristic of the cubic phase at approximately 250/cm, and of the tetragonal phase at 450/cm and at 630/cm and 620/cm for the YSZ-1 and YSZ-2, respectively. The spectra of the other coatings revealed only the characteristic peaks of the cubic phase, except for the YSZ-4 case, which also exhibited a peak at 460/cm indicative of the tetragonal phase. Furthermore, by analysing the shift in the ~645/cm band in the Raman spectra and referencing the study [170], the Yttria content was determined and extrapolated values are collected in Table 3-5.

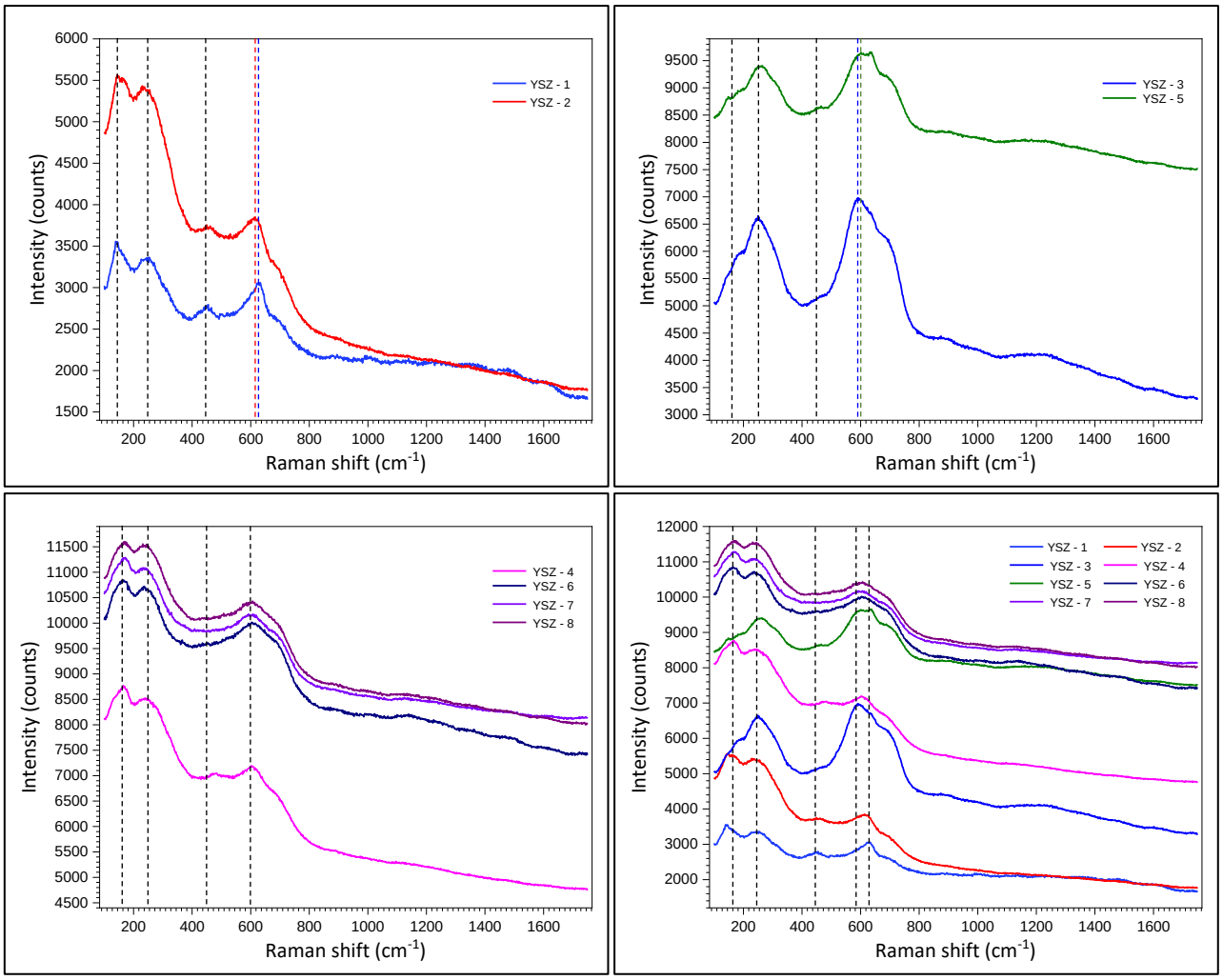

Figure 3.1-11 - Raman spectra collected for all the YSZ coatings of the screening phase.

Table 3-5 – Extrapolated values of Yttria content in YSZ-coatings (screening phase).

Coating type	cm^{-1}	wt.% Yttria	mol.% Yttria
YSZ - 1	630	≈11	≈6
YSZ - 2	620	≈14	≈8
YSZ - 3	590	>22	>13
YSZ - 4-8	600	≈22	≈13

3.1.8. XRD analysis

X-ray diffraction (XRD) analysis was performed on a single coating from the screening deposition to determine the composition of the constituent phases. The YSZ-4 coating was chosen as the reference standard for all screening coatings.

The zirconia crystal exhibits diffraction peaks at various position depending on the phase. Monoclinic, tetragonal and cubic exhibits diffraction peaks at specific 2-theta angles.

Figure 3.1-12 show the spectrum of the YSZ-4 coating. The detected phases are cubic and tetragonal, as indicated by their respective diffraction peaks. The obtained pattern is in accordance to that founded in literature [171]–[174]. The diffraction peak at 30° is observed in both cubic and tetragonal zirconia phases.

The peaks at 35°, 50° and 60° vary with the yttria concentration. Specifically, a double peak corresponding to the tetragonal phase is observed at 3 mol.% yttria, which transitions to a single peak indicative of the cubic phase at 5 mol.% yttria [172]. This observation aligns well with other studies that report a single cubic phase peak at 35° when zirconia is doped with yttria concentrations exceeding 6 mol.% [174], and a double tetragonal peak at 4 mol.% yttria [171]. The peak at 50° exhibits a double tetragonal peak at yttria concentrations at 3 mol.%, transitioning to a single cubic phase peak at 5 mol.% of yttria content [172]. Similarly, the peak at 60° shows a double tetragonal peak at yttria concentrations of 3 mol.%, which becomes a single cubic phase peak at 5 mol.% of yttria [171], [172]. The concentration at 4 mol.% of yttria is a transition state between the tetragonal and cubic phases. In this study, a zirconium target doped with 7 mol.% yttrium was adopted, which approximately corresponds to 4 mol.% yttria in the coating. Consequently, the XRD spectrum of the YSZ-4 coating confirms all the peaks reported in the literature, specifically the cubic/tetragonal one at 30°, the cubic peaks at 35° and 50°, and a double tetragonal peak at 60°. Details of the peak positions and the related phases are summarized in Table 3-6.

Additional peaks correspond to grade 5 titanium which are characteristic of the substrate. Notably, the monoclinic phase is absent in the realized structure, as no corresponding peaks were detected in the XRD analysis.

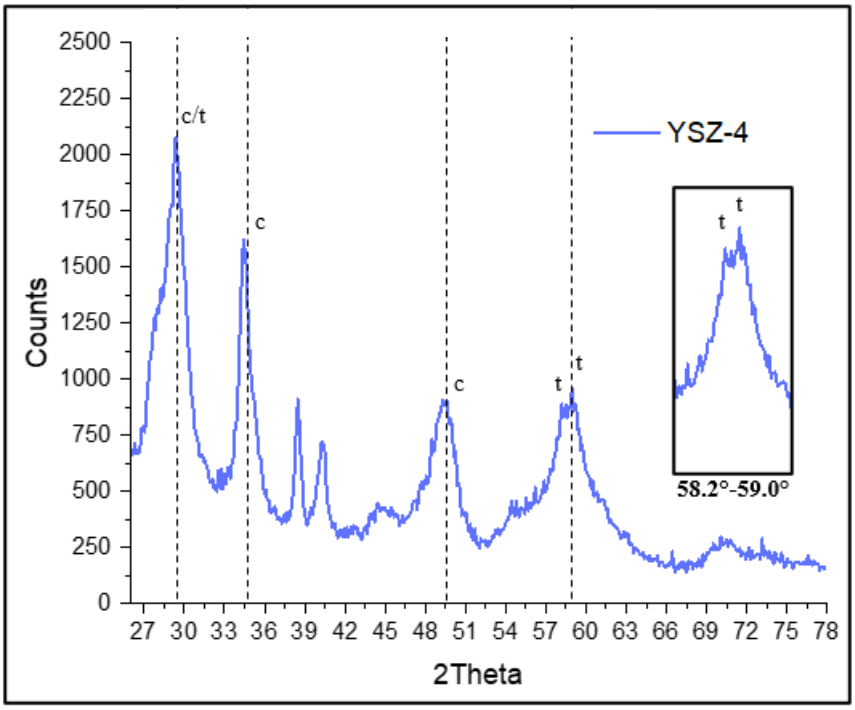

Figure 3.1-12 - XRD spectrum of YSZ-4

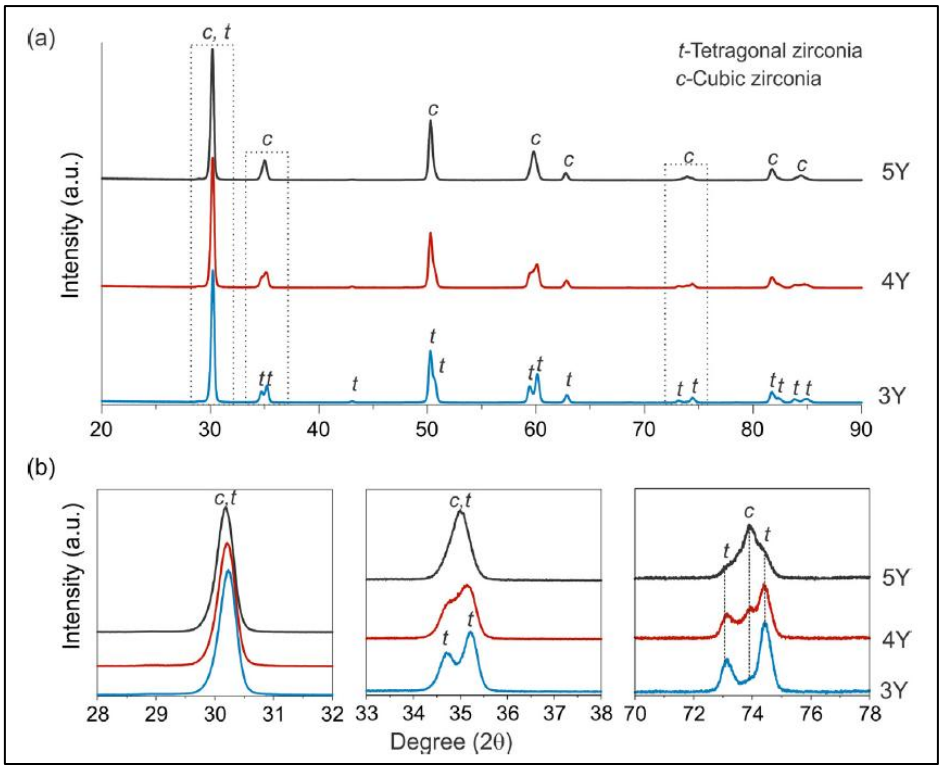

Figure 3.1-13 - XRD patterns of as-sintered samples. The characteristic peaks of cubic zirconia and tetragonal zirconia are indexed in the pattern of 5Y and 3Y, respectively. (b) Expanded view of 28–32, 33–38 and 70–78 diffraction 2h degrees [172].

Table 3-6 - Positions and phases of the YSZ-4 coating (screening phase)

2Theta	Zirconia Phase
29.36°	c/t
34.42°	c
49.27°	c
58.2-58.95°	t-t

3.1.9. Wear test

Wear tests are conducted on one plate of the deposited coating of the screening phase. The coating YSZ-4 was chosen as representative of the screening investigation. Objective of the test is to evaluate the response in terms of wear behaviour.

The wear tracks were collected as images through optical microscope and scanning electron microscope with the aim of detecting the track. Further EDS analysis could help to understand the wear behaviour.

- 0.25 N without toothpaste: no track was detected after the test.
- 1 N without toothpaste: a dark trace was observed on the surface. Further SEM-EDS investigations highlighted significant presence of calcium, potassium and magnesium. Lower concentrations of magnesium, silicon e sodium was detected. All these elements are attributable to the Hank's balanced salt solution. The other detected elements, such as oxygen and zirconium, were attributed to the surrounding coating (Figure 3.1-16).

- 1 N load with 3% of toothpaste: a slight wear trace was detected. Subsequent SEM investigations did not reveal any significant chemical variation through the back scatter electrons between the trace and the coating.
- 0.25 N with 10% of toothpaste: despite the lower load, the higher toothpaste concentration was the cause of a more noticeable trace compared to the previous case. Subsequent SEM-EDS analyses revealed areas of coating detachment along the trace, although not extensively. This is supported by EDS analysis, which revealed high concentrations of titanium substrate elements (titanium and aluminium) and lower concentrations of zirconium and oxygen (Figure 3.1-18).

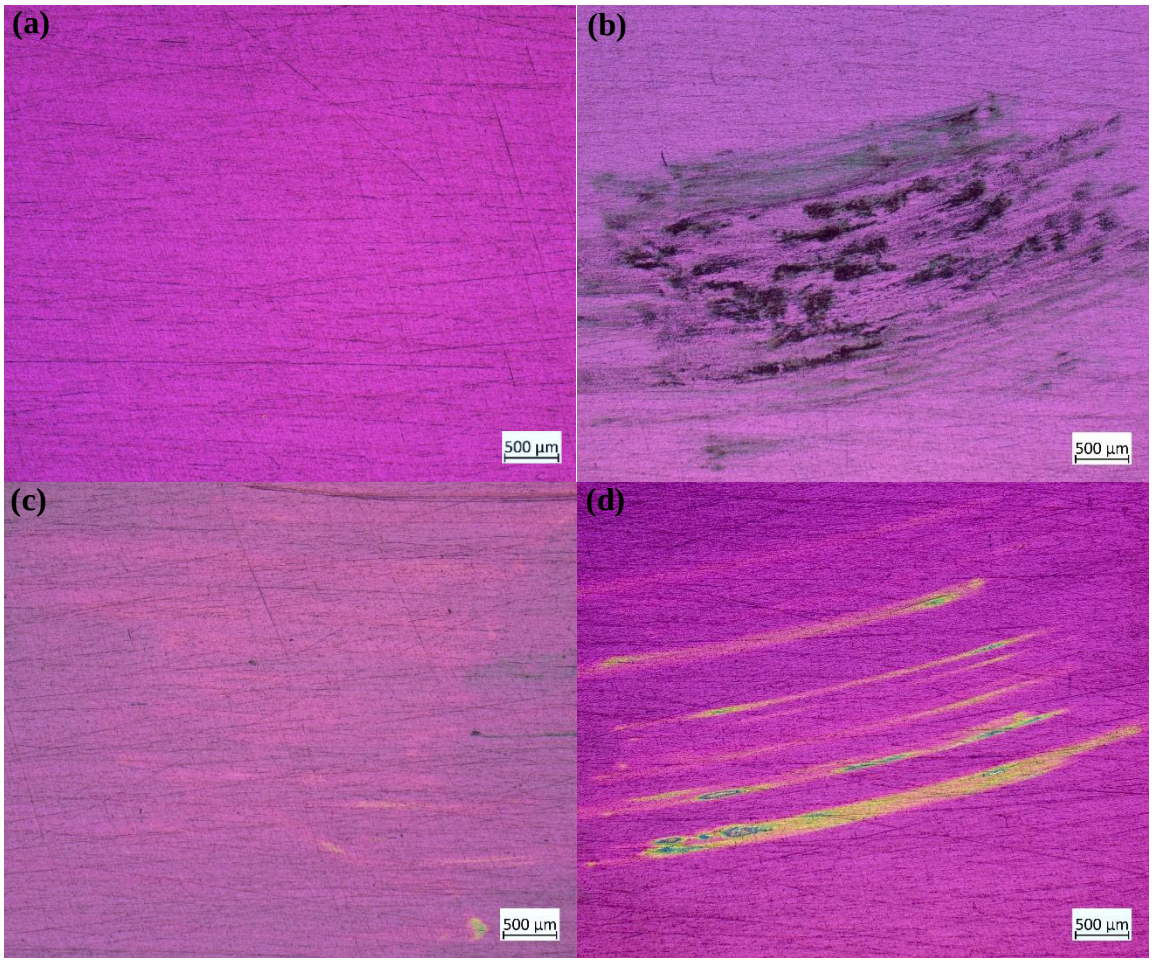

Figure 3.1-14 - optical microscope images of wear traces (a) 0.25 N without toothpaste; (b) 1 N without toothpaste; (c) 1 N with 3% of toothpaste and (d) 0.25 N with 10% of toothpaste.

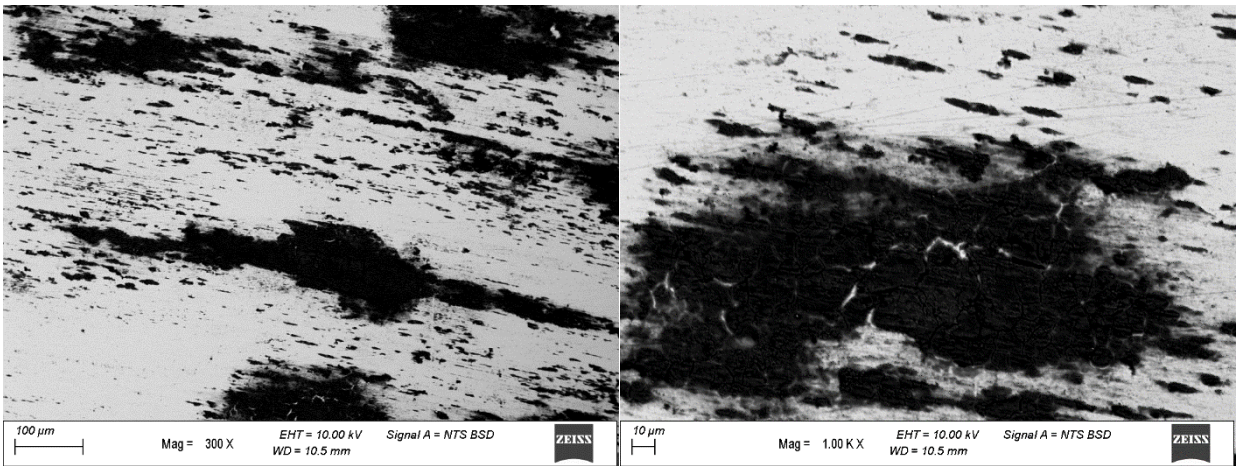

Figure 3.1-15 - BSE images of the trace after the application of 1 N without toothpaste.

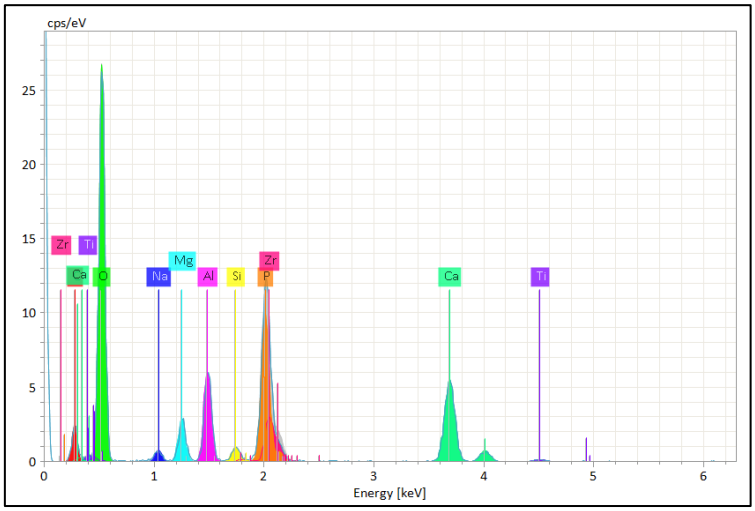

Element	Mass Norm. [%]	Atom [%]
	100,00	**100,00**
Oxygen	47,09	62,96
Calcium	17,77	9,49
Phosphorus	11,13	7,69
Zirconium	8,91	2,09
Carbon	5,90	10,51
Aluminium	4,84	3,84
Magnesium	2,10	1,85
Silicon	0,85	0,65
Titanium	0,76	0,34
Sodium	0,64	0,60

Figure 3.1-16 – EDS analysis of the trace after the application of 1 N without toothpaste.

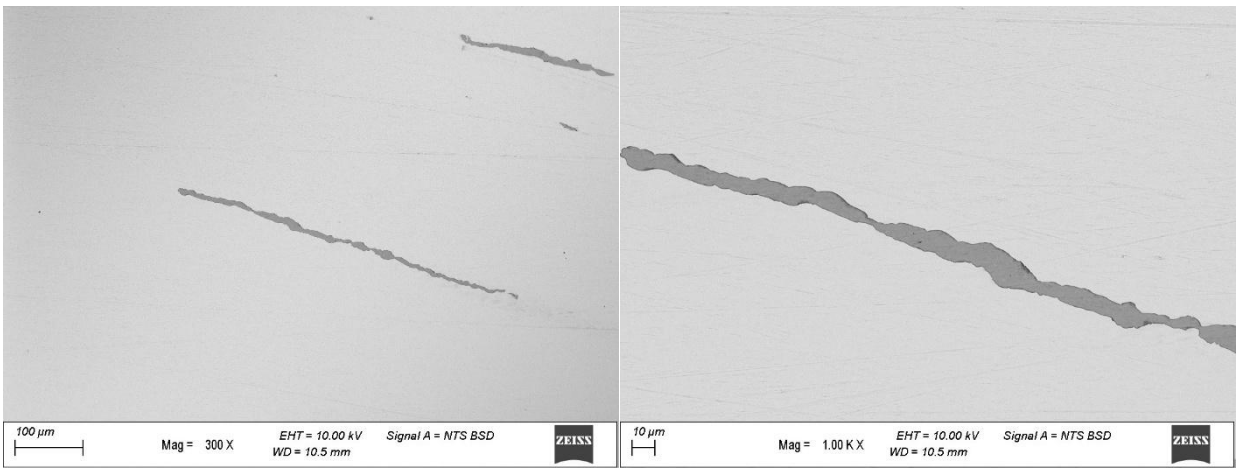

Figure 3.1-17 - BSE images of the trace after the application of 0.25 N with 10% of toothpaste.

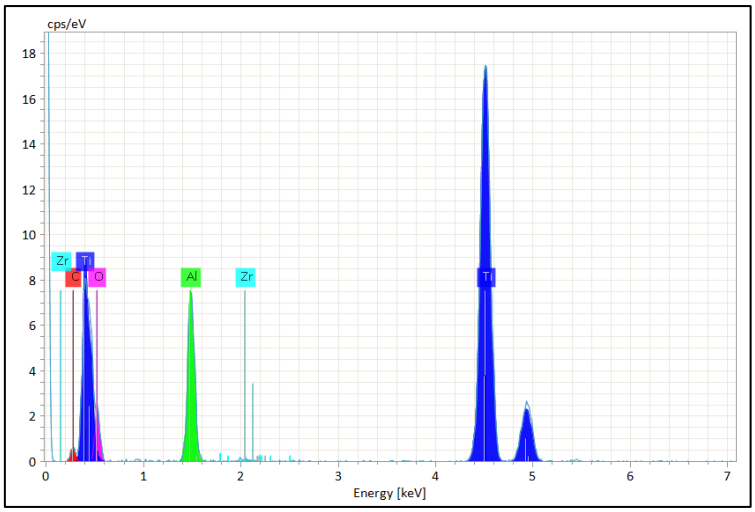

Element	Mass Norm. [%]	Atom [%]
	100,00	**100,00**
Titanium	86,95	72,82
Oxygen	7,86	19,69
Aluminium	4,97	7,39
Zirconium	0,22	0,10
Carbon	0,00	0,00

Figure 3.1-18 - EDS analysis of the trace after the application of 0.25 N with 10% of toothpaste.

3.1.10. Conclusions

During the screening phase, YSZ coatings were successfully deposited with defect-free surfaces and cross-sections, as confirmed by SEM analyses. The produced coatings exhibited thicknesses ranging from 150 nm to 600 nm, which is representative of the type of thin film produced using the PVD-PECVD technique, i.e. oxide layers deposited by reactive sputtering with the risk of target poisoning. This low thickness significantly affected nano-hardness measurements because, according to ISO 14577, the coating thickness should be at least ten times the indentation depth. Similarly, the roughness evaluation remained comparable to that of the bulk material, with average values between 0.3 µm and 0.5 µm.

A colorimetric analysis was performed to assess the appearance of the coatings. However, the applied method did not yield fully reliable quantitative data, likely due to the specific setup conditions. In particular, the use of D50 illumination combined with a 2° observer angle may have influenced the measured CIELAB coordinates, as thin-film interference effects can significantly alter colour perception based on the angles of incidence and observation.

The maximum wavelength corresponding to the perceptible colour can be expressed as:

$$\lambda_{MAX} = \frac{2\pi\,\Delta x}{\Delta\varphi}$$

where

$$\Delta x = n_C\, t_C + n_S\, t_S$$

with n and t representing the refractive index and thickness, subscripts C and S indicating the coating and the substrate, respectively, and

$$\Delta\varphi = \Delta\varphi = \frac{2\pi\, OPD}{\lambda_0}$$

Here, the optical path difference (OPD) between the light waves reflected at the air-coating and coating-substrate interfaces determines the phase shift and, it is expressed as:

$$OPD = OP_C - OP_T + \delta$$

with OP = $2nt$ and δ calculated according to Fresnel's law, which in this case study is taken as 1 due to the double inversion of the light path in the YSZ coating–titanium substrate system.

This formulation shows that λ_{MAX} is strongly dependent on the coating thickness. As the coating thickness increases during deposition, the OPD varies cyclically, leading to periodic changes in the observed colour, from blue to green to yellow to pink and then repeating.

Despite the limitations inherent the colorimetric method, visual inspection confirmed that two promising coatings, designated YSZ-2 and YSZ-4, exhibited a pink hue, which is known to minimize peri-implant discoloration [30]–[32]. Based on its favourable aesthetic impact, the YSZ-2 coating met both the aesthetic and technical requirements of clinical dental implantology and was therefore identified as a particularly promising candidate. The RF-PECVD deposition method was excluded due to noticeable variations in surface appearance, such as colour differences. Although both the YSZ-2 and YSZ-7 coatings were produced under identical deposition parameters, the application of RF-PECVD for YSZ-7 resulted in inconsistencies that suggest uncontrolled variables may be affecting the uniformity of the film, as indicated by irregular colour patterns, which are typically associated with variations in film thickness. (Figure 3.1-19).

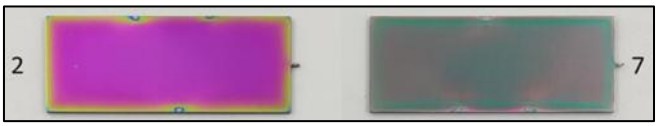

Figure 3.1-19 - Appearance of YSZ-2 and YSZ-7 coatings, with and without RF-PECVD, respectively.

A comprehensive structural investigation was carried out using several techniques to elucidate the phase composition of the coatings. The expected phase was the tetragonal one with an yttria content of around 4 mol.%, based on the use of a target containing 7 mol.% yttrium [175].

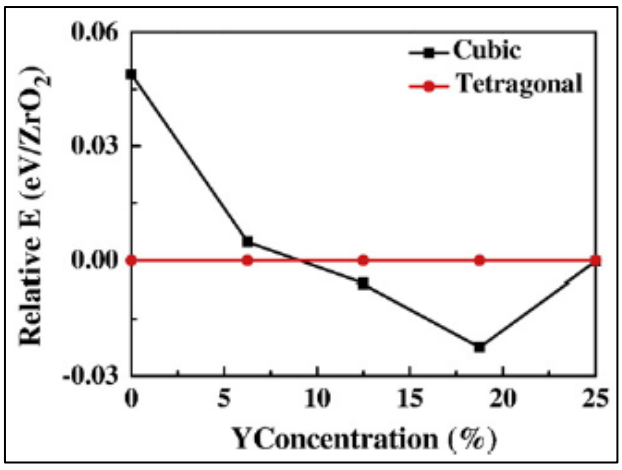

Figure 3.1-20 - Relative energy of cubic and tetragonal YSZ vs. Y concentration. The tetragonal phase is set as the reference of zero energy [175].

Energy-dispersive X-ray spectroscopy (EDS) revealed an yttrium concentration of approximately 4.5 wt.%, around 4 mol.%, which is lower than the nominal target concentration. However, since EDS is semi-quantitative analysis, more reliable insights were obtained from X-ray diffraction (XRD) analysis.

The XRD results revealed the presence of both cubic and tetragonal phases. In particular, the YSZ-4 coating, used as a reference among the eight coatings, exhibited an yttria content of about 4 mol.%, which is in good agreement with the expected composition, especially considering that the yttrium content in the target is near the level required to produce the cubic phase. Raman spectroscopy provided an interesting observation detecting predominantly the cubic phase and based on peak evaluations, suggested an yttria concentration of 13 mol.%. This unexpectedly high value, typically achieving with a target containing around 14 mol.% yttria, is hypothesized to result from the deposition system. Unlike small-scale magnetron sputtering setups, the industrial system used in this study features a significantly larger target-to-substrate distance. Consequently, sputtered atoms undergo numerous inelastic collisions that lower their energy before reaching the substrate. The reduced kinetic energy impedes atomic rearrangement during film growth, preventing the coating from reaching equilibrium and promoting the formation of various defects, notably oxygen vacancies, which may affect the optical properties of the film, potentially influencing colour variations. Literature indicates that, during magnetron sputtering, the relative energy of the cubic phase decreases compared to that of the tetragonal phase when the oxygen vacancy concentration exceeds 3 at.% [176], [177]. Therefore, the extracted value of 14 mol.% essentially not only the yttria content but also the contribution of oxygen vacancies that alter the vibrational modes detected by Raman analysis. Additionally, the ultrathin coating may be characterized by amorphous fractions or a distorted lattice structure, which can also influence the observed vibrational characteristics.

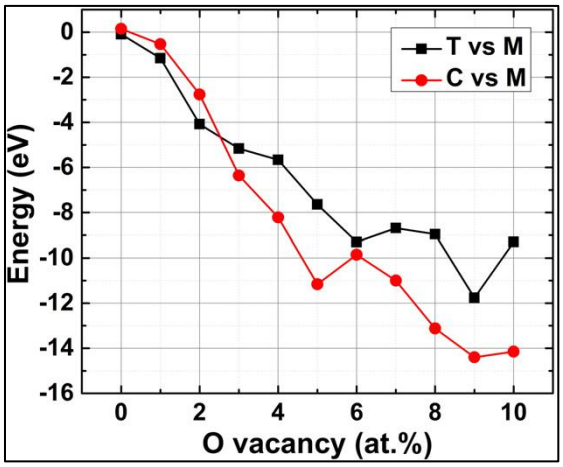

Figure 3.1-21 - Influence of O vacancies on the phase constitution [177].

Mechanical performance was assessed through scratch and wear tests to simulate in-service loads on abutments. Although the maximum force applied to an abutment in vivo is about 1 N, typically only reached when the gum is receded or compromised, scratch tests demonstrated that all coatings exhibited good adhesion, with critical loads well above 1 N. Notably, coatings YSZ-1, YSZ-3, and YSZ-5 did not show total delamination, while for the others, delamination initiated at loads around 16 N, significantly higher than the clinical forces.

Customized wear tests, designed to simulate three months of abutment-toothbrush contact, a scenario especially relevant in cases of periodontal disease, indicated that no wear occurred under low loads; however,

in the presence of a 10% toothpaste solution, some delamination was observed. Overall, the mechanical behaviour of the deposited coatings was deemed satisfactory.

Based on these comprehensive screening results, the YSZ-2 plate was selected as the reference for the subsequent optimization phase, and its deposition parameters, detailed in Table 3-7, were adopted as the baseline for further refinement.

Table 3-7 – MS deposition – ZrO adopted for the YSZ-2 coating.

STEP	Time	Temperature	O2 gas flow	Ar gas flow	He gas flow	Magnetron Sputtering (MS)					RF potential
						Current	Potential	Tension	Frequence	duty cycle	
	[s]	[°C]	[sccm]	[sccm]	[sccm]	[A]	[kW]	[V]	[kHz]	[%]	[W]
YSZ 2 plate	**7200**	180	**60**	500	**0**	24 (monopulsed)	6	**400**	80	80	**0**

3.2. Yttria-Stabilized Zirconia coatings – optimization phase

3.2.1. Macroscopic observations

Variations in colour were observed in the YSZ coatings deposited during the optimization phase, as shown in Figure 3.2-1.

The YSZ-9 and YSZ-10 coatings were excluded from evaluation due to issues encountered during their deposition cycles.

Since the objective was to achieve pink or yellow hues to minimize peri-implant discoloration [30]–[32], the YSZ-14 and YSZ-16 coatings emerged as the most promising candidates, exhibiting distinct yellow and pink coloration, respectively.

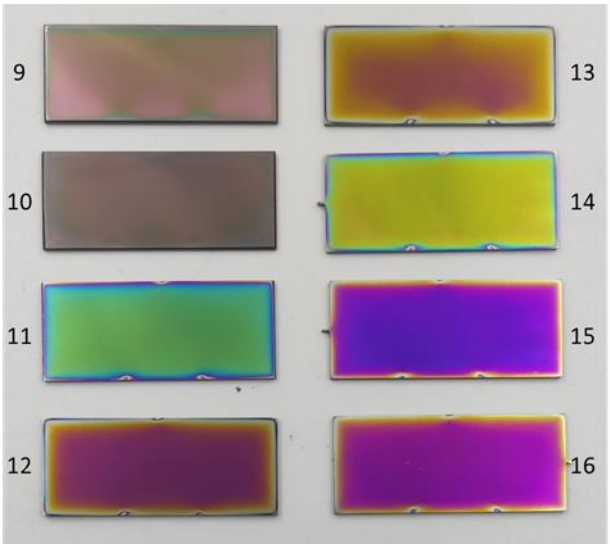

Figure 3.2-1 - Appearance of YSZ plates of the optimization phase.

3.2.2. Electron Microscopy observations

Scanning electron microscopy (SEM) was conducted on the coating surface to ensure that the characteristics established during the optimization phase are maintained. The analysis reveals that all deposited coatings exhibit a homogeneous and defect-free surface. In particular, Figure 3.2-2Figure 3.1-2 showcases an image captured using the SE detector providing a detailed view of the surface morphology of the YSZ-16 coating, which is representative of the overall quality observed across all eight coatings deposited.

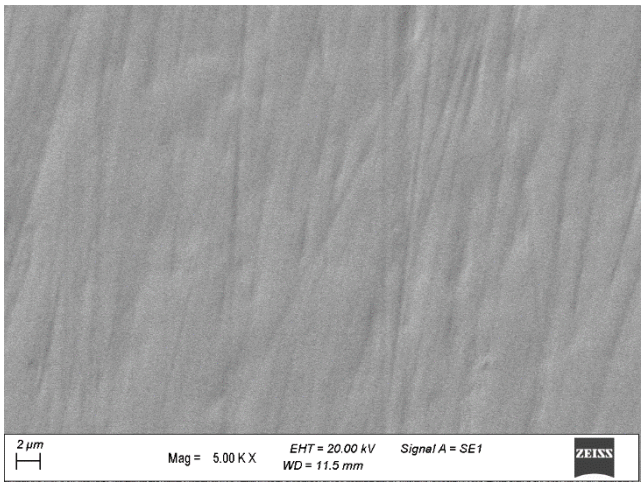

Figure 3.2-2 - SEM image through SE detector of YSZ-16

EDS spectra were collected from each coating surface to quantify the concentrations of the element within the coatings. Consistent with the findings from the screening phase, the EDS analysis detected the presence of zirconium, oxygen, yttrium, argon, and hafnium in all the coatings. The specific concentrations of these elements are detailed in the graphs shown in Figure 3.2-3.

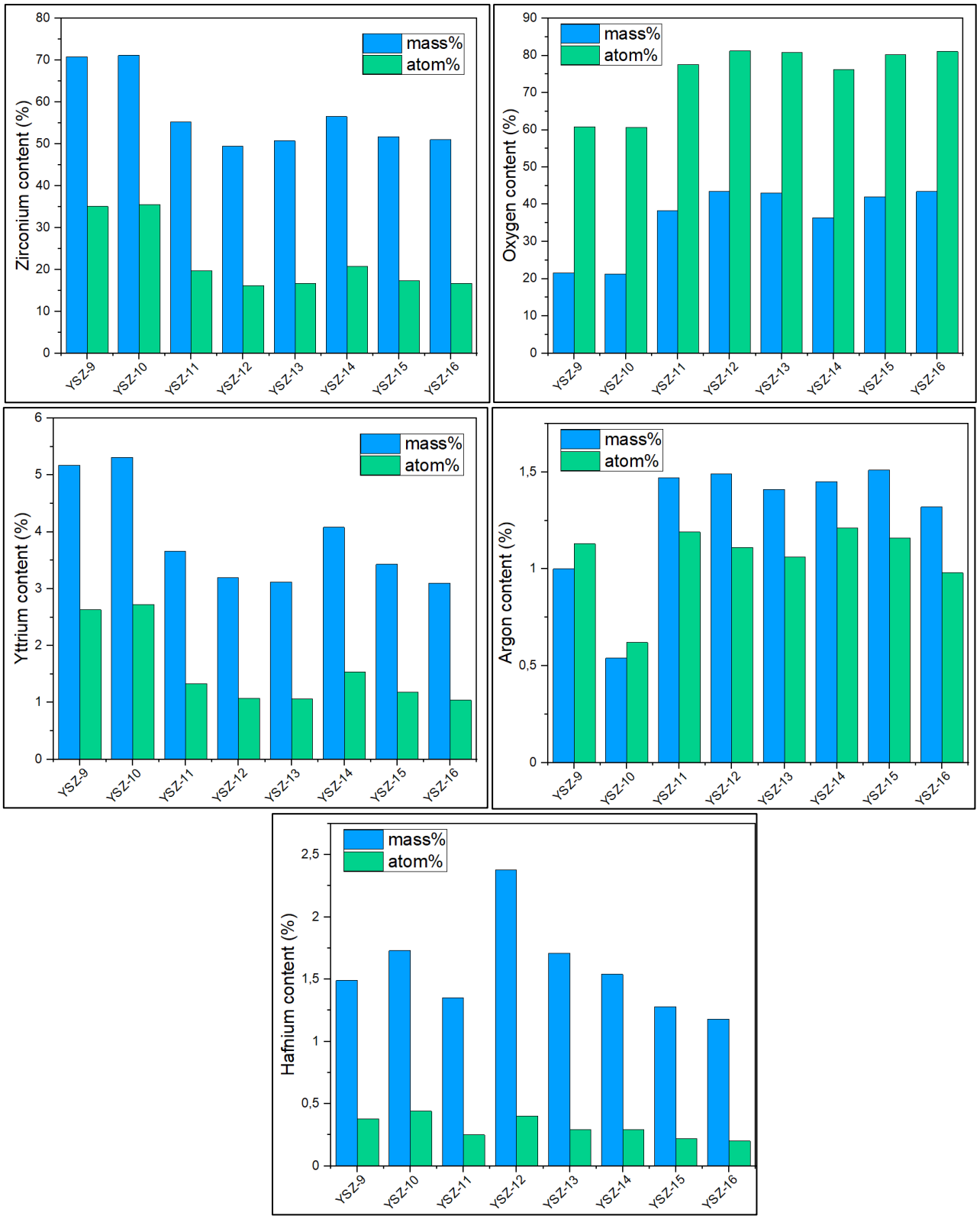

Figure 3.2-3 - Element contents of the YSZ coatings deposited in the optimization phase through EDS analysis.

The average weight percentages of zirconium (Zr), yttrium (Y), and oxygen (O) in the sample are 70 wt.%, 5 wt.%, and 20 wt.%, respectively, for the coatings YSZ-9 and YSZ-10. In contrast, the other coatings exhibited average weight percentages 50 wt.% for zirconium, 3.5 wt.% for yttrium, and 40 wt.% for oxygen. Additionally, for the first two depositions (YSZ-9 and YSZ-10), hafnium and argon were found in average concentrations of 1.5 wt.% and 0.7 wt.%, respectively. For the remaining coatings, both hafnium and argon

were present at an average concentration of 1.5 wt.% each. When comparing these results to the expected values of 68 wt.% for zirconium, 5 wt.% for yttrium, and 25 wt.% for oxygen, it becomes evident that the first two depositions (YSZ-9 and YSZ-10) have a lower oxygen content. This deficiency in oxygen is insufficient to stabilize both the ZrO_2 and Y_2O_3 phases, which are crucial for the desired coating properties. On the other hand, the other six depositions exhibit an excess of oxygen compared to the stoichiometric condition. This analysis can be further refined by evaluating the stoichiometric ratios under both conditions. For the coatings YSZ-9 and YSZ-10, the average weight concentrations of zirconium, yttrium, and oxygen are 72.7 wt.%, 5.3 wt.%, and 22 wt.%, respectively. These concentrations correspond to mole amounts of 0.8 for zirconium, 0.06 for yttrium, and 1.38 for oxygen. For the formation of zirconium dioxide (ZrO_2), two moles of oxygen are required for each mole of zirconium. The current ratio of oxygen to zirconium is 1.7, which is lower than the stoichiometric requirement, indicating a deficiency in oxygen relative to zirconium. In contrast, for the formation of yttrium oxide (Y_2O_3), 1.5 moles of oxygen are needed for each mole of yttrium. The current ratio of oxygen to yttrium is 23, which is significantly higher than the stoichiometric requirement, suggesting an excess of oxygen relative to yttrium. For the other six depositions, the average weight concentrations of zirconium, yttrium, and oxygen are 54.1 wt.%, 3.5 wt.%, and 42.3 wt.%, respectively. These concentrations translate to mole amounts of 0.6 for zirconium, 0.04 for yttrium, and 2.65 for oxygen. The ratio of oxygen to zirconium is 4.5, which is higher than the stoichiometric requirement, indicating an excess of oxygen relative to zirconium. Similarly, the ratio of oxygen to yttrium is 67, which is significantly higher than the stoichiometric requirement, indicating a substantial excess of oxygen relative to yttrium. This surplus of oxygen could potentially lead to different phase compositions. This necessitates further evaluation to ensure that these variations do not negatively affect the performance and stability of the coatings.

Also, for the optimization phase, some of these coatings was subjected to FEG-SEM analysis to observe their cross-section at higher resolution. The coatings chosen for this examination are YSZ-12, YSZ-14, and YSZ-16. Although the EDS results were unsatisfactory, additional observations were carried out on YSZ-9 to examine the condition of the coating in cross-section. The FEG-SEM analysis revealed variations in the thickness of the YSZ-12, YSZ-14 and YSZ-16 coatings, which ranged from 150 nm to 250 nm. Additionally, the coatings appeared to be homogeneously deposited, with no visible defects along the entire cross-section. The YSZ-9 coating demonstrates a greater thickness, approximately 800 nm, and an incoherent layer deposition, with three distinct layers clearly observed. This increased thickness can be attributed to the deposition conditions, which were more metallic condition, resulting in a higher deposition rate compared to subsequent coatings. The brighter intermediate layer could correspond, in fact, to a Zr-rich/oxygen-poor area. Furthermore, these three coatings were also analysed through FIB instrument for evaluating their microstructure in greater detail. Figure 3.2-5 shows the structure of all the coatings, highlighting a nanostructure and a columnar structure, with no visible defects.

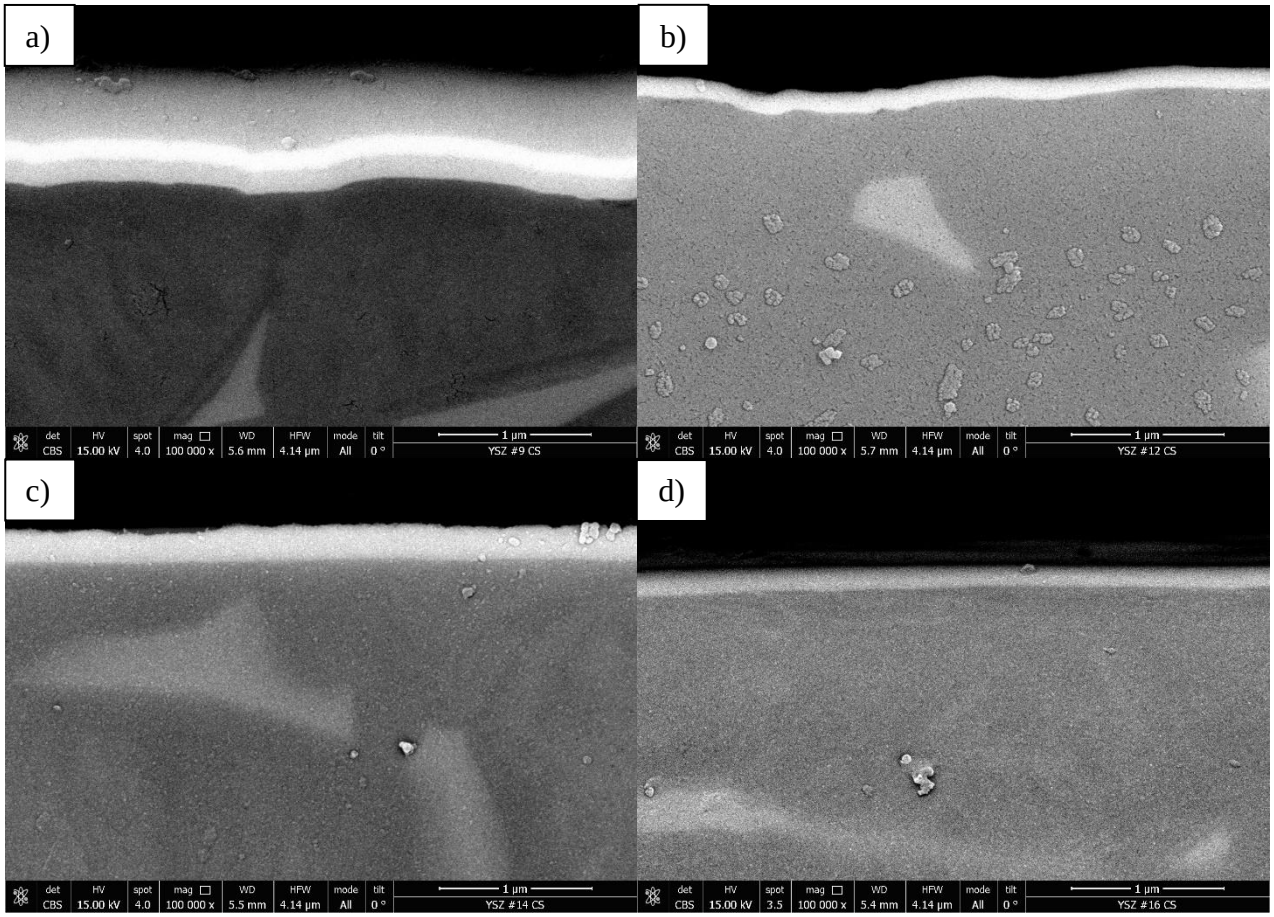

Figure 3.2-4 - FEG-SEM observation of cross-sectioned YSZ samples: a) YSZ-9; b) YSZ-12; c) YSZ-14 and d) YSZ-16.

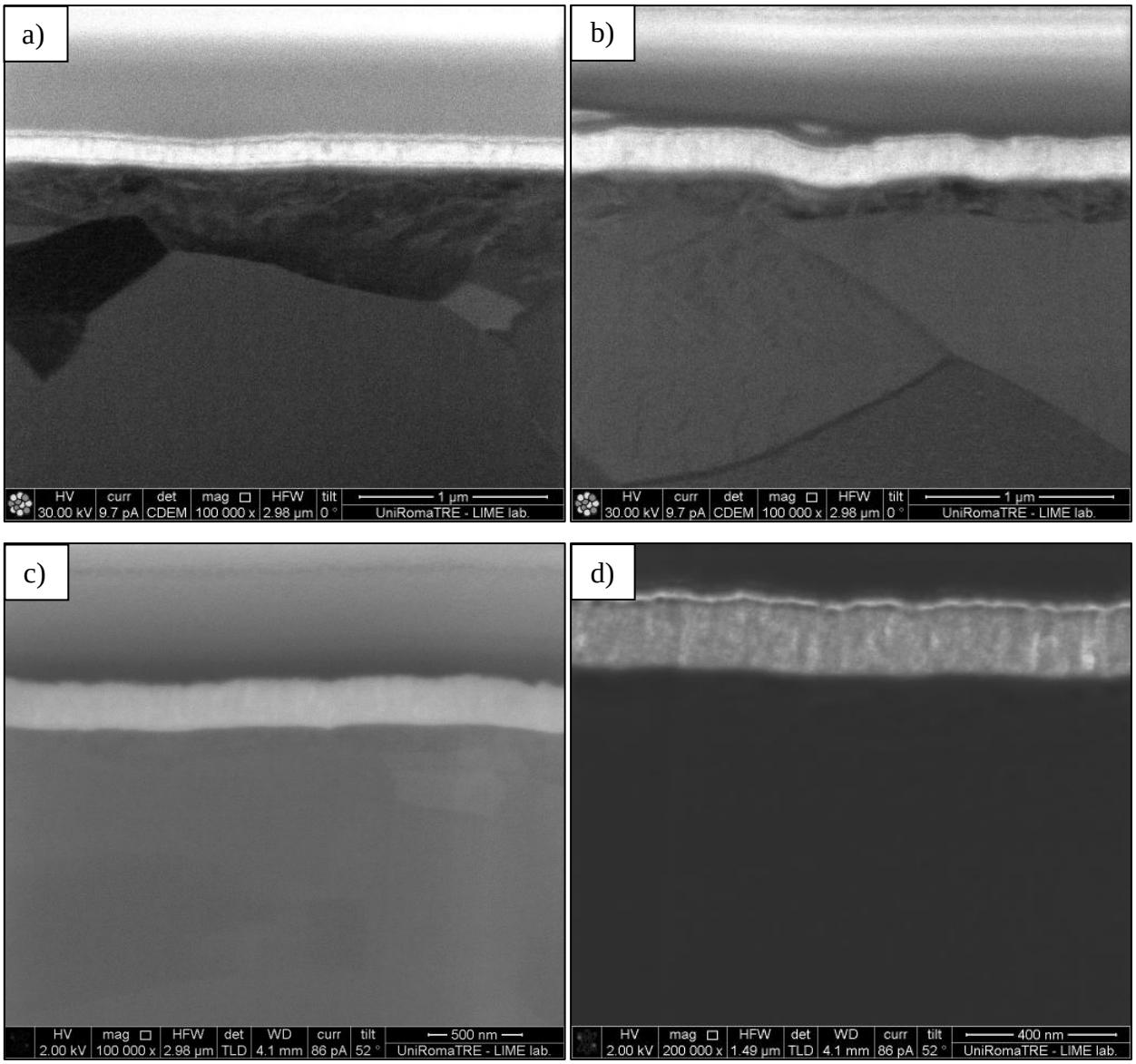

Figure 3.2-5 - FIB-SEM observation of cross-sectioned YSZ samples: a) YSZ-12; b) YSZ-16; c) YSZ-14 at 100000 x; d) YSZ-14 at 200000 x.

3.2.3. Roughness measurements

The results of the roughness measurements on the YSZ coating, which was deposited during the optimization phase, indicate no significant variation compared to the values recorded on the bare titanium substrate. This outcome was anticipated, given the deposition of a thin film. The recorded roughness values averaged around 0.022 µm. As explained in the previous section about the screening phase, this low roughness value is crucial for meeting the surface finishing requirements when the coating is exposed to the oral environment. A smooth surface is essential to prevent bacterial colonization and subsequent infection. All the roughness values are collected in Table 3-8.

Table 3-8 - Roughness measurements on YSZ coatings during optimization phase

	naked Ti plate		YSZ-coated Ti plate	
YSZ	**Average [um]**	**Std Dev [um]**	**Average [um]**	**Std Dev [um]**
9	0,043	0,001	0,043	0,002
10	0,025	0,002	0,024	0,002
11	0,045	0,003	0,046	0,002
12	0,047	0,003	0,048	0,004
13	0,045	0,002	0,046	0,002
14	0,043	0,001	0,042	0,001
15	0,044	0,003	0,044	0,003
16	0,043	0,002	0,046	0,002

3.2.4. Nano-hardness measurements

The nano-hardness values were extracted from all the Yttria-Stabilized Zirconia (YSZ) coatings deposited during the optimization phase at varying depths, extending up to 300 nm. To assess the influence of the substrate, the hardness values obtained from the Ti6Al4V alloy plate were used as a reference. Additionally, the hardness values of the biomedical-grade zirconia plate were adopted as a reference standard.

The results are collected in Figure 3.2-6, where two distinct groups can be observed: the YSZ-9 and YSZ-10 coatings exhibit higher and more consistent hardness values, approximately 11 GPa, across the depth range. In contrast, the other coatings display lower hardness values, ranging from 8 GPa to 6 GPa, as the depth increases from 100 nm to 300 nm. As previously discussed, the thickness of the coatings is crucial for accurate hardness assessment. The first two coatings, with a thickness of approximately 800 nm, provided more accurate hardness values, closer to those of the biomedical-grade zirconia. The other coatings, with thicknesses ranging from 150 nm to 250 nm, yielded hardness results that were less accurate and further from the reference zirconia plate.

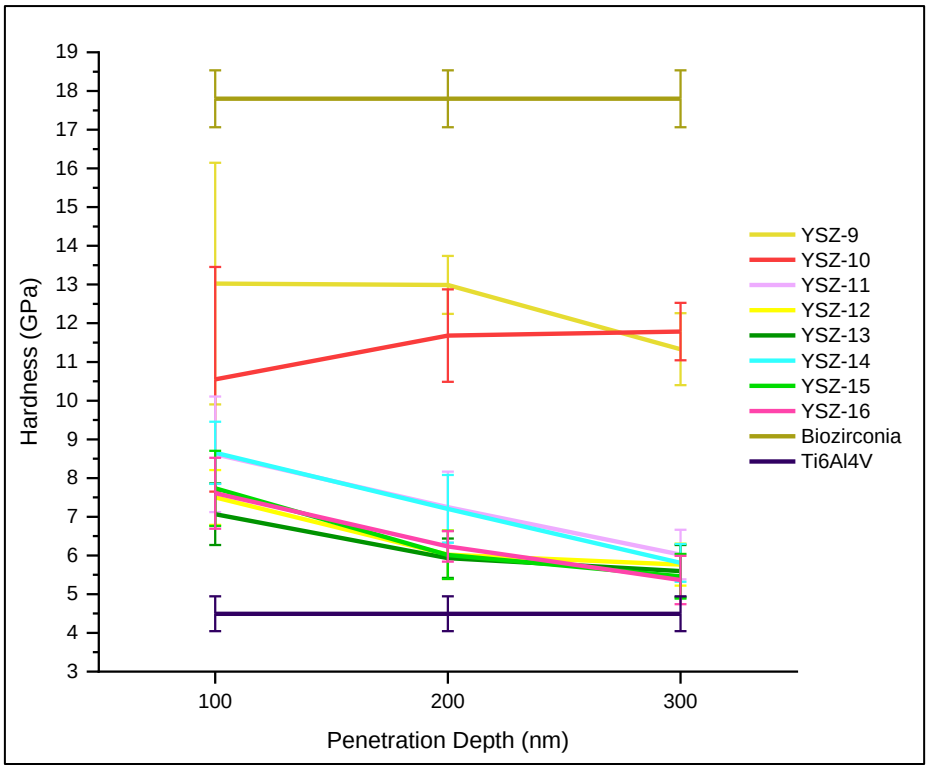

Figure 3.2-6 - Nano-hardness values of the YSZ coating deposited during the optimization phase.

3.2.5. Colorimetric analysis

The eight plates deposited during the optimization phase underwent colorimetric analysis. The CIELAB coordinates (L*, a*, and b*) are detailed in Table 3-9Table 3-2, and the ΔE* values were calculated for each plate using gingival values as a reference [30].

In the screening phase, the YSZ-2 plate was identified as having the most favourable appearance, exhibiting a pink colour. This selection was based on the observation that pink and gold colours tend to cause the least peri-implant discoloration [30], [31], meeting the clinical requirements for aesthetic outcomes in implantology.. During the optimization phase, initial visual inspections validated the results for plates YSZ-14 and YSZ-16, which displayed yellow and pink colours, respectively. However, the extrapolated colorimetric coordinates did not support these visual observations, as the calculated ΔE* values were significantly higher than the threshold value of 8.74, which is recognized as the limit for distinguishing mucosal colour differences between an optimal match and those perceptible to the human eye. Conversely, the lower ΔE* values were associated with plates that exhibited the least favourable visual appearance (YSZ-9 and YSZ-10). This discrepancy underscores the limitations of the colorimetric analysis in accurately reflecting the effective results.

Table 3-9 - CIELAB coordinates of the eight plates of the optimization phase.

YSZ plate	L*	a*	b*	ΔE
YSZ-9	58.4	7.0	9.1	17.7
YSZ-10	46.6	3.0	8.4	20.8
YSZ-11	59.9	-39.3	36.6	64.3
YSZ-12	24.3	41.0	-20.9	50.5
YSZ-13	31.0	41.6	6.9	30.4
YSZ-14	60.8	1.9	59.6	47.9
YSZ-15	14.5	40.8	-57.2	85.0
YSZ-16	19.8	44.4	-32.4	62.9

3.2.6. Scratch test

The scratch tests were also conducted during the optimization phase to evaluate the adhesion quality of the YSZ coatings on the Ti6Al4V bulk substrate. For each coating, at least two scratch tests were performed to ensure the reliability of the results. In Table 3-10, one scratch track for coating was collected. The critical loads recorded during this phase are consistent with those obtained during the screening phase, allowing for a direct comparison of the values.

The initial type of damage, labelled as Lc1, corresponds to the formation of semicircular microcracks along the transversal section of the track. The Lc1 values ranged from 3 N to 6 N, with the YSZ-16 coating exhibiting the lowest value (Figure 3.2-8 (a)) and the YSZ-10 coating showing the highest. As the load increased, these microcracks began to extend towards the edge of the track, labelled as Lc2. This extension occurred at loads ranging from 4 N to 8 N. Among the coatings, YSZ-11 and YSZ-12 ((Figure 3.2-8Figure 3.2-7 (b)) exhibited the minimum Lc2 values, while YSZ-13 showed the maximum.

Partial delamination, referred to as Lc3, became observable at load values starting from approximately 8 N for the YSZ-12 coating (Figure 3.2-8 (c)) and extended up to 18 N for the YSZ-13 and YSZ-14 coatings. In this phase, total delamination averaged 16N and was detectable in the YSZ-9 (Figure 3.2-8 (c)) and YSZ-12 coatings, as well as in one of the two repetitions for the YSZ-11 coating. Additionally, the YSZ-16 coating exhibited Lc4 in one of the two repetitions at a load of approximately 20N.

Table 3-10 - panorama view of the scratch tracks – campaign (optimization phase)

YSZ-9 V=400V t=7h, RF off	
YSZ-10 V=420V t=7h, RF off	
YSZ-11 V=400V t=2h, RF off	
YSZ-12 V=385V t=2.5h, RF off	
YSZ-13 V=390V t=2.5h, RF off	
YSZ-14 V=385V t=2h, RF off	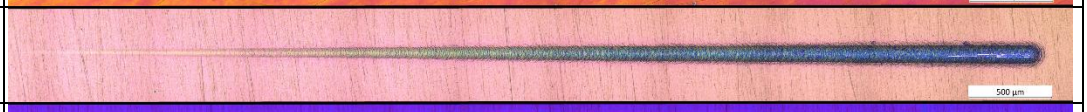
YSZ-15 V=385V t=1.5h, RF off	
YSZ-16 V=380V t=1.5h, RF off	

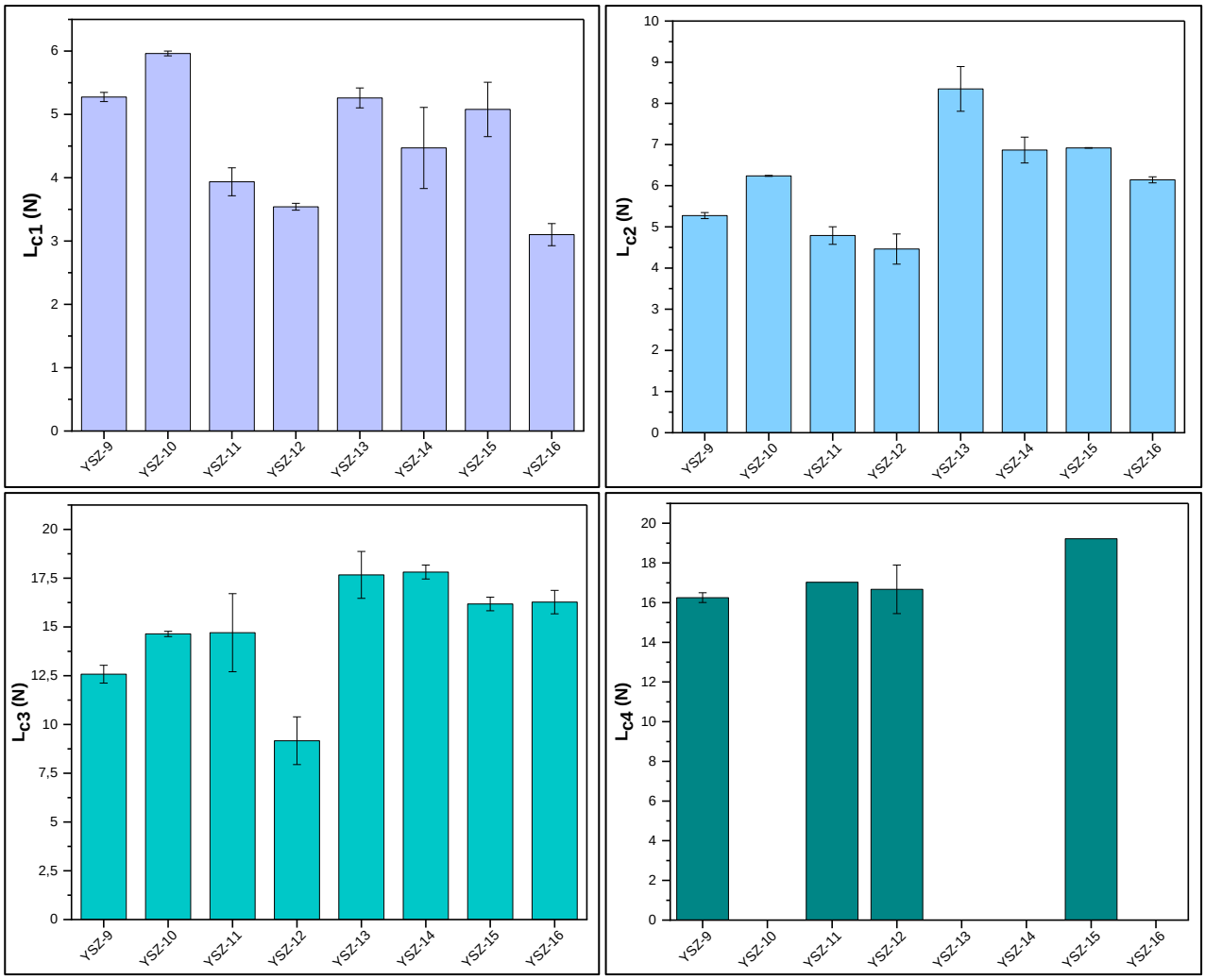

Figure 3.2-7 - Critical load values (optimization phase)

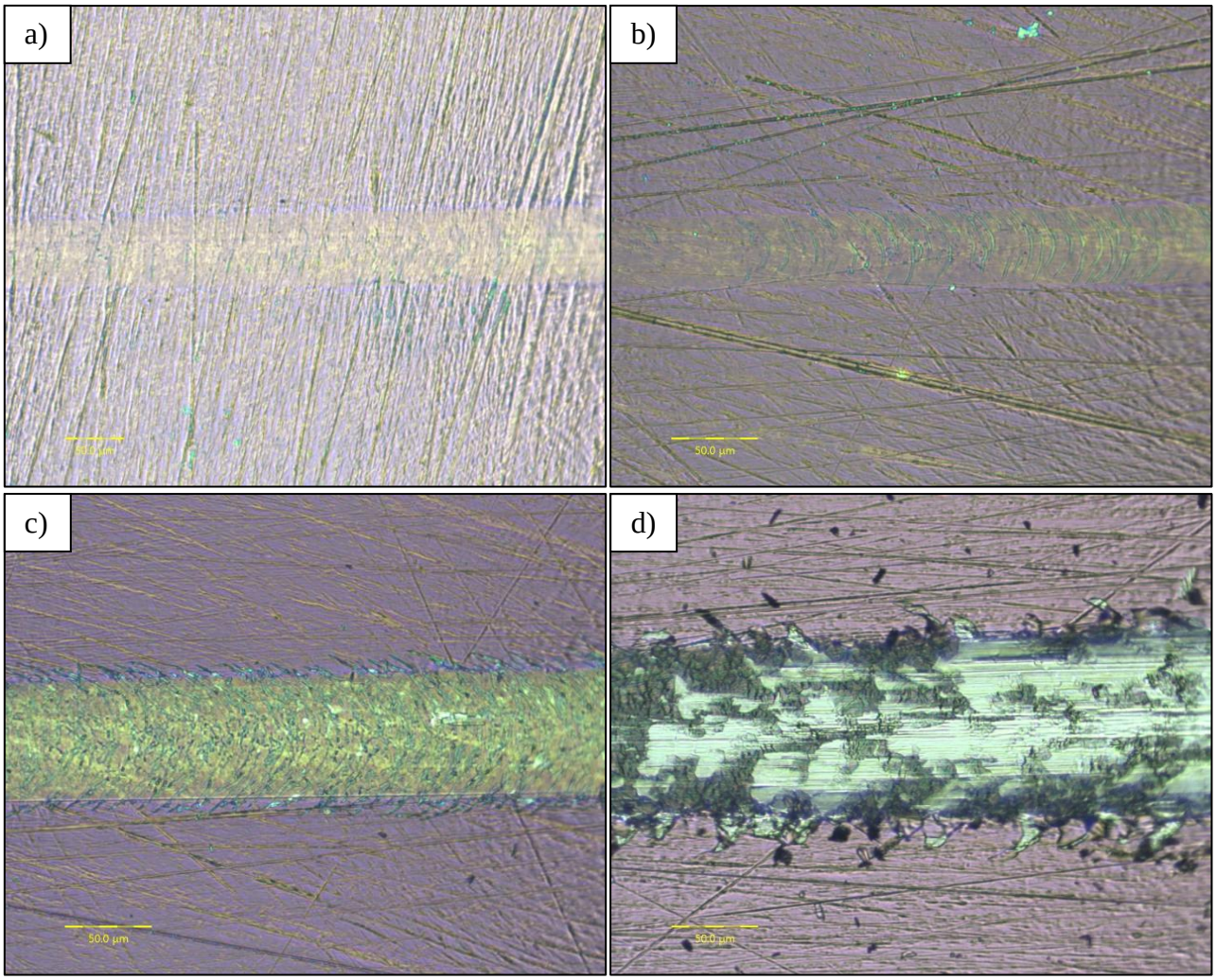

Figure 3.2-8 - critical load image examples. a) Lc1 (YSZ-16), b) Lc2 (YSZ-12), c) Lc3 (YSZ-12), d) and Lc4 (YSZ-9).

3.2.7. Raman analysis

Raman spectroscopy was also performed on the coatings deposited during the optimization phase to evaluate phase formation at this stage. As described in the section dedicated to the screening phase, different vibrational modes are related to the cubic and tetragonal phase. Particularly, the stretching mode corresponding to ~645/cm shows a crucial shift distinguishing the tetragonal from the cubic phase. The shift moves towards lower frequencies as the amount of the stabilizing agent Y_2O_3 increases and it is primarily attributed to changes in oxygen vacancies (O2-) and the consequent increase in binding strength [170].

Moreover, these observations are valid for the sintered zirconia as for the zirconia films, since no influence has been found regarding peak position shifting based on the production technology [178], [179]. Each phase of zirconia exhibited a specific Raman spectrum characterized by distinct peaks [169]. The peak at 150/cm was common to both the tetragonal and cubic phases. In contrast, the peaks at ~245/cm and ~460/cm were representative of the cubic and tetragonal phases, respectively. Finally, the peak at ~645/cm, characteristic of the tetragonal phase, shifted to ~600/cm in the cubic phase [170].

Spectra for all the YSZ coatings of the optimization phase are collected in Figure 3.2-9. Two groups of behaviour were observable. The YSZ-9 and YSZ-10 coatings exhibited peaks ~250/cm and ~590/cm

characteristic of the cubic phase, and the peak ~700/cm that can be attributed to the tetragonal phase. Additionally, a peak at 190/cm was detected and can be attributed to the monoclinic phase, rather than to a mixed oxide or the formation of substoichiometric zirconia (ZrOx) due to oxygen deficiency preventing the formation of ZrO2. The other coatings were characterized by peaks corresponding to the cubic phase: ~150/cm, ~250/cm and ~600/cm. Ultimately, YSZ-9 and YSZ-10 coatings appeared to be characterized by a distorted structure, which could be attributed to oxygen non-stoichiometry. In contrast, the other coatings are characterized by a cubic phase and, analysing the shift in the ~645/cm band in the Raman spectra and referencing the study [170], the Yttria content was approximately 22 wt. %.

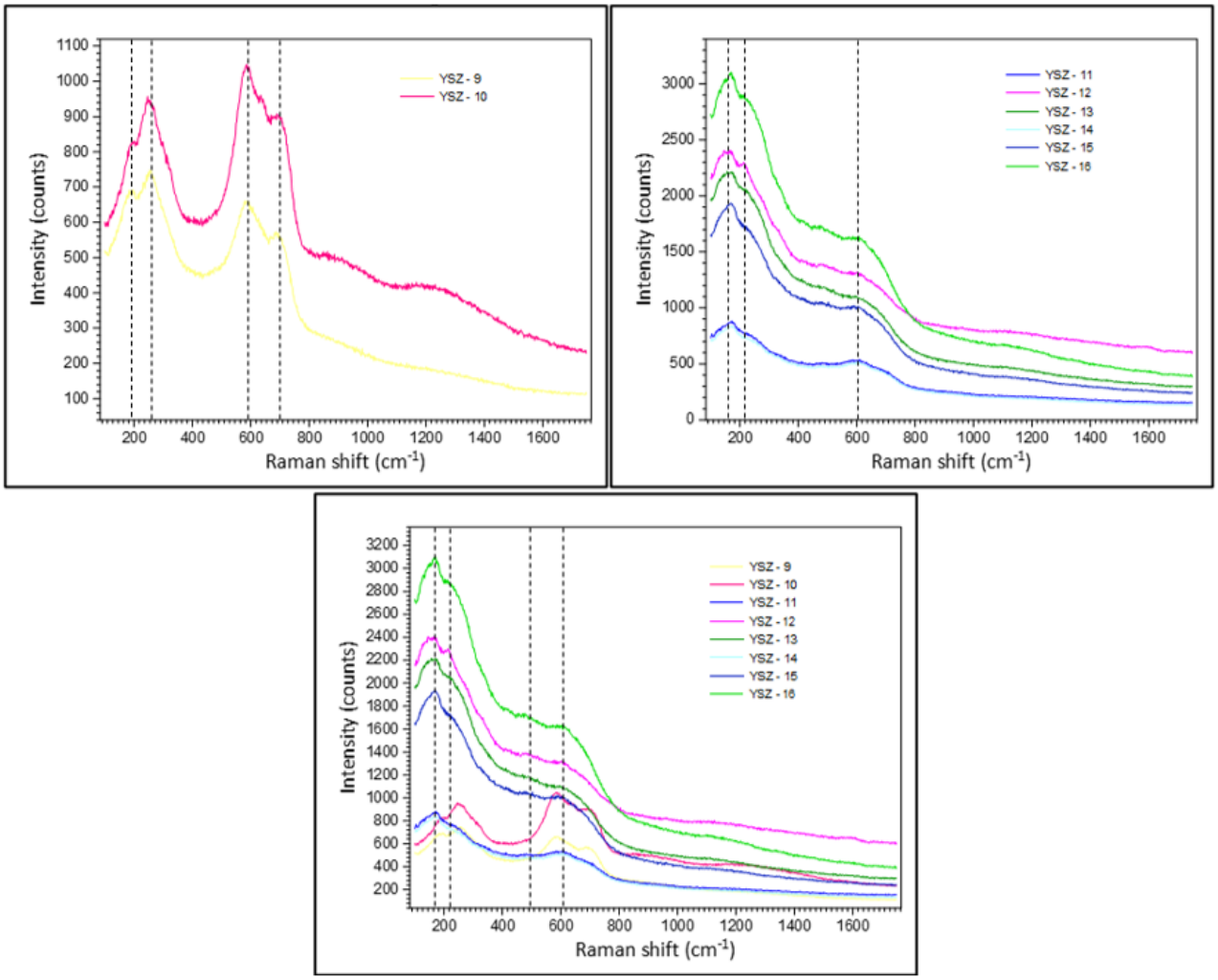

Figure 3.2-9 - Raman spectra collected for all the YSZ coatings of the optimization phase.

3.2.8. XRD analysis

X-ray diffraction (XRD) analysis was conducted during the assessment of the coatings deposited in the optimization phase. Three coatings of interest were tested: YSZ-12, YSZ-14, and YSZ-16. The XRD spectra for each coating are presented in Figure 3.2-10. To facilitate understanding of the differences between the coatings, a comparison graph has been included where the curves appear well overlapped.

The detected phases are cubic and tetragonal, as indicated by their respective diffraction peaks. Also in this phase the coatings exhibit pattern in accordance to that founded in literature [171]–[174].

To summarize, the diffraction peak at 30° is observed in both cubic and tetragonal zirconia phases. The other peaks correspond to the cubic phase when the yttria content is 5 mol.%. Conversely, they appear as double peaks of the tetragonal phase when the yttria concentration decreases to 3 mol. % [171], [172], [174]. Therefore, the yttria concentration of 4 mol.% represents a transitional condition where both cubic and tetragonal peaks may be observed.

The yttria concentration in the YSZ coatings is expected to be 4 mol.% because a zirconium target doped with 7 mol.% yttrium was selected for this study. The XRD spectra of the YSZ-12, YSZ-14 and YSZ-16 coatings confirm all the peaks reported in the literature. Particularly, the cubic/tetragonal one at 30°, the double tetragonal peak at 35°, and the single cubic peaks at 50° and 60°. Details of the peak positions and the related phases are summarized in Table 3-11.

Additional peaks correspond to grade 5 titanium which are characteristic of the substrate. Notably, the monoclinic phase is absent in the realized structure, as no corresponding peaks were detected in the XRD analysis.

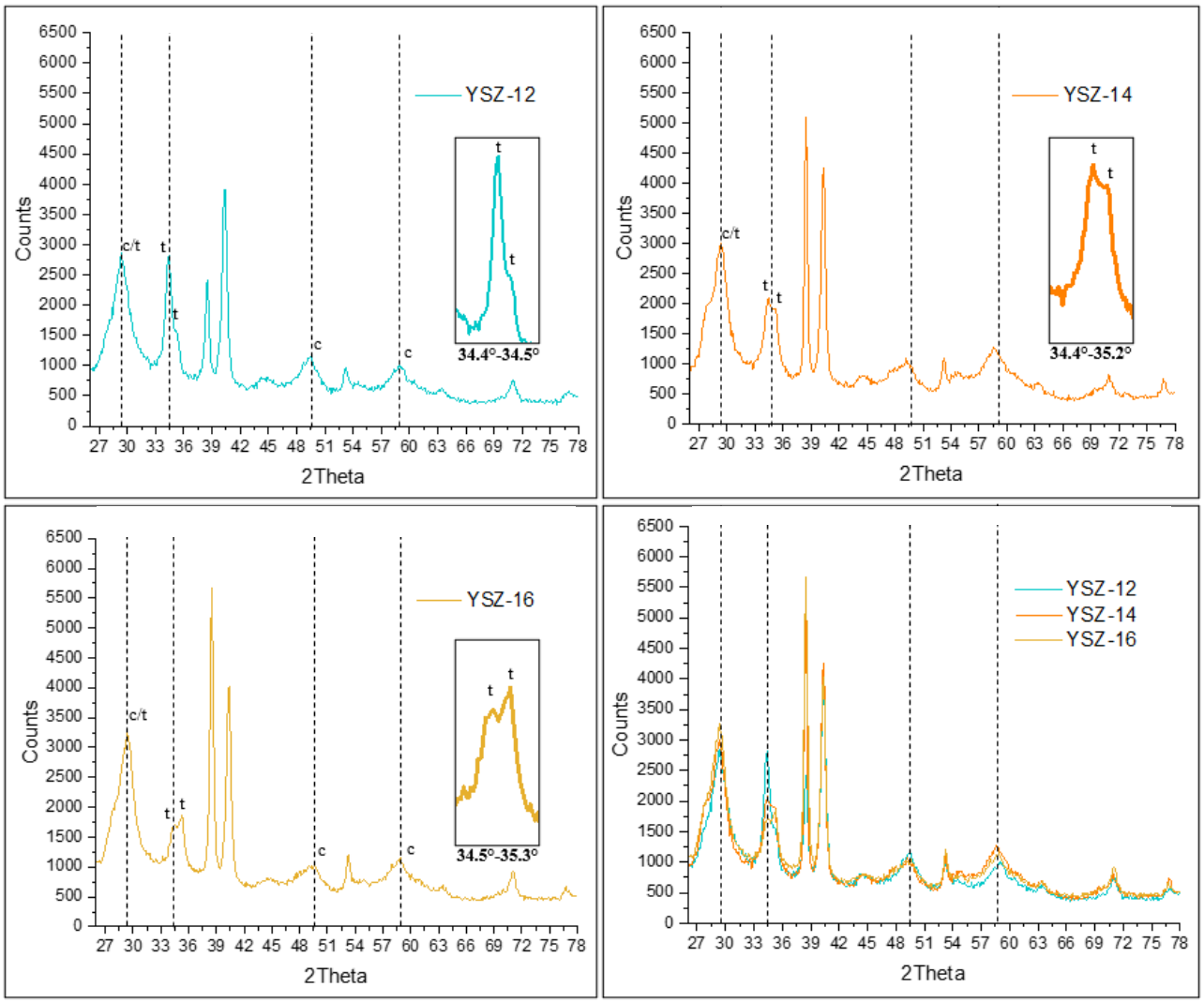

Figure 3.2-10 - XRD spectra of YSZ-12, YSZ-14 and YSZ-16 (optimization phase)

Table 3-11 - Positions and phases of YSZ coatings during the optimization phase.

Peak number	YSZ-12		YSZ-14		YSZ-16	
	2Theta	phase	2Theta	phase	2Theta	phase
1	29.36°	c/t	29.36°	c/t	29.36°	c/t
2	34.42°-34.53°	t-t	34.42°-35.19°	t-t	34.53°-35.3°	t-t
3	49.6°	c	49.16°	c	49.6°	c
4	58.95°	c	58.62°	c	58.84°	c

3.2.9. Low temperature degradation testing

Raman spectroscopy was conducted on the YSZ-14 coating following exposure to low-temperature degradation. The YSZ-14 coating was the subject of this investigation. The primary objective was to verify the presence of the monoclinic phase after aging cycles of 1 hour and 5 hours. The resulting spectra, presented in Figure 3.2-11, showed no detectable differences in peak positions. Consequently, the monoclinic phase was

not observed, even after 5 hours of aging, which corresponds to an equivalent exposure of 75 years in the oral environment [39].

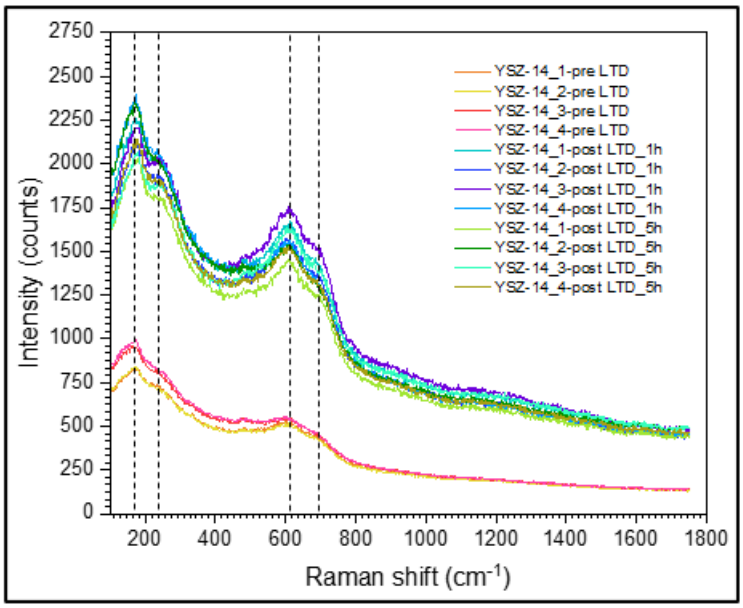

Figure 3.2-11 - Raman spectra collected for the YSZ-14 in pre-LTD condition and subjected to LTD after 1h and 5h.

3.2.10. Conclusions

During the optimization phase, several important issues emerged that required adjustments to the initial process. Although an initial hysteresis cycle was performed before the deposition runs of screening, it proved insufficient for the entire campaign. The first two deposition cycles of the optimization phase failed due to changes in the target behaviour caused by repeated oxidation cycles during deposition. To address this, an enhanced hysteresis cycle was implemented prior to each deposition run. This approach allowed for a clearer understanding of the evolution of the target behaviour and ensured that the correct deposition parameters were selected. As a result, coatings YSZ-9 and YSZ-10 did not meet the required parameters and did not yield the desired coating characteristics.

With the new approach in place, the deposition of the other six YSZ coatings was successful. SEM analyses confirmed that the surfaces and cross-sections were defect-free evidencing thickness values ranging from 150 nm to 250 nm, in accordance with the thickness of YSZ-2 reference established during the screening phase. During optimization, nano-hardness measurements and colorimetric analyses were repeated to verify the observations from the screening phase, and the results were effectively confirmed. Particularly, visual inspection identified the YSZ-14 and YSZ-16 plates as promising, as they exhibited yellow and pink hue, respectively. Both colours are favourable for minimizing peri-implant discoloration [30]–[32], aligning with the aesthetic and technical requirements of clinical dental implantology. The cyclic variation in colour observed during deposition, transitioning from blue to green to yellow to pink and then repeating, is attributed to the increasing coating thickness and the consequent cyclic variation in the optical path difference (OPD). Among these, the yellow hue is particularly advantageous due to the broader spectral range over which yellow

interference occurs, leading to a more stable and homogeneous colour perception. This rendered the yellow hue the optimal aesthetic choice for the final application.

To confirm the structural phase composition observed during the screening phase, EDS, XRD and Raman analyses were again conducted. EDS revealed an yttrium concentration of approximately 3.5 wt.%, around 3 mol.%, which is, also in this case, lower than the nominal target concentration. XRD results confirmed the coexistence of both cubic and tetragonal phases with an yttria content of about 4 mol.%, which aligns with the initial target composition. Raman spectroscopy once again predominantly detected the cubic phase and suggested an yttria concentration of 13 mol.%, supporting the hypothesis that oxygen vacancies, induced by the industrial deposition system, play a key role in stabilizing the cubic phase [176], [177]. The YSZ-14 coating underwent low-temperature degradation tests, and even after 5 hours, equivalent to 75 years of exposure in the oral environment, the cubic phase remained intact. In fact, the cubic phase demonstrated no cytotoxic effects on fibroblasts promoting a better cell organization then the naked titanium. Moreover, the presence of oxygen vacancies contributed to enhanced cell differentiation [180].

Additional scratch tests were performed to verify the durability of the YSZ coatings under conditions simulating clinical loads. Similar to the screening phase, all coatings in the optimization phase demonstrated excellent adhesion, with critical loads well above 1 N. In particular, YSZ-13, YSZ-14, and YSZ-16 exhibited no total delamination, while the remaining coatings experienced delamination only at loads around 16 N, which is far above the forces expected in clinical conditions.

At the conclusion of the optimization phase, a well-defined deposition method and a specific set of deposition parameters (as detailed in Table 3-12) were established. In particular, the YSZ-14 coating was identified as the optimal candidate for further deposition on the cylindrical section and, ultimately, on the final abutment component.

Table 3-12 - MS deposition – ZrO adopted for the YSZ-14 coating.

STEP	**Time**	**Temp.**	**O2 flow**	**Ar flow**	**He flow**	**Magnetron Sputtering (MS)**					**RF potential**
						Current	Potential	Tension	Frequence	duty cycle	
	[s]	[°C]	[sccm]	[sccm]	[sccm]	[A]	[kW]	[V]	[kHz]	[%]	[W]
YSZ 14 plate	**7200**	180	**60**	500	**0**	24 (monop.)	6	**385**	80	80	**0**

3.3. Yttria-Stabilized Zirconia coatings – from plates to abutments

3.3.1. Macroscopic observations

During the final phase of the YSZ coating deposition, optimal parameters were applied to cylindrical stainless-steel samples and abutments, specifically the healing and Variobase® abutments. The parameters used were those of the YSZ-14 sample, as its yellow coloration was deemed most promising for the intended application. The resulting appearance was consistent across all samples, including the two abutments, which exhibited the expected yellow hue. This coloration is advantageous for minimizing peri-implant discoloration, as supported

by previous studies [30]–[32]. Furthermore, the depositions appeared quite homogeneous along the entire surface of the abutments, indicating a uniform and effective coating process.

Figure 3.3-1 shows the YSZ-coated abutments, illustrating the results of the zirconia layer applied to the final components.

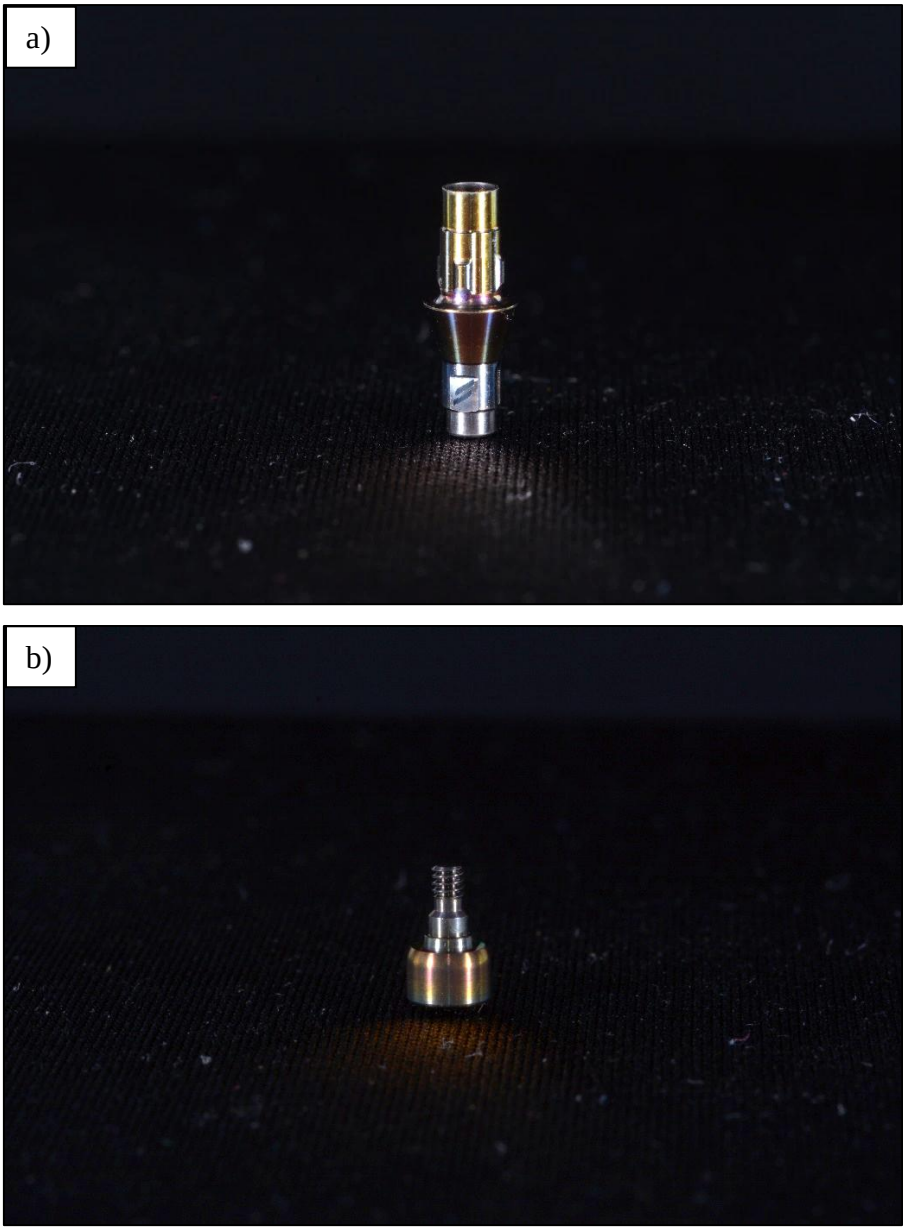

Figure 3.3-1 - Photos of YSZ-coated abutments: (a) healing abutment, (b) Variobase® abutment, and (c) both abutments.

3.3.2. Electron Microscopy observations

Scanning electron microscopy was performed on the coating surfaces of cylindrical samples and abutments to verify the retention of characteristics observed in planar geometry. Figure 3.3-2 presents an SE image highlighting the surface morphology of the YSZ-4 coating on the cylinder, representative of the overall quality observed across all four coatings deposited on the cylindric samples. The thin coating accurately mirrors the morphology of the substrate. However, in this context, the morphology is not significantly important since the substrate is merely used as a dummy and is not the focus of this study. Additionally, Figure 3.3-3 includes images captured using the SE detector of the two abutments, providing an overview of the quality at lower magnification and a detailed view of the surface morphology at the same magnification as the other SE observations. Particularly, the coating on the abutments appears to be uniformly deposited and free of defects.

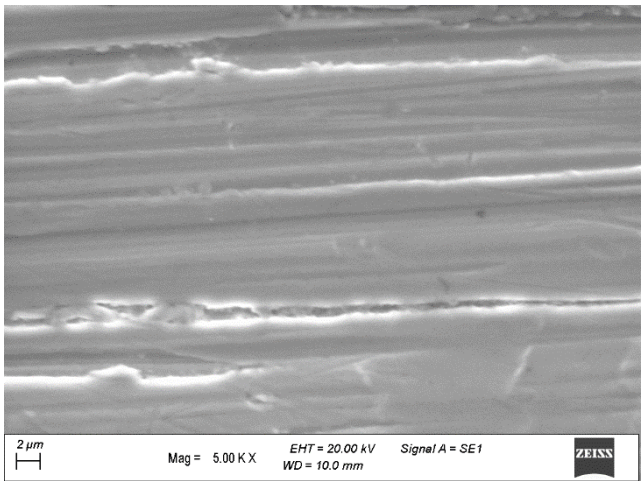

Figure 3.3-2 - SEM image through SE detector of YSZ cylinder – 4

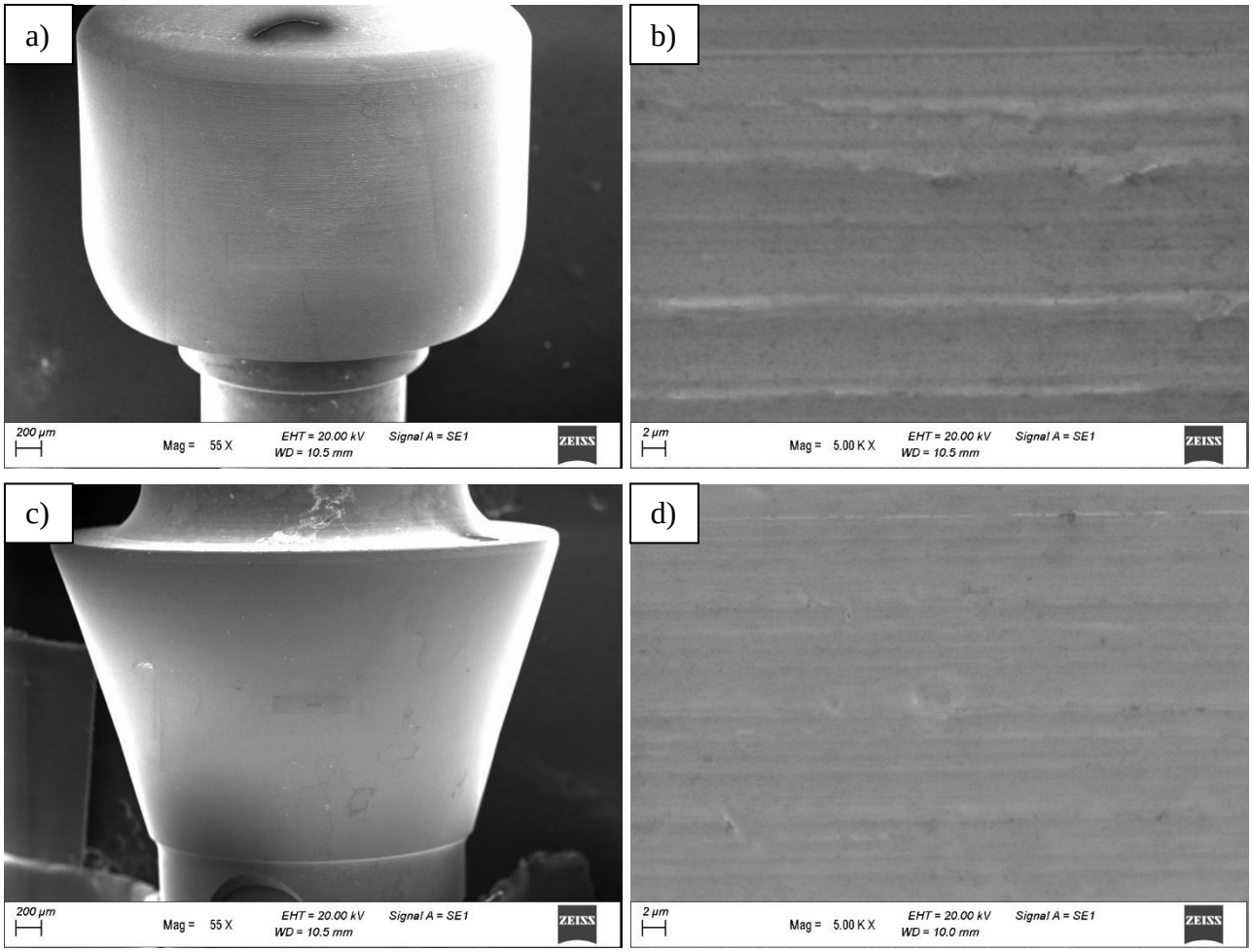

Figure 3.3-3 - SEM images captured using the SE detector show (a) low magnification and (b) high magnification views of abutment 3, and (c) low magnification and (d) high magnification views of abutment 4.

EDS spectra were collected from each coating surface to quantify the elemental concentrations within the coatings. Consistent with the findings from planar geometry, the EDS analysis detected zirconium, oxygen, yttrium, argon, and hafnium in all coatings. The specific concentrations of these elements are detailed in the graphs shown in Figure 3.3-4 for the cylindrical geometry. In this case, the analysis was conducted on two different sides to evaluate the homogeneity of the coating Particularly, it has been confirmed that the element values remain largely consistent between the two observed positions, with the exception of deposition 2, which shows greater deviations in the measured element values (Table 3-13). Conversely, the analyses of the abutment surfaces are presented in Figure 3.3-5.

The average weight percentages of zirconium (Zr), yttrium (Y), and oxygen (O) in the cylindrical samples were 49 wt.% for zirconium, 3.5 wt.% for yttrium, and 41.7 wt.% for oxygen. Hafnium and argon were found in average concentrations of 4.2 wt.% and 1.6 wt.%, respectively. For the abutments, the average weight percentages were 47 wt.% for zirconium, 3.6 wt.% for yttrium, and 45.1 wt.% for oxygen, with hafnium and argon at 2.8 wt.% and 1.8 wt.%, respectively.

Comparing these results to the expected values of 68 wt.% for zirconium, 5 wt.% for yttrium, and 25 wt.% for oxygen, the four depositions on the cylindrical samples exhibited an excess of oxygen compared to the stoichiometric condition. Evaluating the stoichiometric ratios, the mole amounts were 0.54 for zirconium, 0.04

for yttrium, and 2.61 for oxygen. The ratio of oxygen to zirconium is 4.8, which is higher than the stoichiometric requirement, indicating an excess of oxygen relative to zirconium. Similarly, the ratio of oxygen to yttrium is 67, significantly higher than the stoichiometric requirement.

A similar result was observed for the abutments, characterized by mole amounts of 0.52 for zirconium, 0.04 for yttrium, and 2.82 for oxygen. The ratio of oxygen to zirconium is 5.4, also higher than the stoichiometric requirement, indicating an excess of oxygen relative to zirconium. Similarly, the ratio of oxygen to yttrium is 70, indicating a substantial excess of oxygen relative to yttrium.

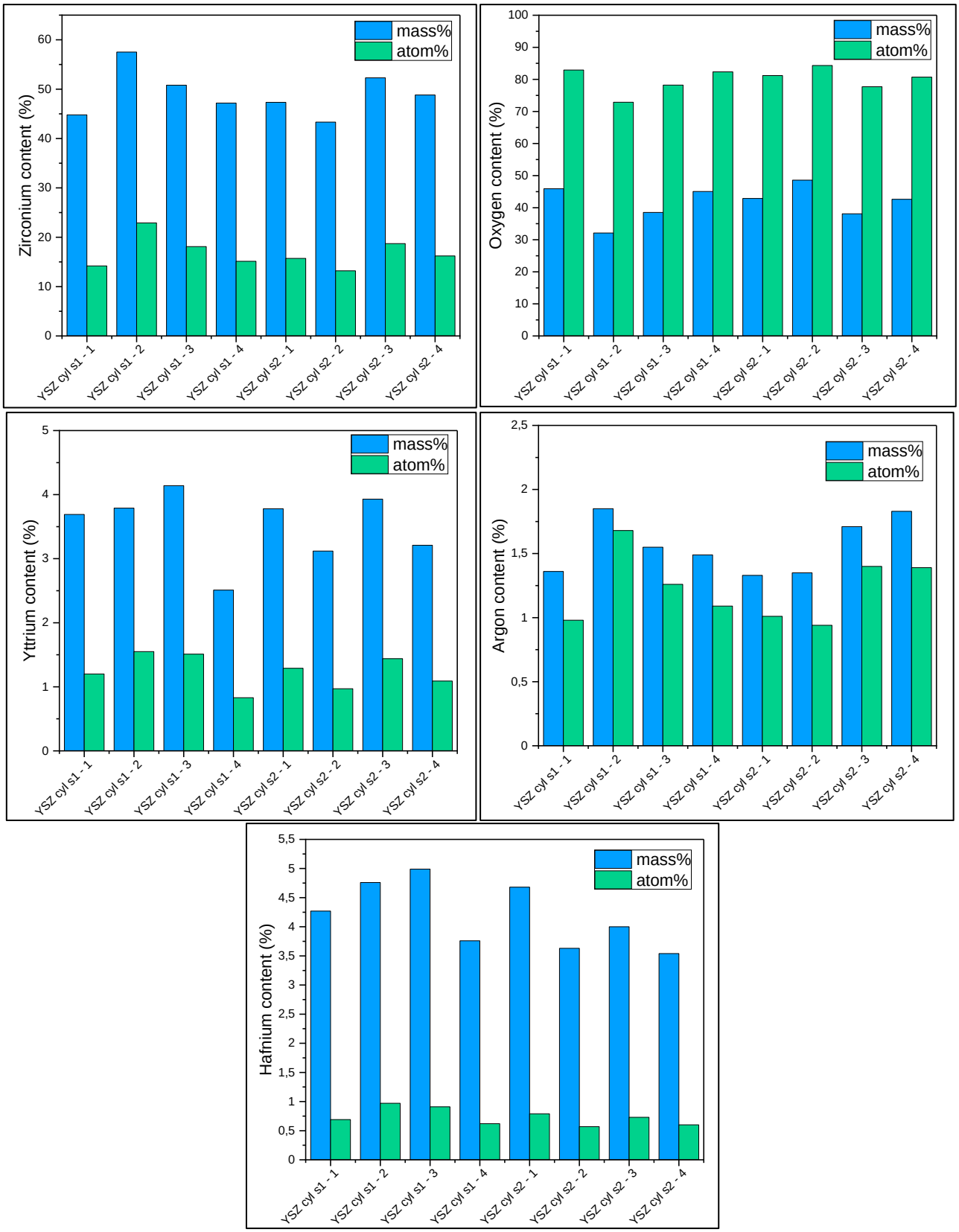

Figure 3.3-4 - Element contents of the YSZ coatings deposited on the cylindric geometry through EDS analysis.

Table 3-13 - Average values of the two observed positions of the cylindric sample coatings.

		YSZ cyl - 1	YSZ cyl - 2	YSZ cyl - 3	YSZ cyl - 4
Zr	Average	46,1	50,4	51,6	48,0
	Std Dev	1,80	10,03	1,05	1,16
Y	Average	3,7	3,5	4,0	2,9
	Std Dev	0,06	0,47	0,15	0,49
O	Average	44,4	40,3	38,3	43,8
	Std Dev	2,13	11,66	0,30	1,73
Hf	Average	4,5	4,2	4,5	3,7
	Std Dev	0,29	0,80	0,70	0,16
Ar	Average	1,3	1,6	1,6	1,7
	Std Dev	0,02	0,35	0,11	0,24

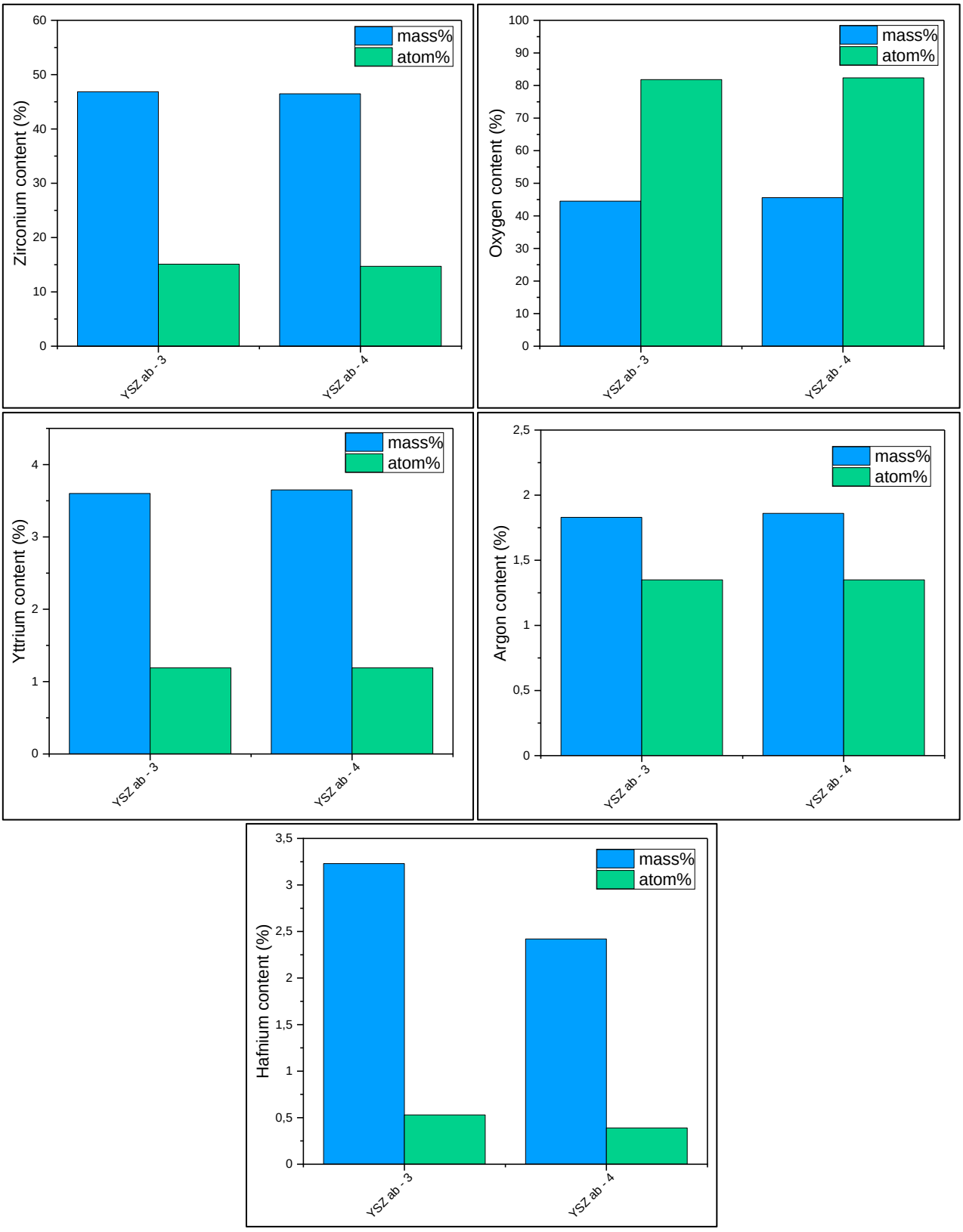

Figure 3.3-5 - Element contents of the YSZ coatings deposited on abutments through EDS analysis

Table 3-14 - Average values of the two observed positions of the abutment coatings.

	YSZ ab - 3	YSZ ab - 4
Zr	46,9	46,5
Y	3,6	3,7
O	44,5	45,6
Hf	3,2	2,4
Ar	1,8	1,9

3.3.3. Raman analysis

Raman spectroscopy was performed on the coatings deposited on the cylindrical samples and the two abutments. Initially, we confirmed the presence of the cubic phase in the coatings on the cylindrical sample and subsequently on both the healing and Variobase® abutments.

The resulting spectra, presented in Figure 3.3-6, exhibited similar characteristic peaks. The cylindrical samples, C1 and C2, displayed a peak at ~150 cm^{-1}, which is common to both the tetragonal and cubic phases. Additionally, peaks at ~245 cm^{-1} and ~460 cm^{-1} were observed, corresponding to the cubic and tetragonal phases, respectively. Notably, the peak at ~645 cm^{-1}, characteristic of the tetragonal phase, was found to shift to ~600 cm^{-1} in the cubic phase [170]. As previously discussed, the stretching mode at ~645 cm^{-1} undergoes this crucial shift, which distinguishes the tetragonal from the cubic phase, and is strongly influenced by the oxygen vacancy content [136]. By analysing this shift and referencing study [170], the estimated yttria content in the coating is approximately 22 wt.%, as expected from the previous Raman analyses.

In particular, the spectra were well aligned with prior observations of YSZ-14, here referred to as P14, which served as a reference for these depositions.

The coatings applied to the two abutments exhibited spectra similar to those of the cylindrical samples. However, additional peaks at approximately 1350 cm^{-1} and 1580 cm^{-1} were detected [181], [182], indicating the presence of amorphous carbon. This contamination likely occurred during the deposition process. If avoiding this contamination proves difficult, it will be necessary to evaluate its impact on cell behaviour, despite specific studies confirming improved cellular adhesion and proliferation on the amorphous carbon coating [183]–[185]. Finally, the extracted yttria content of approximately 22 wt.% further confirmed the presence of the cubic phase.

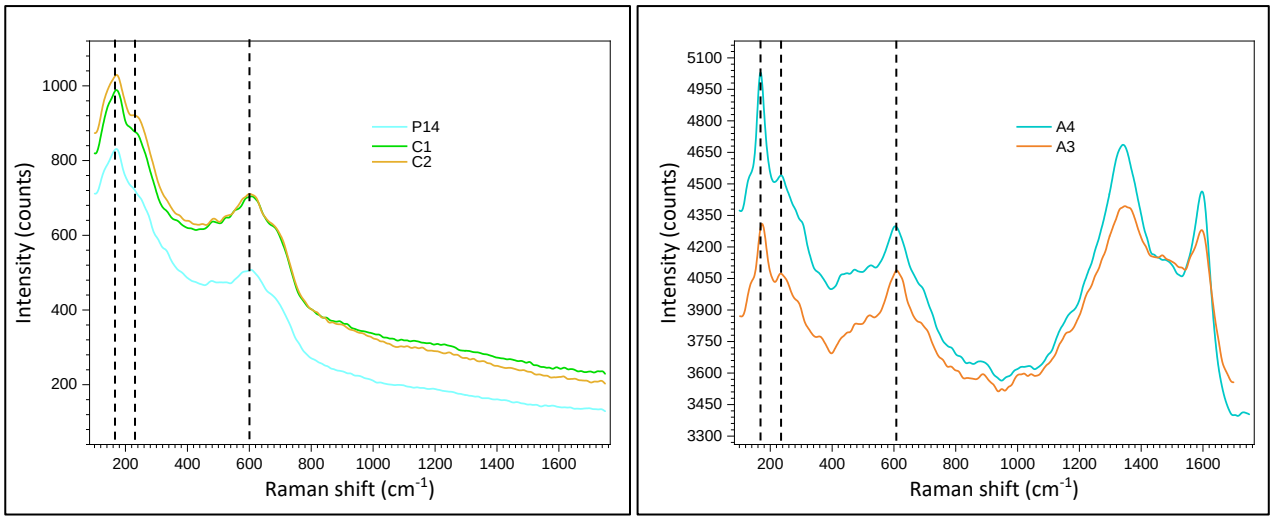

Figure 3.3-6 - Raman spectra collected for the YSZ coatings on the cylindric samples (C1 and C2) and on the abutments (A3 and A4).

3.3.4. Conclusions

The depositions on the cylindrical geometry were successfully achieved, resulting in homogeneous and defect-free coatings. This ensured the satisfactory application of the optimal YSZ coating on the healing and Variobase® abutments.

The obtained yellow coloration was promising for the intended application, as it is beneficial in minimizing peri-implant discoloration [30]–[32], thereby meeting the aesthetic and technical requirements of clinical dental implantology.

To verify the repeatability of the coating deposition, EDS and Raman analyses were performed. EDS analysis confirmed an yttrium concentration of approximately 3.6 wt.% on the abutment coating, consistent with previous depositions during the optimization phase. Additionally, Raman spectroscopy confirmed the presence of the cubic phase, indicating an yttria concentration of 13 mol.%. These results demonstrate the repeatability and reliability of the YSZ coating deposition, successfully reproducing the characteristics observed from the planar samples to the final component.

3.4.Collagen-based hydrogel

3.4.1. SEM observations

Scanning electron microscopy (SEM) was conducted on the hydrogel surface to evaluate the eventual formed structured during the fibrillogenesis of the collagen portion. A first analysis, conducted on the hydrogels at different concentrations, 4,2 mg/mL and 5,8 mg/mL, revealed effectively different structure.

Specifically, as shown in Figure 3.4-1, the dehydrated hydrogel exhibited a fibrillar structure was observed in both cases, but the collagen fibrils were thicker when the solution was less concentrated. Additionally, smaller porosities were detected in the hydrogel with a concentration of 5.8 mg/mL, the higher one, aligning well with literature that indicates a reduction in pore size with increased collagen concentration. This suggests a potential improvement in cell attachment, as the exposed area increases [129], [130].

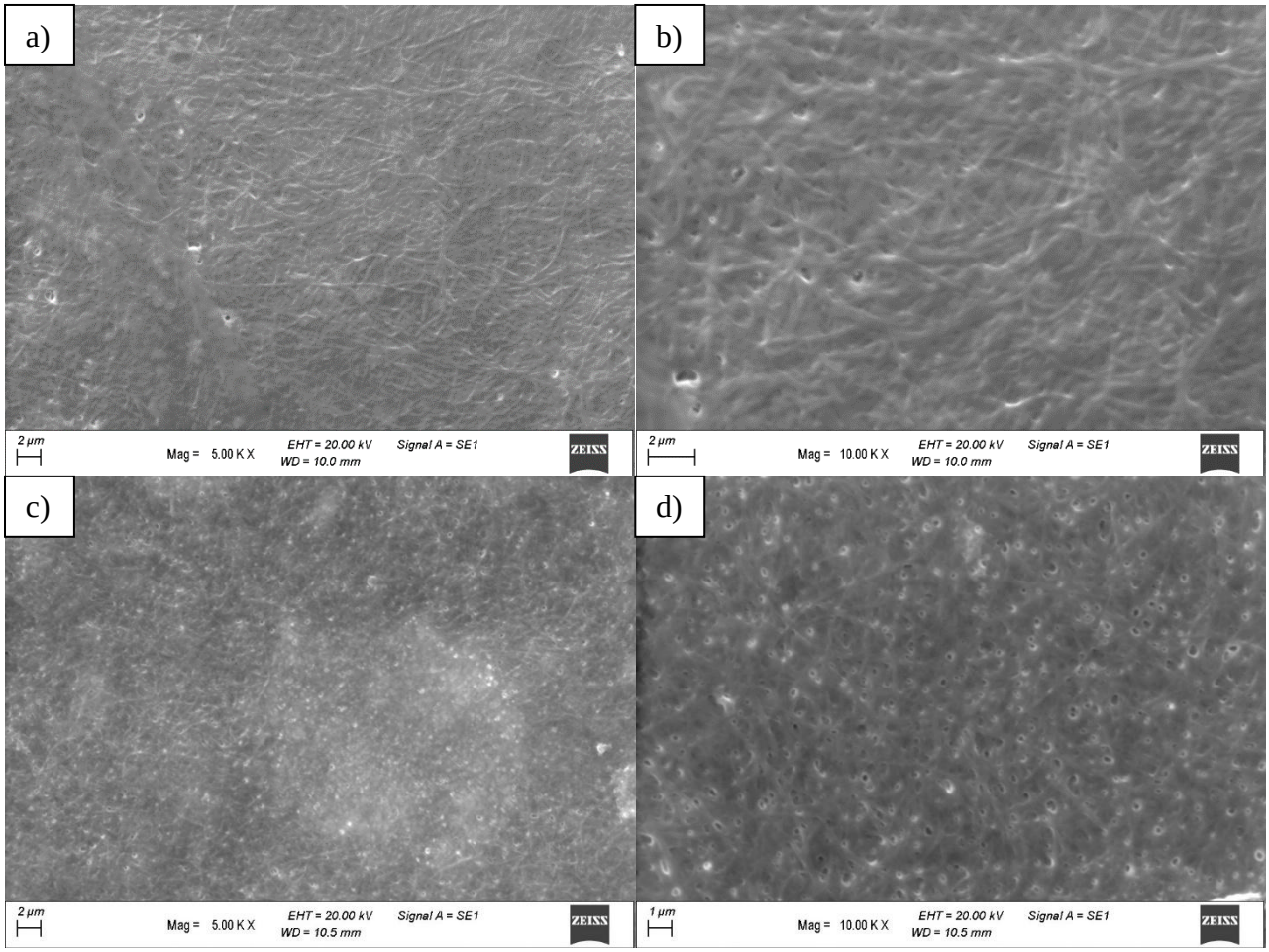

Figure 3.4-1 - SEM images of hydrogels with different collagen concentrations:(a) and (b) 4,2 mg/mL; (c) and (d) 5,8 mg/mL.

3.4.2. Rheometric test

The rheological properties of collagen solutions were initially investigated through flow curve analyses. The first set of experiments was conducted at 4°C. When plotting the data as shear stress versus shear rate (Figure 3.4-2 (a)), the collagen exhibited pseudoplastic behaviour. Both the pure collagen solution and the solution with 0.1% w/v Laponite showed an increase in shear stress with increasing shear rate. Instead, the solution containing 0.3% w/v of Laponite exhibited a deviation in behaviour corresponding to 200 s^{-1}, likely due to structural breakage.

The shear stress at low shear rate at 4°C was approximately 0.0030, 0.20 and 1.60 Pa for pure collagen, collagen with 0.1% w/v Laponite, and collagen with 0.3% w/v Laponite, respectively.

At 25°C, the collagen began to gel, and the flow curves appeared more incoherent, likely due to phase transformation and the resulting inhomogeneity of the solution (Figure 3.4-2 (b)). The characteristic curves of

the Laponite-containing solutions showed higher shear stress at low shear rates, attributed to the interaction between clay particles. In particular, the shear stress at low shear rate, the yield stress, at 25°C was approximately 1.30, 1.50 and 2.70 Pa for pure collagen, collagen with 0.1% w/v Laponite, and collagen with 0.3% w/v Laponite, respectively. Following a transient phase, the particles aligned with the flow, resulting in a plateau in the curve and ensuring low shear stress at high shear rates, which decreased with increasing Laponite concentration.

This observations was anticipated due to the shear-thinning effect induced by the addition of Laponite to the collagen solution [33], [34].

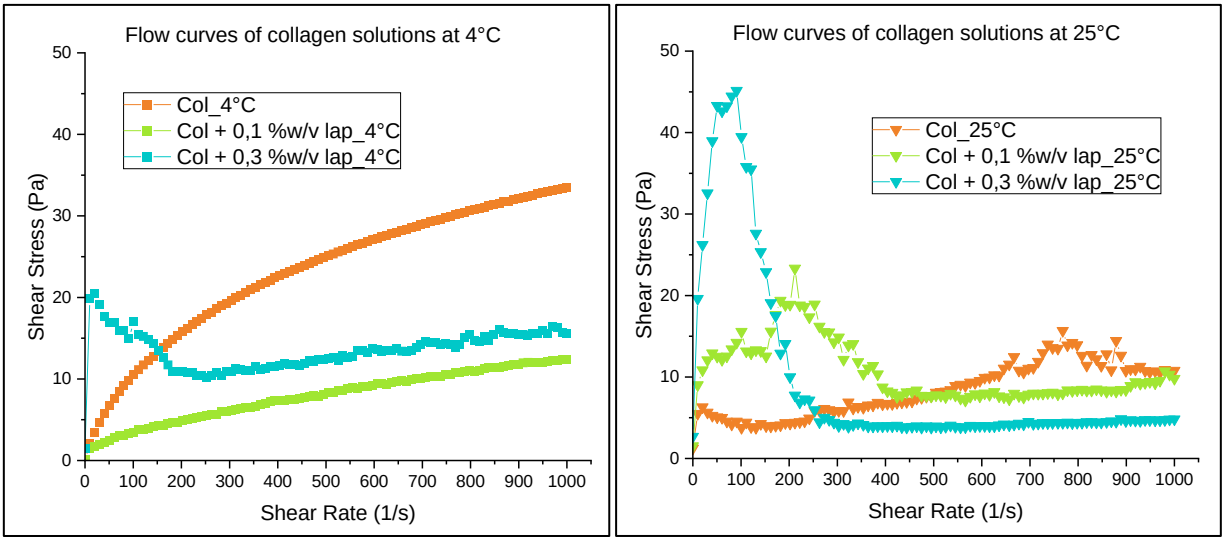

Figure 3.4-2 - flow curves of collagen solution plotting the shear stress as a function of the shear rate at (a) 4°C and (b) 25°C.

The shear stress limit values were determined for each scenario to evaluate the flow behaviour under static conditions that simulate the deposition phase. The yield point values showed an increase with both the rise in Laponite concentration and temperature. Specifically, at 4°C, which is the effective condition during the deposition phase, the highest shear stress was observed with a Laponite concentration of 3% w/v. This concentration appears to provide the most stability during hydrogel deposition.

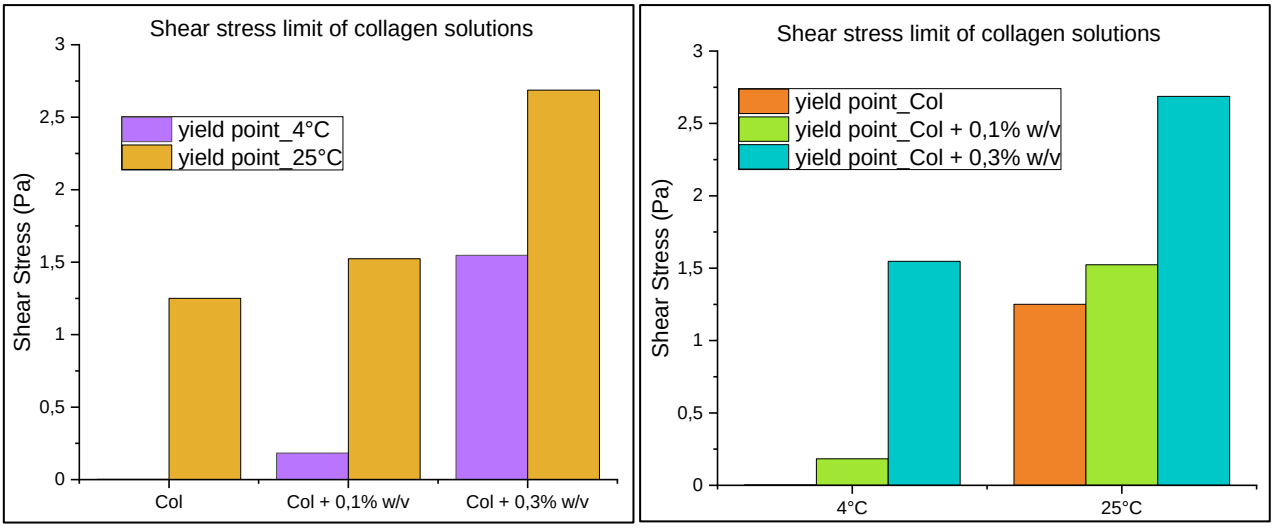

Figure 3.4-3 - Shear stress limit values in function of the (a) formulation type and (b) temperature value.

When plotting viscosity against shear rate, it was evident that viscosity at lower shear rates increased with Laponite concentration at 4°C: 0.25, 18, and 155 Pa·s for pure collagen, collagen with 0.1% w/v Laponite, and collagen with 0.3% w/v Laponite, respectively. Instead, at higher shear rates, the viscosities of Laponite-containing solutions decreased more than those of pure collagen solutions.

At 25°C, as the collagen began to gel, its contribution to the overall viscosity became more significant compared to the Laponite. The viscosities at this temperature were approximately 125, 153, and 272 Pa·s for pure collagen, collagen with 0.1% w/v Laponite, and collagen with 0.3% w/v Laponite, respectively.

However, according to the previous observation of the shear stress, the viscosity exhibited the highest values at low shear rate in the presence of Laponite, as expected due to the shear-thinning effect provided by this clay.

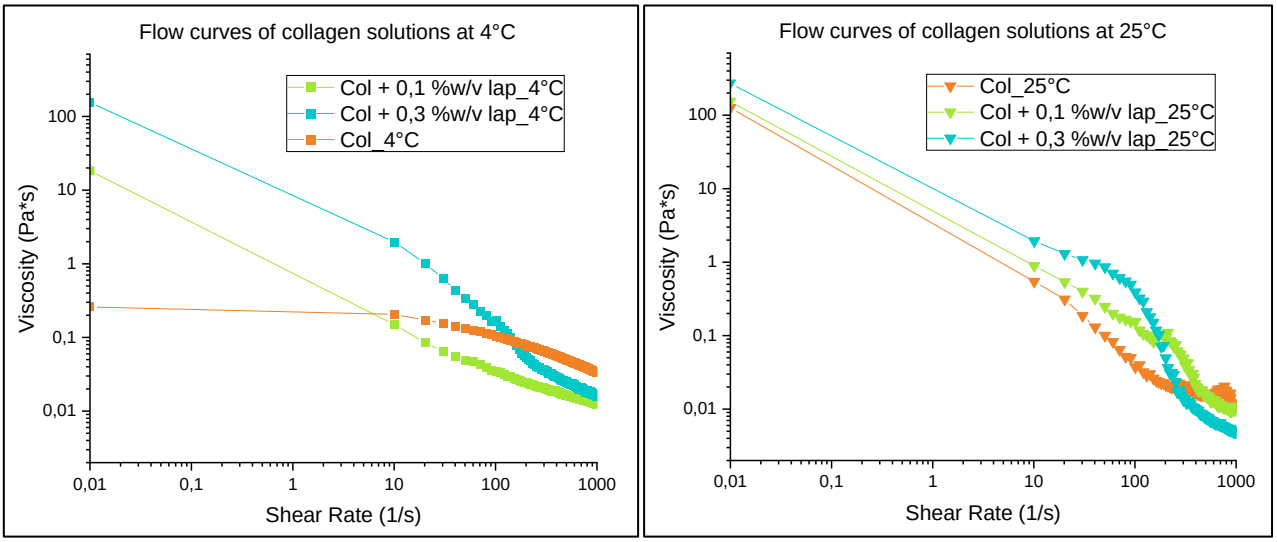

Figure 3.4-4 - flow curves of collagen solution plotting the viscosity as a function of the shear rate at (a) 4°C and (b) 25°C.

To thoroughly investigate the gelation behaviour of collagen solutions, a series of tests were conducted on three different samples: pure collagen, collagen with 0.1% w/v Laponite, and collagen with 0.3% w/v Laponite. These experiments were carried out at a constant temperature of 37°C. During the tests, both the storage modulus (G') and the loss modulus (G'') were measured and plotted as functions of time. The resulting curves are illustrated in Figure 3.4-5.

The data analysis revealed that all solutions remained in the gel phase throughout the observation period (G' > G''), preventing the identification of a distinct gel point. However, the completion of the gelation process was indicated by the observation of a plateau in the curves. Specifically, the increase in storage modulus signified the formation of molecular cross-links, suggesting the establishment of a robust hydrogel network [186], [187].

Both the pure collagen solution and the collagen solution containing 0.1% w/v Laponite exhibited similar trends, with no clear plateaus observed in the moduli, except for the final data points in the 0.1% w/v Laponite sample. This suggests that the addition of 0.1% w/v Laponite did not significantly affect the gelation behaviour compared to the pure collagen solution.

In contrast, the collagen solution with 0.3% w/v Laponite displayed a markedly different pattern. Both the storage and loss moduli increased rapidly, reaching a plateau approximately 40 minutes into the gelation

process, indicating a more pronounced gelation effect at this higher Laponite concentration. However, despite the rapid increase, the overall contribution of Laponite to the moduli was not substantial. The pure collagen solution ultimately reached the highest modulus values at 90 minutes of gelation, surpassing those of the Laponite-containing samples.

Furthermore, an inverse relationship was observed between Laponite concentration and the moduli values. As the concentration of Laponite increased, the moduli values decreased, as depicted in Figure 3.4-6. This suggests that higher concentrations of Laponite may slightly inhibit the gelation process or alter the network structure of the collagen gel.

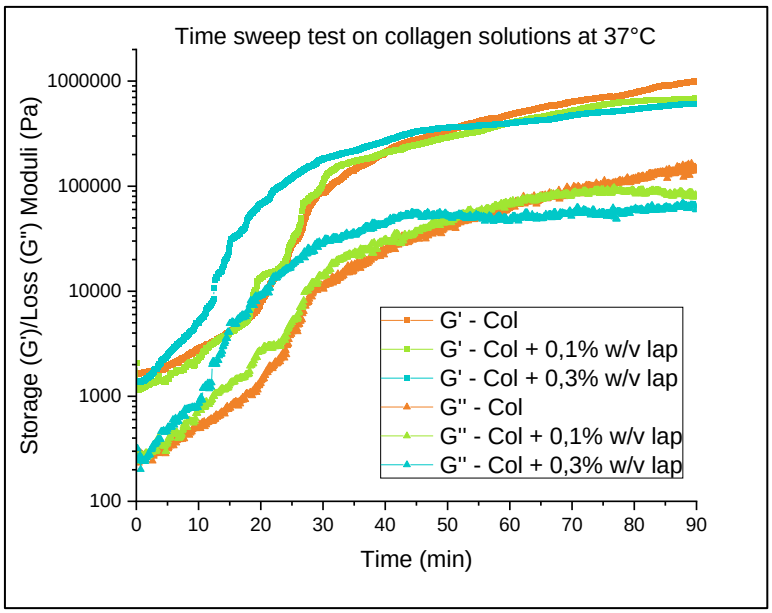

Figure 3.4-5 - Time sweep test on collagen solutions at 37°C – Storage and Loss moduli in function of the gel time.

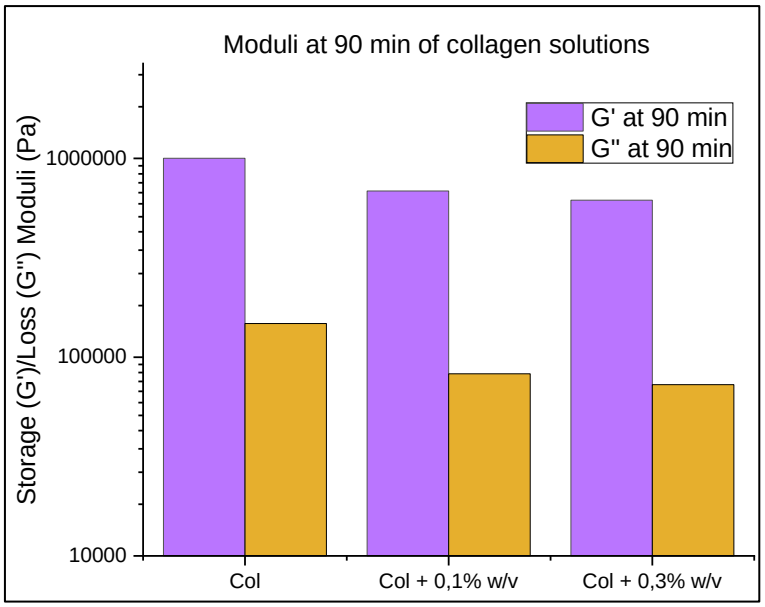

Figure 3.4-6 - Storage and Loss moduli of different collagen solutions at 90 min.

The storage modulus values of collagen hydrogels during rheological tests at 37°C typically fall within the range of 10^1 to 10^2 Pa, as reported in previous studies [188]–[190]. However, in this study, the storage modulus

values observed were significantly higher, ranging from 10^5 to 10^6 Pa. This substantial increase can be attributed to the specific type of collagen used, known as telocollagen.

Telocollagen retains the intact structure of collagen fibrils, which is a crucial factor in its gelation behaviour. The intact fibrillar structure of telocollagen likely promotes stronger intermolecular bonding during the gelation process. This enhanced bonding leads to a more robust gel network, resulting in the observed higher storage modulus values.

Advanced BioMatrix conducted a technical study on various collagen formulations, including telocollagen solutions, which demonstrated storage modulus values in the order of 10^3 Pa [191]. This finding is consistent with the initial storage modulus values observed in the current study, which were also in the order of 10^3 Pa.

3.4.3. Contact angle measurements

The contact angles were measured on biomedical-grade zirconia plates and YSZ-deposited titanium plates to evaluate the effect of alkaline treatment, which acts as an immobilization treatment, on enhancing collagen-based hydrogel adhesion.

Initial measurements were taken on zirconia plates with two different surface finishes: Computer Numerical Control (CNC) - finished and polished.

The as-is surfaces exhibited contact angles of approximately 95° for the CNC-finished surface and 80° for the polished surface. Upon applying the immobilization treatment, a significant reduction in contact angles was observed starting from 0 hours. For the polished surfaces, the contact angles decreased by approximately 87%, while for the CNC-finished surfaces, the reduction was even more pronounced at 93%. The CNC-finished surfaces exhibited such a low contact angle that it fell within the instrumental error range, effectively approaching zero. This dramatic decrease indicates a substantial improvement in surface wettability due to the immobilization treatment. Subsequent measurements over time showed a slight increase in contact angles; however, these values remained significantly lower than those of the untreated surfaces.

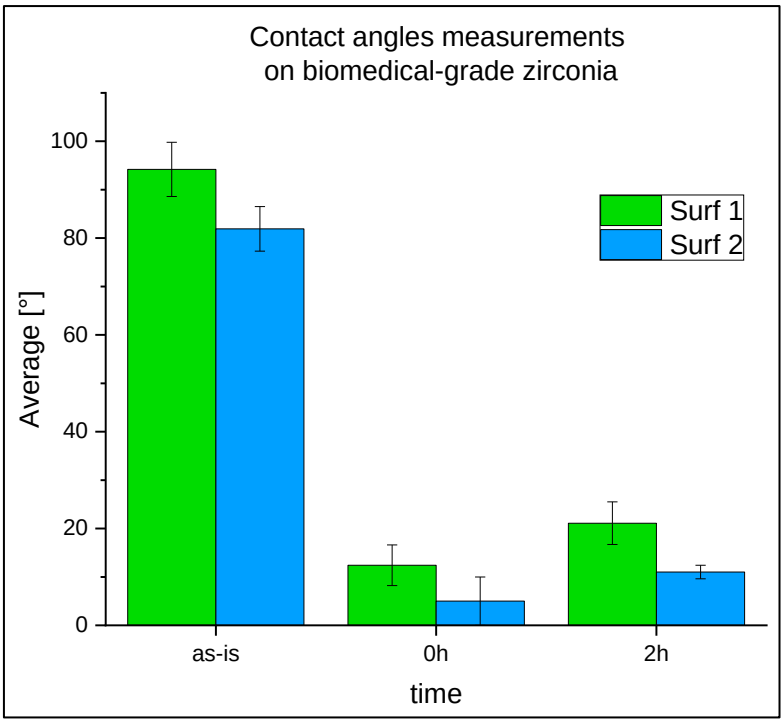

Figure 3.4-7 - contact angle measurements on biomedical-grade zirconia.

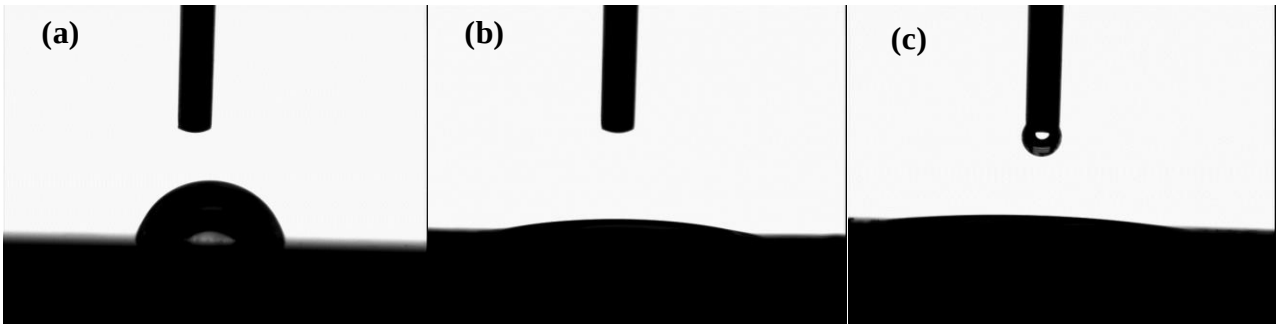

Figure 3.4-8 - water drop shape on biomedical-grade surface (a) pre-treatment and post-treatment with (b) polished finish and (c) CNC finish.

Experiments were also conducted on YSZ coatings with a polished surface finish. The YSZ-16 was used as a reference for the deposited coatings. The initial contact angle value was approximately 90°. Upon immobilization treatment, a significant reduction in contact angle was observed at 0 hours, with the value collapsing by around 93%. This substantial decrease further supports the effectiveness of the immobilization treatment in enhancing surface wettability.

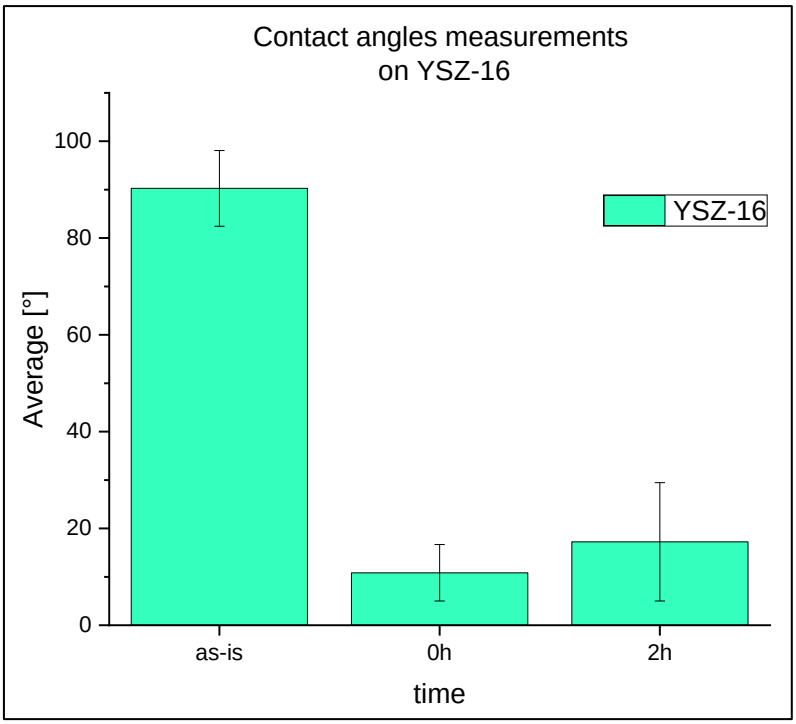

Figure 3.4-9 - contact angle measurements on deposited YSZ-16 coating.

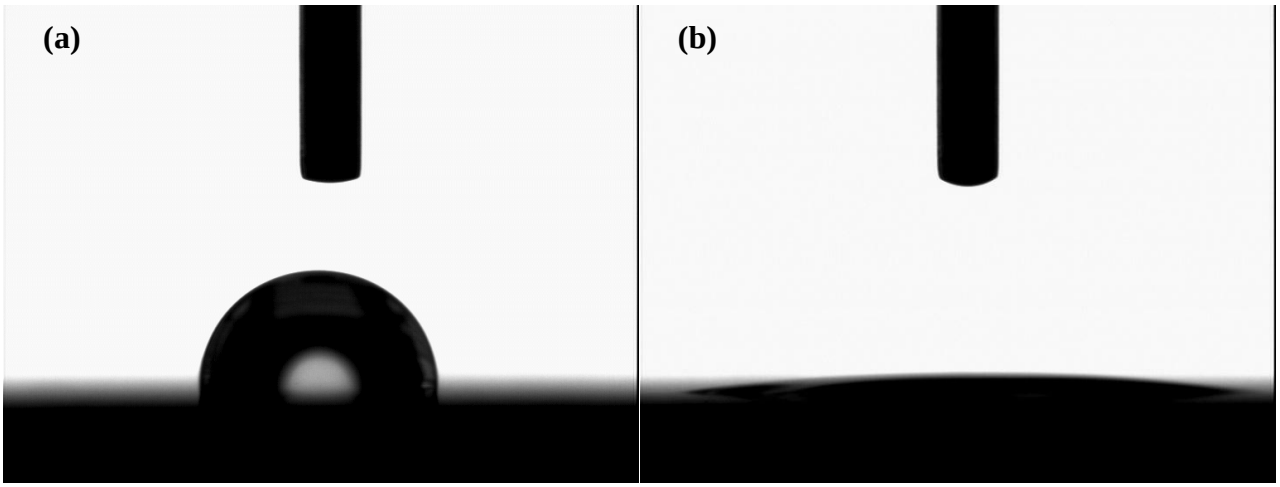

Figure 3.4-10 - water drop shape on YSZ-16 coating: (a) pre-treatment and (b) post-treatment.

Comparing the results of the biomedical grade zirconia plates and the YSZ plates, it is evident that the contribution of surface finishing is crucial. The rougher surface, that is the CNC-finished zirconia, exhibited lower contact angles after treatment. The improvement in wettability characteristics is consistently observed across all three cases (polished zirconia, CNC-finished zirconia, and YSZ on polished titanium plate) due to the immobilization treatment. This indicates that the immobilization method effectively enhances the surface properties, thereby improving the adhesion of the polar groups of the collagen molecule and providing a reliable approach to enhancing the performance of collagen-based hydrogels.

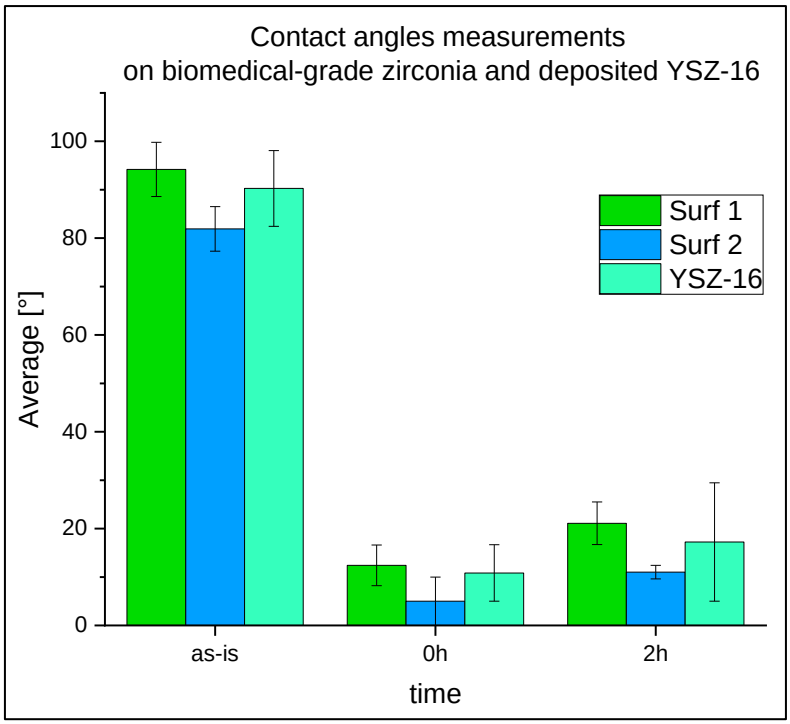

Figure 3.4-11 - contact angle measurements on biomedical-grade zirconia surfaces and deposited YSZ-16 coating.

3.4.4. Optical Microscopy observations

Optical analyses were conducted to investigate the appearance of the hydrogel evaluating the addition of Laponite and the effect of UV cross-linking under its as-produced conditions. The optical images of the collagen-based hydrogels are collected in Figure 3.4-12. Images (a), (c), and (e) represent the pure collagen hydrogels, whereas images (b), (d), and (f) depict the hydrogels composed of a collagen solution with 0.3% w/v Laponite.

For both types of hydrogels, the images are arranged from top to bottom to illustrate the different stages of treatment: post-gelation, post-UV cross-linking for 30 minutes, and post-UV cross-linking for 60 minutes. Specifically, images (a) and (b) show the hydrogels immediately after gelation. Images (c) and (d) display the hydrogels after 30 minutes of UV cross-linking, and images (e) and (f) present the hydrogels following 60 minutes of UV cross-linking.

The hydrogels appeared to be homogeneously deposited onto the zirconia plates. In the images of the collagen-Laponite hydrogels, particles were detected, which were evidently derived from the Laponite. No significant differences were observed as a function of the treatment, indicating that the different treatments did not affect the surface appearance of the hydrogel.

Finally, the collagen layer appears whitish and semi-transparent, with a thickness ranging from several hundred microns to about 1 mm, dimensions that will be optimized in the subsequent deposition phase on the abutment. Its optical impact is minimal, as the hydrogel is bioresorbable and serves as a temporary matrix for soft tissue regeneration.

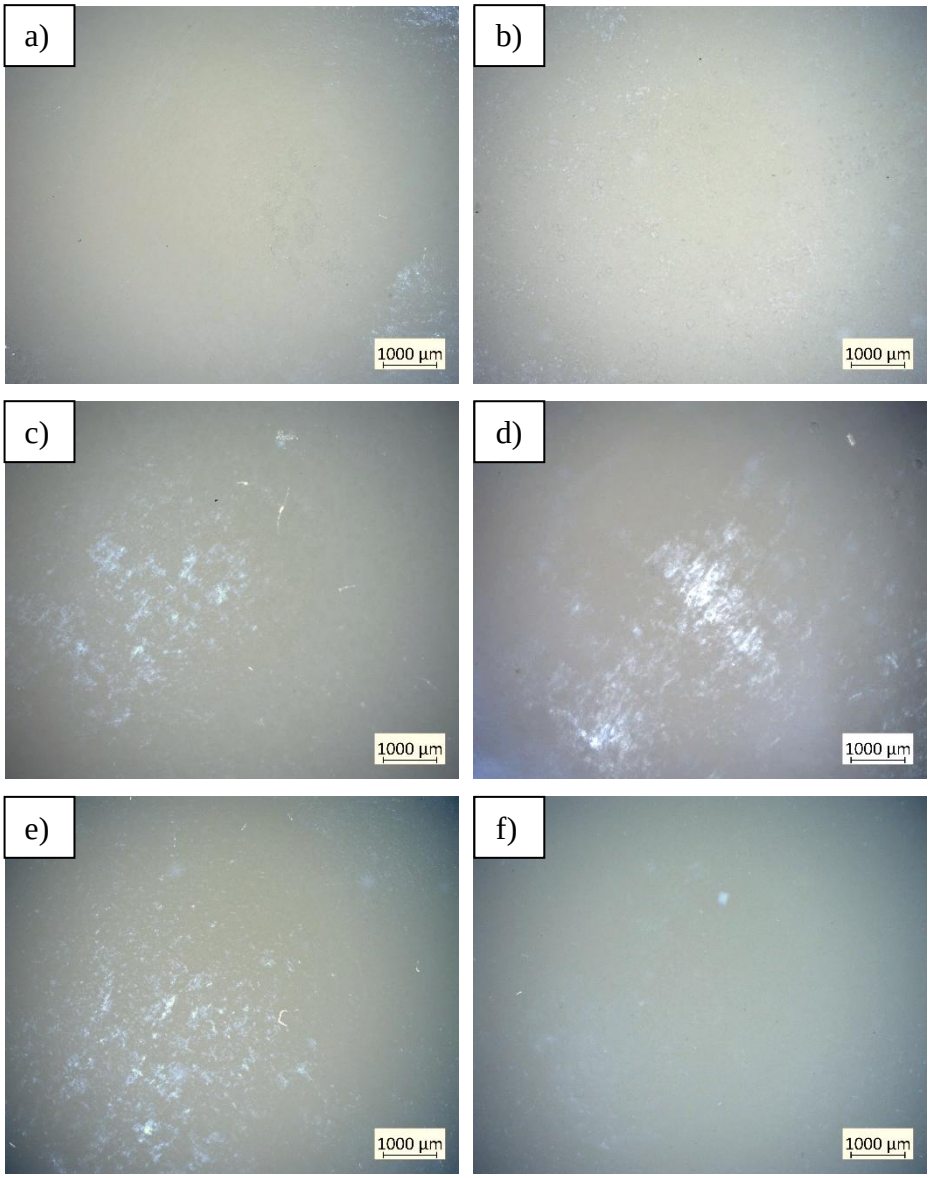

Figure 3.4-12 - collagen-based hydrogels. a) pure collagen post gelation; b) collagen with Laponite post gelation; c) pure collagen post UV cross-linking of 30 min; d) collagen with Laponite post UV cross-linking of 30 min; e) pure collagen post UV cross-linking of 60 min and f) collagen with Laponite post UV cross-linking of 60 min.

3.4.5. FEG-SEM observations

FEG-SEM observations were performed to evaluate the effect of Laponite addition and UV cross-linking on the structural organization of the biopolymeric formulations.

Figure 3.4-13 illustrates a collection of micrographs for each case.

The presence of Laponite resulted in a more homogeneous and ordered fibrillar network, both in gelled and UV-crosslinked samples. The fibres were more uniformly distributed and exhibited a more consistent size compared to the pure collagen formulation. This effect is likely due to electrostatic interactions between the oppositely charged collagen and Laponite particles, which may act as nucleation sites, promoting a more organized fibrillar structure. The adsorption of collagen onto Laponite, driven by electrostatic and hydrogen bonding interactions, enhances the network stability without disrupting the native triple-helix structure of the collagen [192], [193]. Although precise quantitative measurements were difficult due to the resolution limits

of FEG-SEM, the gelled samples exhibited a D-pattern of approximately 60 nm, which is quite close to the natural value of 67 nm, confirming that fibrillogenesis occurred (Figure 3.4-13 (c) and (d)).

UV cross-linking affected the structural organization of both formulations, leading to the formation of a more compact, non-porous layer already after 30 minutes of treatment. This effect is due to the enhanced bonding between collagen fibres, which significantly reduces the voids within the layer. However, a porous structure better mimics the extracellular matrix (ECM), supporting cell infiltration, enhancing migration and proliferation within the scaffold, and improving the diffusion of nutrients, gases, and growth factors, ultimately creating a more physiological environment for tissue remodelling. In contrast, the loss of porosity may limit these processes, although it could lead to greater mechanical stability and resistance to degradation.

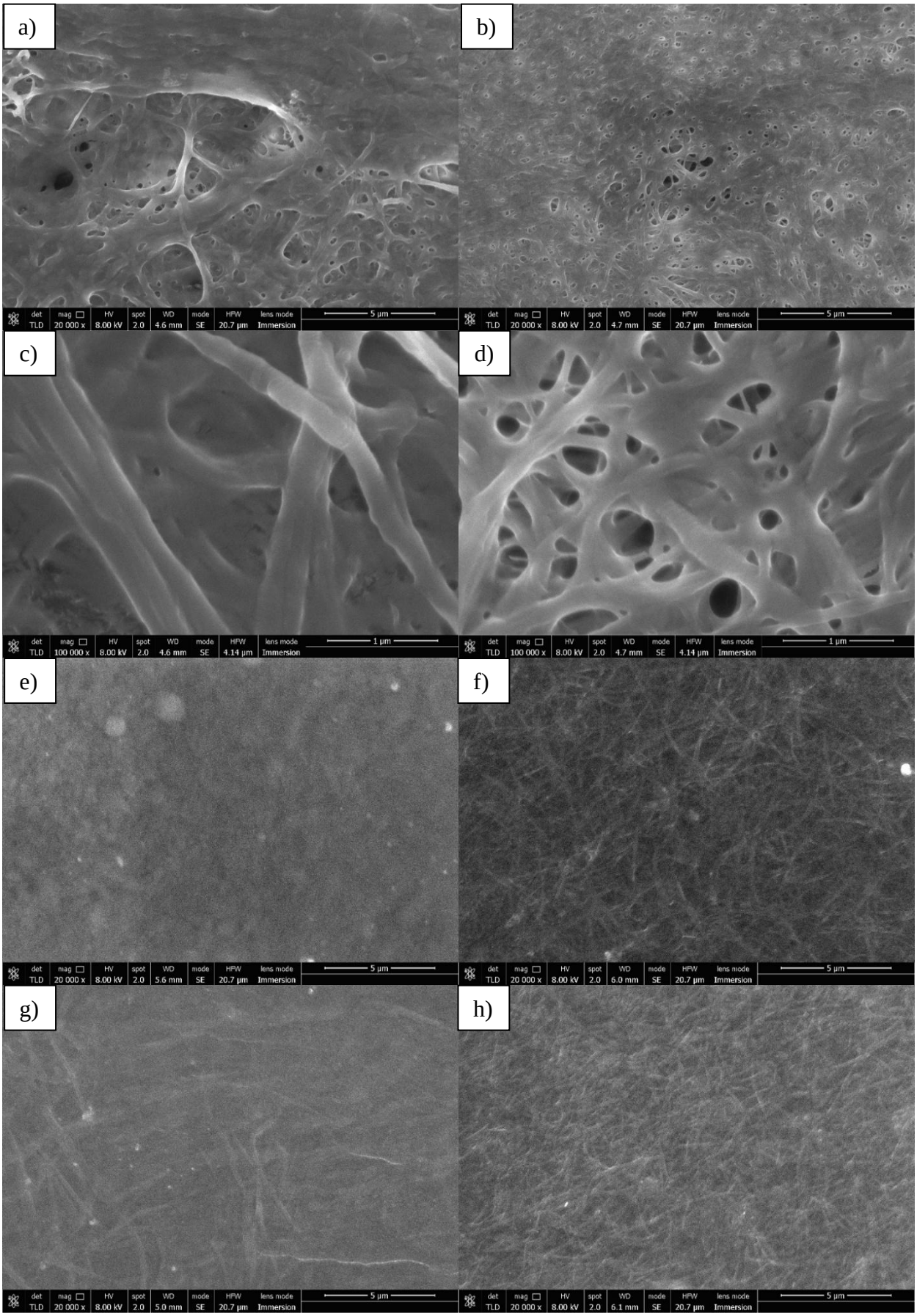

Figure 3.4-13 - FEG-SEM images of collagen-based layers: (a) gelled pure collagen; (b) gelled collagen with 0.3 w/v% Laponite; (c) D-pattern in gelled pure collagen; (d) D-pattern in gelled collagen with 0.3 w/v% Laponite; (e) gelled pure collagen cross-linked with UV for 30 min; (f) gelled collagen with 0.3 w/v% Laponite cross-linked with UV for 30 min; (g) gelled pure collagen cross-linked with UV for 60 min; (h) gelled collagen with 0.3 w/v% Laponite cross-linked with UV for 60 min.

3.4.6. XRD analysis

X-ray diffraction analysis was conducted to assess the structural integrity of the collagen hydrogels. This technique was employed to elucidate the crystalline structure of the hydrogels and to verify the successful formation of collagen fibrils.

During this research, different biopolymeric formulations were analysed to investigate the effects of collagen concentration (4 mg/mL and 6 mg/mL), Laponite concentration (0 w/v%, 0.1 w/v%, and 0.3 w/v%), and applied treatment (gelation alone, gelation followed by 30 minutes of UV cross-linking, and gelation followed by 60 minutes of UV cross-linking) on the hydrogel structure.

Figure 3.4-14 shows that both collagen concentrations resulted in similar structural features. In particular, two characteristic diffraction peaks of collagen were identified:

- The first peak, observed at ~7.7°, corresponds to the intermolecular lateral packing within collagen fibrils, with an associated d-spacing of ~1.14 nm according to Bragg's law. This value aligns closely with that of native skin collagen fibres, which exhibited a denser structure and a higher degree of crystallinity compared to regenerated collagen [194]–[200].
- The second peak, detected in the 16°–25° range, corresponds to the broad diffraction signal representative of the amorphous regions within collagen. This peak arises from diffuse scattering due to multiple structural layers within the fibrils.

Additional diffraction peaks were identified within the broad peak region, likely associated with the buffer solution used during the neutralization phase [201].

The diffraction spectra of the other six formulations, containing 6 mg/mL of collagen, exhibited the same two characteristic peaks (Figure 3.4-15). Importantly, no significant shift in peak positions was observed with increasing Laponite concentration or different cross-linking treatments.

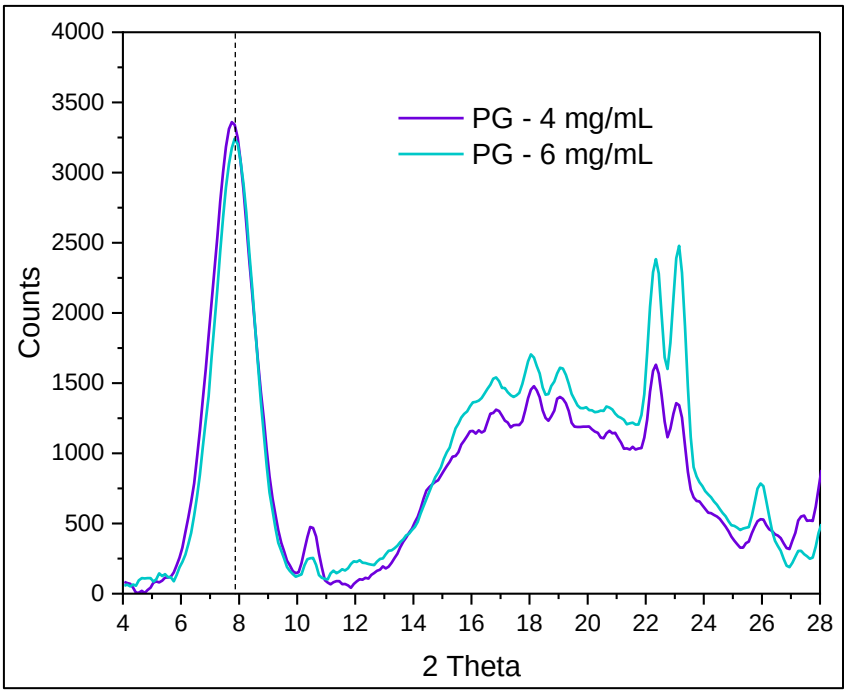

Figure 3.4-14 - XRD of biopolymeric formulation with two collagen concentrations: 4 mg/mL and 6 mg/mL.

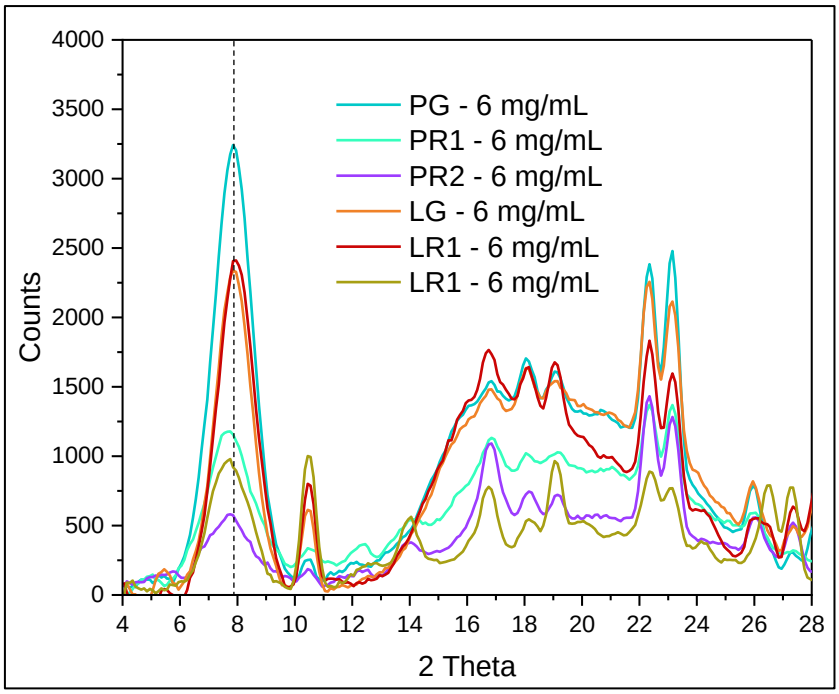

Figure 3.4-15 - XRD of different biopolymeric formulation with 6 mg/mL of collagen concentration.

3.4.7. DSC analysis

Differential Scanning Calorimetry (DSC) analysis was performed on two collagen-based formulations: pure collagen and collagen containing 0.3 w/v% Laponite. These formulations underwent three distinct treatments: gelation, and gelation followed by UV cross-linking for either 30 or 60 minutes. The DSC curves, illustrating the effects of treatment and formulation, are presented in Figure 3.4-16 and in Figure 3.4-17, respectively.

The thermal profiles exhibited similar trends across both cases, with characteristic peaks associated with water evaporation at approximately 90°C, followed by the denaturation peak (T_d) and the inflection point corresponding to the glass transition temperature (T_g) observed during the first and second heating ramps, respectively. These findings were well aligned with literature [164], [165].

Denaturation enthalpy values are inherently influenced by water loss, making direct comparisons challenging. Therefore, a more accurate assessment of the thermal behaviour is provided by the denaturation temperature (T_d) and glass transition temperature (T_g). The collected data for both analyses are summarized in Table 3-15 and Table 3-16. Notably, the denaturation peak consistently appeared around 220°C across all samples, suggesting that the triple-helix structure remains thermally stable up to this temperature and is not significantly influenced by treatment or formulation variations.

During the second heating ramp, where polypeptide chains exhibit increased mobility, a slight glass transition was detected. The T_g data demonstrated sensitivity to processing conditions and formulation variations. Specifically, UV cross-linking resulted in a shift in T_g from approximately 165°C in gelled samples to 175°C in UV cross-linked samples. Furthermore, the incorporation of Laponite led to an additional increase in T_g, with values rising from approximately 175°C in pure collagen to around 185°C in the Laponite-containing formulation.

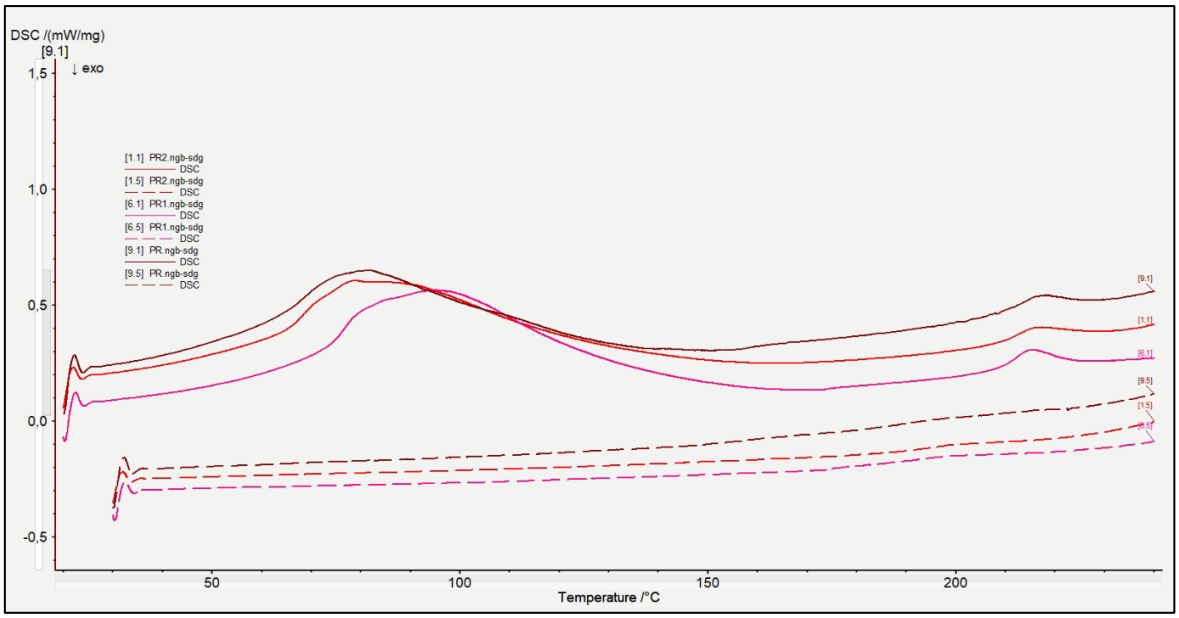

Figure 3.4-16 - DSC curves of pure collagen layers subjected to different treatments, with solid lines representing the first heating ramp and dotted lines indicating the second heating ramp.

Table 3-15 - DSC data of pure collagen subjected to different treatments.

	T_d	H_d	T_g
	[°C]	[J/g]	[°C]
PG	218	9,31	164
PR1	215	12	172
PR2	217	7	173

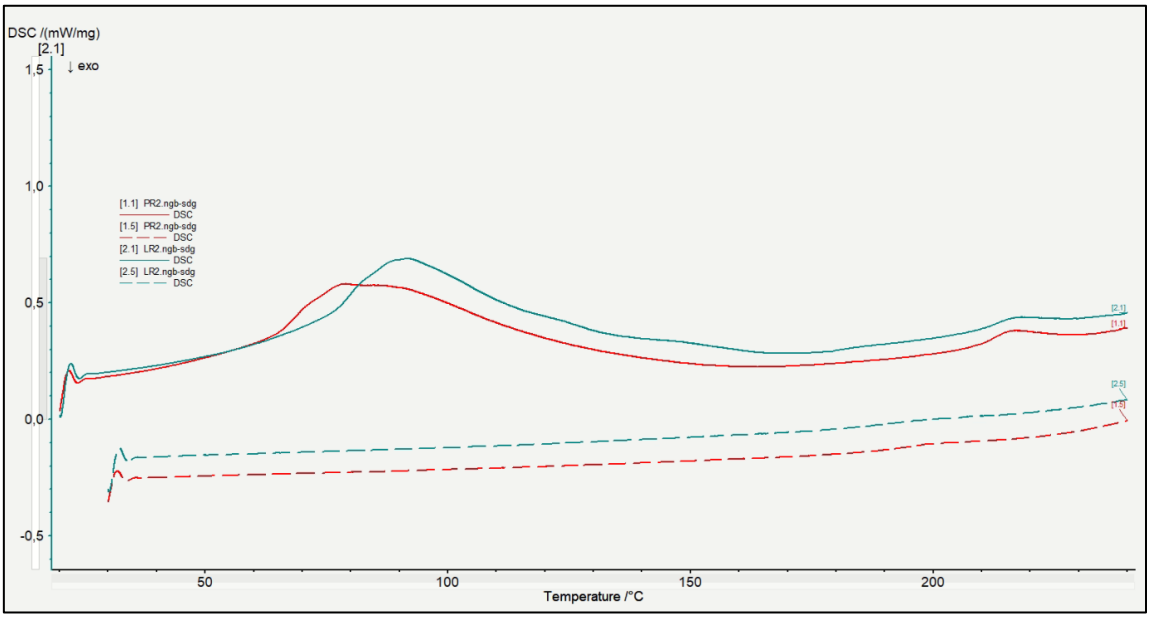

Figure 3.4-17 - DSC curves of collagen-based layers subjected to gelation and UV cross-linking for 60 min, with solid lines representing the first heating ramp and dotted lines indicating the second heating ramp.

Table 3-16 - DSC data of collagen-based layers subjected to gelation and UV cross-linking for 60 min.

	T_d	H_d	T_g
	[°C]	[J/g]	[°C]
PR2	217	7	173
LR2	218	7	185

3.4.8. Conclusions

The initial stage involved defining a collagen-based hydrogel formulation, beginning with the careful selection of collagen.

Type I collagen was chosen to support the regeneration of connective tissues such as gingival tissue. The concentration was maintained close to the standard typically used in tissue engineering to promote cell activity. In addition, telocollagen was selected because it preserves the intact telopeptide terminals of the collagen molecule, thereby maintaining high mechanical properties that are essential for effective cell signalling and proliferation.

Determining the optimal collagen concentration was another important aspect of this study. Tissue engineering (TE) defined the optimal collagen concentration as 5 mg/mL. However, a preliminary study was conducted to explore two different concentrations to better understand their significance. Specifically, we examined a concentration of 5.8 mg/mL, in line with the technical specifications of the provided product, and a concentration of 4.2 mg/mL to assess the effect of a lower concentration than that recommended by TE.

The captured SEM images revealed thinner collagen fibrils and smaller pores in the hydrogel at the higher concentration of 5.8 mg/mL. It is important to highlight that cell attachment improves when the exposed surface area increases, which occurs with the presence of smaller pore sizes directly caused by a higher collagen concentration [130]–[132], as observed in this study. Therefore, the obtained results could lead to significant improvements for TE applications.

X-ray diffraction analysis did not show any significant structural variations, indicating that collagen concentration did not notably influence the crystalline organization of the hydrogel.

Based on these results, the 5.8 mg/mL concentration was selected for the subsequent phases of the study, as it exhibited a denser microstructure in SEM analysis while maintaining structural consistency according to X-ray diffraction.

Laponite powder was incorporated into the collagen solution to improve the deposition process by enhancing the shear-thinning behaviour of the formulation, while still prioritizing the promotion of cell activity. Based on these considerations, three formulations were developed: pure collagen, collagen with 0.1 w/v% Laponite, and collagen with 0.3 w/v% Laponite.

Before deposition, the rheological behaviour of these formulations was evaluated using rheometric tests. At 4°C, the analysis of the flow curves demonstrated that the addition of 0.3 w/v% Laponite increased the viscosity at low shear rates, reaching values of 155 Pa·s compared to only 0.25 Pa·s for the pure collagen solution. In contrast, the formulation with 0.1 w/v% Laponite exhibited a similar behaviour to the pure collagen.

Time sweep tests were then conducted at 37°C, the temperature commonly employed for collagen gelation. These tests revealed that the formulation with 0.3 w/v% Laponite achieved a reduced gelation time, while the pure collagen formulation maintained a predominant mechanical profile. Nonetheless, all formulations exhibited high storage modulus (G') values, from approximately 10^3 Pa during the initial liquid phase up to $10^5 \div 10^6$ Pa once the gel reached stability. Such elevated values can be attributed to the use of telocollagen solution, which typically shows a G' value on the order of 10^3 Pa [191], in contrast to conventional collagen solutions that generally present G' values in the range of $10^1 \div 10^2$ Pa [188]–[190]. This significant enhancement in mechanical properties is particularly noteworthy.

Based on these results, the pure collagen formulation and the collagen with 0.3 w/v% Laponite formulation were selected for the deposition phase.

Deposition was carried out on biomedical-grade zirconia plates that had been pre-treated with a NaOH solution to promote collagen adhesion. Contact angle measurements on both untreated and post-treated zirconia plates confirmed that the treatment improved hydrophilicity, thereby enhancing the adhesion of the hydrophilic groups present in the collagen. This evaluation was also extended to YSZ coatings produced during the study, which demonstrated similarly favourable results.

The preparation and deposition of the two selected formulations were performed at 4°C to prevent premature gelation. Following deposition, the hydrogels were allowed to gel under the conditions determined by the time sweep tests and subsequently subjected to UV cross-linking for 30 and 60 minutes to assess potential modifications in their structure and thermal stability.

Optical microscopy of the six resulting hydrogels revealed a homogeneous deposition, with no significant differences observed among the different formulations and treatments. The hydrogels containing Laponite exhibited a few detectable particles attributable to the added clay. FEG-SEM analysis of the gelled samples revealed a D-pattern, confirming the occurrence of fibrillogenesis, with a value close to the natural 67 nm. The results also demonstrate that Laponite contributes to a more controlled fibrillar assembly, while UV cross-linking affects the overall three-dimensional architecture, which could influence tissue regeneration.

The XRD analysis of the biopolymeric formulations containing 5.8 mg/mL of collagen revealed no significant structural variations, even when considering different Laponite concentrations and applied treatments.

In particular, the two characteristic diffraction peaks of collagen were identified in each case, with the first peak corresponding to an intermolecular lateral packing distance of ~1.14 nm. This value is well aligned with that observed in natural tissue, suggesting a well-structured fibrillar organization and a promising formation of the hydrogel structure [195].

DSC investigations revealed that Td (denaturation temperature) is less sensitive to treatment and formulation variations than Tg. As a result, the thermal stability of the collagen triple helix remained unchanged. In contrast, Tg (glass transition temperature) is more affected by the mobility of the polypeptide chains, which can be influenced by both the treatment and the addition of Laponite.

Finally, these findings confirmed that Laponite, not only improves processability and enhances collagen fibre structuring, but also increases thermal stability without negatively affecting other properties.

4. Conclusion and Future Prospective

This research aimed to develop and optimize a YSZ coating for titanium abutments, ensuring both aesthetic improvements and biocompatibility while minimizing allergic reactions. Additionally, a biopolymeric layer was designed as a top functional coating, applicable on both YSZ films and bulk abutments, with the goal of enhancing cellular activity and, consequently, soft tissue integration.

The study successfully optimized the YSZ deposition process, achieving homogeneous, defect-free coatings with good aesthetic properties, well in accordance with both the aesthetic and technical requirements of clinical dental implantology. Despite its visual improvements, the translucent nature of the coating rendered colorimetric tests unreliable. The final thickness, in the range of a few hundred nanometres, allowed the coating to replicate the surface morphology without altering roughness, an essential factor in preventing bacterial adhesion. Furthermore, long-temperature degradation tests, simulating up to 75 years of exposure in the oral cavity, confirmed the stability of the cubic phase, ensuring durability. Mechanical assessments demonstrated satisfactory results of the coating under clinically relevant forces, particularly in conditions associated with gum disease, where loads remain below 1 N.

Parallelly, the collagen-based biopolymeric layer was carefully formulated and processed to achieve properties known to promote cell adhesion and proliferation. Rheological measurements guided the optimization of deposition parameters, incorporating Laponite RDS to improve shear-thinning behaviour, which led to an increase in post-deposition viscosity, facilitating its application to abutment surface. SEM analyses revealed a homogeneous, fibrillar, and porous structure, which increases the exposed surface area, a feature that improves cellular adhesion, a crucial step for soft tissue integration. This biopolymeric layer is designed to accelerate the integration process, ensuring early-stage tissue integration and preventing delays that could allow bacterial colonization. Additionally, FEG-SEM analysis of the gelled samples showed a D-pattern, confirming fibrillogenesis with a value close to the natural 67 nm. The results also highlight that Laponite promotes controlled fibrillar assembly, while UV cross-linking affects the three-dimensional architecture, potentially influencing tissue regeneration. The crystalline structure closely resembled natural tissue, while high storage modulus values confirmed the mechanical resistance of the formulation, attributed to the use of telocollagen. The rigidity of the substrate further supported cell signalling mechanisms promoting cellular proliferation. DSC analysis revealed an improvement in the thermal stability of the collagen-based layer with both UV cross-linking and Laponite RDS addition.

These findings suggest that the biopolymeric layer has significant potential for improving soft tissue regeneration and integration with a promising formulation consisting of 5.8 mg/mL type I collagen and 0.3 w/v% Laponite for future in vitro cellular studies and in vivo testing. It may also be worthwhile to further investigate the gelled condition alone and the gelled + UV cross-linking (30 minutes) condition to assess potential variations in cellular signalling between these two options.

Despite these promising outcomes, certain limitations must be acknowledged. The lack of reliable colorimetric measurements for the YSZ coating presents a challenge in precisely quantifying its aesthetic properties. Although the biopolymeric layer showed promising characteristics in in vitro assessments, it is important to highlight that the cellular tests, such as cytotoxicity and viability tests, were not conducted due to time and cost constraints. These tests are crucial for evaluating the long-term biocompatibility and effectiveness of the coating, and their absence is a limitation of the present work. However, they are essential for confirming the clinical applicability of the materials developed. Despite the lack of these tests, the results of this research remain significant, and further biological validation through in vitro and in vivo experiments is needed to fully understand the potential of the coating, especially in terms of soft tissue integration and clinical use. Based on the findings of this study, it is already possible to propose the biopolymeric formulation composed of 5.8 mg/mL type I collagen with 0.3 w/v% Laponite, along with specific treatments such as UV cross-linking for further investigation. These conditions will allow for the exploration of their effects on cellular behaviour and tissue integration, marking an important step toward the development of clinically applicable solutions for soft tissue regeneration.

Future research should focus on refining the biopolymeric layer by incorporating bioactive agents, such as growth factors or stem cells, to further stimulate fibroblast activity, which is critical for the transition from inflammation to new soft tissue formation [202]–[205]. Another promising development could involve the lyophilization of the collagen-based solution to obtain a 3D structure that mimics the extracellular matrix, thereby creating a natural environment conducive to cell growth [133], [134], [206].
In conclusion, this research provides a solid foundation for the development of functionalized abutments with enhanced aesthetic and biological properties. Although the results are promising, further in vitro and in vivo studies are essential to fully validate their clinical applicability and assess their potential for successful integration into medical practice. Additionally, the developed strategy could be extended to other biomedical implants that require soft tissue integration, thus expanding its relevance in the fields of implantology and regenerative medicine.

References

[1] J. R. Hupp, "Introduction to Implant Dentistry : Journal of Oral and Maxillofacial Surgery," *J. Oral Maxillofac. Surg.*, vol. 75, no. February, p. 106, 2017.

[2] H. R. Shafie and B. A. White, "Implant Abutment Materials," *Clin. Lab. Man. Dent. Implant Abutments*, pp. 1–16, 2014, doi: 10.1002/9781118928547.ch1.

[3] C. Yurij, "Soft tissue implant integration (part 1)," *UniqaDental*, 2022. https://uniqa.dental/cases/soft-tissue-implant-integration-part-1/

[4] M. Cardoso, J. Sangalli, C. Y. Koga-Ito, L. L. Ferreira, A. S. da Silva Sobrinho, and L. Nogueira, "Abutment Coating With Diamond-Like Carbon Films to Reduce Implant–Abutment Bacterial Leakage," *J. Periodontol.*, vol. 87, no. 2, pp. 168–174, 2016, doi: 10.1902/jop.2015.150362.

[5] T. Odatsu *et al.*, "Antibacterial properties of nano-ag coating on healing abutment: An in vitro and clinical study," *Antibiotics*, vol. 9, no. 6, pp. 1–11, 2020, doi: 10.3390/antibiotics9060347.

[6] N. Areid, F. Abushahba, S. Riivari, and T. Närhi, "Effect of TiO2Abutment Coatings on Peri-Implant Soft Tissue Behavior: A Systematic Review of in Vivo Studies," *Int. J. Dent.*, vol. 2024, 2024, doi: 10.1155/2024/9079673.

[7] D. Lauritano, C. A. Bignozzi, D. Pazzi, F. Cura, and F. Carinci, "Efficacy of a new coating of implantabutment connections in reducing bacterial loading: An in vitro study," *ORAL Implantol.*, vol. 10, no. 1, pp. 1–10, 2017, doi: 10.11138/orl/2017.10.1.001.

[8] M. A. Rodrigues *et al.*, "Antimicrobial profile of a dental implant abutment coating to prevent adhesion and migration of bacteria and screw loosening," *Dent. Mater.*, vol. 37, no. 10, pp. e493–e501, 2021, doi: 10.1016/j.dental.2021.08.016.

[9] M. A. Atieh, N. H. M. Alsabeeha, C. M. Faggion, and W. J. Duncan, "The Frequency of Peri-Implant Diseases: A Systematic Review and Meta-Analysis," *J. Periodontol.*, vol. Reologia f, no. 11, pp. 1586–1598, 2013, doi: 10.1902/jop.2012.120592.

[10] C. T. Lee, Y. W. Huang, L. Zhu, and R. Weltman, "Prevalences of peri-implantitis and peri-implant mucositis: systematic review and meta-analysis," *J. Dent.*, vol. Reologia f, pp. 1–12, 2017, doi: 10.1016/j.jdent.2017.04.011.

[11] P. Diaz, E. Gonzalo, L. J. G. Villagra, B. Miegimolle, and M. J. Suarez, "What is the prevalence of peri-implantitis? A systematic review and meta-analysis," *BMC Oral Health*, vol. Reologia f, no. 1, pp. 1–13, 2022, doi: 10.1186/s12903-022-02493-8.

[12] A. Zangani *et al.*, "Peri-implantitis: a comprehensive review of recent findings," *J. Appl. Cosmetol.*, vol. Reologia f, no. 2, pp. 102–116, 2024, doi: 10.56609/jac.v42i2.396.

[13] P. M. M. Huacho, M. N. M. Nogueira, F. G. Basso, M. J. Junior, R. S. Francisconi, and D. M. P. Spolidorio, "Analyses of biofilm on implant abutment surfaces coating with diamond-like carbon and biocompatibility," *Braz. Dent. J.*, vol. 28, no. 3, pp. 317–323, 2017, doi: 10.1590/0103-6440201601136.

[14] Z. Huang, Z. Wang, K. Yin, C. Li, M. Guo, and J. Lan, "The biocompatibility and mechanical properties

of plasma sprayed zirconia coated abutment," *J. Adv. Prosthodont.*, vol. 12, no. 3, pp. 157–166, 2020, doi: 10.4047/jap.2020.12.3.157.

[15] G. Brunello *et al.*, "Biocompatibility and antibacterial properties of zirconium nitride coating on titanium abutments: An in vitro study," *PLoS One*, vol. 13, no. 6, pp. 1–17, 2018, doi: 10.1371/journal.pone.0199591.

[16] M. E. Jennes, M. Naumann, S. Peroz, F. Beuer, and F. Schmidt, "Antibacterial effects of modified implant abutment surfaces for the prevention of peri-implantitis—a systematic review," *Antibiotics*, vol. 10, no. 11, 2021, doi: 10.3390/antibiotics10111350.

[17] A. Almohandes, I. Abrahamsson, G. Dahlén, and T. Berglundh, "Effect of biofilm formation on implant abutments with an anti-bacterial coating: A pre-clinical in vivo study," *Clin. Oral Implants Res.*, vol. 32, no. 6, pp. 756–766, 2021, doi: 10.1111/clr.13745.

[18] Y. Wang, Y. Zhang, and R. J. Miron, "Health, Maintenance, and Recovery of Soft Tissues around Implants," *Clin. Implant Dent. Relat. Res.*, vol. 18, no. 3, pp. 618–634, 2016, doi: 10.1111/cid.12343.

[19] C. Alves Sousa *et al.*, "Materials Sealing Preventing Biofilm Formation in Implant/Abutment Joints: Which Is the Most Effective? A Systematic Review and Meta-Analysis," *J. Oral Implantol.*, 2020, [Online]. Available: www.joionline.org

[20] B. Zhao *et al.*, "Soft tissue integration versus early biofilm formation on different dental implant materials," *Dent. Mater.*, vol. 30, no. 7, pp. 716–727, 2014, doi: 10.1016/j.dental.2014.04.001.

[21] B. Z. Yijia Wang, Jiebing Zhang, Haoyan Yu, Ning Ding, Ping Ma, "Photothermal modulation of gingival fibroblasts via polydopamine-coated zirconia: A novel approach for promoting peri-implant soft tissue integration," *J. Stomatol. Oral Maxillofac. Surg.*, vol. 125, no. 5, 2024, doi: https://doi.org/10.1016/j.jormas.2024.101925.

[22] F. Cialdai, C. Risaliti, and M. Monici, "Role of fibroblasts in wound healing and tissue remodeling on Earth and in space," *Front. Bioeng. Biotechnol.*, vol. 10, no. October, pp. 1–18, 2022, doi: 10.3389/fbioe.2022.958381.

[23] S. Schultze-Mosgau, M. B. Blatz, F. Wehrhan, K. A. Schlegel, M. Thorwart, and S. Holst, "Principles and mechanisms of peri-implant soft tissue healing.," *Quintessence Int.*, vol. 36, no. 10, pp. 759–69, 2005, [Online]. Available: http://www.ncbi.nlm.nih.gov/pubmed/16261792

[24] J. T. Mingyue Liu, Jianfeng Zhou, Yang Yang, Miao Zheng, Jianjun Yang, "Surface modification of zirconia with polydopamine to enhance fibroblast response and decrease bacterial activity in vitro: A potential technique for soft tissue engineering applications," *Colloids Surfaces B Biointerfaces*, vol. 136, pp. 74–83, 2015, doi: https://doi.org/10.1016/j.colsurfb.2015.06.047.

[25] H. M. Wang, Y. T. Chou, Z. H. Wen, Z. R. Wang, C. H. Chen, and M. L. Ho, "Novel Biodegradable Porous Scaffold Applied to Skin Regeneration," *PLoS One*, vol. 8, no. 6, pp. 2–12, 2013, doi: 10.1371/journal.pone.0056330.

[26] V. Laghezza Masci, A. R. Taddei, G. Gambellini, F. Giorgi, and A. M. Fausto, "Ultrastructural investigation on fibroblast interaction with collagen scaffold," *J. Biomed. Mater. Res. - Part A*, vol.

104, no. 1, pp. 272–282, 2016, doi: 10.1002/jbm.a.35563.

[27] J. Han *et al.*, "Development of Zinc-Containing Chitosan/Gelatin Coatings with Immunomodulatory Effect for Soft Tissue Sealing around Dental Implants," *Tissue Eng. Regen. Med.*, vol. 22, pp. 57–75, 2024, doi: 10.1007/s13770-024-00680-y.

[28] J. Ratanavaraporn, S. Damrongsakkul, N. Sanchavanakit, T. Banaprasert, and S. Kanokpanont, "Comparison of Gelatin and Collagen Scaffolds for Fibroblast Cell Culture," *J. Met. Mater. Miner.*, vol. 16, no. 1, pp. 31–36, 2006.

[29] J. A. M. Ramshaw and V. Glattauer, *Collagen assemblies*. 2019. doi: 10.1088/978-0-7503-2096-2ch4.

[30] T. Wang, L. Wang, Q. Lu, and Z. Fan, "Influence of anodized titanium abutments on the esthetics of the peri-implant soft tissue: A clinical study," *J. Prosthet. Dent.*, vol. 125, no. 3, pp. 445–452, 2021, doi: 10.1016/j.prosdent.2019.12.023.

[31] S. Ishikawa-Nagai, J. D. Da Silva, H. P. Weber, and S. E. Park, "Optical phenomenon of peri-implant soft tissue. Part II. preferred implant neck color to improve soft tissue esthetics," *Clin. Oral Implants Res.*, vol. 18, no. 5, pp. 575–580, 2007, doi: 10.1111/j.1600-0501.2007.01390.x.

[32] M. S. Gil *et al.*, "A prospective clinical trial to assess the optical efficacy of pink neck implants and pink abutments on soft tissue esthetics," *Journal of Esthetic and Restorative Dentistry*, vol. 29, no. 6. pp. 409–415, 2017. doi: 10.1111/jerd.12309.

[33] X. Ding, J. Gao, Z. Wang, H. Awada, and Y. Wang, "A shear-thinning hydrogel that extends in vivo bioactivity of FGF2," *Biomaterials*, vol. 111, pp. 80–89, 2016, doi: 10.1016/j.biomaterials.2016.09.026.

[34] P. Alamán-Díez *et al.*, "Collagen-Laponite Nanoclay Hydrogels for Tumor Spheroid Growth," *Biomacromolecules*, vol. 24, no. 6, pp. 2879–2891, 2023, doi: 10.1021/acs.biomac.3c00257.

[35] E. Puklin-Faucher and M. P. Sheetz, "The mechanical integrin cycle," *J. Cell Sci.*, vol. 122, no. 4, p. 575, 2009, doi: 10.1242/jcs.049544.

[36] P. Kanchanawong and D. A. Calderwood, "Organization, dynamics and mechanoregulation of integrin-mediated cell–ECM adhesions," *Nat. Rev. Mol. Cell Biol.*, vol. 24, no. 2, pp. 142–161, 2023, doi: 10.1038/s41580-022-00531-5.

[37] Y. C. Yeh, J. Y. Ling, W. C. Chen, H. H. Lin, and M. J. Tang, "Mechanotransduction of matrix stiffness in regulation of focal adhesion size and number: Reciprocal regulation of caveolin-1 and β1 integrin," *Sci. Rep.*, vol. 7, no. 1, pp. 1–14, 2017, doi: 10.1038/s41598-017-14932-6.

[38] V. Lughi and V. Sergo, "Low temperature degradation -aging- of zirconia: A critical review of the relevant aspects in dentistry," *Dent. Mater.*, vol. 26, no. 8, pp. 807–820, 2010, doi: 10.1016/j.dental.2010.04.006.

[39] J. E. V. Amarante, M. V. Soares Pereira, G. M. De Souza, M. F. R. Pais Alves, B. G. Simba, and C. dos Santos, "Effect of hydrothermal aging on the properties of zirconia with different levels of translucency," *J. Mech. Behav. Biomed. Mater.*, vol. 109, no. March, 2020, doi: 10.1016/j.jmbbm.2020.103847.

[40] S. Deville *et al.*, “Low-temperature ageing of zirconia-toughened alumina ceramics and its implication in biomedical implants,” *J. Eur. Ceram. Soc.*, vol. 23, no. 15, pp. 2975–2982, 2003, doi: 10.1016/S0955-2219(03)00313-3.

[41] L. O. Massa and J. A. Fraunhofer, *The ADA Practical Guide to Dental Implants*. 2021. doi: 10.1002/9781119630678.

[42] M. Faizullabhoy and G. Wani, “Dental Implants Market - Global Forecast (2024-2032),” *Global Market Insights*, 2023. https://www.gminsights.com/it/industry-analysis/dental-implants-market

[43] F. Schwarz, J. Derks, A. Monje, and H. L. Wang, “Peri-implantitis,” *J. Clin. Periodontol.*, vol. 45, no. June 2016, pp. S246–S266, 2018, doi: 10.1111/jcpe.12954.

[44] B. Klinge, A. Klinge, K. Bertl, and A. Stavropoulos, “Peri-implant diseases,” *Eur. J. Oral Sci.*, vol. 126, no. 10, pp. 88–94, 2018, doi: 10.1111/eos.12529.

[45] A. Mombelli, N. Müller, and N. Cionca, “The epidemiology of peri-implantitis,” *Clin. Oral Implants Res.*, vol. 23, no. SUPPL.6, pp. 67–76, 2012, doi: 10.1111/j.1600-0501.2012.02541.x.

[46] O. Iocca, “Implant abutments,” *Evidence-Based Implant Dent.*, pp. 125–139, 2016, doi: 10.1007/978-3-319-26872-9_8.

[47] K. Holmberg and A. Matthews, *Coatings Tribology: Properties, Mechanisms, Techniques and Applications in Surface Engineering*. 2009. [Online]. Available: https://books.google.com/books?id=SuTrD-AHpyUC&pgis=1

[48] E. John, O. Attia, B. Raton, and C. R. C. Press, “Surface Engineering Of Metals - Principles, Equipment And Technologies,” *Analysis*, no. 1997, pp. 61–83, 1999.

[49] B. S. Saini and V. K. Gupta, “ASM HandBook Volume 05 - Surface Engineering,” *Compr. Guid. Nanocoatings Technol. Vol. 1 Depos. Mech.*, pp. 357–387, 2015, doi: 10.37544/1436-4980-2017-01-02-96.

[50] G. W, “Advanced Protective Coatings for Manufacturing and Engineering,” 2003.

[51] P. M. Martin, *Introduction to Surface Engineering and Functionally Engineered Materials*. 2011. doi: 10.1002/9781118171899.

[52] S. Bull, *Materials Degradation and its Control by Surface Engineering;*, vol. 33, no. 2. 2000. doi: 10.1016/s0301-679x(00)00017-7.

[53] E. Gualteri, “Improving tribological properties of steels by surface texturing and coating,” p. 100, 2008.

[54] M. Eslamian and F. Soltani-Kordshuli, “Development of multiple-droplet drop-casting method for the fabrication of coatings and thin solid films,” *J. Coatings Technol. Res.*, vol. 15, no. 2, pp. 271–280, 2018, doi: 10.1007/s11998-017-9975-9.

[55] Y. Dong, Y. Zou, J. Song, X. Song, and H. Zeng, “Recent progress of metal halide perovskite photodetectors,” *J. Mater. Chem. C*, vol. 5, no. 44, pp. 11369–11394, 2017, doi: 10.1039/c7tc03612d.

[56] B. D. Ratner, *Biomaterials Science: An Introduction to Materials in Medicine*, vol. 7, no. 1. 1996. doi: 10.1088/0305-4624/7/1/408.

[57] D. F. Williams, “On the nature of biomaterials,” *Biomaterials*, vol. 30, no. 30, pp. 5897–5909, 2009,

doi: 10.1016/j.biomaterials.2009.07.027.

[58] A. Hudecki, G. Kiryczyn, and M. J. Łos, *Stem Cells and Biomaterials for Regenerative Medicine, Ch.7 - Biomaterials, Definition, Overview*, no. ii. 2019.

[59] L. Vaiani *et al.*, "Ceramic Materials for Biomedical Applications: An Overview on Properties and Fabrication Processes," *J. Funct. Biomater.*, vol. 14, no. 3, 2023, doi: 10.3390/jfb14030146.

[60] G. P. Jayaswal, S. P. Dange, and A. N. Khalikar, "Bioceramic in dental implants: A review," *J. Indian Prosthodont. Soc.*, vol. 10, no. 1, pp. 8–12, 2010, doi: 10.1007/s13191-010-0002-4.

[61] M. C. Aragón-Duarte *et al.*, "Nanomechanical properties of zirconia- yttria and alumina zirconia- yttria biomedical ceramics, subjected to low temperature aging," *Ceram. Int.*, vol. 43, no. 5, pp. 3931–3939, 2017, doi: 10.1016/j.ceramint.2016.12.033.

[62] R. Riedel, I. Chen, S. K, and D. Strategies, *Ceramic Science and Technology - Volume 2: Properties*. 2010.

[63] T. Kokubo, *Bioceramics and their clinical application*. 2008.

[64] S. Ban, "Classification and Properties of Dental Zirconia as Implant Fixtures and Superstructures," 2021.

[65] R. B. Heimann and H. D. Lehmann, *Bioceramic Coatings for Medical Implants: Trends and Techniques*. 2015. doi: 10.1002/9783527682294.

[66] T. Vagkopoulou, S. O. Koutayas, P. Koidis, and J. R. Strub, "Zirconia in dentistry: Part 1. Discovering the nature of an upcoming bioceramic.," *Eur. J. Esthet. Dent.*, vol. 4, no. 2, pp. 130–151, 2009.

[67] P. M. Martin, *Handbook of Deposition Technologies for Films and Coatings - 3rd edition*, vol. i. 2009.

[68] R. F. Bunshah, *Handbook of Deposition Technologies for Films and Coatings - 2nd edition*. 2001.

[69] D. M. Mattox, *Deposition (PVD) Processing Second edition Dedication To my wife Vivienne*. 2009. [Online]. Available: http://www.elsevier.com/wps/find/bookdescription.cws_home/717814/description#description

[70] A. Zarkov *et al.*, "On the synthesis of yttria-stabilized zirconia: a comparative study," *J. Sol-Gel Sci. Technol.*, vol. 76, no. 2, pp. 309–319, 2015, doi: 10.1007/s10971-015-3778-1.

[71] C. Laberty-Robert, F. Ansart, S. Castillo, and G. Richard, "Synthesis of YSZ powders by the sol-gel method: Surfactant effects on the morphology," *Solid State Sci.*, vol. 4, no. 8, pp. 1053–1059, 2002, doi: 10.1016/S1293-2558(02)01366-3.

[72] M. F. Carolan and J. N. Michaels, "Chemical vapor deposition of yttria stabilized zirconia on porous supports," *Solid State Ionics*, vol. 25, no. 2–3, pp. 207–216, 1987, doi: 10.1016/0167-2738(87)90122-6.

[73] In Deok Jeon; Latifa Gueroudji; Nong M. Hwang, "Deposition of Yttria Stabilized Zirconia by the Thermal CVD Process."

[74] M. K. Baek, S. J. Park, and D. J. Choi, "Synthesis of zirconia (ZrO2) nanowires via chemical vapor deposition," *J. Cryst. Growth*, vol. 459, no. December 2016, pp. 198–202, 2017, doi: 10.1016/j.jcrysgro.2016.12.033.

[75] K. Juškevičius *et al.*, "High-rate reactive magnetron sputtering of zirconia films for laser optics applications," *Appl. Phys. A Mater. Sci. Process.*, vol. 116, no. 3, pp. 1229–1240, 2014, doi: 10.1007/s00339-013-8214-1.

[76] E. S. T. L. S. W. T. O. M. S. A. Barnett, "Deposition and properties of yttria-stabilized zirconia thin films using reactive direct current magnetron sputtering."

[77] F. Smeacetto *et al.*, "Yttria-stabilized zirconia thin film electrolyte produced by RF sputtering for solid oxide fuel cell applications," *Mater. Lett.*, vol. 64, no. 22, pp. 2450–2453, 2010, doi: 10.1016/j.matlet.2010.08.016.

[78] J. Zhang *et al.*, "Fabrication of YSZ ceramic thin films with sol-gel method for mixed potential-type zirconia-based NO2 sensor," *Ceram. Int.*, vol. 50, no. 7, pp. 10698–10705, 2024, doi: 10.1016/j.ceramint.2023.12.385.

[79] C. Wolf and C. Rüssel, "Sol-gel formation of zirconia: preparation, structure and rheology of sols," *J. Mater. Sci.*, vol. 27, no. 14, pp. 3749–3755, 1992, doi: 10.1007/BF00545451.

[80] A. H. Simon, *Handbook of Thin Film Deposition, Ch.4 - Sputter Processing*, Third Edit. Elsevier Inc., 2012. doi: 10.1016/B978-1-4377-7873-1.00004-8.

[81] D. P. Having and V. D. Vapor, "Thin Film Processes," *Thin Film Process.*, 2020, doi: 10.3390/books978-3-03936-265-3.

[82] H. Adachi, T. Hata, and K. Wasa, "Basic Process of Sputtering Deposition," *Handb. Sputter Depos. Technol. Fundam. Appl. Funct. Thin Film. Nano-Materials MEMS Second Ed.*, no. Lcd, pp. 295–359, 2012, doi: 10.1016/B978-1-4377-3483-6.00005-X.

[83] T. Preconditioning, "18 Reactive Sputter Deposition — Setup and Control".

[84] J. Sarkar, *Sputtering and Thin Film Deposition*, vol. 2. 2014. doi: 10.1016/b978-0-8155-1593-7.00002-3.

[85] S. Depla, D.; Mahieu, *Reactive Sputtering Deposition*. Springer, 2008.

[86] R. Buschhaus, M. Prenzel, and A. Von Keudell, "Ion-induced secondary electron emission of oxidized nickel and copper studied in beam experiments," *Plasma Sources Sci. Technol.*, vol. 31, no. 2, p. 25017, 2022, doi: 10.1088/1361-6595/ac4c4c.

[87] C. Corbella, A. Marcak, T. De Los Arcos, and A. Von Keudell, "Revising secondary electron yields of ion-sputtered metal oxides," *J. Phys. D. Appl. Phys.*, vol. 49, no. 16, p. 16LT01, 2016, doi: 10.1088/0022-3727/49/16/16LT01.

[88] S. Sønderby, A. Aijaz, U. Helmersson, K. Sarakinos, and P. Eklund, "Deposition of yttria-stabilized zirconia thin films by high power impulse magnetron sputtering and pulsed magnetron sputtering," *Surf. Coatings Technol.*, vol. 240, pp. 1–6, 2014, doi: 10.1016/j.surfcoat.2013.12.001.

[89] S. Sønderby *et al.*, "Reactive magnetron sputtering of uniform yttria-stabilized zirconia coatings in an industrial setup," *Surf. Coatings Technol.*, vol. 206, no. 19–20, pp. 4126–4131, 2012, doi: 10.1016/j.surfcoat.2012.04.007.

[90] J. Lin and T. C. Stinnett, "Development of thermal barrier coatings using reactive pulsed dc magnetron

sputtering for thermal protection of titanium alloys," *Surf. Coatings Technol.*, vol. 403, no. August, p. 126377, 2020, doi: 10.1016/j.surfcoat.2020.126377.

[91] J. H. Lee and H. W. Kim, "Emerging properties of hydrogels in tissue engineering," *J. Tissue Eng.*, vol. 9, pp. 0–3, 2018, doi: 10.1177/2041731418768285.

[92] B. K. Roy, I. Tahmid, and T. U. Rashid, "Natural-Based Hydrogels for Tissue Engineering Applications," *Eng. Mater. Stem Cell Regen.*, pp. 519–571, 2021, doi: 10.1007/978-981-16-4420-7_19.

[93] H. Choi and W. Choi, "A Review of Advanced Hydrogel Applications for Tissue Engineering and Drug Delivery Systems as Biomaterials," pp. 1–23, 2024.

[94] F. P. Luyten, "Hydrogel Properties and Their Impact on Regenerative Medicine and Tissue Engineering," *Kelley's Textb. Rheumatol. Vol. 1-2, Ninth Ed.*, vol. 1, pp. 90–96, 2012, doi: 10.1016/B978-1-4377-1738-9.00007-4.

[95] M. U. A. Khan, M. A. Aslam, M. F. Bin Abdullah, W. S. Al-Arjan, G. M. Stojanovic, and A. Hasan, "Hydrogels: Classifications, fundamental properties, applications, and scopes in recent advances in tissue engineering and regenerative medicine – A comprehensive review," *Arab. J. Chem.*, vol. 17, no. 10, p. 105968, 2024, doi: 10.1016/j.arabjc.2024.105968.

[96] H. He, L. Wang, X. Cai, Q. Wang, P. Liu, and J. Xiao, "Biomimetic collagen composite matrix-hydroxyapatite scaffold induce bone regeneration in critical size cranial defects," *Mater. Des.*, vol. 236, no. October, p. 112510, 2023, doi: 10.1016/j.matdes.2023.112510.

[97] M. M. Villa, L. Wang, J. Huang, D. W. Rowe, and M. Wei, "Bone tissue engineering with a collagen-hydroxyapatite scaffold and culture expanded bone marrow stromal cells," *J. Biomed. Mater. Res. - Part B Appl. Biomater.*, vol. 103, no. 2, pp. 243–253, 2015, doi: 10.1002/jbm.b.33225.

[98] F. Chen, P. Le, G. M. Fernandes-Cunha, S. C. Heilshorn, and D. Myung, "Bio-orthogonally crosslinked hyaluronate-collagen hydrogel for suture-free corneal defect repair," *Biomaterials*, vol. 255, no. February, p. 120176, 2020, doi: 10.1016/j.biomaterials.2020.120176.

[99] M. Xeroudaki *et al.*, "A porous collagen-based hydrogel and implantation method for corneal stromal regeneration and sustained local drug delivery," *Sci. Rep.*, vol. 10, no. 1, pp. 1–18, 2020, doi: 10.1038/s41598-020-73730-9.

[100] S. R. Moxon, N. J. Corbett, K. Fisher, G. Potjewyd, M. Domingos, and N. M. Hooper, "Blended alginate/collagen hydrogels promote neurogenesis and neuronal maturation," *Mater. Sci. Eng. C*, vol. 104, no. December 2018, p. 109904, 2019, doi: 10.1016/j.msec.2019.109904.

[101] K. Roshanbinfar, M. Fiedler, and F. B. Engel, "Collagen Hydrogel Containing Polyethylenimine-Gold Nanoparticles for Drug Release and Enhanced Beating Properties ofEngineered Cardiac Tissues," *Adv. Healthc. Mater.*, 2023.

[102] K. Roshanbinfar and F. B. Engel, "Electrically Conductive Collagen-PEDOT:PSS Hydrogel Prevents Post-Infarct Cardiac Arrhythmia and Supports hiPSC-Cardiomyocyte Function," *Adv. Mater.*, 2024.

[103] M. Roccuzzo, A. Roccuzzo, C. Marruganti, and S. Fickl, "The importance of soft tissue condition in bone regenerative procedures to ensure long-term peri-implant health," *Periodontol. 2000*, vol. 93, no.

1, pp. 129–138, 2023, doi: 10.1111/prd.12496.

[104] J. M. Pachence, "Collagen-based devices for soft tissue repair," *J. Biomed. Mater. Res.*, vol. 33, no. 1, pp. 35–40, 1996, doi: 10.1002/(SICI)1097-4636(199621)33:1<35::AID-JBM6>3.0.CO;2-N.

[105] J. Meyle *et al.*, "Soft-tissue integration of implants Consensus report of Working Group 2 Björn Klinge Joerg Meyle On behalf of Working Group 2 n," *Clin. Oral Impl. Res*, vol. 17, pp. 93–96, 2006.

[106] M. Li, M. J. Mondrinos, X. Chen, M. R. Gandhi, F. K. Ko, and P. I. Lelkes, "Elastin Blends for Tissue Engineering Scaffolds," *J. Biomed. Mater. Res. Part A*, vol. 79, no. 4, pp. 963–73, 2006, doi: 10.1002/jbm.a.

[107] E. Tamariz and F. Grinnell, "Modulation of Fibroblast Morphology and Adhesion during Collagen Matrix Remodeling," *Mol. Biol. Cell*, vol. 13, no. November, 2002.

[108] D. Williams, "Fibrous proteins in medical technology," *Med. Device Technol.*, vol. 19, no. 6, 2008.

[109] N. A. Hotchin, *Cell biology of extracellular matrix, 2nd edn*, vol. 17, no. 7. 1992. doi: 10.1016/0968-0004(92)90411-2.

[110] J. Brinckmann, "Collagens at a glance," *Top. Curr. Chem.*, vol. 247, pp. 1–6, 2005, doi: 10.1007/b103817.

[111] D. F. Holmes, H. K. Graham, J. A. Trotter, and K. E. Kadler, "STEM/TEM studies of collagen fibril assembly," *Micron*, vol. 32, no. 3, pp. 273–285, 2001, doi: 10.1016/S0968-4328(00)00040-8.

[112] K. M. Pawelec, S. M. Best, and R. E. Cameron, "Collagen: A network for regenerative medicine," *J. Mater. Chem. B*, vol. 4, no. 40, pp. 6484–6496, 2016, doi: 10.1039/c6tb00807k.

[113] D. R. Stamov, E. Stock, C. M. Franz, T. Jähnke, and H. Haschke, "Imaging collagen type I fibrillogenesis with high spatiotemporal resolution," *Ultramicroscopy*, vol. 149. pp. 86–94, 2015. doi: 10.1016/j.ultramic.2014.10.003.

[114] K. E. Michael, D. W. Dumbauld, K. L. Burns, S. K. Hanks, and A. J. García, "Focal adhesion kinase modulates cell adhesion strengthening via integrin activation," *Mol. Biol. Cell*, vol. 20, no. 9, pp. 2508–2519, 2009, doi: 10.1091/mbc.E08-01-0076.

[115] A. C. Theos *et al.*, "Functions of adaptor protein (AP)-3 and AP-1 in tyrosinase sorting from endosomes to melanosomes," *Mol. Biol. Cell*, vol. 16, no. November, pp. 5356–5372, 2005, doi: 10.1091/mbc.E05.

[116] C. Y. Chang Chien, S. H. Chou, and H. H. Lee, "Integrin molecular tension required for focal adhesion maturation and YAP nuclear translocation," *Biochem. Biophys. Reports*, vol. 31, no. 155, 2022, doi: 10.1016/j.bbrep.2022.101287.

[117] H. P. Bachinger, N. P. Morris, and J. M. Davis, "Thermal stability and folding of the collagen triple helix and the effects of mutations in osteogenesis imperfecta on the triple helix of type I collagen," *Am. J. Med. Genet.*, vol. 45, no. 2, pp. 152–162, 1993, doi: 10.1002/ajmg.1320450204.

[118] S. Jimenez, M. Harsch, and J. Rosenbloom, "Hydroxyproline stabilizes the triple helix of chick tendon collagen," *Biochem. Biophys. Res. Commun.*, vol. 52, no. 1, pp. 106–114, 1973, doi: 10.1016/0006-291X(73)90960-1.

[119] E. Bianchi, G. Conio, A. Ciferri, D. Puett, and L. Rajagh, "The role of pH, temperature, salt type, and

salt concentration on the stability of the crystalline, helical, and randomly coiled forms of collagen.," *J. Biol. Chem.*, vol. 242, no. 7, pp. 1361–1369, 1967, doi: 10.1016/s0021-9258(18)96100-4.

[120] J. Rauterberg and K. Kühn, "The Renaturation Behaviour of Modified Collagen Molecules," *Hoppe. Seylers. Z. Physiol. Chem.*, vol. 349, no. 1, pp. 611–622, 1968, doi: 10.1515/bchm2.1968.349.1.611.

[121] J. Spadaro, "Structural Implications of Banding in Unstained Collagen," *Nat. Publ. Gr.*, pp. 78–79, 1970, doi: https://doi.org/10.1038/228078a0.

[122] B. R. Williams, R. A. Gelman, D. C. Poppke, and K. Piez, "Collagen fibril formation. Optimal in vitro conditions and preliminary kinetic results," *J. Biol. Chem.*, vol. 253, no. 18, pp. 6578–6585, 1978, doi: 10.1016/s0021-9258(19)46970-6.

[123] J. F. White, J. A. Werkmeister, I. A. Darby, T. Bisucci, D. E. Birk, and J. A. M. Ramshaw, "Collagen fibril formation in a wound healing model," *J. Struct. Biol.*, vol. 137, no. 1–2, pp. 23–30, 2002, doi: 10.1006/jsbi.2002.4460.

[124] J. R. Harris and A. Reiber, "Influence of saline and pH on collagen type I fibrillogenesis in vitro: Fibril polymorphism and colloidal gold labelling," *Micron*, vol. 38, no. 5, pp. 513–521, 2007, doi: 10.1016/j.micron.2006.07.026.

[125] J. R. Harris, A. Soliakov, and R. J. Lewis, "In vitro fibrillogenesis of collagen type I in varying ionic and pH conditions," *Micron*, vol. 49. pp. 60–68, 2013. doi: 10.1016/j.micron.2013.03.004.

[126] Y. Li, A. Asadi, M. R. Monroe, and E. P. Douglas, "pH effects on collagen fibrillogenesis in vitro: Electrostatic interactions and phosphate binding," *Materials Science and Engineering C*, vol. 29, no. 5. pp. 1643–1649, 2009. doi: 10.1016/j.msec.2009.01.001.

[127] J. Ratanavaraporn, S. Kanokpanont, Y. Tabata, and S. Damrongsakkul, "Effects of acid type on physical and biological properties of collagen scaffolds," *J. Biomater. Sci. Polym. Ed.*, vol. 19, no. 7, pp. 945–952, 2008, doi: 10.1163/156856208784613505.

[128] J. Gross, "Influence of time on the reversible association between large molecules: The collagen system [12]," *Nature*, vol. 181, no. 4608. p. 556, 1958. doi: 10.1038/181556a0.

[129] C. M. Tierney, M. G. Haugh, J. Liedl, F. Mulcahy, B. Hayes, and F. J. O'Brien, "The effects of collagen concentration and crosslink density on the biological, structural and mechanical properties of collagen-GAG scaffolds for bone tissue engineering," *J. Mech. Behav. Biomed. Mater.*, vol. 2, no. 2, pp. 202–209, 2009, doi: 10.1016/j.jmbbm.2008.08.007.

[130] C. M. Tierney, M. J. Jaasma, and F. J. O'Brien, "Osteoblast activity on collagen-GAG scaffolds is affected by collagen and GAG concentrations," *J. Biomed. Mater. Res. - Part A*, vol. 91, no. 1, pp. 92–101, 2009, doi: 10.1002/jbm.a.32207.

[131] E. Suesca, A. M. A. Dias, M. E. M. Braga, H. C. de Sousa, and M. R. Fontanilla, "Multifactor analysis on the effect of collagen concentration, cross-linking and fiber/pore orientation on chemical, microstructural, mechanical and biological properties of collagen type I scaffolds," *Mater. Sci. Eng. C*, vol. 77, pp. 333–341, 2017, doi: 10.1016/j.msec.2017.03.243.

[132] M. Madaghiele, A. Sannino, I. V. Yannas, and M. Spector, "Collagen-based matrices with axially

oriented pores," *J. Biomed. Mater. Res. - Part A*, vol. 85, no. 3, pp. 757–767, 2008, doi: 10.1002/jbm.a.31517.

[133] F. J. O'Brien, B. A. Harley, I. V. Yannas, and L. J. Gibson, "The effect of pore size on cell adhesion in collagen-GAG scaffolds," *Biomaterials*, vol. 26, no. 4, pp. 433–441, 2005, doi: 10.1016/j.biomaterials.2004.02.052.

[134] F. J. O. O'Brien, B. A. Harley, I. V Yannas, and L. Gibson, "Influence of freezing rate on pore structure in freeze-dried collagen-GAG scaffolds," vol. 25, pp. 1077–1086, 2004, doi: 10.1016/S0142-9612(03)00630-6.

[135] M. Nair, R. K. Johal, S. W. Hamaia, S. M. Best, and R. E. Cameron, "Tunable bioactivity and mechanics of collagen-based tissue engineering constructs: A comparison of EDC-NHS, genipin and TG2 crosslinkers," *Biomaterials*, vol. 254. 2020. doi: 10.1016/j.biomaterials.2020.120109.

[136] N. Davidenko *et al.*, "Control of crosslinking for tailoring collagen-based scaffolds stability and mechanics," *Acta Biomater.*, vol. 25, pp. 131–142, 2015, doi: 10.1016/j.actbio.2015.07.034.

[137] N. Davidenko *et al.*, "Optimisation of UV irradiation as a binding site conserving method for crosslinking collagen-based scaffolds," *J. Mater. Sci. Mater. Med.*, vol. 27, no. 1, pp. 1–17, 2016, doi: 10.1007/s10856-015-5627-8.

[138] K. S. Weadock, E. J. Miller, L. D. Bellincampi, J. P. Zawadsky, and M. G. Dunn, "Physical crosslinking of collagen fibers: Comparison of ultraviolet irradiation and dehydrothermal treatment," *J. Biomed. Mater. Res.*, vol. 29, no. 11, pp. 1373–1379, 1995, doi: 10.1002/jbm.820291108.

[139] C. Yang, "Enhanced physicochemical properties of collagen by using EDC/NHS-crosslinking," *Bull. Mater. Sci.*, vol. 35, no. 5, pp. 913–918, 2012, doi: 10.1007/s12034-012-0376-5.

[140] A. Lu, Y. Gao, T. Jin, X. Luo, Q. Zeng, and Z. Shang, "Effects of surface roughness and texture on the bacterial adhesion on the bearing surface of bio-ceramic joint implants: An in vitro study," *Ceram. Int.*, vol. 46, no. 5, pp. 6550–6559, 2020, doi: 10.1016/j.ceramint.2019.11.139.

[141] S. Al-Amshawee, M. Y. B. M. Yunus, J. G. Lynam, W. H. Lee, F. Dai, and I. H. Dakhil, "Roughness and wettability of biofilm carriers: A systematic review," *Environ. Technol. Innov.*, vol. 21, 2021, doi: 10.1016/j.eti.2020.101233.

[142] H. G. Scott, "Phase relationships in the zirconia-yttria system," *J. Mater. Sci.*, 1975, doi: 10.1007/bf01031853.

[143] J. Chevalier and L. Gremillard, *Zirconia ceramics*. Woodhead Publishing Limited, 2008. doi: 10.1533/9781845694227.2.243.

[144] U. Sutharsini *et al.*, "Effect of two-step sintering on the hydrothermal ageing resistance of tetragonal zirconia polycrystals," *Ceram. Int.*, vol. 43, no. 10, pp. 7594–7599, 2017, doi: 10.1016/j.ceramint.2017.03.052.

[145] E. Rosado, S. Marín-Cortés, and R. Moreno, "Sintering, mechanical properties and hydrothermal resistance of ZrO2/ZrSiO4 slip cast composites," *J. Eur. Ceram. Soc.*, vol. 44, no. 11, pp. 6576–6585, 2024, doi: 10.1016/j.jeurceramsoc.2024.04.039.

[146] Sigma - Aldrich, “Bovine Collagen Solutions - Product Information,” 2016.

[147] Advanced BioMatrix, “Collagen Gelation Diagnosis.” 2019. [Online]. Available: file:///S:/LAB PROJECTS/2020/2020-2098 - Abutment coating study/02_TECHNICAL/Testing/3.TESI/2.TEST METHOD AND RESULTS/Collagene/1.PREPARAZIONE/BIBLIOGRAFIA/2) Advanced BioMatrix - Collagen Gelation Diagnosis.html

[148] Ibidi GmbH, “Preparation of Collagen I Gels.” 2023.

[149] D. C. Harris, *Quantitative Chemical Analysis*. 2010.

[150] N. Corporation, “Collagen coating protocol”, [Online]. Available: https://www.neuvitro.com/collagen-coating-protocol#:~:text=Dilute collagen to 50ug%2Fml with 0.01M HCl. Add,with PBS or culture medium to remove acid.

[151] J. E. Lee, J. C. Park, Y. S. Hwang, J. K. Kim, J. G. Kim, and H. Sub, “Characterization of UV-irradiated dense/porous collagen membranes: morphology, enzymatic degradation, and mechanical properties.,” *Yonsei Med. J.*, vol. 42, no. 2, pp. 172–179, 2001, doi: 10.3349/ymj.2001.42.2.172.

[152] Hutchison, *Electron Microscopy: Principles and Fundamentals*, vol. 190, no. 3. 1998. doi: 10.1046/j.1365-2818.1998.0358c.x.

[153] Y. Nan, *Focused ion beam systems: Basics and applications*, vol. 9780521831. 2007. doi: 10.1017/CBO9780511600302.

[154] R. L. McCreery, *Raman Spectroscopy for Chemical Analysis*, vol. 12, no. 5. 2001. doi: 10.1088/0957-0233/12/5/704.

[155] G. F. Harrington and J. Santiso, “Back-to-Basics tutorial: X-ray diffraction of thin films,” *J. Electroceramics*, vol. 47, no. 4, pp. 141–163, 2021, doi: 10.1007/s10832-021-00263-6.

[156] S. Points, “An International Organization for Standardization,” *Science (80-.).*, vol. 63, no. 1639, pp. 539–539, 1926, doi: 10.1126/science.63.1639.539.a.

[157] ISO 3274, “Geometrical Product Specifications (GPS) - Surface texture: Profile method - Nominal characteristics of contact (stylus) instruments,” no. 1. p. 13, 1996.

[158] Datacolor, “Colorimetric Fundamentals CIELAB”.

[159] CIE and Commission Internationale de l’Eclairage, “Colorimetry - Part 4: CIE 1976 L*a*b* COLOUR SPACE,” pp. 1–16, 2007.

[160] International Standard International Standard, *ISO 14577 - Instrumented indentation test for hardness and materials parameters - Test method for metallic and non-metallic coatings*. 2007.

[161] International Organization for Standardization, *Fine ceramics (advanced ceramics, advanced technical ceramics) — Determination of adhesion of ceramic coatings by scratch testing*. 2005.

[162] P. Sánchez-Cid, M. Jiménez-Rosado, V. Perez-Puyana, A. Guerrero, and A. Romero, “Rheological and microstructural evaluation of collagen-based scaffolds crosslinked with fructose,” *Polymers (Basel).*, vol. 13, no. 4, pp. 1–11, 2021, doi: 10.3390/polym13040632.

[163] R. Vulpe *et al.*, “Rheological study of in-situ crosslinkable hydrogels based on hyaluronanic acid, collagen and sericin,” *Mater. Sci. Eng. C*, vol. 69, pp. 388–397, 2016, doi: 10.1016/j.msec.2016.07.003.

[164] K. Pietrucha, “Changes in denaturation and rheological properties of collagen-hyaluronic acid scaffolds as a result of temperature dependencies,” *Int. J. Biol. Macromol.*, vol. 36, no. 5, pp. 299–304, 2005, doi: 10.1016/j.ijbiomac.2005.07.004.

[165] V. Samouillan, J. Dandurand, C. Lacabanne, R. J. Thoma, A. Adams, and M. Moore, “Comparison of chemical treatments on the chain dynamics and thermal stability of bovine pericardium collagen,” *J. Biomed. Mater. Res. - Part A*, vol. 64, no. 2, pp. 330–338, 2003, doi: 10.1002/jbm.a.10326.

[166] D. Y. Kwok and A. W. Neumann, *Contact angle measurement and contact angle interpretation*, vol. 81, no. 3. 1999. doi: 10.1016/S0001-8686(98)00087-6.

[167] R. S. Hebbar, A. M. Isloor, and A. F. Ismail, *Contact Angle Measurements*. Elsevier B.V., 2017. doi: 10.1016/B978-0-444-63776-5.00012-7.

[168] E. Fernandez Lopez, V. Sanchez Escribano, M. Panizza, M. M. Carnasciali, and G. Busca, “Vibrational and electronic spectroscopic properties of zirconia powders,” *J. Mater. Chem.*, vol. 11, no. 7, pp. 1891–1897, 2001, doi: 10.1039/b100909p.

[169] S. N. Basahel, T. T. Ali, M. Mokhtar, and K. Narasimharao, “Influence of crystal structure of nanosized ZrO2 on photocatalytic degradation of methyl orange,” *Nanoscale Res. Lett.*, vol. 10, no. 1, 2015, doi: 10.1186/s11671-015-0780-z.

[170] Y. Hemberger, N. Wichtner, C. Berthold, and K. G. Nickel, “Quantification of yttria in stabilized zirconia by Raman spectroscopy,” *Int. J. Appl. Ceram. Technol.*, vol. 13, no. 1, pp. 116–124, 2016, doi: 10.1111/ijac.12434.

[171] S. Sathish, M. Geetha, S. T. Aruna, N. Balaji, K. S. Rajam, and R. Asokamani, “Studies on plasma sprayed bi-layered ceramic coating on bio-medical Ti-13Nb-13Zr alloy,” *Ceram. Int.*, vol. 37, no. 4, pp. 1333–1339, 2011, doi: 10.1016/j.ceramint.2010.12.012.

[172] F. Zhang, H. Reveron, B. C. Spies, B. Van Meerbeek, and J. Chevalier, “Trade-off between fracture resistance and translucency of zirconia and lithium-disilicate glass ceramics for monolithic restorations,” *Acta Biomater.*, vol. 91, no. April, pp. 24–34, 2019, doi: 10.1016/j.actbio.2019.04.043.

[173] D. G. Lamas and N. E. Walsöe De Reca, “X-ray diffraction study of compositionally homogeneous, nanocrystalline yttria-doped zirconia powders,” *J. Mater. Sci.*, vol. 35, no. 22, pp. 5563–5567, 2000, doi: 10.1023/A:1004896727413.

[174] G. Zhou, P. Jin, Y. Wang, G. Pei, J. Wu, and Z. Wang, “X-ray diffraction analysis of the yttria stabilized zirconia powder by mechanical alloying and sintering,” *Ceram. Int.*, vol. 46, no. 7, pp. 9691–9697, 2020, doi: 10.1016/j.ceramint.2019.12.236.

[175] H. Ding, A. V. Virkar, and F. Liu, “Defect configuration and phase stability of cubic versus tetragonal yttria-stabilized zirconia,” *Solid State Ionics*, vol. 215, pp. 16–23, 2012, doi: 10.1016/j.ssi.2012.03.014.

[176] S. Fabris, A. T. Paxton, and M. W. Finnis, “A stabilization mechanism of zirconia based on oxygen vacancies only,” *Acta Mater.*, vol. 50, no. 20, pp. 5171–5178, 2002, doi: 10.1016/S1359-6454(02)00385-3.

[177] M. Raza, D. Cornil, J. Cornil, S. Lucas, R. Snyders, and S. Konstantinidis, “Oxygen vacancy stabilized

zirconia (OVSZ); a joint experimental and theoretical study," *Scr. Mater.*, vol. 124, pp. 26–29, 2016, doi: 10.1016/j.scriptamat.2016.06.025.

[178] S. Sprio, S. Guicciardi, A. Bellosi, and G. Pezzotti, "Yttria-stabilized zirconia films grown by radiofrequency magnetron sputtering: Structure, properties and residual stresses," *Surf. Coatings Technol.*, vol. 200, no. 14–15, pp. 4579–4585, 2006, doi: 10.1016/j.surfcoat.2005.04.003.

[179] L. D. Huy, P. Laffez, P. Daniel, A. Jouanneaux, N. T. Khoi, and D. Siméone, "Structure and phase component of ZrO2 thin films studied by Raman spectroscopy and X-ray diffraction," *Mater. Sci. Eng. B*, vol. 104, no. 3, pp. 163–168, 2003, doi: 10.1016/S0921-5107(03)00190-9.

[180] G. S. Kaliaraj *et al.*, "Bio-inspired YSZ coated titanium by EB-PVD for biomedical applications," *Surf. Coatings Technol.*, vol. 307, pp. 227–235, 2016, doi: 10.1016/j.surfcoat.2016.08.039.

[181] A. Dychalska, P. Popielarski, W. Franków, K. Fabisiak, K. Paprocki, and M. Szybowicz, "Study of CVD diamond layers with amorphous carbon admixture by Raman scattering spectroscopy," *Mater. Sci. Pol.*, vol. 33, no. 4, pp. 799–805, 2015, doi: 10.1515/msp-2015-0067.

[182] C. C. Zhang, S. Hartlaub, I. Petrovic, and B. Yilmaz, "Raman Spectroscopy Characterization of Amorphous Coke Generated in Industrial Processes," *ACS Omega*, vol. 7, no. 3, pp. 2565–2570, 2022, doi: 10.1021/acsomega.1c03456.

[183] R. Olivares, S. E. Rodil, and H. Arzate, "In vitro studies of the biomineralization in amorphous carbon films," *Surf. Coatings Technol.*, vol. 177–178, pp. 758–764, 2004, doi: 10.1016/j.surfcoat.2003.08.018.

[184] S. E. Rodil, R. Olivares, H. Arzate, and S. Muhl, "Properties of carbon films and their biocompatibility using in-vitro tests," *Diam. Relat. Mater.*, vol. 12, no. 3–7, pp. 931–937, 2003, doi: 10.1016/S0925-9635(02)00217-0.

[185] S. E. Rodil, R. Olivares, H. Arzate, and S. Muhl, "Biocompatibility, cytotoxicity and bioactivity of amorphous carbon films," *Top. Appl. Phys.*, vol. 100, no. April 2006, pp. 55–75, 2006, doi: 10.1007/11378235_3.

[186] B. Balakrishnan, D. Soman, U. Payanam, A. Laurent, D. Labarre, and A. Jayakrishnan, *A novel injectable tissue adhesive based on oxidized dextran and chitosan*, vol. 53. 2017. doi: 10.1016/j.actbio.2017.01.065.

[187] J. M. Zuidema, C. J. Rivet, R. J. Gilbert, and F. A. Morrison, "A protocol for rheological characterization of hydrogels for tissue engineering strategies," *J. Biomed. Mater. Res. - Part B Appl. Biomater.*, vol. 102, no. 5, pp. 1063–1073, 2014, doi: 10.1002/jbm.b.33088.

[188] A. Sancho, L. Vázquez, and E. M. De-Juan-Pardo, "Effect of cold storage on collagen-based hydrogels for the three-dimensional culture of adipose-derived stem cells," *Biofabrication*, vol. 6, no. 3, 2014, doi: 10.1088/1758-5082/6/3/035017.

[189] K. Slater, J. Partridge, and H. Nandivada, "Tuning the Elastic Moduli of Corning ® Matrigel ® and Collagen I 3D Matrices by Varying the Protein Concentration Application Note," *Corning Inc. Life Sci.*, vol. 1, no. I, pp. 1–8, 2018.

[190] C. Valero, H. Amaveda, M. Mora, and J. M. García-Aznar, "Combined experimental and computational

characterization of crosslinked collagen-based hydrogels," *PLoS One*, vol. 13, no. 4, pp. 1–16, 2018, doi: 10.1371/journal.pone.0195820.

[191] Advanced Biomatrix, "Mechanical Stiffness Testing of Collagen Products," *White Pap.*, vol. 2, no. Clm, pp. 1–3, 2019.

[192] A. Nelson and T. Cosgrove, "A Small-Angle Neutron Scattering Study of Adsorbed Poly(ethylene oxide) on Laponite," *Langmuir*, vol. 20, no. 6, pp. 2298–2304, 2004, doi: 10.1021/la035268t.

[193] J. Shi, C. Wang, T. Ngai, and W. Lin, "Diffusion and Binding of Laponite Clay Nanoparticles into Collagen Fibers for the Formation of Leather Matrix," *Langmuir*, vol. 34, no. 25, pp. 7379–7385, 2018, doi: 10.1021/acs.langmuir.8b00923.

[194] S. Y. Bak, S. W. Lee, C. H. Choi, and H. W. Kim, "Assessment of the influence of acetic acid residue on type I collagen during isolation and characterization," *Materials (Basel).*, vol. 10, no. 12, 2018, doi: 10.3390/ma11122518.

[195] Z. Meng, X. Zheng, K. Tang, J. Liu, Z. Ma, and Q. Zhao, "Dissolution and regeneration of collagen fibers using ionic liquid," *Int. J. Biol. Macromol.*, vol. 51, no. 4, pp. 440–448, 2012, doi: 10.1016/j.ijbiomac.2012.05.030.

[196] M. Vedhanayagam, S. Anandasadagopan, B. U. Nair, and K. J. Sreeram, "Polymethyl methacrylate (PMMA) grafted collagen scaffold reinforced by PdO–TiO2 nanocomposites," *Mater. Sci. Eng. C*, vol. 108, no. July 2020, 2020, doi: 10.1016/j.msec.2019.110378.

[197] B. Wu, C. Mu, G. Z. And, and W. Lin, "Effects of Cr3+ on the structure of collagen fiber," *Langmuir*, vol. 25, no. 19, pp. 11905–11910, 2009, doi: 10.1021/la901577j.

[198] Z. Tian, Y. Wang, H. Wang, and K. Zhang, "Regeneration of native collagen from hazardous waste: chrome-tanned leather shavings by acid method," *Environ. Sci. Pollut. Res.*, vol. 27, no. 25, pp. 31300–31310, 2020, doi: 10.1007/s11356-020-09183-4.

[199] W. Liao, X. Guanghua, Y. Li, X. R. Shen, and C. Li, "Comparison of characteristics and fibril-forming ability of skin collagen from barramundi (Lates calcarifer) and tilapia (Oreochromis niloticus)," *Int. J. Biol. Macromol.*, vol. 107, no. PartA, pp. 549–559, 2018, doi: 10.1016/j.ijbiomac.2017.09.022.

[200] C. Li, Z. Tian, W. Liu, and G. Li, "Structural properties of pepsin-solubilized collagen acylated by lauroyl chloride along with succinic anhydride," *Mater. Sci. Eng. C*, vol. 55, pp. 327–334, 2015, doi: 10.1016/j.msec.2015.05.055.

[201] M. Banach, Z. Kowalski, Z. Wzorek, and K. Gorazda, "A chemical method of the production of 'heavy' sodium tripolyphosphate with the high content of Form i or Form II," *Polish J. Chem. Technol.*, vol. 11, no. 2, pp. 13–20, 2009, doi: 10.2478/v10026-009-0018-x.

[202] R. G. Young, D. L. Butler, W. Weber, A. I. Caplan, S. L. Gordon, and D. J. Fink, "Use of mesenchymal stem cells in a collagen matrix for achilles tendon repair," *J. Orthop. Res.*, vol. 16, no. 4, pp. 406–413, 1998, doi: 10.1002/jor.1100160403.

[203] Z. Zhang *et al.*, "Sodium alginate/collagen hydrogel loaded with human umbilical cord mesenchymal stem cells promotes wound healing and skin remodeling," *Cell Tissue Res.*, vol. 383, no. 2, pp. 809–

821, 2021, doi: 10.1007/s00441-020-03321-7.

[204] A. Y. Wang, S. Leong, Y. C. Liang, R. C. C. Huang, C. S. Chen, and S. M. Yu, "Immobilization of growth factors on collagen scaffolds mediated by polyanionic collagen mimetic peptides and its effect on endothelial cell morphogenesis," *Biomacromolecules*, vol. 9, no. 10, pp. 2929–2936, 2008, doi: 10.1021/bm800727z.

[205] Y. Yang *et al.*, "Collagen-binding human epidermal growth factor promotes cellularization of collagen scaffolds," *Tissue Eng. - Part A*, vol. 15, no. 11, pp. 3589–3596, 2009, doi: 10.1089/ten.tea.2008.0648.

[206] F. J. O'Brien, B. A. Harley, I. V. Yannas, and L. Gibson, "Influence of freezing rate on pore structure in freeze-dried collagen-GAG scaffolds," *Biomaterials*, vol. 25, no. 6, pp. 1077–1086, 2004, doi: 10.1016/S0142-9612(03)00630-6.